Lawrence Berkeley National Laboratory

Title

TWO DIMENSIONAL NMR OF LIQUIDS AND ORIENTED MOLECULES

Permalink

https://escholarship.org/uc/item/5xb022ks

Author

Gochin, M.

Publication Date

1987-02-01

Peer reviewed

Lawrence Berkeley Laboratory
UNIVERSITY OF CALIFORNIA

Materials & Chemical Sciences Division

TWO DIMENSIONAL NMR OF LIQUIDS AND ORIENTED MOLECULES

M. Gochin
(Ph.D. Thesis)

February 1987

Two Dimensional NMR of Liquids

and Oriented Molecules

by

Miriam Gochin

Lawrence Berkeley Laboratory
University of California
Berkeley, California 94720

February 1987

ABSTRACT

This thesis concerns the development and application of two dimensional multiple quantum NMR to the study of molecules in liquid and liquid crystal media. New methods have been devised for obtaining information about previously intractable chemical systems. In addition, a high speed parallel interface for data transmission between a mini- and main-frame computer is described, as well as a two-dimensional programming facility for data processing and plotting.

Chapter 1 discusses the quantum mechanical formalism used for describing the interaction between magnetic dipoles that dictates the appearance of a spectrum. The NMR characteristics of liquids and liquid crystals are stressed. Chapter 2 reviews the theory of multiple quantum and two dimensional NMR, as it applies to the present study. Properties of typical spectra and phase cycling procedures are discussed.

Chapter 3 describes a specific application of heteronuclear double quantum coherence to the removal of inhomogeneous broadening in liquids. Pulse sequences have been devised which cancel out any contribution from this inhomogeneity to the final spectrum. An interpretation of various pulse sequences for the case of ^{13}C and ^{1}H is given, together with methods of spectral editing by removal or retention of the homo- or heteronuclear J coupling. The technique is applied to a demonstration of high resolution in both frequency and spatial dimensions with a surface coil.

In Chapter 4, multiple quantum filtered 2-D spectroscopy is demonstrated as an effective means of studying randomly deuterated

molecules dissolved in a nematic liquid crystal. Magnitudes of dipole coupling constants have been determined for benzene and hexane, and their signs and assignments found from high order multiple quantum spectra. For the first time, a realistic impression of the conformation of hexane can be estimated from these results.

Chapter 5 is a technical description of the MDB DCHIB-DR11W parallel interface which has been set up to transfer data between the Data General Nova 820 minicomputer, interfaced to the 360 MHz spectrometer, and the Vax 11/730. It covers operation of the boards, physical specifications and installation, and programs for testing and running the interface.

To my parents and to Larry

Acknowledgements

I have had the good fortune to carry out my graduate research with Prof. Alex Pines, who provided a constant source of inspiration, encouragement and enthusiasm and endowed me with a sense of the high standards that he has always pursued in science. My thanks also go to members of the Pines group, for providing a stimulating intellectual environment, and for help in many ways. Particular thanks go to Kurt Schenker and Deirdre Hugi, who participated in the 2-D work, and to Dan Weitekamp who helped me to understand the wily ways of coherence. Jean Baum, Joel Garbow, Michael Munowitz and Jim Murdoch helped me in the early days to understand the vagaries of spectrometers, computers and multiple quantum NMR. Chuck Connor helped me to design the surface coil probe. Paul Jonsen always provided advice, a ready smile, and also asked to be remembered for his negative feedback (positive feedback being explosive). Peter Neidig and A.J. Shaka have been very helpful in patiently explaining any questions that I've had. Kurt, Paul and A.J. have been constant Roma companions.

I am also indebted to Dr. Mel Klein and to his former graduate students Alan Koretsky and Greg Karczmar for their support and confidence in me. Help from Professors Luz and Vega at the Weizmann Institute of Science made my short visit there both pleasant and productive. Herbert Zimmermann has been of invaluable assistance in the preparation of samples. Thanks go to the technical staff in the machine shop, electronics shop, glass shop and stockrooms for ready and cheerful assistance. Dione Carmichael has always been very helpful. Pete Goodeve assisted with programming on the Data General.

Finally, I would like to thank all my friends and family, especially Larry.

TABLE OF CONTENTS

CHAPTER 1

Introduction

Much of the development of modern day NMR is directed towards finding ways to reduce the complexity of NMR spectra from interesting but complex spin systems, and increase the information available about their structure and chemical composition. This work will focus on certain aspects of simplification or manipulation of NMR spectra of liquids and liquid crystal samples, mainly by the application of multiple quantum coherence[1-4].

The interactions which determine the appearance of the NMR spectrum are dictated by the Hamiltonian:

$$\mathcal{H}_{NMR} = \mathcal{H}_{ext} + \mathcal{H}_{int},\qquad(1.1)$$

where $\mathcal{H}_{ext}$ is the external Hamiltonian involving the interaction of the nuclear spins with the external magnetic field(s), and $\mathcal{H}_{int}$ is the internal Hamiltonian describing the interaction between pairs of spins or between spins and their electronic environment.

$$\mathcal{H}_{ext} = \mathcal{H}_z + \mathcal{H}_{rf}\qquad(1.2a)$$

$$\mathcal{H}_{int} = \mathcal{H}_{cs} + \mathcal{H}_J + \mathcal{H}_D + \mathcal{H}_Q\qquad(1.2b)$$

These terms will be described in sufficient detail below. At the moment we just indicate that each of these interactions takes the form

$$\mathcal{H} \sim \underline{X}.\underline{\underline{A}}.\underline{I}\qquad(1.3)$$

$\underline{I}$ is the vector operator (I_x, I_y, I_z) of the nucleus being considered, $\underline{X}$ can be, depending on the type of interaction, a vector operator or a

magnetic field vector. $\underset{\approx}{A}$ is a symmetric second rank Cartesian tensor describing the physical interaction between $\underline{I}$ and $\underline{X}$. $\mathcal{H}_{ext}$ arises from the fact that we perturb the system in order to measure it, but it is the components of $\mathcal{H}_{int}$ that are interesting for structural information. A spectrum of a solid material with spin $I > 1/2$ will contain all of the above terms of $\mathcal{H}_{int}$ and may be complex. On the other hand, in a liquid, $\mathcal{H}_D$ and $\mathcal{H}_Q$ are averaged to zero by natural rapid molecular tumbling. Hence, liquid state spectra usually appear extremely simple and provide a well established technique for chemical identification. A lot of NMR development is directed towards coherent averaging of the tensor $\underset{\approx}{A}$ in Cartesian space, or of the vector product $\underline{I} \times \underline{X}$ in spin space, in order to obtain high resolution solid state spectra.

Each of the interactions in the Hamiltonian will be briefly considered in turn, with particular emphasis placed on the partial averaging of these interactions in a liquid crystal environment.

The External Hamiltonian

1.1 THE ZEEMAN HAMILTONIAN

The Zeeman Hamiltonian describes the direct coupling of nuclear magnetic dipoles with an externally applied static magnetic field. It has the form

$$\mathcal{H}_z = \underline{H}_0 \cdot \underset{\approx}{Z} \cdot \underline{I} \tag{1.4}$$

$\underline{H}_0$ is the static field along z, $(0, 0, H_0)$, and $\underset{\approx}{Z}$ is the coupling matrix between $\underline{I}$ and $\underline{H}_0$:

$$\underset{\approx}{Z} = -\gamma_I \begin{bmatrix} 1 & 0 & 0 \\ 0 & 1 & 0 \\ 0 & 0 & 1 \end{bmatrix}$$

γ_I is the gyromagnetic ratio. Expansion of equation (1.4) yields

$$\mathcal{H}_z = -\gamma_I H_0 I_z \tag{1.5}$$

. $\mathcal{H}_z$ is usually the largest interaction in the nuclear spin Hamiltonian, and defines the separation of nuclear energy levels in a magnetic field, and the frequency of precession of the nucleus about the applied field:

$$\Delta E = \gamma \hbar H_0 = \hbar \omega_0 = h \nu_0. \tag{1.6}$$

ν_0 is the characteristic Larmor frequency in Hz. ω_0 is the corresponding value in radians/sec. While spectral parameters such as line positions, line widths and splittings are usually expressed in Hz, it is often convenient to use ω as an expression for frequency in the Hamiltonian. Often, it appears as "ωt", an angle in radians, which is more concise than "$2\pi\nu t$". All of the Hamiltonians given here will be given in units of radians/sec.

For a spectrometer operating at 360 MHz, the proton energy level splitting results in a Boltzmann population distribution of

$$p_1/p_2 = \exp (\Delta E/kT) \tag{1.7}$$
$$= 1.000058 \text{ at } 25^0 \text{C},$$

where p_1 is the ground and p_2 the excited state. This very small difference implies that spins experience a very small magnetization in an applied field, and that the biggest inherent difficulty in NMR is low sensitivity. The problem is greater for lower γ nuclei such as ^{13}C or ^{15}N. Detection of these nuclei suffers from the additional

fact that they occur with very low natural abundance. In these cases, we often make use of the abundant protons in the surroundings to transfer polarization to the dilute spins in order to improve their sensitivity.

In the case where the externally applied static field is inhomogeneous, H_O in equation (1.5) must be replaced by $H_O + \Delta H_0(\tilde{r})$; $\tilde{r}$ is a position vector. The line position ω now becomes $\omega_0 + \Delta\omega_0(\tilde{r})$, where $\Delta\omega_0(\tilde{r}) = \gamma \Delta H_0(\tilde{r})$, so that the spectrum is broadened. This may be caused by field inhomogeneity or by local susceptibility inhomogeneity effects within the sample. It will be one of the subjects of discussion in Chapter 3.

1.2 THE RADIOFREQUENCY HAMILTONIAN, $\mathcal{H}_{rf}$

Radiofrequency pulses are used to induce transitions between energy levels. The interaction between the radiofrequency field and spin I is given by:

$$\mathcal{H}_{rf} = \underline{H}_1 \cdot \underset{\approx}{Z} \cdot \underline{I}$$

$\underline{H}_1$ is the field applied by rf irradiation in the x,y plane. Along x, this equation reduces to:

$$\mathcal{H}_{rf} = - \gamma_I \ 2H_{1x} \cos \omega t$$
$$= - 2\omega_1 \cos \omega t. \qquad (1.8)$$

ω is the frequency of the applied rf (in radians) and $2H_{1x}$ is its intensity. If $\omega = \omega_o$, the pulse is on resonance. The presence of an oscillating applied field has the effect of making the Hamiltonian time-dependent, and the result of a sequence of pulses difficult to calculate. The problem is overcome by applying a coordinate

transformation into a frame rotating at frequency ω. This is equivalent to the observer sitting always on an axis in the x,y plane which is moving at exactly the same rate as the radiofrequency field. This is in fact how a spectrometer works, by comparing the incoming signal to the local oscillator signal that is sent out to the probe, and examining the difference between them. The large Larmor frequency component is subtracted away leaving smaller frequency modulations due to internal interactions that can be accurately measured. The rotating frame transformation is mathematically effected by rotation matrix $U = \exp(i\omega t I_z)$. By using a time dependent wavefunction,

$$|\psi(t)> = \exp(i\omega t I_z)\,|\psi_0>,$$

a time independent Hamiltonian can be written in the Schroedinger representation[5]:

$$\mathcal{H}_{ext}^{R} = -(\omega_0 - \omega)\,I_z - \omega_1\,I_x \qquad (1.9)$$
$$= -\Delta\omega\,I_z - \omega_1 I_x.$$

$\Delta\omega$ is the resonance offset of the radiofrequency from ω_0:

$$\mathcal{H}_{offset}^{R} = -\Delta\omega\,I_z \qquad .$$

In the rotating frame, transverse magnetization appears to oscillate at $\Delta\omega$, not at ω_0. Terms oscillating in -2ω have been dropped in this calculation under the presumption that they are oscillating twice as fast in the opposite direction as the rotating frame, and effectively average out to zero[5]. This is the high field approximation. It will manifest itself in that all non-secular (time dependent relative to the rotating frame) terms of the internal Hamiltonian will vanish, provided that their oscillation is rapid relative to the rotating

frame. Non-secular terms are those which do not commute with I_z:

$$[\ I_z,\mathcal{H}_{nonsec}] \neq 0, \qquad\qquad (1.10)$$

i.e. they are sensitive to rotation about z. Note that a non-secular term may survive if it is not oscillating very rapidly compared to ω. The rotating frame, or interaction representation, is used throughout this thesis and the superscript R is dropped.

The Internal Hamiltonian

The terms in the internal Hamitonian which are time independent in the rotating frame contribute, to first order, to the appearance of an NMR spectrum.

1.3 CHEMICAL SHIFT

Nuclei in an atom or molecule do not experience the applied static external magnetic field exactly. They are shielded by surrounding electrons, whose motion modifies the effective field. The extent of shielding depends on the relative orientation of the electron cloud with respect to the magnetic field. The chemical shift interaction is therefore an interaction between the magnetic field and the nuclear spin via a Cartesian shielding tensor:

$$\mathcal{H}_{cs} = - \gamma\ \underline{H}_0 \cdot \underset{\approx}{S} \cdot \underline{I} \qquad\qquad (1.11)$$

$\underset{\approx}{S}$ is the chemical shielding tensor. Because of the quantization along the z-axis, the chemical shift Hamiltonian simplifies to

$$\mathcal{H}_{cs} = -\gamma H_0 S_{zz} I_z$$

$$= -\sigma_{zz} I_z \qquad\qquad (1.12)$$

σ_{zz} is related to the chemical shift tensor in the molecular principal axis system (PAS) by[6]:

$$\sigma_{zz} = \sum_{\alpha,\beta} \cos\theta_\alpha \; \sigma_{\alpha\beta}^{MOL} \; \cos\theta_\beta \qquad (1.13)$$

where θ_α is the angle between the α axis of the molecular frame and the laboratory z axis. By addition and subtraction of the trace of σ to equation (1.13),

$$\sigma_{zz} = \frac{\sigma_{11} + \sigma_{22} + \sigma_{33}}{3} + \frac{2}{3} \sum_{\alpha,\beta} \frac{(3\cos\theta_\alpha\cos\theta_\beta - \delta_{\alpha\beta})}{2} \; \sigma_{\alpha\beta} \qquad (1.14)$$

where subscripts 1,2,3 are henceforth used to represent molecular axes, and the superscript MOL is dropped. α,β are summed over all molecular axes. Hence

$$\sigma_{zz} = \sigma_{iso} + \frac{2}{3} \sum_{\alpha,\beta} S_{\alpha\beta} \; \sigma_{\alpha\beta} \qquad (1.15)$$

where
$$S_{\alpha\beta} = \frac{3\cos\theta_\alpha\cos\theta_\beta - \delta_{\alpha\beta}}{2} \qquad (1.16)$$

The transformation matrix S is termed the order matrix in liquid crystals; it defines the orientation between the molecular PAS and the director. The director specifies the overall axial direction of a nematic liquid crystal in space. Because of orientational fluctuation, the order matrix is an average quantity over time:

$$S_{\alpha\beta} = \left\langle \frac{3\cos\theta_\alpha\cos\theta_\beta - \delta_{\alpha\beta}}{2} \right\rangle_t \qquad (1.17)$$

In the case where the director points along the magnetic field direction, the transformation (1.15) in a liquid crystal gives the

final component along z. If the director makes an angle α with the magnetic field, an additional scaling of σ_{zz} by $(3\cos^2\alpha-1)/2$ is required.

Aside on tensors in general

Every tensor measured in NMR can be written as equation (1.15) for σ. In general, for tensor A, the measured quantity

$$A_{zz} = A_{iso} + \frac{2}{3} \sum_{\alpha,\beta} S_{\alpha\beta} A_{\alpha\beta} = A_{iso} + A_{aniso} \qquad (1.18)$$

This equation can be expanded, using the fact that the $Tr(S) = 0$, into the form[7]:

$$A_{zz} = A_{iso} + \frac{2}{3}\left[S_{33}(A_{33} - \frac{1}{2}(A_{11}+A_{22})) + \frac{1}{2}(S_{11}-S_{22})(A_{11}-A_{22}) \right.$$
$$\left. + 2 S_{12}A_{12} + 2 S_{13}A_{13} + 2 S_{23}A_{23} \right] \qquad (1.19)$$

Symmetric properties of the motion will cause certain terms to vanish. For example, in isotropic solution, $S_{\alpha\beta} = 0$ for all α,β, i.e. the anisotropic component vanishes altogether. Molecular symmetry plays an important part in determining the number of non zero order parameters in anisotropic media; this is discussed in section 1.9.

The orientational coefficients can be expressed in terms of the Wigner rotation matrices. Tables 1.I and 1.II are derived in Appendix A and define the $S_{\alpha\beta}$ and the required Wigner matrix elements.

In the PAS of σ:

$$\sigma_{zz} = \sigma_{iso} + \frac{2}{3}\left[S_{33}(\sigma_{33} - \frac{1}{2}(\sigma_{11}+\sigma_{22})) + \frac{1}{2}(S_{11}-S_{22})(\sigma_{11}-\sigma_{22}) \right]$$
$$\text{———(1.20)}$$

Table 1.I

Representation of S-matrix elements in terms of Wigner Rotation Matrix elements

$$S_{11} = \left[\frac{3}{8}\right]^{1/2} [<D_{2,0}^{2}> + <D_{-2,0}^{2}>] - <D_{0,0}^{2}>/2$$

$$S_{12} = i\left[\frac{3}{8}\right]^{1/2} [<D_{2,0}^{2}> - <D_{-2,0}^{2}>]$$

$$S_{13} = -\left[\frac{3}{8}\right]^{1/2} [<D_{1,0}^{2}> + <D_{-1,0}^{2}>]$$

$$S_{22} = -\left[\frac{3}{8}\right]^{1/2} [<D_{2,0}^{2}> + <D_{-2,0}^{2}>] - <D_{0,0}^{2}>/2$$

$$S_{23} = -i\left[\frac{3}{8}\right]^{1/2} [<D_{1,0}^{2}> - <D_{-1,0}^{2}>]$$

$$S_{33} = <D_{0,0}^{2}>$$

Table 1.II

Explicit Expressions for Relevant Wigner Rotation Matrix elements

$$\langle D_{0,0}{}^2 \rangle = \frac{3\cos^2\beta - 1}{2} \qquad\qquad \langle D_{1,0}{}^2 \rangle = -\left(\frac{3}{2}\right)^{1/2} \sin\beta \, \cos\beta \, e^{-i\alpha}$$

$$\langle D_{2,0}{}^2 \rangle = \left(\frac{3}{8}\right)^{1/2} \sin^2\beta \, e^{-2i\alpha} \qquad\qquad \langle D_{-1,0}{}^2 \rangle = -\left(\frac{3}{2}\right)^{1/2} \sin\beta \, \cos\beta \, e^{i\alpha}$$

$$\langle D_{-2,0}{}^2 \rangle = \left(\frac{3}{8}\right)^{1/2} \sin^2\beta \, e^{2i\alpha}$$

Table 1.III

Components of Second Rank Spherical Tensors in terms of the Cartesian Tensors

$$T_{2,0} = \frac{1}{\sqrt{6}} \left(3T_{zz} - (T_{xx} + T_{yy} + T_{zz})\right)$$

$$T_{2,\pm 1} = \mp \frac{1}{2} \left(T_{xz} + T_{zx} \pm i(T_{yz} + T_{zy})\right)$$

$$T_{2,\pm 2} = \frac{1}{2} \left(T_{xx} - T_{yy} \pm i(T_{xy} + T_{yx})\right)$$

Using $\delta = A_{33} - A_{iso}$, the anisotropy of A, $\eta = (A_{11} - A_{22})/\delta$, the asymmetry parameter, and Tables 1.I and 1.II, equation (1.20) becomes

$$\sigma_{zz} = \sigma_{iso} + \delta <(3\cos^2\theta-1)/2> + 1/2 \; \eta\delta <\sin^2\theta\cos 2\phi> \quad (1.21)$$

θ,ϕ are the polar and azimuthal angles respectively. They are defined in figure 1.1. The angular brackets imply a time average over molecular motion.

1.4 SCALAR COUPLING

$\mathcal{H}_J$ is the indirect coupling of two nuclei mediated by the surrounding electrons. The homonuclear form of this equation is

$$\mathcal{H}_J = \sum_{i<j} I_i \cdot J_{ij} \cdot I_j \quad (1.22)$$

which can be expanded and truncated in accordance with the high field approximation:

$$\mathcal{H}_J = \sum_{i<j} J_{ijzz} I_{zi} I_{zj} + 1/2(J_{ijxx} + J_{ijyy})(I_{xi}I_{xj} + I_{yi}I_{yj}) \quad (1.23)$$

J_{ijxx}, J_{ijyy}, J_{ijzz} are the components of J in the space fixed coordinate system. Using equation (1.18) for the definition of J_{ijzz} and

$$J_{ij}^{iso} = J_{ij} = \frac{1}{3} Tr(J), \qquad \text{gives}$$

$$\mathcal{H}_J = \sum_{i<j} J_{ij} I_i I_j + J_{ij}^{aniso}(I_{zi}I_{zj} - \frac{1}{2}(I_{xi}I_{xj} + I_{yi}I_{yj})) \quad (1.24)$$

$$= \sum_{i<j} J_{ij} I_i I_j + J_{ij}^{aniso}(I_{zi}I_{zj} - \frac{1}{4}(I_{+i}I_{-j} + I_{-i}I_{+j})) \quad (1.25)$$

In oriented samples, J_{ij}^{aniso}, the anisotropy of the electron spin-spin coupled interaction, can be neglected for proton - proton
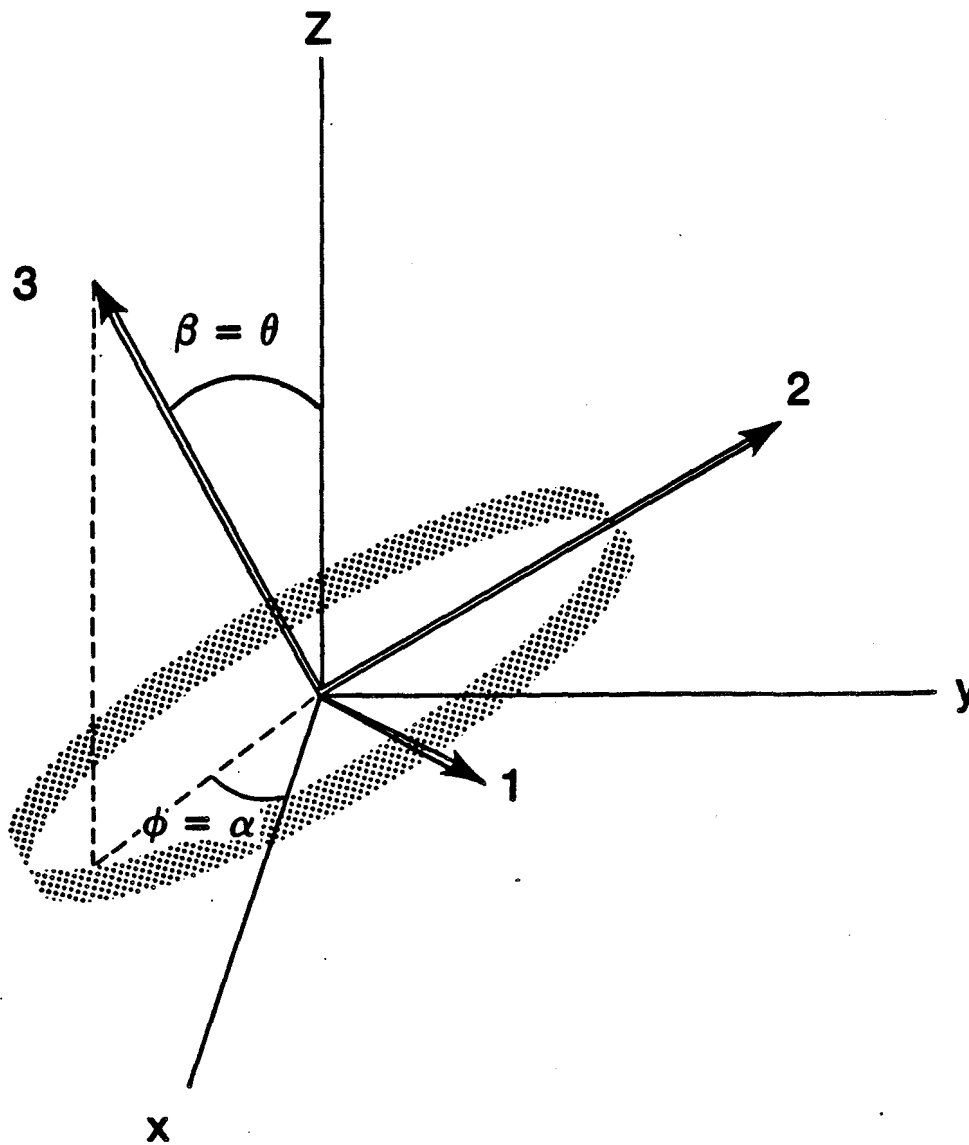
XBL 8610-11727

Figure 1.1

Relative orientation of the molecular PAS (1,2,3) and laboratory (x,y,z) axes.

interactions, since it is very small, leaving

$$\mathcal{H}_J = \sum_{i<j} J_{ij} I_i I_j \qquad (1.26)$$

J_{ij}^{aniso} can have a significant contribution in the case of ^{13}C-^{13}C, ^{19}F-^{19}F and some ^1H-^{19}F couplings[6]. As will be seen below, the spin operator part of the anisotropic J coupling term has exactly the same form as the dipole coupling Hamiltonian, and it is often termed the pseudodipolar coupling.

For a first order spectrum, where $J \ll \Delta\nu$, the chemical shift difference, the Hamiltonian can be truncated to

$$\mathcal{H}_J = \sum_{i<j} J_{ij} I_{zi} I_{zj} \qquad (1.27)$$

1.4.1 J-coupled AB systems

In a first order spectrum, each proton A, coupled to k identical protons B, has a well resolved resonance which is a multiplet of k+1 lines split by J_{AB}. In a strongly coupled system, $J_{AB} \geq \Delta\nu_{AB}$, the coupling pattern becomes more complicated. Figure 1.2 shows the AB coupling pattern for various values of $\Delta\nu = \nu_A - \nu_B$ and J. For $J/\Delta\nu = 1/8$, the spectrum is almost first order. Note that as $\Delta\nu \to 0$, the splitting disappears; i.e. equivalent protons show no J-coupling in an NMR spectrum. Figure 1.3 shows the energy level diagram for an AB spin system. The four transitions are marked together with their energies and intensities. For the scalar J coupling, they are calculated assuming that $J^{aniso} = 0$. In a liquid, the intensities of transitions 1 and 2, the outer lines in the AB spectrum, tend to zero as $\nu \to 0$, and $\theta \to \pi/4$. At this point, $c_1 = c_2 = 1/\sqrt{2}$, so state III

IV

$|\beta\beta>$

$\bar{\nu} + 1/2$ (T−C)
$1 + \sin 2\theta$
④

② $\bar{\nu} + 1/2$ (T+C)
$1 - \sin 2\theta$

II

$C_1 |\alpha\beta> + C_2 |\beta\alpha>$

III

$C_2 |\alpha\beta> - C_1 |\beta\alpha>$

③

$\bar{\nu} - 1/2$ (T−C)
$1 + \sin 2\theta$

① $\bar{\nu} - 1/2$ (T+C)
$1 - \sin 2\theta$

I

$|\alpha\alpha>$
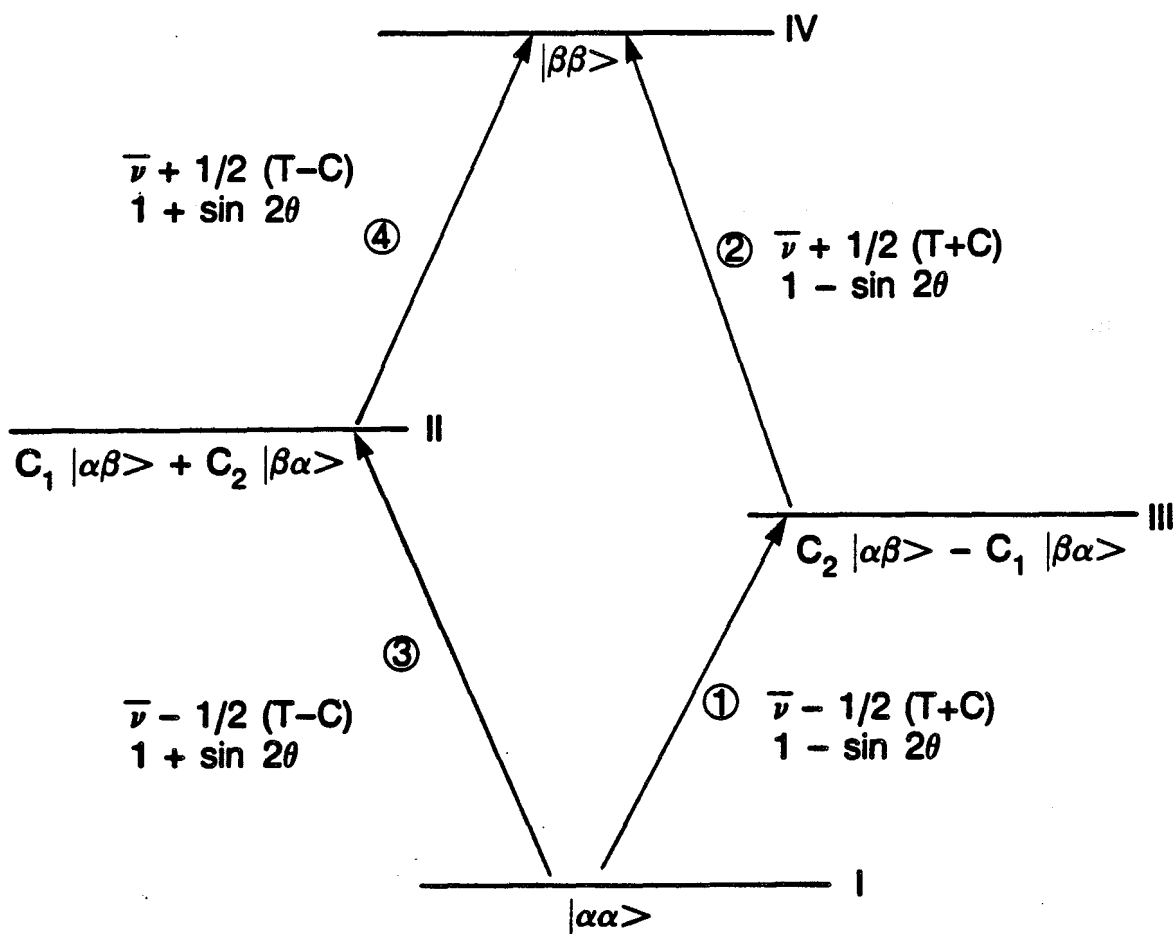
$C_1 = \sin \theta$

$C_2 = \cos \theta$

$\tan 2\theta = (J−D/2)/\Delta\nu$

$T = J+D$

$$\bar{\nu} = \frac{\nu_1 + \nu_2}{2}$$

$$C = \sqrt{\Delta\nu^2 + (J - D/2)^2}$$

XBL 8610-11726

Figure 1.2

Energy levels, transition frequencies and intensities of a two
spin system.
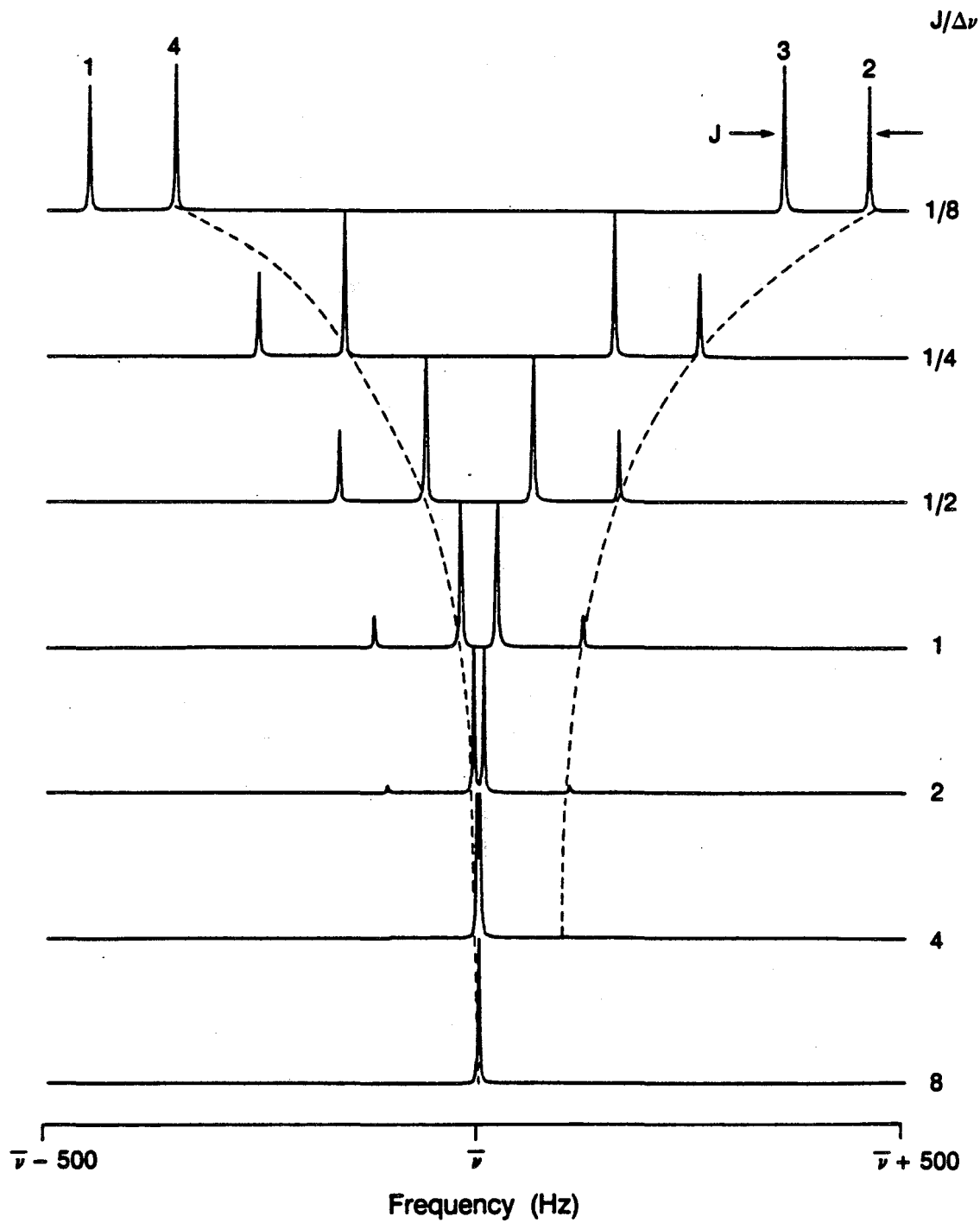
Figure 1.3

Appearance of a J-coupled AB spin system as a function of $J/\Delta\nu$. The transitions are labelled in figure 1.2.

becomes a pure antisymmetric state $(|\alpha\beta> - |\beta\alpha>)/\sqrt{2}$ to which the symmetric states I,II and IV do not couple. At the same time, transitions 3 and 4 have the same frequency, $\bar{\nu} = (\nu_A + \nu_B)/2$.

In a strongly coupled AB spin system, a π pulse at the centre of the evolution, in an attempt to echo chemical shifts for example, results in additional lines in the spectrum, because $[I_z, \mathcal{H}_J] \neq 0$. Six lines can been seen in these spectra as shown in figure 1.4; they are linear combinations of the transitions in figure 1.3. This occurs because of the mixing of states 2 and 3 by a π pulse[8]. Therefore coherence 1 will be mixed into coherences 2 and 4. The result is 3 pairs of lines with frequencies and intensities

Frequency	Intensity	Transition
$\pm 1/2(J-C)$	$(1+\sin2\theta)\sin2\theta$	$\pm(4-3)$
$\pm 1/2J$	$2\cos^2 2\theta$	$\pm(2-3),(4-1)$
$\pm 1/2(J+C)$	$-(1-\sin2\theta)\sin2\theta,$	$\pm(2-1)$

where $C = \sqrt{J^2+\Delta\nu^2}$, $\sin 2\theta = J/C$, $\cos 2\theta = \Delta\nu/C$[9].

1.4.2 The heteronuclear scalar coupling

The heteronuclear form of the scalar coupling Hamiltonian of an I_nS spin system truncates to:

$$\mathcal{H}_J = \sum_i J_{iS} I_{zi} S_z \qquad (1.28)$$

The flip-flop terms do not conserve energy. The energy change involved is much larger than the flip-flop in the homonuclear case; it joins states differing by $h(\nu_o^I - \nu_o^S)$ in energy which amounts to a negligible second order perturbation on the energy levels, and can be ignored.
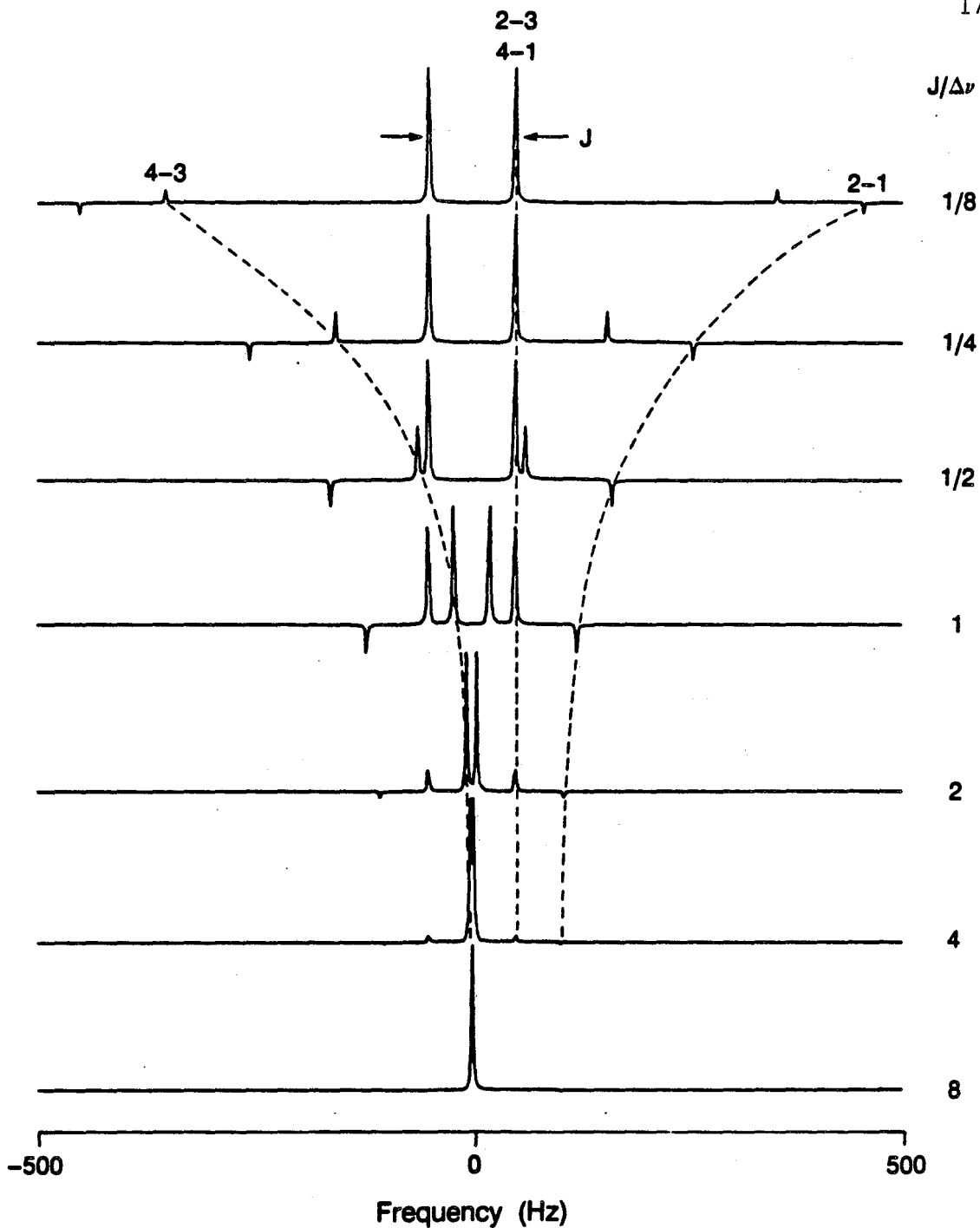
XBL 8610-11724

Figure 1.4

Effect of a π pulse in the centre of the evolution period of a J-coupled AB spin system, as a function of $J/\Delta\nu$.

1.5 DIPOLAR COUPLING

$\mathcal{H}_D$ is the through space direct magnetic dipole interaction between pairs of nuclei. In the homonuclear case,

$$\mathcal{H}_D = \sum_{i<j} \underline{I}_i \cdot \underline{\underline{D}}_{ij} \cdot \underline{I}_j \qquad (1.29)$$

The tensor $\underline{D}_{ij}$ has elements·

$$D_{ij\alpha\beta} = -h\gamma^2/4\pi^2 r_{ij}^3 \; (3\cos\theta_{ij\alpha}\cos\theta_{ij\beta} - \delta_{\alpha\beta}) \qquad (1.30)$$

in Hz, where α,β are varied over the molecular axes 1,2,3; $\theta_{ij\alpha}$ is the angle that bond ij makes with molecular axis α and r_{ij} is the distance between atoms i and j. D_{ij} is symmetric and traceless - i.e. there is no residual dipole coupling in isotropic solution.

$\mathcal{H}_D$ can be expanded in the high field approximation to:

$$\begin{aligned} \mathcal{H}_D &= \sum_{i<j} D_{ijzz}(I_{zi}I_{zj} - 1/4(I_{+i}I_{-j}+I_{-i}I_{+j})) \\ &= \sum_{i<j} (1/2) D_{ijzz} (3I_{zi}I_{zj} - I_1 \cdot I_2) \end{aligned} \qquad (1.31)$$

The component of D_{ij} along the laboratory z axis, D_{ijzz}, is related to D_{ij} in the molecular frame as in equation (1.19):

$$\begin{aligned} D_{ijzz} &= S_{33}D_{ij33} + \frac{2}{3} [1/2(S_{11}-S_{22})(D_{ij11}-D_{ij22}) \\ &\quad + 2S_{12}D_{ij12} + 2S_{13}D_{ij13} + 2S_{23}D_{ij23}] \end{aligned} \qquad (1.32)$$

Using equation (1.30) and $\cos\theta_{ij3} = z_{ij}/r_{ij}$; $\cos\theta_{ij1} = x_{ij}/r_{ij}$; $\cos\theta_{ij2} = y_{ij}/r_{ij}$, where x_{ij}, y_{ij}, z_{ij} are the components of bond ij along the molecular axes $\underline{1},\underline{2},\underline{3}$ and $r_{ij}^2 = x_{ij}^2 + y_{ij}^2 + z_{ij}^2$, gives
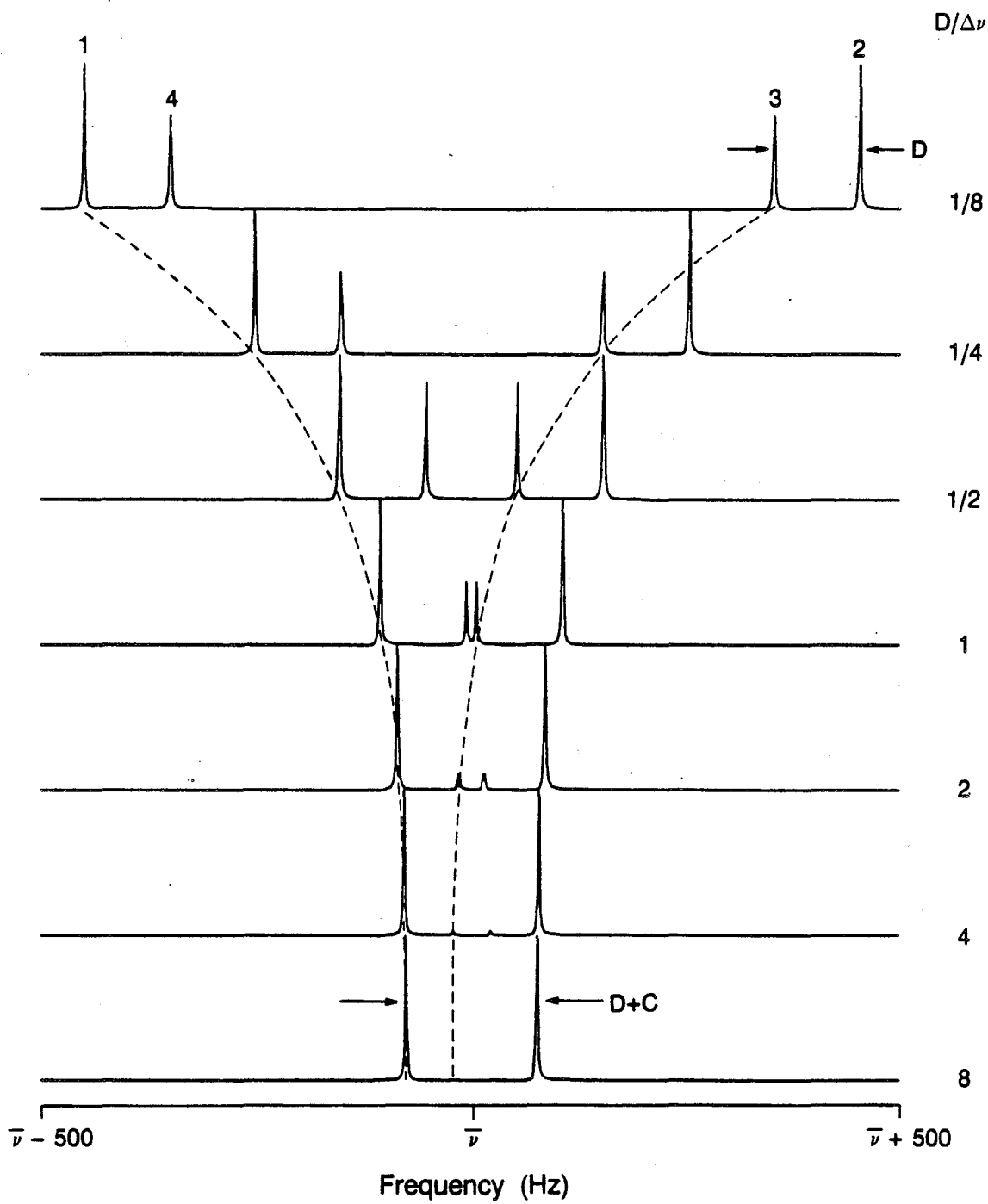
XBL 8610-11722

Figure 1.5

Appearance of a dipole coupled AB spin system as a function of $D/\Delta\nu$. The transitions are labelled in figure 1.2.
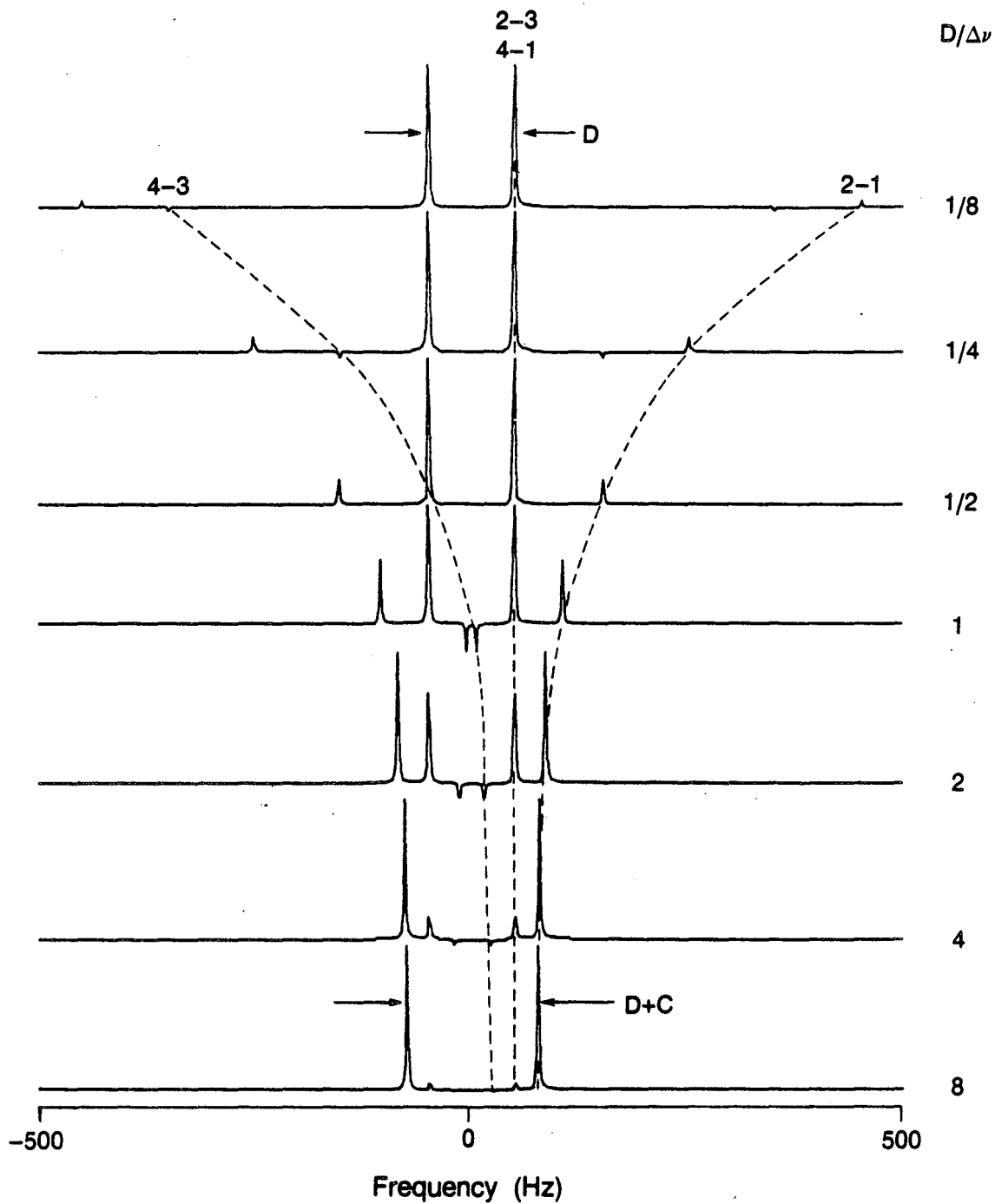
XBL 8610-11725

Figure 1.6

Effect of a π pulse in the middle of the evolution period of a dipole coupled AB spin system, as a function of $D/\Delta\nu$.

$$D_{ijzz} = -2K \left[\frac{S_{33}(z_{ij}^2 - 1/2(x_{ij}^2 + y_{ij}^2))}{r_{ij}^5} + \frac{(S_{11} - S_{22})(x_{ij}^2 - y_{ij}^2)}{2\, r_{ij}^5} \right.$$

$$\left. + 2S_{12} \frac{x_{ij} y_{ij}}{r_{ij}^5} + 2S_{13} \frac{x_{ij} z_{ij}}{r_{ij}^5} + 2S_{23} \frac{y_{ij} z_{ij}}{r_{ij}^5} \right] \qquad (1.33)$$

$K = h\gamma^2/4\pi^2 = 120.067 \text{ KHz for } {}^1\text{H}.$

This equation is useful for the calculation of dipole coupling constants from molecular structure[10]. It is clear that the dipole coupling constants are very sensitive to both molecular geometry and to the order parameter in a liquid crystal.

1.5.1 D-coupled AB systems

Figure 1.5 shows the behaviour of the AB coupling pattern for a pair of nuclei A and B in an anisotropic environment for various ratios of D and the chemical shift difference $\Delta\nu$. For $D/\Delta\nu = 1/8$, an approximately first order spectrum is obtained. This is an atypical spectrum, since usually $D \gg \Delta\nu$. At $D/\Delta\nu = 8$, the spectrum is converging to its strong coupling limit in which the line splitting is given by 3/2 D = D + C. In the case of dipolar coupling, angle θ as defined in figure 1.2 is negative, implying that state II becomes the antisymmetric state when $\Delta\nu = 0$, and that transitions 3 and 4 have zero intensity.

As with J coupling, the presence of a π pulse in the centre of the evolution period causes the appearance of extra lines in the intermediate region of the AB spin system. Figure 1.6 shows this effect.

Three pairs of lines are produced at the frequencies and intensities:

| Frequency	Intensity	Transition
$\pm\ 1/2(D-C)$	$(1+\sin2\theta)\sin2\theta$	$\pm(4-3)$
$\pm\ 1/2\ D$	$2\cos^2 2\theta$	$\pm(2-3),(4-1)$
$\pm\ 1/2(D+C)$	$-(1-\sin2\theta)\sin2\theta$	$\pm(2-1)$

where $C = \sqrt{\Delta\nu^2 + D^2/4}$, $\sin 2\theta = -D/2C$, $\cos 2\theta = \Delta\nu/C$. The line positions and intensities differ from the case of J coupling because of the different definitions of θ and C.

Figure 1.3 defines θ and C for the general case where both J and D occur. The spectral characteristics are typically described by figures 1.5 and 1.6, since usually $\|D\| \gg \|J\|$.

1.6 QUADRUPOLE COUPLING

$\mathcal{H}_Q$ arises from the electrostatic interaction between the electron charge distribution and the nuclear charge distribution. It is non-zero only for nuclei with $I \geq 1$ which are non-spherical. It is described by:

$$\mathcal{H}_Q = \frac{eQ}{2\hbar I(2I-1)}\ \underset{\sim}{I}\cdot\underset{\approx}{V}\cdot\underset{\sim}{I} \tag{1.34}$$

which, when truncated in high field, yields

$$\mathcal{H}_Q = \frac{eQ}{4\hbar I(2I-1)}\ V_{zz}(3I_z^2 - I(I+1)) \tag{1.35}$$

The quadrupole coupling can in many instances in the solid state be larger than the Zeeman interaction, making the high field approximation invalid. This is not the case in liquid crystals, in general, because of the order parameter scaling effect on the quadrupole coupling, and equation (1.35) can be considered to be valid. From equation (1.19) applied to the traceless nuclear

quadrupole tensor V in its PAS, and using $eq = V_{33}$, $\eta = (V_{11}-V_{22})/V_{33}$, and the quantities in Table 1.I and 1.II, we get

$$V_{zz} = eq <(3\cos^2\theta-1)/2> + 1/2 \ eq\eta<\sin^2\theta\cos2\phi> \qquad (1.36)$$

Thus

$$\mathcal{H}_Q = \frac{e^2qQ}{8\hbar I(2I-1)} \ [<3\cos^2\theta-1> + \eta<\sin^2\theta\cos2\phi>](3I_z^2-I(I+1)) \qquad (1.37)$$

For deuterium, spin I=1,

$$\mathcal{H}_Q = \omega_Q \ (I_z^2-2/3)$$

where

$$\omega_Q = 3/8 \ (e^2qQ/\hbar) \ (<3\cos^2\theta-1> + \eta<\sin^2\theta\cos2\phi>) \qquad (1.38)$$

The quadrupole energies of the m = -1,0,1 levels, where the Zeeman interaction dominates, are $-\omega_o+\omega_Q/3$, $-2\omega_Q/3$, and $\omega_o+\omega_Q/3$ respectively, resulting in a pair of lines centred around ω_o and split by $2\omega_Q$.

1.7 THE DENSITY MATRIX, ρ

Density matrix formalism is very useful for following the evolution of a spin system under a set of pulses and delays. It will be introduced here as a tool for subsequent chapters.

1.7.1 Definition of the density matrix

The density operator is used to describe an ensemble of spins which cannot be represented by a single wavefunction. A wave function $|\psi>$ can be expanded in the complete set of orthonormal basis functions $|n>$ which define the $(2I+1)^N$ energy levels of an N spin system:

$$|\psi\rangle = \sum_n c_n |n\rangle$$

$$= \sum_n \langle n|\psi\rangle |n\rangle$$

The expectation value of an operator A is given by:

$$\langle A\rangle = \langle\psi|A|\psi\rangle$$

$$= \sum_n \sum_m c_n c_m^* \langle m|A|n\rangle \qquad (1.39a)$$

$$= \sum_n \sum_m \langle n|\psi\rangle\langle\psi|m\rangle A_{mn} \qquad (1.39b)$$

The basis set $|n\rangle$ and the matrix elements A_{mn} are constant and independent of ψ. An ensemble of spins coupled to a bath (i.e. at thermal equilibrium) have a Boltzmann energy distribution. It is impossible to describe the state of all the spins by a single wavefunction. Attempting to do so contradicts the random phase assumption which leads to 0 transverse coherence. As an exercise, let

$$|\psi\rangle = a|+\rangle + b|-\rangle$$
$$a = A\exp(i\alpha); \quad b = B\exp(i\beta).$$

Then, looking at the expectation value of I_x, we get

$$\langle\psi|I_x|\psi\rangle = AB\cos(\alpha-\beta) \qquad (1.40)$$

To get zero transverse magnetization, we require random phase, and must ensemble average over ψ:

$$\overline{\langle\psi|I_x|\psi\rangle} = AB\,\overline{\cos(\alpha-\beta)} = 0. \qquad (1.41)$$

Equation (1.39) then yields

$$\langle\bar{A}\rangle = \sum_n \sum_m \langle n|\overline{\psi\rangle\langle\psi}|m\rangle A_{mn}$$

$$\sum_n \sum_m \rho_{nm} A_{mn} = |\underline{Tr\ (\rho A)}| \qquad (1.42)$$

where $|\psi\rangle\langle\psi|$ is the density operator, ρ. A knowledge of ρ suffices to determine the expectation value.

1.7.2 Properties of the density matrix

1) $Tr(\rho) = 1$

2) ρ is Hermitian; $\rho_{ij} = \rho_{ji}^{*}$

3) The diagonal elements of ρ represent ensemble averaged populations of the states of the spin system:

$$\rho_{ii} = \overline{\langle i|\psi\rangle\langle\psi|i\rangle} = \overline{c_i c_i^{\dagger}} = \overline{c_i^2} \qquad (1.43)$$

ρ_{ii} satisfies a Boltzmann distribution:

$$\rho_{ii} = \exp(-E_i/kT) / Z,$$

where Z is the partition function $\Sigma \exp(-E_j /kT) \approx (2I+1)^N$.

In operator form the density matrix of an unperturbed spin system is given by

$$\rho_{eq} = \frac{1}{Z} \exp(-\mathcal{H}/kT) = \frac{1}{Z}(1 - \frac{\mathcal{H}}{kT} + \ldots)$$

In NMR, the magnitude of the spin system energy, $\|\mathcal{H}\| \ll kT$, so that this series may be truncated after the second term. In the high field approximation, where the Larmor frequency dominates,

$$\rho_{eq} = (2I+1)^{-N} (1 + \gamma H_0 I_z/kT) \qquad (1.44)$$

The constant term is ignored in calculations of time evolution. We write

$$\rho_{eq} = \beta I_z, \text{ where } \beta = (2I+1)^{-N}\gamma H_0/kT \tag{1.45}$$

4) The off-diagonal elements of ρ describe coherences between states.

$$\rho_{ij} = \overline{\langle i|\psi\rangle\langle\psi|j\rangle} = \overline{c_i^\dagger c_j \cos(\alpha_i - \alpha_j)} \tag{1.46}$$

There is no phase coherence at initial equilibrium, and these elements are zero. They are created by the application of one or more radiofrequency pulses. These terms have order, $\Delta M = m_i - m_j$ and are displaced ΔM positions from the main diagonal.

5) The time dependence of ρ is given by the Liouville equation:

$$\frac{d\rho}{dt} = i[\rho, \mathcal{H}]$$

which can be integrated if $\mathcal{H}$ is time-independent for interval t to give

$$\rho(t) = e^{-i\mathcal{H}t}\rho\, e^{i\mathcal{H}t} \tag{1.47}$$

Equation (1.47) can be expanded using the general operator equation[11]:

$$e^{-A}Be^A = B - [A,B] + \frac{1}{2!}[A,[A,B]] - \frac{1}{3!}[A,[A,[A,B]]] + \ldots \tag{1.48}$$

6) A nucleus with spin I has $2I+1$ eigenstates, and for N interacting spins, there are $(2I+1)^N$ eigenstates and a density matrix of square size

$$\prod_{n=1}^{N} 2^{(2I+1)}$$

is required to describe its evolution.

Equations (1.45), (1.47), (1.49) and (1.42)) are sufficient to completely determine the NMR spectrum of any spin system under the influence of a set of pulses and delays. See Section 2.1 for an example.

1.8 THE ANGULAR MOMENTUM OPERATORS

$\underline{I}$ is the angular momentum vector operator (I_x, I_y, I_z), where I_x, I_y, I_z are the Pauli spin matrices.[12] Important relations that hold are:

$$I^2|\psi> = I(I+1)\ |\psi>$$

$$I_z|\psi> = m|\psi>; \qquad\qquad -I \le m \le I$$

$$[I_p, I_q] = iI_r; \qquad\qquad p,q,r = x,y,z \text{ or a cyclic}$$
$$\text{permutation} \quad .$$

In the special case of $I = 1/2$, we have in addition,

$$I_p^{\ 2} = 1/4; \qquad\qquad p = x,y,z$$

$$\{I_p, I_q\}_+ = 0$$

1.8.1 Rotations

The following conventions[13,14] will be adopted throughout this thesis. A right handed coordinate system is used (figure 1.1). The direction of rotation is given by the right hand rule with the thumb pointing away from the origin along the appropriate axis. Rotations are counter-clockwise. Thus a $(\pi/2)_x$ pulse brings z-magnetization to the -y axis. In general,

$$e^{-i\theta I_p} I_q e^{i\theta I_p} = I_q \cos\theta + I_r \sin\theta$$

$$e^{-i\theta I_p} I_r e^{i\theta I_p} = I_r \cos\theta - I_q \sin\theta$$

(1.49)

p,q,r = x,y,z or a cyclic permutation.

1.9 COMMENTS ON THE ORDER PARAMETER

The order parameter was introduced in equations (15-19) as a transformation matrix from the molecular frame to the laboratory frame. The dominant element in equation (1.19) is S_{33}, often called S_{zz}. S_{33} is typically ~ 0.2 in a nematic liquid crystal. S_{11}-S_{22} (often seen as S_{xx}-S_{yy}) describes the extent of anisotropic motion perpendicular to the z-axis; in a cigar shaped molecule, S_{11}-S_{22} = 0; in a flat molecule, S_{11}-$S_{22} \neq 0$.

In any arbitrary frame, S can have up to five independent non-zero elements, due to the fact that it is a symmetric traceless tensor (eqn (1.19)). S can always be diagonalized so that it has only two non-zero elements. The required transformation to the PAS of S may be determined a priori from the symmetry group of the molecule, provided that the symmetry is high enough[15]. Some examples will be given below.

Suppose the molecule has a C_k axis. The effect of a rotation of $2\pi/k$ around 3 on a Wigner matrix element is[16]:

$$\langle D_{m,n}^L \rangle \rightarrow \langle D_{m,n}^L \rangle \exp(-im \, 2\pi/k)$$

The requirement that a symmetry operation effect no change implies that m can be 0, ±k, ±2k, ... only. For example, for a two-fold axis, we see from Table 1.I that S_{23} and S_{13} disappear, leaving 3 order

parameters. Physically, this means that the axis C_2 is identified as the S_{33} axis, and that axis $\underline{3}$ is orthogonal to the remaining (as yet unidentified) axes, so that S_{13} and S_{23} become zero. For a three or more fold axis, m can be zero only, i.e. only $\langle D_{00}^2 \rangle$ remains, so the motion is defined by one order parameter, S_{33} along C_3. The molecule is axially symmetric.

A vertical mirror plane, σ_{23}, causes

$$\langle D_{m,n}^L \rangle \rightarrow \langle D_{-m,n}^L \rangle.$$

Thus, σ_{23} causes $S_{12} = S_{23} = 0$, leaving three unique order parameters. A horizontal mirror plane, σ_{12} causes

$$\langle D_{m,n}^L \rangle \rightarrow (-)^{L+m} \langle D_{m,n}^L \rangle$$

implying that $m = 0, \pm 2$, i.e. $S_{13} = S_{23} = 0$.

S is a motional parameter. It determines the extent of molecular motion along three molecular axes with respect to the director. The PAS of this motion is often taken to be aligned with the inertia tensor of the molecule in cases where interpretation by symmetry arguments is not clear. We shall estimate the deviation of the S-matrix PAS from the inertia tensor PAS in Chapter 4.

CHAPTER 2

Two Dimensional and Multiple Quantum NMR

In this chapter, some of the basics of two-dimensional and multiple quantum NMR are introduced. These subjects have been reviewed in considerable detail in the literature[1-4,8,17-21]. Emphasis is placed here on those aspects which are of use in subsequent chapters.

In Section 2.1, the single quantum FID is reviewed. Two-dimensional (2-D) NMR is introduced in Section 2.2. In Section 2.3, coherence transfer, the essence of the two dimensional experiment, is discussed. In Section 2.4, three different two-dimensional sequences are introduced, for homonuclear single quantum, homonuclear multiple quantum (MQT) and heteronuclear MQT correlation experiments. Phase cycling is introduced in Section 2.5 as a means of overcoming some of the shortcomings of the basic experiments. Phase cycling provides solutions to non-quadrature signals, pulse errors, mixed phase signals, separation of multiple quantum orders and generation of multiple quantum filters.

2.1 THE SINGLE PULSE, SINGLE QUANTUM EXPERIMENT

The basic Fourier Transform NMR experiment begins with the application of a $\pi/2$ pulse to the equilibrium spin system:

$$\rho_{eq} = \beta I_z \qquad\qquad (2.1)$$

$$\text{where} \quad \beta = \frac{\gamma \hbar H_0}{kTZ} \qquad\qquad (\text{eqn } 1.45)$$

Application of a $(\pi/2)_y$ pulse gives, according to equation (1.49)

$$\rho(0) = \beta I_x \tag{2.2}$$

The evolution of this operator is followed using the integrated Liouville equation (1.47):

$$\rho(t) = \beta \, e^{-i\mathcal{H}t} \, I_x \, e^{i\mathcal{H}t}$$

According to equation (1.42), the signal detected during time t is

$$S(t) = \epsilon \, \mathrm{Tr} \, (\rho(t)I_+)$$

for a spectrometer operating in quadrature. Expanding in the eigenbasis of $\mathcal{H}$:

$$
\begin{aligned}
S(t) &= \epsilon \sum_i \langle i| \, e^{-i\mathcal{H}t} \, \beta I_x \, e^{i\mathcal{H}t} \, I_+ |i\rangle \\
&= \epsilon\beta \sum_i \sum_j e^{-iE_i t/\hbar} \, e^{iE_j t/\hbar} \left(I_x\right)_{ij} \left(I_+\right)_{ji} \\
&= \frac{1}{2} \, \epsilon\beta \sum_i \sum_j e^{-i\omega_{ij}t} \left|\left(I_+\right)_{ji}\right|^2
\end{aligned}
\tag{2.3}
$$

the last step utilizing the fact that $\mathrm{Tr} \, (I_+I_+) = 0$. ϵ is a factor accounting for the signal amplitude, which depends on γ of the detected nucleus, but also on a number of experimental considerations[8]. Fourier transforming gives the signal

$$S(t) = \epsilon\beta \sum_i \sum_j \delta(\omega-\omega_{ij}) \left|\left(I_+\right)_{ji}\right|^2 \tag{2.4}$$

with lines occurring at frequencies ω_{ij} and intensities $|I_+|^2_{ji}$. It is apparent from equation 2.3 that only single quantum transitions can be detected in a free induction decay. The operator I_+ connects states differing by 1 in their Zeeman quantum number, i.e. $m_i - m_j = 1$.

Equation 2.3 also demonstrates that **all lines are in phase** after a single pulse (no complex numbers in the intensity coefficient). The magnetization is all aligned along I_x at time t=0.

2.2 THE TWO-DIMENSIONAL EXPERIMENT

In 1973, Jeener[17] proposed the first two dimensional experiment. The idea was based on correlation of the NMR response in two time domains. An FID is observed in t_2 as a function of some prior time interval t_1, leading to a signal $S(t_1,t_2)$. Double Fourier transformation leads to the 2-D spectrum $S(\omega_1,\omega_2)$.

The two great advantages of 2-D NMR are that (1) it replaces, by a single experiment, a whole series of double resonance experiments for the determination of internuclear couplings, and (2) it allows the indirect detection of coherences which might not be observable in single quantum spectroscopy[2,18].

Figure 2.1 shows a schematic pulse sequence for the 2-D experiment. U is termed the preparation propagator, since it prepares the density operator for its evolution during t_1. V is a mixing propagator; it mixes coherence back to single quantum magnetization for detection in t_2. The first experiment used $U = V = \pi/2$[17]. It became known as the COSY experiment[22-26]. Many variations of the 2-D experiment have been developed for different U and V and by manipulation of the Hamiltonian during t_1 with pulses. Examples include the heteronuclear COSY[27-32], MQT correlated spectroscopy[33-48], 2-D NOE (NOESY) spectroscopy[49-52], J-resolved spectroscopy[27,53-56]. Of this list, the interest for this thesis lies in homonuclear and heteronuclear COSY and MQT correlation
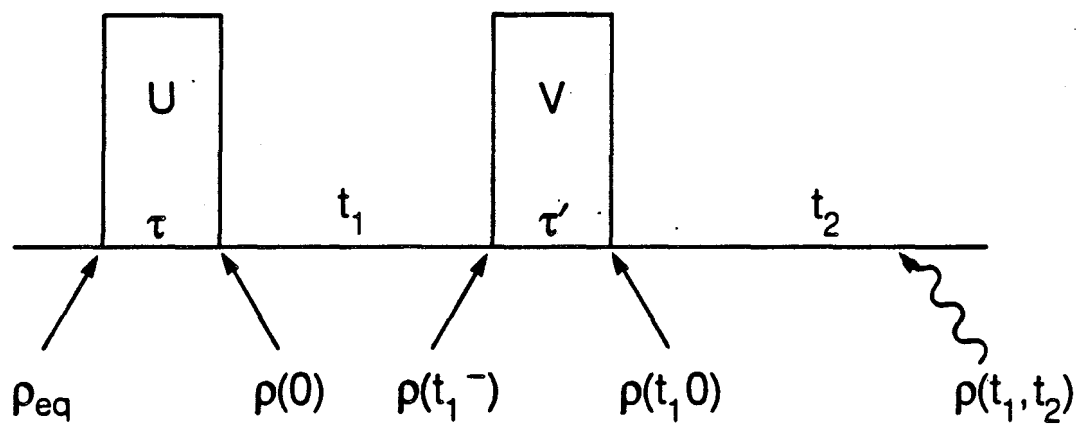
XBL 871-9539

Figure 2.1

Schematic pulse sequence for the 2-D experiment, defining the various stages of the evolution of the density matrix, ρ.

experiments. Heteronuclear single and MQT correlations are used in Chapter 3; homonuclear single and MQT correlation experiments are used in Chapter 4. Table 2.I summarizes the U and V propagators used for these experiments.

2.2.1 Evolution of the density matrix

The equilibrium density matrix is given by equation (2.1). The result of propagator $U(\tau)$, evolution during t_1, and mixing $V(\tau')$ gives a density operator

$$\rho(t_1,0) = V(\tau')\, e^{-i\mathcal{H}_1 t_1}\, U(\tau)\, \beta I_z\, U^\dagger(\tau)\, e^{i\mathcal{H}_1 t_1}\, V^\dagger(\tau') \qquad (2.5)$$

The evolution during t_2 need not be explicitly determined. The phase and intensity of all lines is determined by $\rho(t_1,0)$. The frequencies in the detection period are known from $\mathcal{H}_2$.

The signal at the beginning of detection is given by:

$$S(t_1,0) = \epsilon\, \mathrm{Tr}\, (V(\tau') e^{-i\mathcal{H}_1 t_1}\, U(\tau)\beta I_z U^\dagger(\tau) e^{i\mathcal{H}_1 t_1}\, V^\dagger(\tau')\, I_+) \qquad (2.6)$$

Expanding in the basis of the Hamiltonian $\mathcal{H}_1$ gives:

$$S(t_1,0) = \epsilon\beta\, \sum_i \sum_j e^{-i\omega_{ij} t_1}\, (UI_z U^\dagger)_{ij}\, (V^\dagger I_+ V)_{ji} \qquad (2.7)$$

and at time t_2:

$$S(t_1,t_2) = \epsilon\beta\, \sum_i \sum_j e^{-i\omega_{ij} t_1}(UI_z U^\dagger)_{ij}\, (V^\dagger e^{i\mathcal{H}_2 t_2} I_+ e^{-i\mathcal{H}_2 t_2}\, V)_{ji} \qquad (2.8)$$

Writing $P(\tau) = \beta\, U(\tau)I_z U^\dagger(\tau),$

$\qquad\qquad Q(\tau') = \epsilon\, V^\dagger(\tau')I_+ V(\tau'),$

__Table 2.I__   35

Preparation (U) and mixing (V) propagators of interest.

<table>
<tr><td align="center">__U__</td><td align="center">__V__</td></tr>
</table>

Homonuclear COSY

$$\frac{\pi}{2} \qquad\qquad \frac{\pi}{2}$$

Homonuclear MQT

$$\left(\frac{\pi}{2} - \tau - \frac{\pi}{2} \right)_{\varphi} \qquad\qquad \frac{\pi}{2}$$

Heteronuclear MQT

$$I \; \frac{\frac{\pi}{2} - \tau - \;}{S \; - \tau - \left(\frac{\pi}{2} \right)_{\varphi}} \qquad\qquad \frac{\tau}{\frac{\pi}{2} \; - \tau -}$$

MQT filter

$$\left(\frac{\pi}{2} \right)_{\varphi} \qquad\qquad \left(\frac{\pi}{2} \right)_{\varphi} - \tau - \frac{\pi}{2}$$

XBL 871-9538

we have

$$S(t_1, t_2) = \sum_i \sum_j \sum_k \sum_l e^{-i\omega_{ij}t_1} e^{-i\omega_{kl}t_2} P_{ij}(\tau) Q_{ji}(\tau') \qquad (2.10)$$

The Fourier transform with respect to t_1 and t_2 gives

$$S(\omega_1, \omega_2) = \sum_i \sum_j \sum_k \sum_l P_{ij}(\tau) Q_{ji}(\tau') \delta(\omega_1 - \omega_{ij}) \delta(\omega_2 - \omega_{kl}) \qquad (2.11)$$

2.2.2 Properties of the 2-D correlated spectrum

(1) Peaks occur at frequencies $(\omega_{ij}, \omega_{kl})$ in a 2-D map, where the intensity $P_{ij}(\tau)Q_{ji}(\tau') \neq 0$, with the following properties:

    $i = k$, $j = l$: diagonal peak (D)

    $i = j$: axial peak (A) in ω_1 caused by T_1 relaxation during t_1

    $i \neq k$ or $j \neq l$: cross peak (C), which occurs when matrix elements V_{lj} and $V_{ki} \neq 0$.

    D, A and C peaks are illustrated in Figure 2.2.

(2) An **amplitude modulated** spectrum occurs when the signal $S(t_1, 0)$ is an oscillating function of t_1, but independent of its phase. The sequences in Table 2.I are all examples of amplitude modulated spectra. No sign discrimination occurs in ω_1.

    For a weakly coupled spin system, a pure phase[*] amplitude modulated spectrum can be obtained. In a strongly coupled spin

---

[*] Pure phase means that each line in the spectrum is either pure absorption or pure dispersion. No mixing occurs within one line; however, mixing within one spectrum can occur.
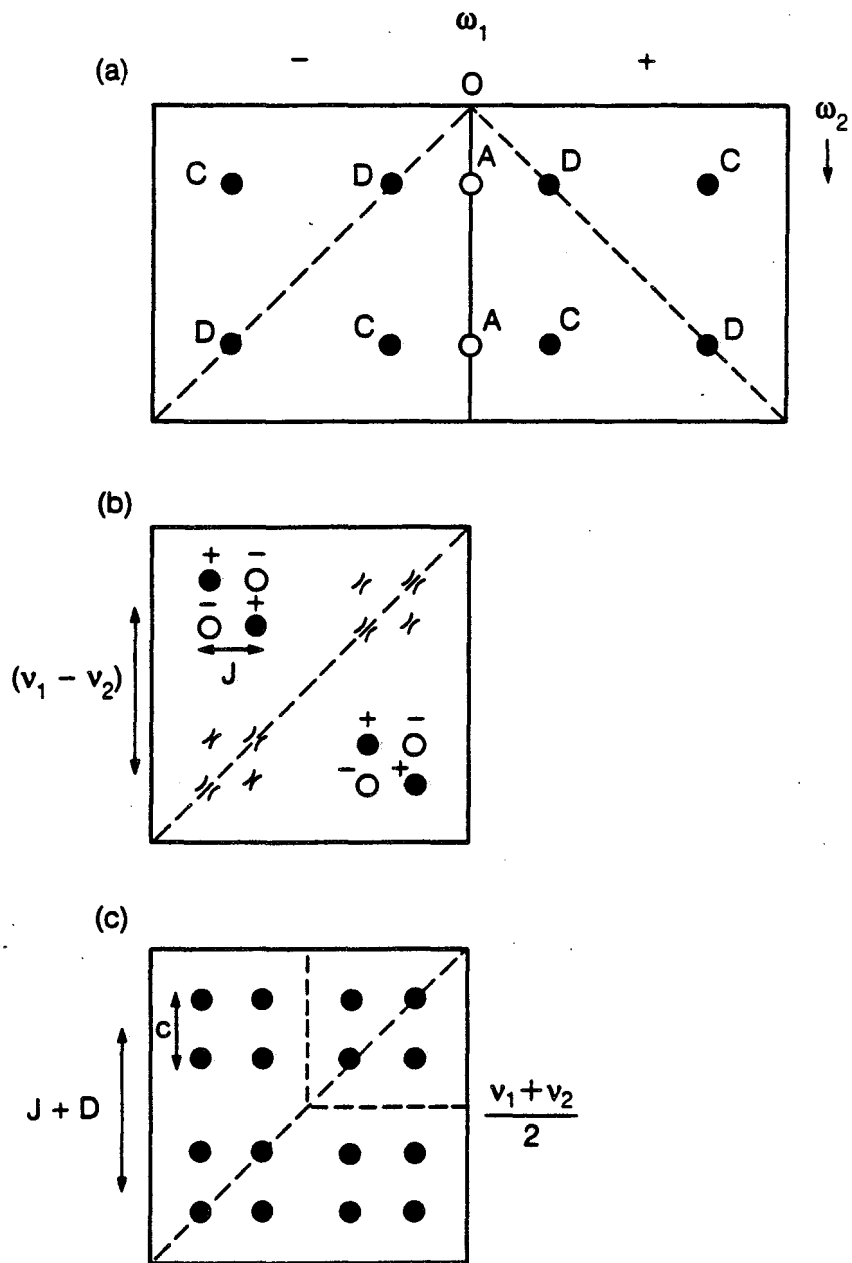
XBL 871-9541

Figure 2.2

(a) Low resolution amplitude modulated COSY spectrum, showing diagonal (D), cross (C) and axial (A) peaks. (b) High resolution phased spectrum of half of (a), for a weakly coupled two spin system. (c) High resolution absolute value spectrum for a strongly coupled two spin system.

system, mixed phase spectra usually result, because the read sequence (V) does not act on isolated transitions.

(3) A **phase modulated** spectrum is one in which $S(t_1,0)$ depends both on the amplitude and on the phase of the signal as a function of t_1. Such a spectrum shows frequency discrimination in ω_1, but gives mixed phase signals[8].

Recently, methods have been developed[57] for obtaining pure phase spectra with quadrature in ω_1.

(4) Echoes (τ - π - τ -) prior to detection preclude any possibility of obtaining phased spectra. Signal oscillating during 2τ under the Hamiltonian $\mathcal{H}_J + \mathcal{H}_D$ leaves different J and D components with different phases[56]. Echoes are often used during COSY and MQT sequences on liquid crystals to avoid receiver saturation by liquid crystal signal.

(5) The following two experiments are examples of amplitude modulated experiments on strongly coupled spin systems which produce pure absorption mode signals.

Total Spin Coherence is the spin inversion transition between the state with all spins up (M = N/2) and the state with all spins down (M = -N/2). It corresponds to density matrix element $\rho_{N/2,-N/2} = -\rho_{-N/2,N/2}$[2,58-9]. Since ρ is Hermitian, $\rho_{N/2,-N/2}$ must be purely imaginary, hence they are of a single phase. Therefore, a multiple quantum filter of order ΔM will produce pure absorption mode spectra from molecules having ΔM protons. The MQT filter selects one phase of the magnetization.

<u>Time-reversal</u> In equation (2.11), the intensity is given by a complex number $P_{ij}(\tau)Q_{ji}(\tau')$. Pulse sequences exist for the generation of MQT transitions[41] in dipolar coupled systems which, for $\tau = \tau'$, set $Q_{ji}(\tau) = P_{ij}^*(\tau)$, hence setting all lines of a MQT spectrum in pure absorption mode.

2.3 THE COHERENCE TRANSFER STEP IN 2-D CORRELATION EXPERIMENTS

Coherence transfer between the two time domains of a 2-D correlation experiment relies on the existence of coupling between the coherent states in each domain. The coupling can be longitudinal or coherent.

Longitudinal coupling occurs via relaxation processes, chemical exchange or motion. Such processes affect the population levels in a density operator $\alpha\ I_z$. They are studied by 2-D NOE spectroscopy.

Coherent coupling is the scalar or dipolar coupling between pairs of spins. It modulates the off-diagonal elements of the density operator.
COSY, INADEQUATE, MQT, etc. spectroscopies study coherent coupling effects.

The remainder of this thesis will be applied to coherence transfer experiments involving coherent coupling. The appropriate Hamiltonian will contain a selection of terms

$$\mathcal{H}_{cs}^{I}\ ,\ \mathcal{H}_{cs}^{S}\ ,\ \mathcal{H}_{offset}^{I},\ \mathcal{H}_{offset}^{S}\ ,\ \mathcal{H}_{J}^{I,I}\ ,\ \mathcal{H}_{D}^{I,I}\ ,\ \mathcal{H}_{J}^{I,S}$$

The various terms are described in Chapter 1. Dipolar and scalar homonuclear couplings are included, but only scalar heteronuclear

coupling is studied. The coupling Hamiltonians are bilinear in the spin operators. Their effect on the density matrix during a precession period is to cause coherence transfer[60-61] by a rotation known as a bilinear rotation[62].

We will first study the bilinear rotation as applied to the heteronuclear I_nS spin system. The same principles apply in homonuclear correlation.

2.3.1 Bilinear rotation

2.3.1.1 A heteronuclear spin system, I_nS

The spin system I_nS consists of n identical spins I coupled to a single spin S, the heteronucleus. The explicit Hamiltonian for an I_nS spin system with scalar I-S coupling is

$$\mathcal{H} = - \sum_i \Delta\omega_i{}^I - \Delta\omega^S + J_{IS}I_zS_z \qquad (2.12)$$

where J_{IS} is the heteronuclear coupling, eg. J_{CH} is ~ 120-240 Hz. J_{II} = 0 under the condition of identical I spins (Section 1.4.1).

The simplest pulse sequence which effects coherence transfer between I and S, and removes the Zeeman term from equation (2.12)[63] (for efficiency), is

$$\frac{\tau}{2} - \pi^{I,S} - \frac{\tau}{2} - (\pi^{I,S}) \qquad (2.13)$$

$\pi^{I,S}$ is a π pulse applied to both I and S spins, the second $\pi^{I,S}$ is ineffective in an experiment, but makes this pulse sequence cyclic. The corresponding propagator is

$$V(\tau) = e^{-i(\pi_x \mathcal{H} \pi_{\bar{x}})\tau} e^{-i\mathcal{H}\tau}$$

where $\pi_x \mathcal{H} \pi_{\overline{x}} = + \sum_i \Delta\omega_i^I + \Delta\omega^S + J_{IS}I_zS_z$

Hence,

$$V(\tau) = e^{-iJ_{IS}I_zS_z\tau} \qquad\qquad (2.14)^*$$

The assumption of weak coupling made in this calculation is accurate, because of the large difference in precession frequency of the I and S spins. The action of $V(\tau)$ on an operator I_p or S_p, $p = x,y,z$, is a rotation by angle $(2\pi J_{IS}S_z\tau)$ or $(2\pi J_{IS}I_z\tau)$ respectively, e.g.

$$e^{-iJ_{IS}I_zS_z\tau} I_x e^{iJ_{IS}I_zS_z\tau} = I_x\cos(2\pi J_{IS}S_z\tau) + I_y\sin(2\pi J_{IS}S_z\tau)$$
$$\text{——— (2.15)}$$

$$e^{-iJ_{IS}I_zS_z\tau} S_x e^{iJ_{IS}I_zS_z\tau} = S_x\cos(2\pi J_{IS}I_z\tau) + S_y\sin(2\pi J_{IS}I_z\tau)$$
$$\text{——— (2.16)}$$

etc. $V(\tau)$ can be modified to the form

$$e^{-iJ_{IS}I_pS_q\tau} , \qquad\qquad p,q = x,y,z$$

by sandwiching it between appropriate pairs of $\pi/2$ pulses, and can therefore act as a general rotation about any designed axis. The angle of the rotation can also be modified by changing τ or for different J values.

The simplification of the sine and cosine terms of equation (2.16) requires knowledge of the number of equivalent I spins connected to

---

* Typically, units of Hz will be used in the exponent, as in equation (2.14). The corresponding angle in radians is always represented in sine and cosine functions.

the S-spin. Expressions for the three most common cases IS, I_2S and I_3S are derived in Appendix B and given below:

$$\text{IS} \qquad \cos(2\pi J_{IS} I_z \tau) = \cos(\pi J_{IS} \tau) \qquad\qquad (2.17a)$$

$$\sin(2\pi J_{IS} I_z \tau) = 2I_z \sin(\pi J_{IS} \tau) \qquad\qquad (2.17b)$$

$$I_2S \qquad \cos(2\pi J_{IS} I_z \tau) = 1 + (\tfrac{1}{2} + 2I_{z1}I_{z2})(\cos(2\pi J_{IS} \tau)-1) \qquad (2.18a)$$

$$\sin(2\pi J_{IS} I_z \tau) = I_z \sin(2\pi J_{IS} \tau) \qquad\qquad (2.18b)$$

$$I_3S \qquad \cos(2\pi J_{IS} I_z \tau) = \cos^3(\pi J_{IS} \tau) - 4(I_{z1}I_{z2} + I_{z1}I_{z3} + I_{z2}I_{z3})$$
$$\times \sin^2(\pi J_{IS} \tau) \cos(\pi J_{IS} \tau) \qquad (2.19a)$$

$$\sin(2\pi J_{IS} I_z \tau) = 2I_z \sin(\pi J_{IS} \tau) \cos^2(\pi J_{IS} \tau) - 8I_{z1}I_{z2}I_{z3}\sin^3(\pi J_{IS} \tau)$$
$$\text{------} (2.19b)$$

For equation (2.15), since there is only 1 S spin, the conditions always hold:

$$I_nS \qquad\qquad \cos(2\pi J_{IS} S_z \tau) = \cos(\pi J_{IS} \tau) \qquad\qquad (2.20a)$$

$$\sin(2\pi J_{IS} S_z \tau) = 2S_z \sin(\pi J_{IS} \tau) \qquad\qquad (2.20b)$$

Expanding for example, equation (2.15) using equation (2.20), shows that the effect of the J_{IS} coupling on I_x is to create a term in I_yS_z:

$$e^{-iJ_{IS} I_z S_z \tau} I_x \, e^{iJ_{IS} I_z S_z \tau} = I_x \cos(\pi J_{IS} \tau) + 2\, I_y S_z \sin(\pi J_{IS} \tau)$$
$$\text{------} (2.21)$$

Transfer of coherence from I_x to I_yS_z is the first step in the generation of pure S_x coherence, or heteronuclear MQT coherence. A $(\pi/2)_x^{I,S}$ pulse leads to I_zS_y which decays after a further time τ to

a term in S_x (among other terms), according to equations (2.15) and (2.17)-(2.19). A $(\pi/2)_y^{I,S}$ leads to zero and double QT coherence, $I_y S_x$. Table 2.II shows the use of heteronuclear bilinear rotations in the double quantum[39,60], INEPT[64] and DEPT[65] sequences.

2.3.1.2 A homonuclear I_n spin system

Scalar coupling: $\mathcal{H}_J^{I,I}$ replaces $\mathcal{H}_J^{I,S}$ in equation (2.12). In the case of weak scalar I-I coupling, equation (2.14) is simply

$$V(\tau) = e^{-iJ_{II}I_{1z}I_{2z}\tau} \qquad (2.22)$$

For protons, $J_{II} \ll J_{CH}$, so that much longer times τ are needed for effective coherence transfer between spins than in the heteronuclear case. Equations such as (2.15) still hold. Since $[\mathcal{H}_J^{ij}, \mathcal{H}_J^{jk}] = 0$, equation (2.15) can be applied repeatedly for the case $n > 2$, and can be expanded as in (2.17) - (2.19) for up to 4 weakly coupled spins.

Dipolar coupling: $V(\tau)$ has a more complex form. For two spins:

$$V(\tau) = e^{-iD(I_{z1}I_{z2} - (I_{x1}I_{x2}+I_{y1}I_{y2})/2)\tau} \qquad (2.23)$$

where for the present purpose chemical shift is excluded. The bilinear rotation by a dipolar operator can be much more easily represented in the spherical tensor notation (Tables 1.II and 1.III):

$$\mathcal{H}_D = \sqrt{6}\frac{(-2K)}{r^3} T_{2,0} D_{0,0}^2(\Omega)$$

$$\text{and} \quad e^{-i\mathcal{H}_D\tau} T_{1,\pm1} e^{i\mathcal{H}_D\tau} = T_{1,\pm1}\cos(\omega_D\tau) \mp \frac{i}{\sqrt{2}} T_{2,\pm1}\sin(\omega_D\tau)$$

from equation (1.48), where $\omega_D = (3/2)D$ is the frequency of the dipole transition between the two spins. This translates in Cartesian

Table 2.II   44

Examples of the use of bilinear rotation operators

U   Coherence generated

(a) MQT

I $\frac{\pi}{2}_y$ $\frac{1}{4J}$ π $\frac{1}{4J}$ $\frac{\pi}{2}_y$

$2\,\beta I_y S_y : 0,\, 2\,QT$

S π $\frac{\pi}{2}_x$ $2\beta I_y S_y$

$e^{-i\frac{\pi}{2} I_z S_z}$

(b) INEPT

I $\frac{\pi}{2}_y$ $\frac{1}{4J}$ π $\frac{1}{4J}$ $\frac{\pi}{2}_x$ τ π τ

$\beta I_{\uparrow} S_x : 1\,QT$

S π $\frac{\pi}{2}_x$ $2\beta I_z S_y$ π $\propto \beta I_{\uparrow} S_x$

$e^{-i\frac{\pi}{2} I_z S_z}$ $e^{-iJ I_z S_z \tau}$

(c) DEPT

I $\frac{\pi}{2}_y$ $\frac{1}{2J}$ π $\frac{1}{2J}$ θ_x $\frac{1}{2J}$

$\beta I_{\uparrow} S_y : 1\,QT$

S $\frac{\pi}{2}_y$ $2\beta I_y S_z$ π $\propto \beta I_{\uparrow} S_y$

$e^{i\pi I_z S_z}$ $e^{-2i\theta I_z S_z}$
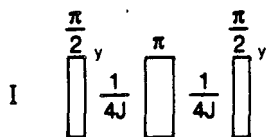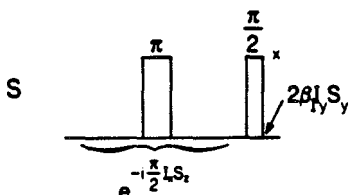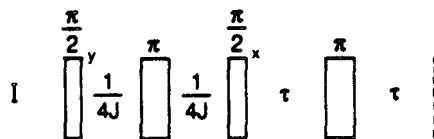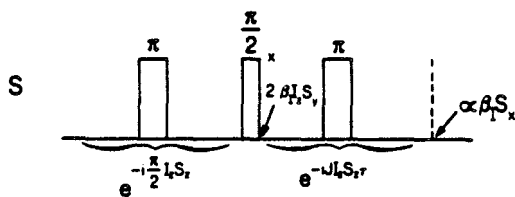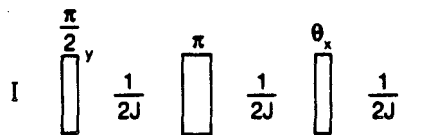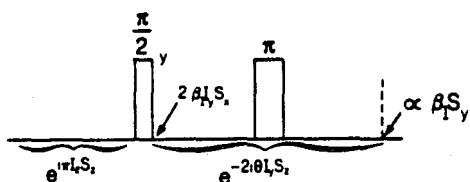
operators to the result:

$$e^{-i\mathcal{H}_D\tau}\, I_{1x}\, e^{i\mathcal{H}_D\tau} = I_{1x}\cos(\omega_D\tau) + \frac{1}{2}(I_{1z}I_{2y} - I_{1y}I_{2z})\sin(\omega_D\tau)$$

$$\text{———— (2.24)}$$

We see that in the case of strong coupling, the bilinear rotation is not a pure rotation about one axis of a single spin. Also, for more than two spins, the result is complex so that a computer is usually consulted.

2.4 SOME EXPLICIT 2-D SEQUENCES

Three 2-D experiments will be considered as examples of experiments which will be illustrated in Chapters 3 and 4.

2.4.1 The Homonuclear COSY experiment

$$U = \frac{\pi}{2} \qquad\qquad V = \frac{\pi}{2}$$

The spectrum of a weakly coupled two spin system, I_2, will be explicitly calculated here, to demonstrate important features of the experiment.

2.4.1.1 A weakly coupled spin system

The evolution of the density matrix is followed[66] according to the definitions in figure 2.1. A $(\pi/2)_y$ pulse gives

$$\rho(0) = \beta I_x = \beta(I_{x1} + I_{x2})$$

i.e. U creates transverse magnetization with order $m = \pm 1$. Evolution in t_1 is defined by the propagator

$$e^{-i\mathcal{H}t_1} = e^{-i(-\nu_1 I_{z1} - \nu_2 I_{z2} + J I_{z1} I_{z2})t_1}$$

$$= e^{i(\nu_1 I_{z1} + \nu_2 I_{z2})t_1} e^{-iJ I_{z1} I_{z2} t_1} \qquad (2.25)$$

This separation is possible because the chemical shift and coupling Hamiltonians commute in the limit of weak coupling. Thus:

$$\rho(t_1^-) = \beta \left\{ [I_{x1} \cos(2\pi\nu_1 t_1) + I_{y1} \sin(2\pi\nu_1 t_1) \right.$$
$$+ I_{x2} \cos(2\pi\nu_2 t_2) + I_{y2} \sin(2\pi\nu_2 t_1)] \cos(\pi J t_1)$$
$$+ [2 I_{y1} I_{z2} \cos(2\pi\nu_1 t_1) - 2 I_{x1} I_{z2} \sin(2\pi\nu_1 t_1)$$
$$\left. + 2 I_{z1} I_{y2} \cos(2\pi\nu_2 t_1) - 2 I_{z1} I_{x2} \sin(2\pi\nu_2 t_1)] \sin(\pi J t_1) \right\}$$
$$\text{———}(2.26)$$

Applying $V = (\pi/2)_y$ gives

$$\rho(t_1^+, 0) = \beta \left\{ [-I_{z1} \cos(2\pi\nu_1 t_1) + I_{y1} \sin(2\pi\nu_1 t_1) \right.$$
$$+ -I_{z2} \cos(2\pi\nu_2 t_1) + I_{y2} \sin(2\pi\nu_2 t_1)] \cos(\pi J t_1)$$
$$+ [2 I_{y1} I_{x2} \cos(2\pi\nu_1 t_1) + 2 I_{z1} I_{x2} \sin(2\pi\nu_1 t_1)$$
$$\left. + 2 I_{x1} I_{y2} \cos(2\pi\nu_2 t_1) + 2 I_{x1} I_{z2} \sin(2\pi\nu_2 t_1)] \sin(\pi J t_1) \right\}$$
$$\text{———} (2.27)$$

Equation (2.27) is the algebraic form of equation (2.7) for a weakly coupled pair of spins. Observable terms are those of the single quantum operators I_{x1}, I_{y1}, I_{x2}, I_{y2}. Antiphase magnetization, $I_{z1} I_{x2}$ and $I_{x1} I_{z2}$, will also lead to observable magnetization after a period of free precession, τ, according to the equivalent of equations (2.15) and (2.20) for a pair of homonuclear spins. For example, $I_{z1} I_{y2}$ leads to the observable operator

$$-\frac{1}{2} (I_{x2} \cos(2\pi\nu_2 \tau) + I_{y2} \sin(2\pi\nu_2 \tau) \sin(\pi J \tau) \qquad (2.28)$$

after time τ.

Equation (2.27) can be truncated to observable terms and manipulated using trigonometric functions to give:

$$\rho(t_1^+,0) = \frac{\beta}{2}\left\{ I_{y1}[\ \sin(2\pi(\nu_1+\tfrac{J}{2})t_1)\ -\ \sin(2\pi(\nu_1-\tfrac{J}{2})t_1)\ ]\right.$$

$$+ I_{y2}[\ \sin(2\pi(\nu_2+\tfrac{J}{2})t_1)\ -\ \sin(2\pi(\nu_2-\tfrac{J}{2})t_1)\ ]$$

$$+ 2I_{z1}I_{x2}[\ \cos(2\pi(\nu_1-\tfrac{J}{2})t_1)\ -\ \cos(2\pi(\nu_1+\tfrac{J}{2})t_1)\ ]$$

$$\left. + 2I_{x1}I_{z2}[\ \cos(2\pi(\nu_2-\tfrac{J}{2})t_1)\ -\ \cos(2\pi(\nu_2+\tfrac{J}{2})t_1)\ ]\right\}\quad (2.29)$$

A number of details of the COSY spectrum can be observed from equation (2.29).

(1) Frequencies in ω_1 (and ω_2) are at $\nu_1 \pm J/2$, $(\nu_2 \pm J/2)$.

(2) The first two terms continue to precess at the same frequency in t_2 as in t_1. These terms therefore give rise to peaks on (or associated with) the diagonal. Two pairs of J-separated doublets occur at ν_1 and ν_2 in each dimension. These two pairs are in phase, because magnetization is aligned at $t_2 = 0$. The lines of each doublet are inverted relative to each other (in antiphase). The sine dependence of t_1 implies that the intensity at $t_1 = 0$ and $t_2 = 0$ is zero, so that the sum of all lines in the spectrum must be zero.

(3) The third and fourth terms precess in t_2 at a different frequency from their t_1 precession. They constitute cross peaks. Both these terms have zero intensity at $t_1 = 0$ and $t_2 = 0$, and are antiphase relative to J (equation 2.28). The cross peaks are in phase with respect to each other, but 90^0 out of phase with respect to the diagonal peaks.

(4) The COSY experiment is amplitude modulated. The experiment is non-quadrature in t_1.

(5) The 1-D spectrum is always reproduced along the diagonal.

The diagram of the Fourier transformed COSY experiment is shown in Figure 2.2 Figure 2.2(a) shows a low resolution map of the positions of all peaks. Non-zero intensity of the cross peaks indicates non-zero coupling between nuclei 1 and 2. Figure 2.2(b) is the high resolution phased spectrum of the left hand side of figure 2.2(a)[8]. To ensure proper phased lines as shown, it is often desirable to phase the spectrum in ω_2 after the first FT and discard the imaginary buffer[8] before the second complex FT in t_1. The problem of phasing 2-D spectra will be discussed in Section 2.5.3.

2.4.1.2 A strongly coupled or multiply coupled spin system

For a strongly coupled spin system, or for a many-spin weakly coupled system, direct calculation becomes difficult or tedious. With strong coupling, equation 2.25 no longer holds. The eigenbasis of the Hamiltonian is no longer the product basis, and the frequencies are no longer transparently obvious. The calculation is most easily done on a computer. The Hamiltonian is diagonalized, and all spin and rotation operators are represented in the eigenbasis of the Hamiltonian. Equation (2.9) with $U = V = (\pi/2)_y$ becomes

$$S(t_1,t_2) = \epsilon\beta \sum_i \sum_j \sum_k \sum_l e^{-i\omega_{ij}t_1} e^{-i\omega_{kl}t_2} \left(I_x\right)_{ij}\left(I_+\right)_{lk} R_{ki\ lj}$$

$$\text{———— (2.30)}$$

where $R = e^{-i\frac{\pi}{2}I_y}$

For n coupled spins-1/2, the size of each matrix is $2^n \times 2^n$. Calculations and computer programs for various pulse sequences exist[46-7,58].

We note the following general features:

(1) The coupling, rather than the chemical shift dominates the spectrum.

(2) Lines are not generally phaseable; the read pulse ($\pi/2$) does not select one phase of the magnetization, because the spins are strongly coupled.

(3) The spectrum is non-quadrature in t_1.

Figure 2.2c shows a schematic COSY spectrum of a strongly coupled two spin system in absolute value mode, for comparison with figure 2.2(b).

Figure 2.3 is an example of a COSY spectrum on a strongly coupled 6-spin system: benzene dissolved in the liquid crystal EK 15320. In the strongly coupled case, cross peaks do not indicate coupling between individual nuclei, since every transition involves all spins on the molecule. Cross peaks instead indicate transitions of the same symmetry, which are correlated. Figure 2.4 shows the COSY spectrum on 20% randomly deuterated benzene. The spectrum looks very complex compared to figure 2.3 because it contains signals from a mixture of different isomers. However, only transitions which correspond to spins on the same isomer can have cross peaks. Intramolecular coupling is averaged to zero by translational motion in liquid crystals. Signals from different molecules can be recognized by the absence of cross peaks between them. This is an important application of COSY for the analysis of mixtures[18], which will be extensively used in Chapter 4.
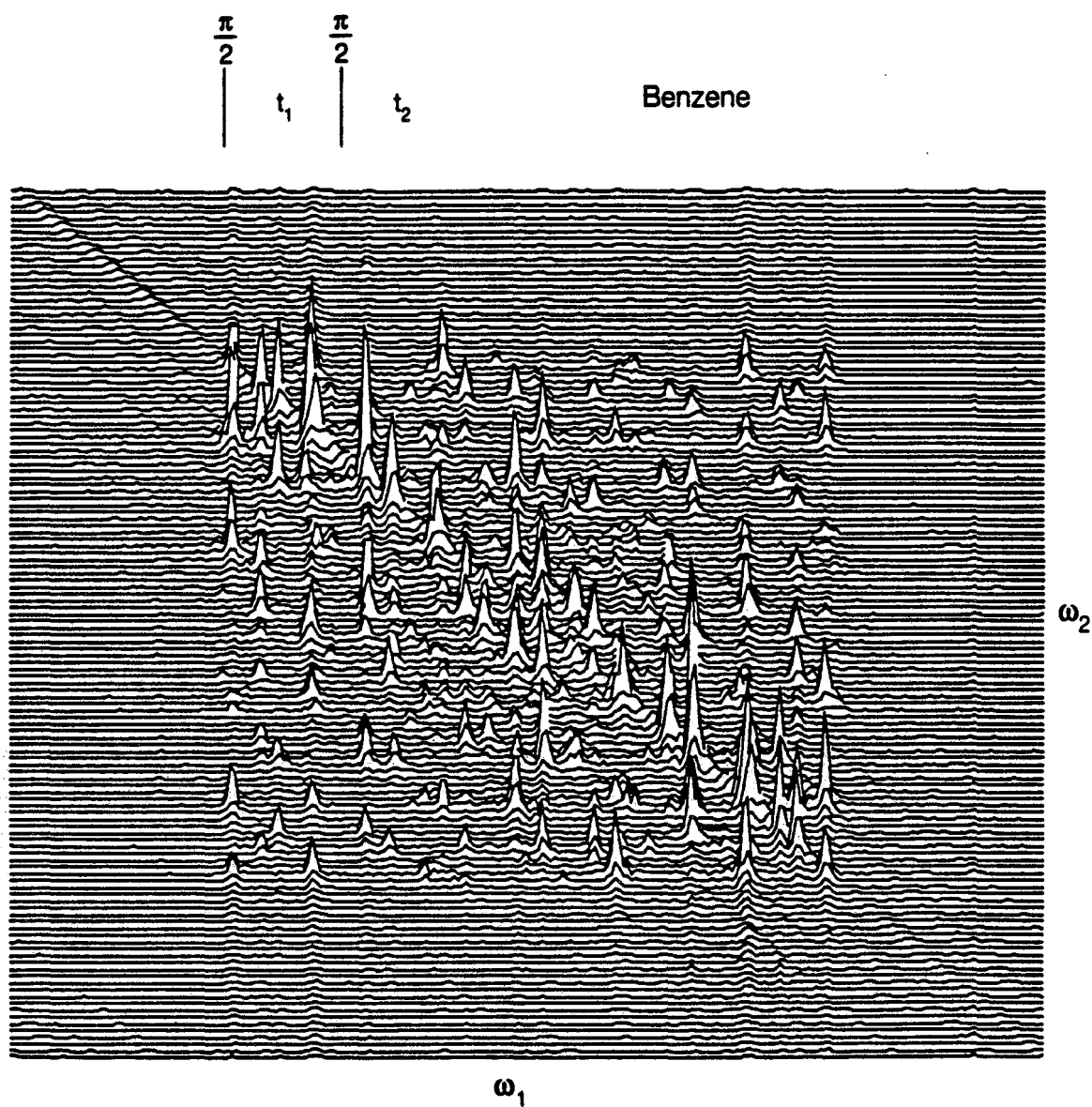
Figure 2.3

Cosy spectrum of benzene. Spectral width was 10 KHz in both
dimensions.

$$\frac{\pi}{2} \qquad \frac{\pi}{2}$$

| t_1 | | t_2 |

20% Deuterated benzene

ω_2

ω_1
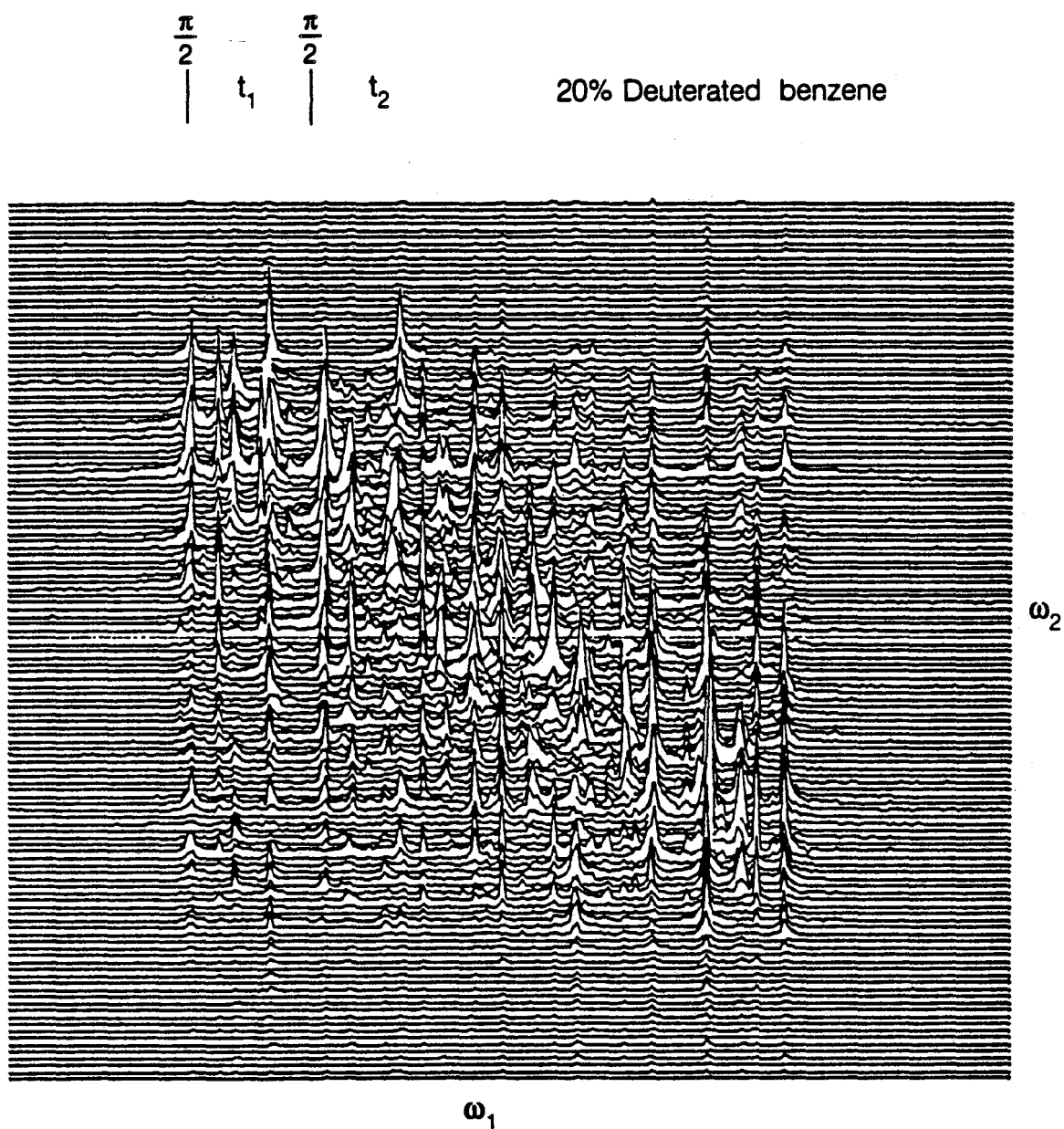
XBL 871-9545

Figure 2.4

COSY spectrum of 20% deuterated benzene. Spectral width was 8 KHz in both dimensions.

2.4.2 **Homonuclear MQT correlation**

2.4.2.1 Calculation of the spectrum

Figure 2.5a shows the simplest multiple quantum pulse sequence, consisting of three pulses. Also shown in figure 2.5 are two variations including π pulses in the preparation or evolution periods. The following calculation will concentrate on sequence 2.5(b), for which

$$U = \left(\frac{\pi}{2}\right)_{\overline{y}} - \frac{\tau}{2} - \pi - \frac{\tau}{2} - \left(\frac{\pi}{2}\right)_{y}; \qquad V = \left(\frac{\pi}{2}\right)_{\overline{y}} - \frac{\tau}{2} - \pi - \frac{\tau}{2}$$

Coherence transfer is effected by a bilinear rotation due to homonuclear coupling. The effective Hamiltonian operating during τ is $\mathcal{H}_{zz} = \mathcal{H}_D + \mathcal{H}_J$, to first order.

The effect of two pulses separated by a time delay is to generate multiple quantum coherence. The preparation propagator is given by

$$U(\tau) = e^{-i\pi/2 \, I_y} \, e^{-i\mathcal{H}_{zz}\tau} \, e^{i\pi/2 \, I_y} = e^{-i\mathcal{H}_{xx}\tau} \qquad (2.31)$$

where $\mathcal{H}_{xx} = \sum_{i<j} D_{ij} I_{xi} I_{xj} - \frac{1}{2}(I_{yi}I_{yj} + I_{zi}I_{zj}) + \mathcal{H}_J$

$$= -\frac{1}{2}\mathcal{H}_{zz} + \sum_{i<j} \frac{3}{8} D_{ij}(I_{+i}I_{+k} - I_{-j}I_{-k}) + \mathcal{H}_J \qquad (2.32)$$

$\mathcal{H}_{xx}$ contains 0 quantum operators ($-\mathcal{H}_{zz}/2$, $\mathcal{H}_J$) and 2 quantum operators ($I_{+i}I_{+j}$, $I_{-i}I_{-j}$). For figure 2.5a, with no π pulse during the preparation, one quantum operators ($\mathcal{H}_x$) would also be included, where

$$\mathcal{H}_x = -\sum_i \nu_i I_{xi} - \Delta\omega \, I_x$$

The density matrix at the end of preparation is given by:

Typical Multiple Quantum Pulse Sequences
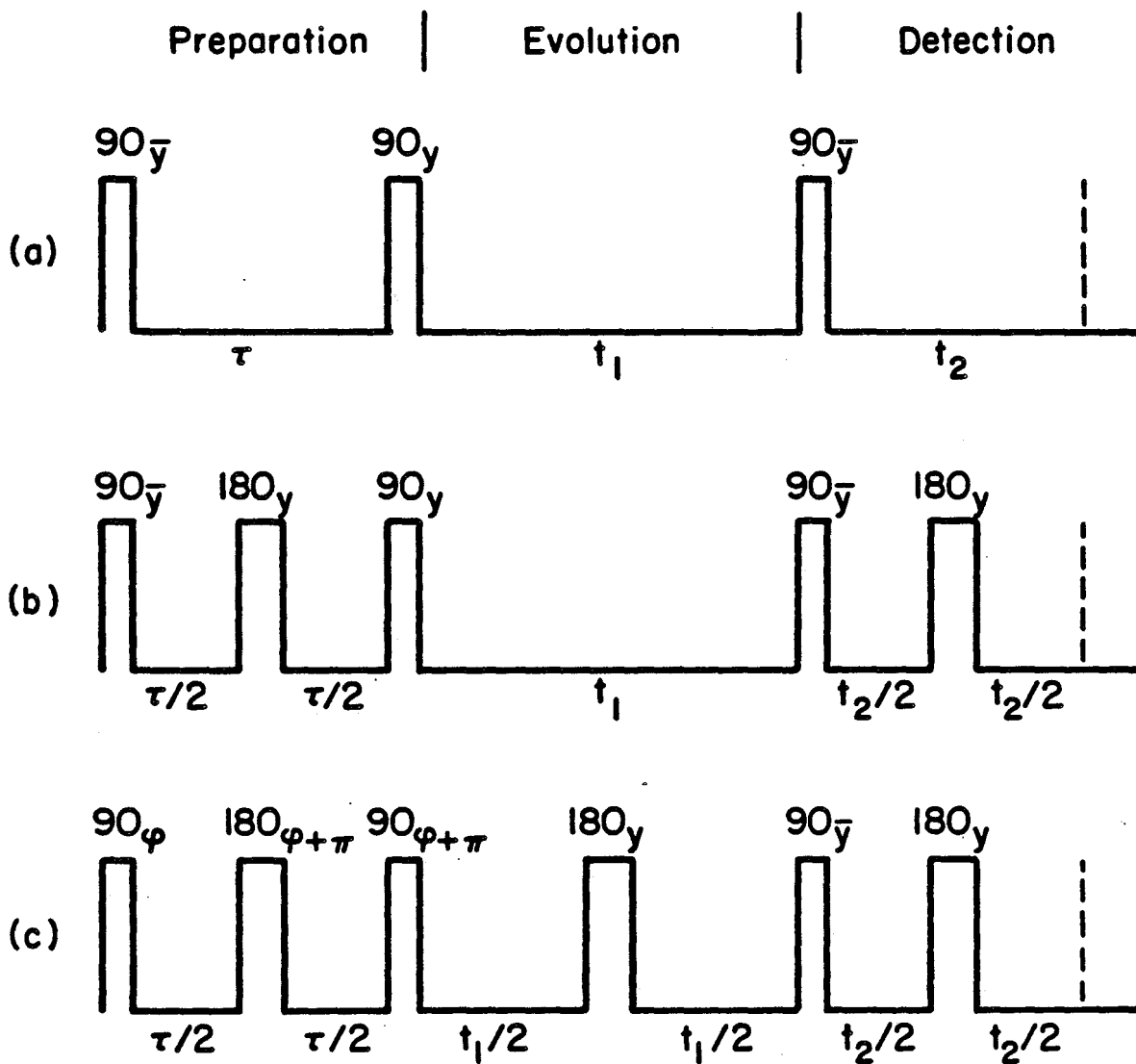
XBL 821-7589

Figure 2.5

Multiple quantum pulse sequences used and described in the text. (Figure courtesy of reference (58)).

$$\rho(0) = e^{-i\mathcal{H}_{xx}\tau}\beta I_z e^{i\mathcal{H}_{xx}\tau}$$

$$= \beta I_z(1 + i[I_z,\mathcal{H}_{xx}]\tau - \frac{1}{2}[[I_z,\mathcal{H}_{xx}],\mathcal{H}_{xx}]\tau^2 + \dots \qquad (2.33)$$

The higher the value of $\|H_{xx}\|$, the smaller τ need be in equation (2.33) for the creation of significant high order multiple quantum intensity. Thus, strongly coupled systems are predisposed towards observation of their MQT spectra. At the same time, such systems usually have complex single quantum spectra, so that analysis of their more sparse higher order spectra is desirable.

The evolution and mixing periods result in a signal

$$S(t_1, 0) = \sum_i \sum_j \rho_{ij}(0) e^{-i\omega_{ij}t_1} Q_{ji}(\tau) \qquad (2.34)$$

where ω_{ij} are the evolution frequencies in t_1 defined by equation (2.33), and

$$Q(\tau) = \epsilon\, e^{i\pi/2\, I_y}\, e^{i\mathcal{H}_{zz}\tau}\, I_+\, e^{-i\mathcal{H}_{zz}\tau}\, e^{-i\pi/2\, I_y}$$

$V(\tau)$ can be made exactly equal to $U(\tau)$ by assuming a fourth pulse $(\pi/2)_{\bar{y}}$, with "detection" of I_z[58]. This is equivalent to writing

$$Q(\tau) = \epsilon\, e^{i\pi/2\, I_y}\, e^{i\mathcal{H}_{zz}\tau}\, e^{-i\pi/2\, I_y}\, I_z\, e^{i\pi/2\, I_y}\, e^{-i\mathcal{H}_{zz}\tau}\, e^{-i\pi/2\, I_y},$$

retaining only "observable" terms $\propto I_z$. Thus

$$Q(\tau) = e^{i\mathcal{H}_{xx}\tau}\, I_z\, e^{i\mathcal{H}_{xx}\tau}, \qquad \text{and}$$

$$Q_{ji}(\tau) = \frac{\epsilon}{\beta}\, \rho_{ij}(0)$$

Hence equation (2.34) becomes

$$S(t_1,0) = \frac{\epsilon}{\beta} \sum_i \sum_j \rho_{ij}^2(0) \; e^{-i\omega_{ij}t_1} \qquad (2.35)$$

2.4.2.2 Properties of the MQT spectrum

The signal will be neither in quadrature nor phaseable with respect to t_1. $\rho_{ij}^2(0)$ is a complex number with a different phase for each transition ij.

2.4.2.2.1 Even quantum selection

For figure 2.5b and equation 2.33, $\rho(0)$ contains only even quantum operators, eg.

$$[I_z, \mathcal{H}_{xx}] = \sum_{i<j} \frac{3}{4} D_{ij} (I_{i+}I_{j+} + I_{i-}I_{j-}) \text{ is a two quantum operator,}$$

$[[I_z, \mathcal{H}_{xx}], \mathcal{H}_{xx}]$ contains zero and two quantum operators,

and higher order terms introduce higher order even MQT coherences.

2.4.2.2.2 Odd quantum selection

Figure 2.5b with the second pulse 90^0 out of phase with respect to the first becomes selective for odd orders only[58]. The sequence $(\pi/2)_{\overline{x}} - \tau - (\pi/2)_y$ acting on the operator βI_z is the same as the sequence $(\pi/2)_{\overline{y}} - \tau - (\pi/2)_y$ operating on βI_y. $\rho(0)$ can be written exactly as in equation (2.33) for the even order case, except with βI_z replaced by βI_y. Thus every even order operator becomes an odd order operator, and the sequence is selective for odd orders.

2.4.2.2.3 Non-selective MQT preparation

Figure 2.5a, in the presence of $\mathcal{H}_{cs}$ or $\mathcal{H}_{offset}$ during τ leads to

both odd and even orders generated in the final spectrum. Figure 2.5b, with the second pulse a $(\pi/4)$ pulse does likewise.[63]

2.4.2.3 Resonance offset for separation of MQT orders

During t_1, the various MQT operators evolve according to the frequencies defined by $\mathcal{H}$ and ΔM. In the absence of chemical shift or resonance offset, Fourier transformation with respect to t_1 of the experiment 2.5b will produce a spectrum containing all the MQT orders superimposed about the same centre. This can be seen simply by looking at the energy level diagram in figure 2.6.

The presence of a resonance offset will serve to separate the MQT orders as a function of t_1.

$$\mathcal{H}_{offset} = - \Delta\omega\, I_z$$

$$S(t_1,0) = \sum_i \sum_j \langle i | e^{-i\Delta\omega I_z t_1} \rho(0)\, e^{i\Delta\omega I_z t_1} | j \rangle\, Q_{ji}(\tau)\, e^{i\omega_{ij} t_1}$$

$$\text{------ (2.36)}$$

where ω_{ij} are the frequencies of the system in the absence of resonance offset. Resonance offset introduces a frequency shift $\Delta M\Delta\omega$ where $\Delta M = m_i - m_j$. The offset is linear with ΔM, so that by setting $\Delta\omega = $ maximum spectral width required by any order, complete separation of the orders is achieved.

One difficulty which arises in this scheme is that field inhomogeneity behaves in a similar way to resonance offset:

$$\langle i | e^{-i\omega(\tilde{r})I_z t_1} \rho(0)\, e^{i\omega(\tilde{r})I_z t_1} | j \rangle = e^{-i\Delta M\,\omega(\tilde{r})\, t_1} \rho_{ij}(0) \quad (2.37)$$

The broadening caused by magnetic field inhomogeneity is amplified linearly with ΔM, so that higher quantum orders may become obscured.
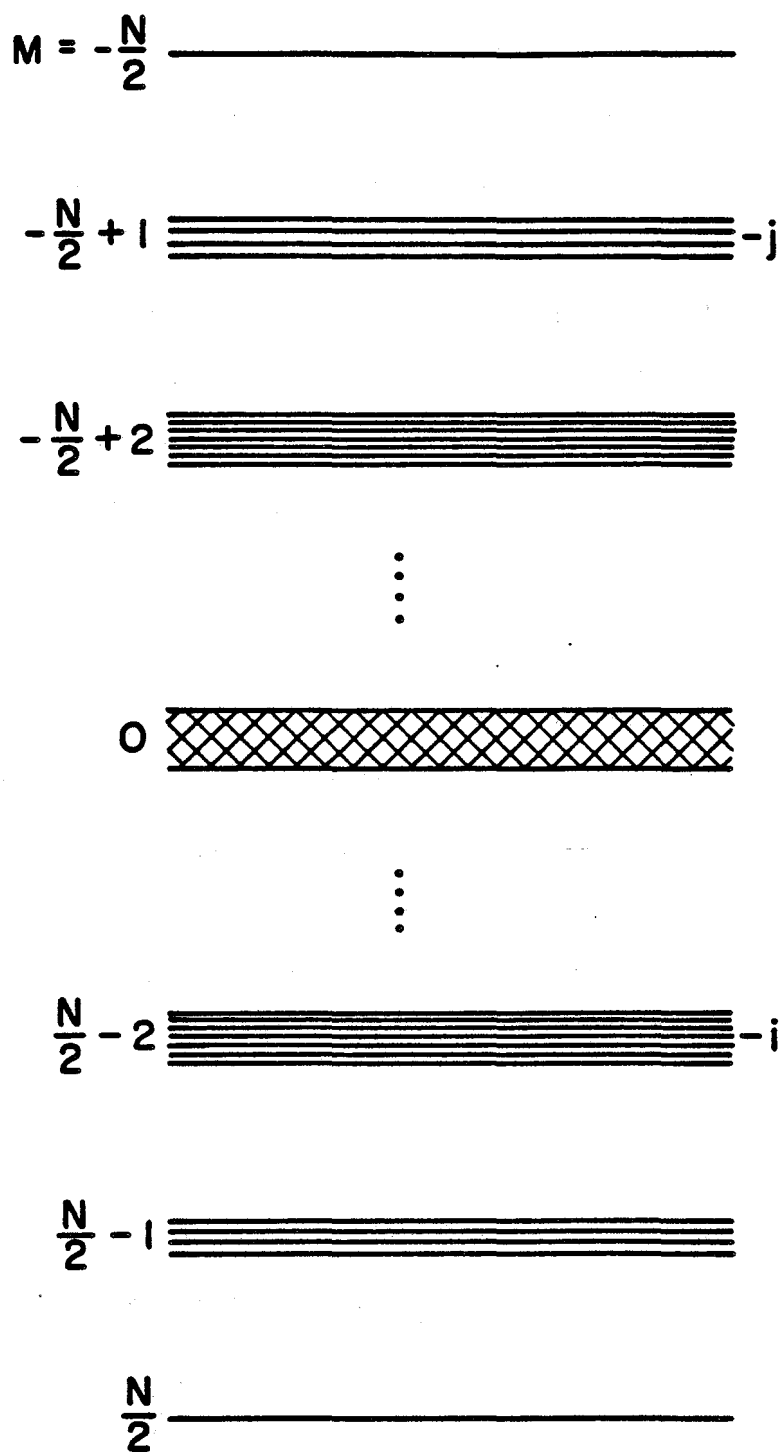
XBL 7710-10022

Figure 2.6

Energy level diagram for a dipole coupled N spin system.

Transitions of all orders are centred about 0 frequency. (Figure

courtesy of reference (58)).

A better solution is to use phase cycling as indicated in figure 2.5c. Offset, inhomogeneity and chemical shift are cancelled by a π pulse in t_1, and phase incrementation proportional to t_1 (TPPI) artificially effects a resonance offset. This is described in more detail in Section 2.4.3.5.

Figure 2.7 is an example of a multiple quantum spectrum in which TPPI has been used to separate multiple quantum orders. All orders are present; the spectrum is calculated by the addition of an odd and an even selective experiment. In ω_2, the normal 1 QT spectrum is obtained.

2.4.3 Heteronuclear MQT correlation

The J-coupling between heteronulear spins in liquids is very useful for the observation of connected nuclei in 2-D heteronuclear experiments[27,30,55,67], for the generation of heteronuclear MQT coherence[42,68], selective observation of satellite protons at a labelled site, eg. ^{13}C, ^{15}N, in the presence of protons many times more abundant at NMR inactive sites [60,62,69]. For this thesis, attention is restricted to ^{13}C (S) - ^1H (I) spin systems, but the approach can be easily generalized to other nuclei.

The sequence which will be considered here is

$$U = \left[\frac{\pi}{2}\right]^I - \frac{\tau}{2} - (\pi)^{I,S} - \frac{\tau}{2} - \left[\frac{\pi}{2}\right]^{I,S}; \qquad V = \left[\frac{\pi}{2}\right] - \frac{\tau'}{2} - (\pi)^{I,S} - \frac{\tau'}{2}$$

on a two spin system IS. This is a typical sequence in heteronuclear MQT spectroscopy[2], and has been demonstrated in the study of natural abundance ^{13}C and ^{15}N[28,68,70].

— 5270

ω_2

— -4730

6   5   4   3   2   1   0

62500   0 Hz

ω_1
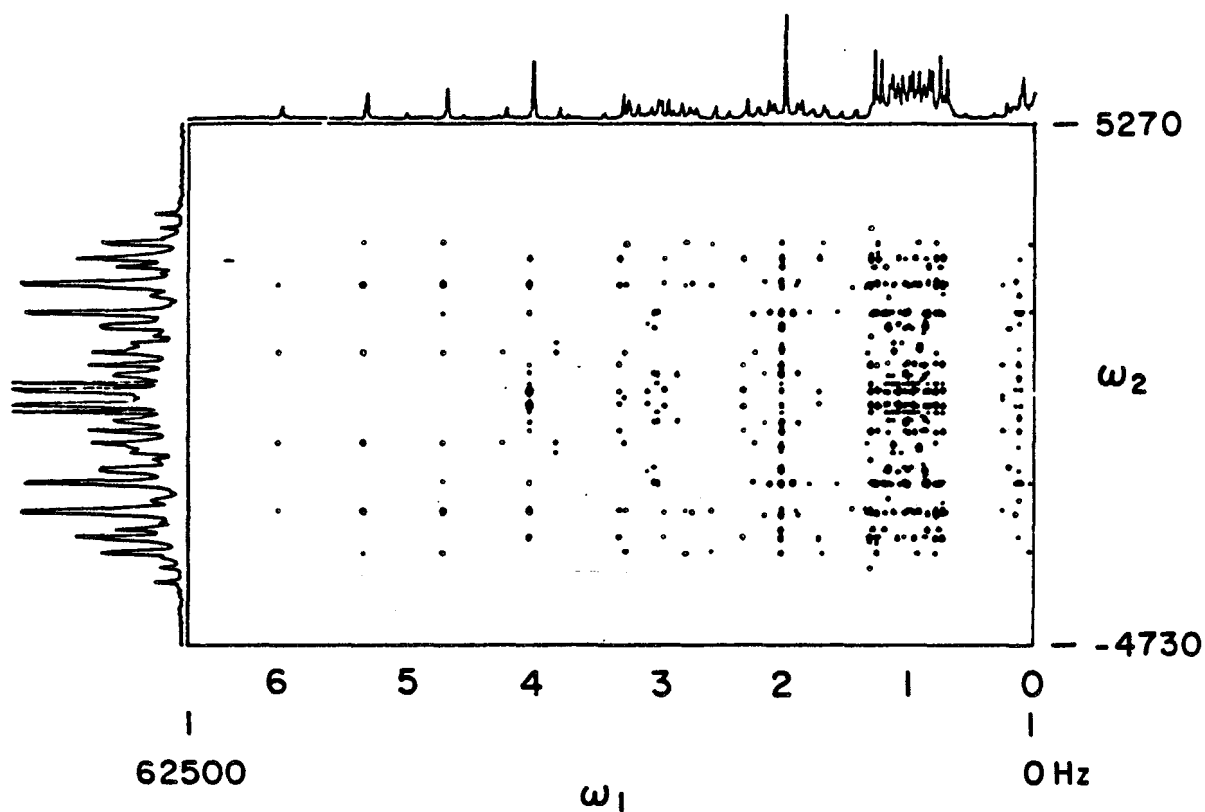
XBL 851-755

Figure 2.7

Example of a MQT spectrum on 20% deuterated benzene. An odd and an even order spectrum obtained using TPPI were coadded. A phase shift of 26.7^{o} was used.

2.4.3.1 Coherence Transfer

$U(\tau)$ corresponds to the propagator:

$$e^{-i\pi/2\ I_y}\ e^{-iJ_{IS}I_zS_z}\ e^{i\pi/2\ I_y} = e^{-iJ_{IS}I_xS_z\tau}$$

Hence, the preparation of heteronuclear coherence is given by

$$e^{-iJ_{IS}I_xS_z\tau}\ \beta I_z\ e^{iJ_{IS}I_xS_z\tau} = \beta\ [I_z\cos(\pi J_{IS}\tau) - 2I_yS_z\sin(\pi J_{IS}\tau)]$$

Setting $\tau = 1/2J_{IS}$, and applying the $(\pi/2)_x^S$ pulse to get transverse magnetization gives:

$$\rho(0) = \beta\ 2I_yS_y, \quad \text{a two-quantum operator.} \tag{2.38}$$

2.4.3.2 Evolution

Writing $\quad I_yS_y = - (I_+S_+ + I_-S_- - I_+S_- - iI_-S_+)/4$,

demonstrates the ± 2 QT and 0 QT operators, which evolve in t_1 at sums and differences of the chemical shifts

$$\rho(t_1^-) = -\frac{1}{2}\beta\ \left\{(I_+S_+)\ e^{-i(\omega_I + \omega_S)t_1} + (I_-S_-)\ e^{i(\omega_I + \omega_S)t_1}\right.$$

$$\left. - (I_+S_-)\ e^{-i(\omega_I - \omega_S)t_1} - (I_-S_+)\ e^{i(\omega_I - \omega_S)t_1}\right\}$$

$$= 2\beta\ \left\{I_xS_x\ \sin\omega_I t_1\sin\omega_S t_1 + I_yS_y\ \cos\omega_I t_1\cos\omega_S t_1\right.$$

$$\left. - I_xS_y\ \cos\omega^I\sin\omega^S - I_yS_x\ \sin\omega^I\cos\omega^S\right\}\ \text{——(2.39)}$$

2.4.3.4 Mixing and Detection

$V(\tau')$ is composed of a $(\pi/2)_y^S$ pulse followed by the propagator
$e^{-iJ_{IS}I_zS_z\tau'}$. Thus antiphase magnetization I_xS_z and I_yS_z is

generated from terms 1 and 4 in equation (2.39), which decay to

observable magnetization under V with $\tau' = \tau = 1/2J$:

$$\rho(t_1, 0) = -\beta I_y \sin \omega_I t_1 \sin \omega_S t_1 - \beta I_x \sin \omega_I t_1 \cos \omega_S t_1 \qquad (2.40)$$

The non-quadrature nature of this spectrum is reflected in 0 and 2 QT

lines of equal intensity. The final signal is given by:

$$S(t_1, 0) = -\frac{\beta\epsilon}{2} \sin(\omega_I t_1) \; e^{i\omega_S t_1}$$

Later, sequences will be shown which give both absortion mode spectra

and quadrature in ω_1, while retaining the S/N advantage of initiating

and detecting magnetization at protons, and eliminating any

contribution of the static field inhomogeneity.

2.5 PHASE CYCLING

There are a number of features in Section 2.4 which can be

considerably improved by phase cycling methods. Shortcomings include

non-quadrature in t_1[25], unwanted axial peaks, pulse errors[55],

phase distortions on double complex Fourier transformation[57]. In

heteronuclear correlations, discrimination between satellite and non-

satellite magnetization is often desirable. In multiple quantum NMR

problems include overlap of different multiple quantum orders,

sensitivity to pulse errors. All of the above can be improved by

phase cycling procedures[19,21]. A brief description of the effect of

phase modulation on a pulse or operator will be followed by

application to several of the experiments discussed above.

2.5.1 Phase shifting of pulses

Phase shifting of rf pulses by angle ϕ is equivalent to rotation about the z-axis by ϕ. Thus, for a $\pi/2$ pulse,

$$\left(\frac{\pi}{2}\right)_{x+\phi} = e^{-i\phi I_z}\, e^{-i\pi/2\, I_x}\, e^{i\phi I_z}$$

$$= e^{-i\pi/2\, (I_x\cos\phi + I_y\sin\phi)}$$

$$= e^{-i\pi/2\, I_\phi} \tag{2.41}$$

and for a π pulse,

$$e^{i\pi\phi} = e^{-i\phi I_z}\, \pi_x\, e^{i\phi I_z}$$

$$= (\pi_x\pi_x)\, e^{-i\phi I_z}\, \pi_x\, e^{i\phi I_z}$$

$$= \pi_x\, e^{2i\phi I_z} \tag{2.42}$$

For an arbitrary propagator U, a phase shift by ϕ is given by

$$U_\phi = e^{-i\phi I_z}\, U\, e^{i\phi I_z} \tag{2.43}$$

2.5.2 Effect of a phase shift on the density operator

The effect of a rotation ϕ on the density matrix element which has order $\Delta M_{ij} = m_i - m_j$ is

$$\langle i| e^{-i\phi I_z}\, \rho\, e^{i\phi I_z} |j\rangle = \rho_{ij} e^{-i\Delta M_{ij}\phi} \tag{2.44}$$

Consider propagator U acting on the density matrix ρ, resulting in $(U\rho U^\dagger)$. Changing the phase of U by ϕ causes the following change in the phases of the elements of $(U\rho U^\dagger)$:

$$\langle k|U_\phi \rho\, U_\phi^\dagger|l\rangle = \langle k|e^{-i\phi I_z} U\, e^{i\phi I_z} \rho\, e^{-i\phi I_z} U^\dagger e^{i\phi I_z}|l\rangle$$

$$= (U\rho U^\dagger)_{kl}\, e^{-i\Delta M_{kl}\phi} \sum_i \sum_j e^{i\Delta M_{ij}\phi} \qquad (2.45)$$

i.e. The phase of the kl-th element of $(U\rho U^\dagger)$ is changed by $(\Delta M_{kl} - \Delta M_{ij})\phi$, where the indices ij correspond to any element of ρ which can be transferred by U into kl coherence in $(U\rho U^\dagger)$. We write

$$\Delta p = (\Delta M_{kl} - \Delta M_{ij}) \qquad (2.46)$$

This is a very important result. By changing the phase of a pulse or propagator by ϕ, the phase of the density matrix elements is changed by $\Delta p \times \phi$, where Δp is the change in coherence level caused by the propagator. This idea is extensively developed in the design of phase cycling precedures for selective sequences[71-72].

For example, consider

$$U_x = \left(\frac{\pi}{2}\right)_{\overline{y}} - \tau - \left(\frac{\pi}{2}\right)_y \quad ; \quad \Delta p = 0, \pm 1, \pm 2, \pm 3 \ldots$$

as the preparation step of a MQT experiment. By keeping the third read pulse at a constant phase, phase cycling U by 180^0, and coadding the resulting two spectra, all even orders can be selected. Only coherences for which $\Delta p\, \pi = 2k\pi$ are retained. Odd order coherence is inverted by the phase change and cancels out.

2.5.3 Examples of phase shifting procedures

In all cases, it is assumed the spectrometer detects in quadrature and samples m = +1 coherence.

2.5.3.1 Removal of axial peaks in COSY or MQT spectra

Axial peaks result from longitudinal relaxation during t_1. Some of the transverse coherence decays to I_z and is converted back into observable coherence by the second pulse. It appears at $\omega_1 = 0$ in the 2-D spectrum. Axial peaks can be large and obscure other resonances. They may be eliminated by the phase cycling procedure[19,21]:

$$
\begin{array}{ccc}
 & & \text{receiver} \\
\begin{bmatrix} U_x & V_x & + \\ U_x & V_{\overline{x}} & + \end{bmatrix}
\end{array}
$$

Coherence changes phase by $\Delta p.\pi$, where $\Delta p = 1$ for longitudinal coherence I_z during t_1, $\Delta p = 0, \pm 2$ for transverse coherence. Thus signal from longitudinal coherence in t_1 is cancelled. Figure 2.8a shows the coherence transfer pathways in the COSY experiment. The pathway shown in dashed lines is eliminated by the phase cycling above.

2.5.3.2 Quadrature in t_1

Figure 2.8a shows that coherence both of $m = +1$ and $m = -1$ in t_1 is detected in t_2. A read pulse of one phase does not discriminate between them. The simplest solution to this problem is to vary the phase of the read pulse, according to the cycle[19,21]:

$$
\begin{array}{ccc}
 & & \text{receiver} \\
\begin{bmatrix} U_x & V_x & + \\ U_x & V_y & - \end{bmatrix}
\end{array}
$$

The dashed pathway in figure 2.8b is eliminated by this procedure. The dashed line is the coherence pathway for which m changes from 0 - +1 - +1. It is termed anti-echo signal. The solid line corresponds to coherence pathway 0 - -1 - +1, and is termed echo signal. Echo signal accumulates a phase factor due to the magnetic field
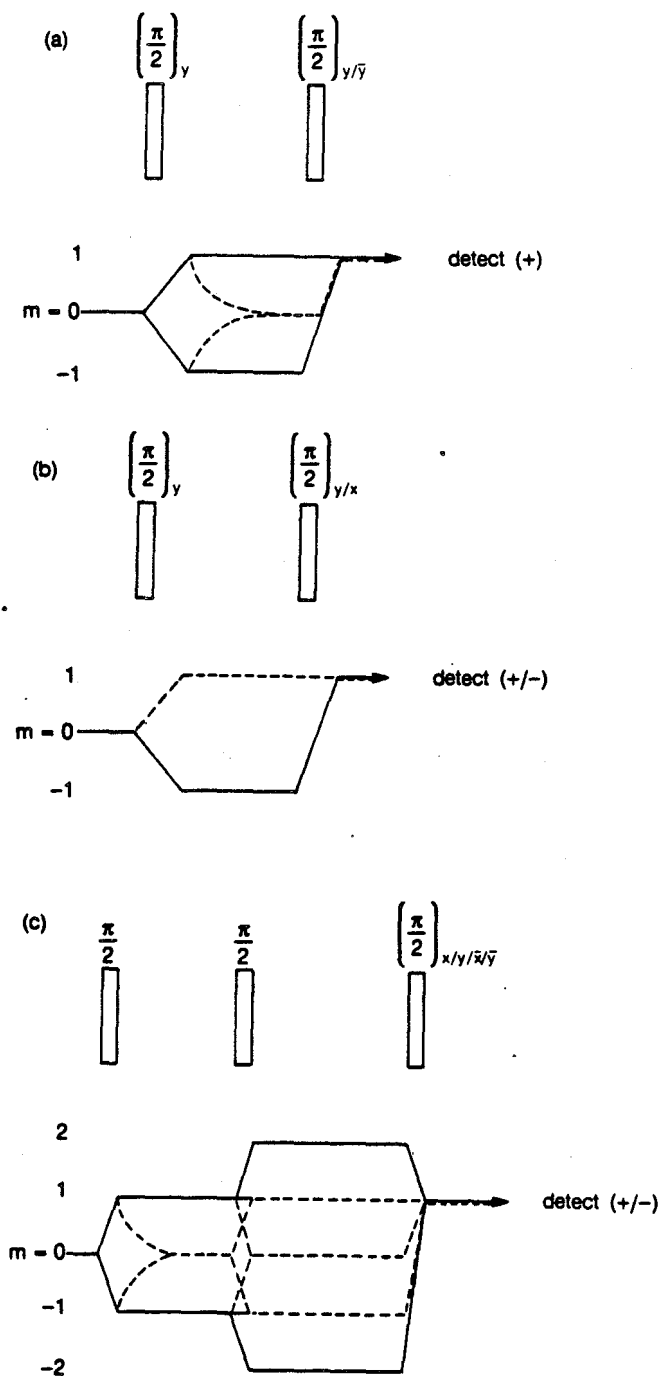
XBL 871-9542

Figure 2.8

Phase cycling procedures and the corresponding coherence pathways. Dotted lines show pathways eliminated by the phase cycling.

(a) COSY, elimination of axial peaks

(b) COSY, selection of quadrature

(c) 2 QT filter.

inhomogeneity of $\exp(-i\omega(\tilde{r})t_1)$ during t_1, and of $\exp(i\omega(\tilde{r})t_2)$ during t_2. A coherence transfer echo is produced at $t_2 = t_1$. Echo peaks are narrower at a 90^0 angle to the main diagonal in a 2-D COSY spectrum and are usually selected over antiecho peaks. In a well shimmed magnet, the difference is negligible.

2.5.3.3 Phasing a quadrature COSY spectrum

The effect of phase cycling the read pulse in Section 2.4.3.2 to get frequency discrimination in t_1 is to additionally cause phase twisted lineshapes in the COSY spectrum[57]. The simplest non-quadrature COSY sequence and a real transform in t_1 gives a phased 2-D spectrum as shown in figure 2.2b:

$$S(\omega_1,\omega_2) \approx (1/2)\ (A_1^+ + iD_1^+ + A_1^- + iD_1^-).A_2$$
$$= (1/2)\ (A_1^+A_2 + A_1^-A_2) + i(D_1^+A_2 + D_1^-A_2) \qquad (2.47)$$

where

$$A_1^+ = \int_0^{t_1} e^{-i\omega_1 t}\cos(\omega t)dt\ ; \qquad A_1^- = \int_0^{t_1} e^{i\omega_1 t}\cos(\omega t)dt\ ;$$

$$D_1^+ = \int_0^{t_1} e^{-i\omega_1 t}\sin(\omega t)dt\ ; \qquad D_1^- = \int_0^{t_1} e^{i\omega_1 t}\sin(\omega t)dt\ ; \qquad (2.48)$$

etc. for subscript 2. (The sign is not specified in the case of subscript 2 since the quadrature nature of the signal in ω_2 is assumed.) Hence, the real part of the spectrum is in phase.

Cycling the read pulse by 90^0 and adding a second spectrum is equivalent to adding dispersion lineshapes to the spectrum.

$$S(\omega_1,\omega_2) = (A_1^+ + iD_1^+)(A_2 + iD_2)$$
$$= (A_1^+A_2 - D_1^+D_2) + i(A_1^+D_2 + D_1^+A_2). \qquad (2.49)$$

Here, the second transform is complex, to ensure saving the sign

information.

Methods have been developed for obtaining pure absorption mode 2-D COSY spectra. The two halves of the phase cycle of Section 2.5.3.2 are separately transformed, with a real transform in t_1[73]. This gives

$$Re(S_c(\omega_1,\omega_2)) = (1/2)\ (A_1^+ + A_1^-)A_2 \qquad (2.50)$$

$$Im(S_s(\omega_1,\omega_2)) = (1/2)\ (A_1^+ - A_1^-)A_2 \qquad (2.51)$$

If the two spectra are now combined by

$$S_c(\omega_1,\omega_2) + i\ S_s(\omega_1,\omega_2) = A_1^+A_2,$$

a pure phase, frequency discriminated spectrum is obtained. This is at the expense of storing twice as much data, but with the same NMR experimental time.

A second method[74] uses the Time Proportional Phase Incrementation[36,38,75] (TPPI) technique to separate between orders with m = +1 and m = -1. The phase of the preparation pulse is shifted by ϕ with each t_1 increment. The density matrix responds accordingly:

$$\rho_{ij}(t_1,\phi) = \rho_{ij}(t_1,\phi=0)\ e^{i\omega_{ij}t_1}\ e^{i\Delta M\ \phi} \qquad (2.52)$$

where ΔM has been written for Δp, since all elements have coherence 0 before the preparation pulse. Marion and Wuthrich indicated that by setting the phase increment to $\phi = t_1\Delta\omega$, the signal becomes

$$\rho(t_1,\omega_2) = A_2\cos(\omega_{ij}+ \Delta M\Delta\omega)t_1 \qquad (2.53)$$

With $\Delta M = \pm 1$, the echo and antiecho signal become shifted by $\pm \Delta\omega$. The minimum requirement is $\Delta\omega = $ (spectral width(SW))/2, which corresponds to $\phi = \pi$ (the SW is defined as $1/\Delta t_1$). The real transformation wrt t_1 assures absorption mode signals. TPPI assures

that all peaks lie between ± SW, so there is no aliasing. The price
paid is that twice the SW is required compared to the basic COSY
experiment.

2.5.3.4. <u>Selection of a MQT order - Phase Fourier transform (PFT)</u>

By cycling the preparation phase U_ϕ through appropriate fractions
of 360°, any multiple quantum order can be selected by a linear
combination of the phase shifted spectra[76-77]. Typically, for
selection of even order ΔM, $\phi = 360/2\Delta M$ ensures elimination of all odd
orders and even orders at least up to $2\Delta M$. For selection of odd
orders, the rule $360/4\Delta M$ has the same effect. Figure 2.8c shows a
relative phase change in 90° steps of U relative to V. 2QT coherence
is selected, with 0 QT, 1 QT and axial signal eliminated.

2.5.3.5 <u>Separation of Multiple Quantum Orders by TPPI</u>

Separation of all orders in the same spectrum is usually more
convenient than PFT because errors caused by imperfect phase
cancellation or dynamic range problems tend to occur in PFT. Using
equation (2.52) with $\phi = t_1\Delta\omega$, gives

$$S(t_1,t_2) = \cos(\omega_1 + \Delta M\Delta\omega)t_1 \, e^{-i\omega_2 t_2} \qquad (2.54)$$

ϕ must be chosen so that $(2\Delta M_{max} + 1)\phi \leq 2\pi$, to separate $(2\Delta M_{max} + 1)$
orders.

2.5.3.6 <u>Correction for a π pulse error</u>

π pulses are often used to echo chemical shifts and
inhomogeneities. Imperfect π pulses lead to spurious peaks[55]. A

perfect example is given in the spectrum of CH_2Cl_2 in figure 2.9.
These are phantom signals due to the transverse magnetization
generated by an imperfect π at $t_1/2$ and $t_2/2$, hence causing signals
which appear at 1/2 the frequency in ω_1 and ω_2.

The solution to this problem is the phase cycle[38] (see equation
(2.42)):

π phase	receiver (odd QT)	receiver (even QT)
0	+	+
90	-	+
180	+	+
270	-	+

At the same time, this cycle leads to improved selection of even or
odd orders only in a MQT experiment.

2.5.3.7 Design of a MQT filter

By a simple rearrangement of the time intervals in the MQT pulse
sequence in figure 2.5a, a MQT filter is created, i.e. set

$$U = \left(\frac{\pi}{2}\right) \; ; \qquad V = \left(\frac{\pi}{2}\right) - \tau - \left(\frac{\pi}{2}\right)$$

V is a mixing propagator which generates MQT coherence by the first
pulse, and after time τ, regenerates single quantum coherence by a
second pulse, for detection. By appropriate phase cycling, any order
of coherence ΔM can be selected, making V a ΔM-quantum filter[78-83].

The required coherence pathway for such an experiment is

$$
\begin{array}{ccccccc}
 & \left(\frac{\pi}{2}\right) & & \left(\frac{\pi}{2}\right) & & \left(\frac{\pi}{2}\right) & \\
\text{coherence} & & & & & & \\
\text{level:} \quad 0 & \rightarrow & \pm 1 & \rightarrow & \Delta M & \rightarrow & 1
\end{array}
$$

Consider a phase change ϕ on the first two pulses of this sequence.

$$\frac{\pi}{2} \quad \frac{t_1}{2} \quad \pi \quad \frac{t_1}{2} \quad \frac{\pi}{2} \quad \frac{t_2}{2} \quad \pi \quad \frac{t_2}{2} \quad \downarrow$$

CH_2Cl_2

ω_2

ω_1
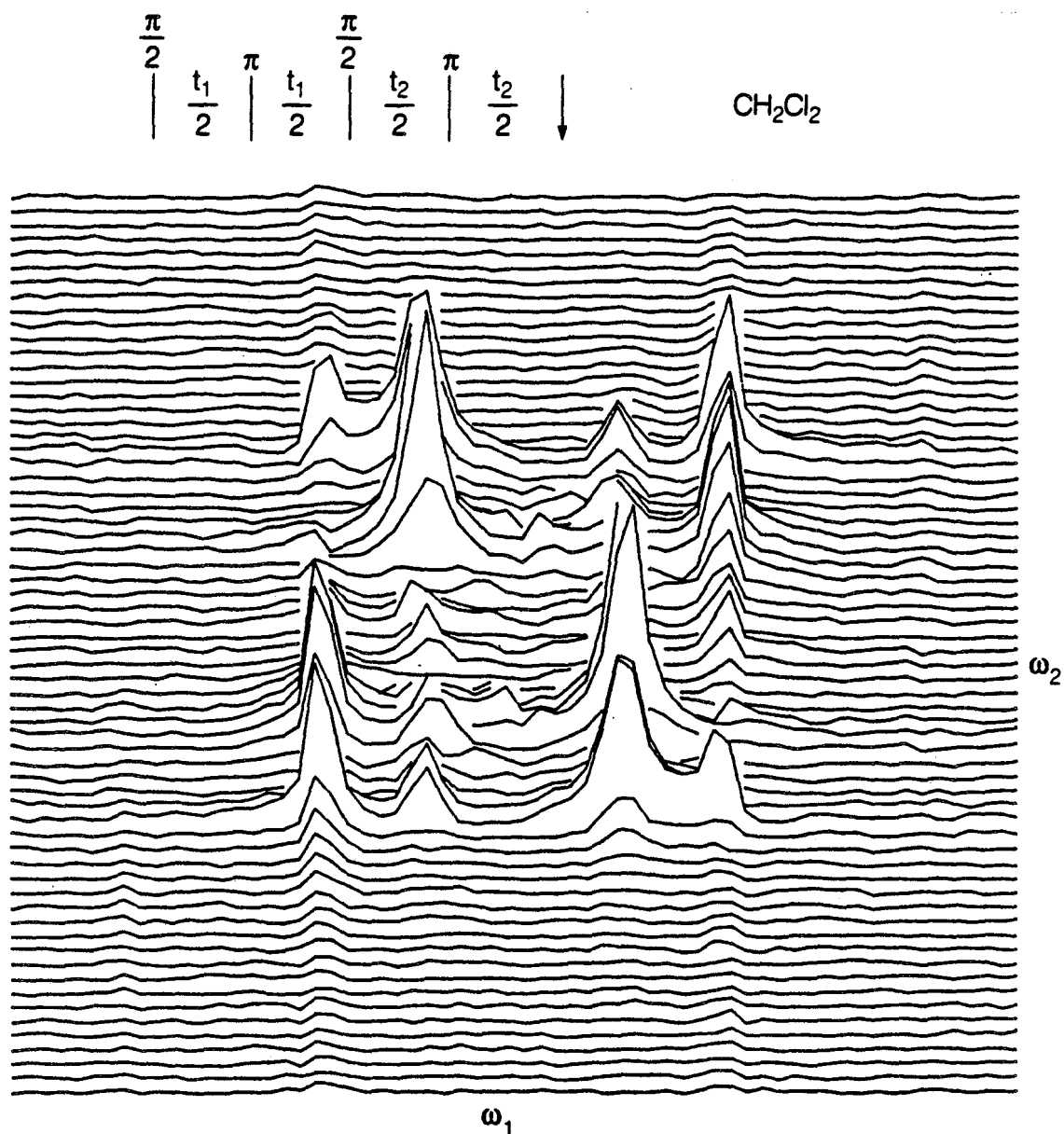
Figure 2.9

A "three" dimensional spectrum of CH_2Cl_2, taken point-by-point in both dimensions, with refocussing in t_1 and t_2, and showing the spurious peaks due to imperfect π pulses.

Both the echo and antiecho pathways indicated above experience a phase change of $\Delta M \phi$. Setting $\phi = 360/2\Delta M$ means that alternating the receiver +/- selects for even order coherence ΔM. (For ΔM odd: use $\phi = 360/4\Delta M$, and the receiver cycled through 90° phases). Table 2.III shows phase cycling for a two quantum filter which includes selection of quadrature signal in t_1.

An n-quantum filter is useful for selecting signals from subunits having at least n coupled protons. It is very useful for simplifying spectra. Chapter 4 shows many examples.

An n-quantum filter can be made slightly more selective by noting that, in the absence of an offset or chemical shift (achieved with a π in the middle of τ in the n-quantum period), the n-quantum coherence of different spin systems behaves differently.

i.e.   n-QT signal

    n coupled spins   constant non-oscillating
                                       signal (zero frequency)

    (n+1) coupled spins   signal oscillating at non-zero
                                       frequencies

    (n+2) coupled spins   signal oscillating at zero and
                                       non-zero frequencies

    (n+3) coupled spins   signal oscillating at non-zero
                                       frequencies

Table 2.III

Phase cycling sequence for 2 QT filtered COSY, with quadrature in t_1

			receiver
x	x	x	+
x	y	y	-
x	$\bar{x}$	$\bar{x}$	+
x	$\bar{y}$	$\bar{y}$	-
y	y	x	-
y	$\bar{x}$	y	+
y	$\bar{y}$	x	-
y	x	$\bar{y}$	+
$\bar{x}$	$\bar{x}$	x	+
$\bar{x}$	$\bar{y}$	y	-
$\bar{x}$	x	$\bar{x}$	+
$\bar{x}$	y	$\bar{y}$	-
$\bar{y}$	$\bar{y}$	x	-
$\bar{y}$	x	y	+
$\bar{y}$	y	$\bar{x}$	-
$\bar{y}$	$\bar{x}$	$\bar{y}$	+

$\Delta M: 0 \rightarrow -1 \rightarrow 2 \rightarrow 1$

By varying τ in small enough increments so that the oscillating signal is sampled a few times during its cycle, this oscillating signal is averaged to zero. Thus, (n+1), (n+3), (n+5), etc. spin systems will not contribute to the final signal. The zero frequency component of (n+2), (n+4), etc. spin systems will still contribute. The τ range required is

$$1/\tau_{max} \geq \nu_{2QT,smallest}$$

$$1/2\Delta\tau \cong \nu_{nQT,largest}.$$

2.6 ECHOES AS AN ALTERNATIVE TO PHASE CYCLING

Using field gradients and echoes is an alternative to many of the phase cycling techniques of the previous section[25]. Figure 2.10a shows how the echo or antiecho signal may be selected from the COSY experiment, by dephasing of the unwanted signal with a field gradient[2,8,40,59]. Figure 2.10b shows how signal which has passed through a 2 QT coherence step may be selectively filtered using an echo (CTEF)[2].

In general, signals detected as echoes are not phaseable in coherence transfer experiments. Only amplitude modulated signals are phaseable. Echo techniques always detect only one component in t_1 and are hence phase modulated. In cases where additional pulses are applied at the point of the echo, these pulses can be used to select one phase.

(a)

(b)
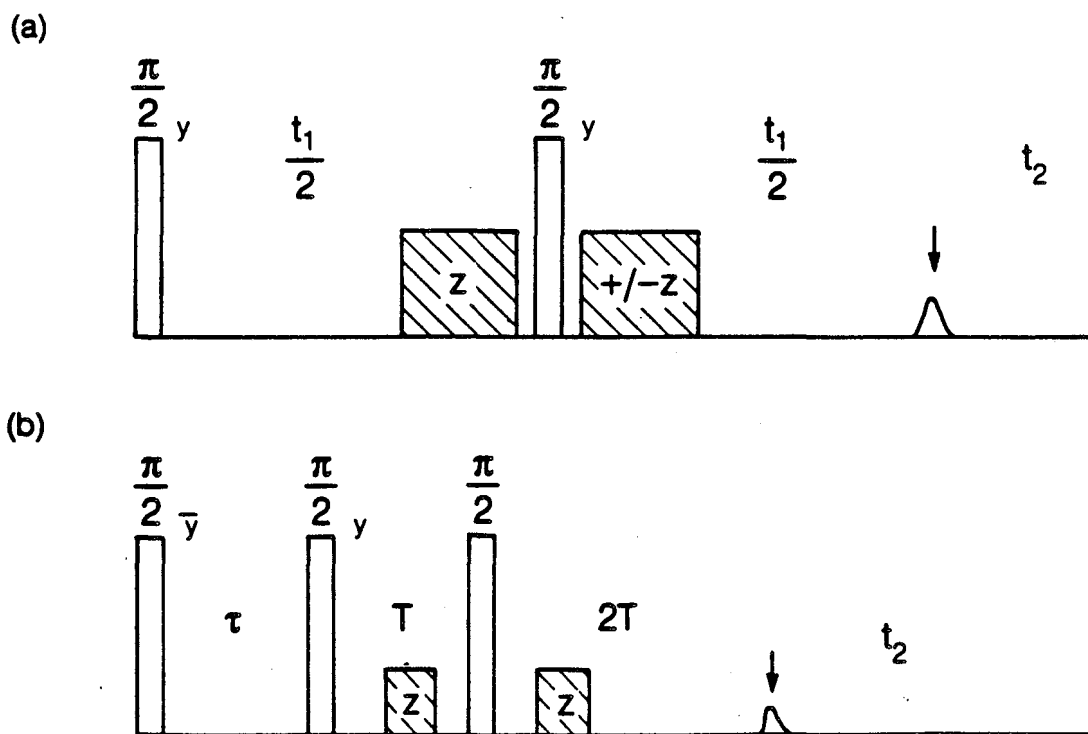
XBL 871-9536

Figure 2.10

Examples of the use of a field gradient as a filter. (a) is the

COSY experiment, where the echo or antiecho component is dephased by a

linear field gradient; (b) is a 2 QT Coherence Transfer Echo Filter.

CHAPTER 3

SHARP:

High Resolution NMR of Heteronuclear Spin Systems

in Inhomogeneous Fields

This Chapter describes an application of heteronuclear coherence transfer echoes to the observation of high resolution chemical shift spectra in inhomogeneous fields. Section 3.1 gives a brief survey of the use of heteronuclear coherence transfer in NMR. Section 3.2 discusses the underlying principle of SHARP, which eliminates the contribution of static field or susceptibility inhomogeneity to the spectrum. In Section 3.3, a variety of pulse sequences are introduced and demonstrated on ^{13}C-enriched ethanol in an inhomogeneous magnet. In Section 3.4, an application of SHARP to natural abundance compounds is given. A gated integrator is described for improving the S/N in multiple echo detection. Section 3.5 shows the use of SHARP in a surface coil experiment and demonstrates that there is a certain inherent selectivity of the sequence for axial distance from the surface coil.

3.1 INTRODUCTION

Heteronuclear 2-D spectroscopy of liquids has been demonstrated in many experiments for the indirect detection of nuclei and for the cross-correlation between spectra of different but coupled nuclear species. Coherence transfer was first reported by Maudsley and Ernst[28] in an experiment in which carbon magnetization prepared

during time t_1 was indirectly measured as proton magnetization during time t_2. Coherence transfer involves the formation of bilinear operators of the form $I_p S_q$ (p — x,y,z). Their generation is described in Section 2.3.1. They are not directly observable, but are easily manipulated with $\pi/2$ pulses and delays r of the order $1/J_{IS}$ [30,64,84] into observable coherence which retains a memory of its origin. In particular, when p,q — x,y, two-quantum (I_+S_+, I_-S_-) or zero quantum (I_+S_-, I_-S_+) heteronuclear coherence is said to be generated, and when p—q—z, the system is said to have J-order[85].

This basic idea has been utilized in a number of experiments:

(1) The INEPT[64,85] and DEPT[65] experiments (alluded to briefly in Section 2.3.1) were designed for the measurement of low sensitivity nuclei (S) by enhancing their initial magnetization from the large proton (I) reservoir. The S spin spectrum is thus measured with much improved sensitivity, though the methods are selective to those S-spins which are directly coupled to protons, and depend on the value of their coupling constants.

These experiments were taken one step further by applying a coherence transfer back to protons at the end of a period of S-spin evolution, and detecting the proton signal rather than the S-spin[28,30,60]. A two-dimensional data acquisition is then required, with the S-spin evolution measured in a point-by-point fashion. Higher sensitivity can be obtained in this way because of the higher gyromagnetic ratio and typically lower filter bandwidth of protons[68,70,86-7]. Figure 3.1 shows a case where signal level is so

(a)

(b)

-1250   1250

Frequency (Hz)
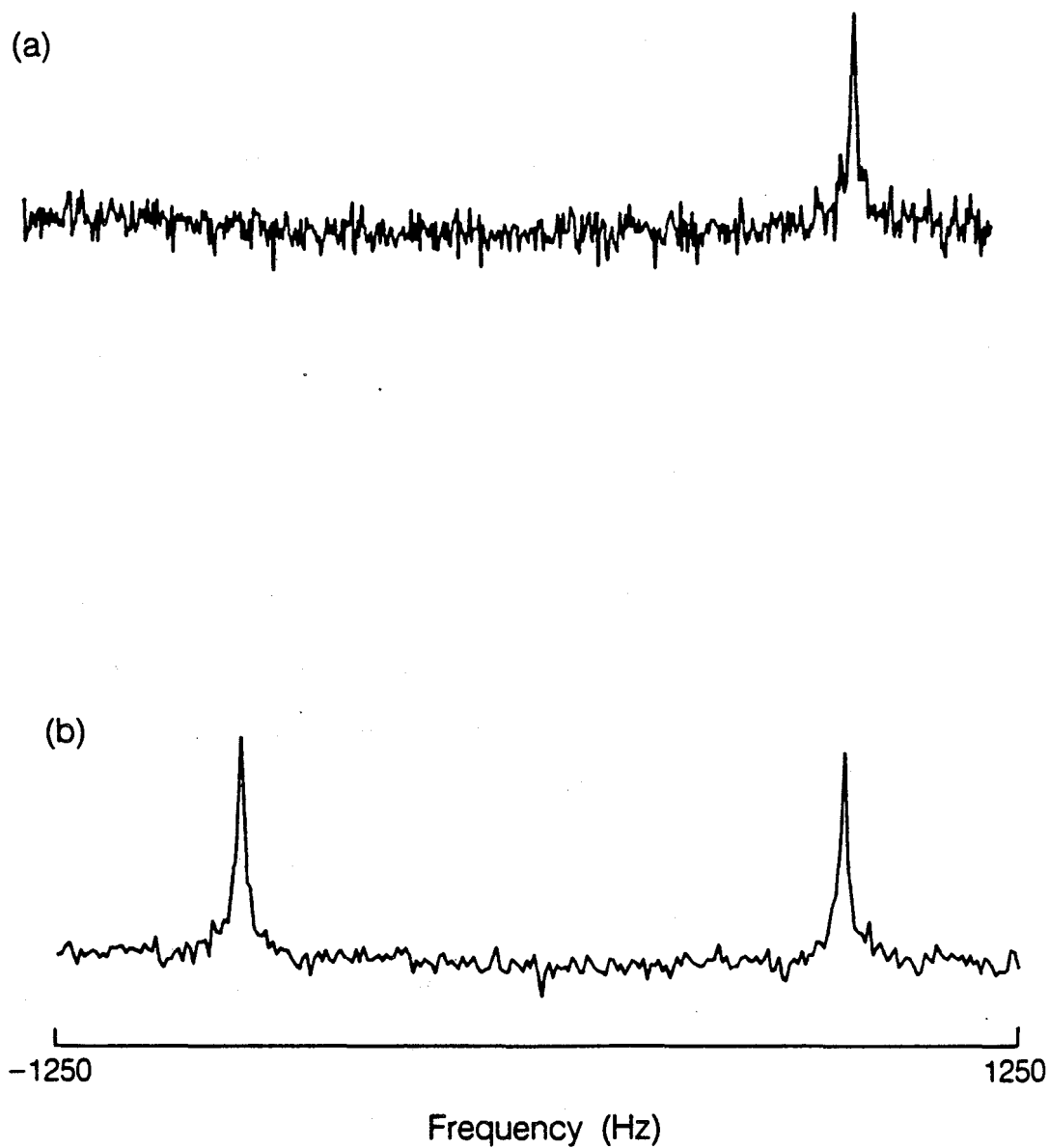
XBL 871-9557

Figure 3.1

Comparison of the ^{1}H NMR spectrum of a strongly attenuated water signal, taken (a) by direct detection, and (b) by indirect detection and multiple echo sampling (Section 3.4.1), and recorded for equal times.

low that point-by-point detection (3.1b) gives an improved signal over direct detection (3.1a) for the same experimental time, with both experiments detecting protons!

(2) Bilinear rotation was used as a means of obtaining broadband homonuclear decoupling (BIRD)[62]. Protons attached directly to a ^{13}C are distinguished from their non-^{13}C-bonded neighbours and hence decoupled from them. A closely related idea was used to determine heteronuclear coupling constants[88] for protons directly bound to carbons. Many examples of these ideas were illustrated[89-93].

(3) Coherence transfer has also been demonstrated in echo phenomena in homo- or heteronuclear coupled systems. Magnetization allowed to decay for some interval of time at protons frequencies has been rephased as a ^{13}C echo in four times the time, in according with the ratio of gyromagnetic constants[31]; dephased homonuclear multiple quantum coherence of order n can be rephased as single quantum coherence, and the echo detected at n times the dephasing interval[40]. Echoes were also alluded to in Section 2.6, in their importance in preserving the quadrature nature of a 2-D experiment.

The SHARP experiment is a heteronuclear coherence transfer echo experiment. The signal is measured as a function of some time t_1 up to an echo. The Hamiltonian is manipulated during t_1 to retain chemical shifts, with or without scalar coupling, and to obtain purely homogeneous lines. The sensitivity is that of protons directly bound to the heteronucleus, while the resolution is determined by the

homogeneous linewidths and the heteronuclear shifts. These features originally suggested the acronym SHARP for Sensitive, Homogeneous and Resolved Peaks[94].

SHARP addresses a number of problems in high resolution and in-vivo spectroscopy. A sample may be too large to enable good static field homogeneity over its whole, hence observation of high resolution spectra would be precluded. Unwanted background signal, such as H_2O, can swamp smaller signals. Inhomogeneous susceptibilities caused by sample shape or internal compartmentalization lead to inhomogeneous lineshapes. These problems are eliminated by SHARP.

3.2 MANIPULATION OF $\mathcal{H}_1$ DURING t_1

The spin system under consideration consists of an isolated S spin directly bonded to n = 0-3 equivalent I spins. I-I coupling between different I_nS groups occurs. The Hamiltonian is given by:

$$\mathcal{H} = \mathcal{H}_z^I + \mathcal{H}_z^S + \mathcal{H}_J^{II} + \mathcal{H}_J^{IS} \tag{3.1}$$

where

$$\mathcal{H}_z^I = - \sum_i \omega_i I_{zi} - \gamma_I \Delta H_0(\tilde{r}) I_z \tag{3.2}$$

$$\mathcal{H}_z^S = - \omega_S S_z - \gamma_S \Delta H_0(\tilde{r}) S_z \tag{3.3}$$

in which ω_i and ω_S include both chemical shift and resonance offset, and the second term decribes field inhomogeneity; and

$$\mathcal{H}_J^{II} = \sum_{i<j} \sum J_{II}^{ij} I_{zi} I_{zj} \tag{3.4}$$

$$\mathcal{H}_J^{IS} = \sum_i J_{IS} I_{zi} S_z \tag{3.5}$$

are the scalar coupling Hamiltonians in the weak coupling limit.

The schematic pulse sequence diagram in figure 3.2 describes the

a)

Preparation | $\frac{4t_1}{5}$ | Coherence Transfer | $\frac{t_1}{5}$ | echo | t2

Evolving Operator: S_- ... I_+

b)

Preparation | $\frac{4t_1}{10}$ | π_I | $\frac{5t_1}{10}$ | π_S DQ echo | $\frac{t_1}{10}$ | Coherence Transfer | echo

Evolving Operator: I_+S_+ ... I_-S_+ ... I_-S_- ... I_+

c)

Preparation | $\frac{4t_1}{20}$ | π_I | $\frac{5t_1}{20}$ | π_S DQ echo x_s | $\frac{t_1}{20}$ | BIRD π | $\frac{4t_1}{20}$ | π_I | $\frac{5t_1}{20}$ | π_S DQ echo | $\frac{t_1}{20}$ | Coherence Transfer | echo

Evolving Operator: I_+S_+ ... I_-S_+ ... I_-S_- ... I_+S_+ ... I_-S_+ ... I_-S_- ... I_+
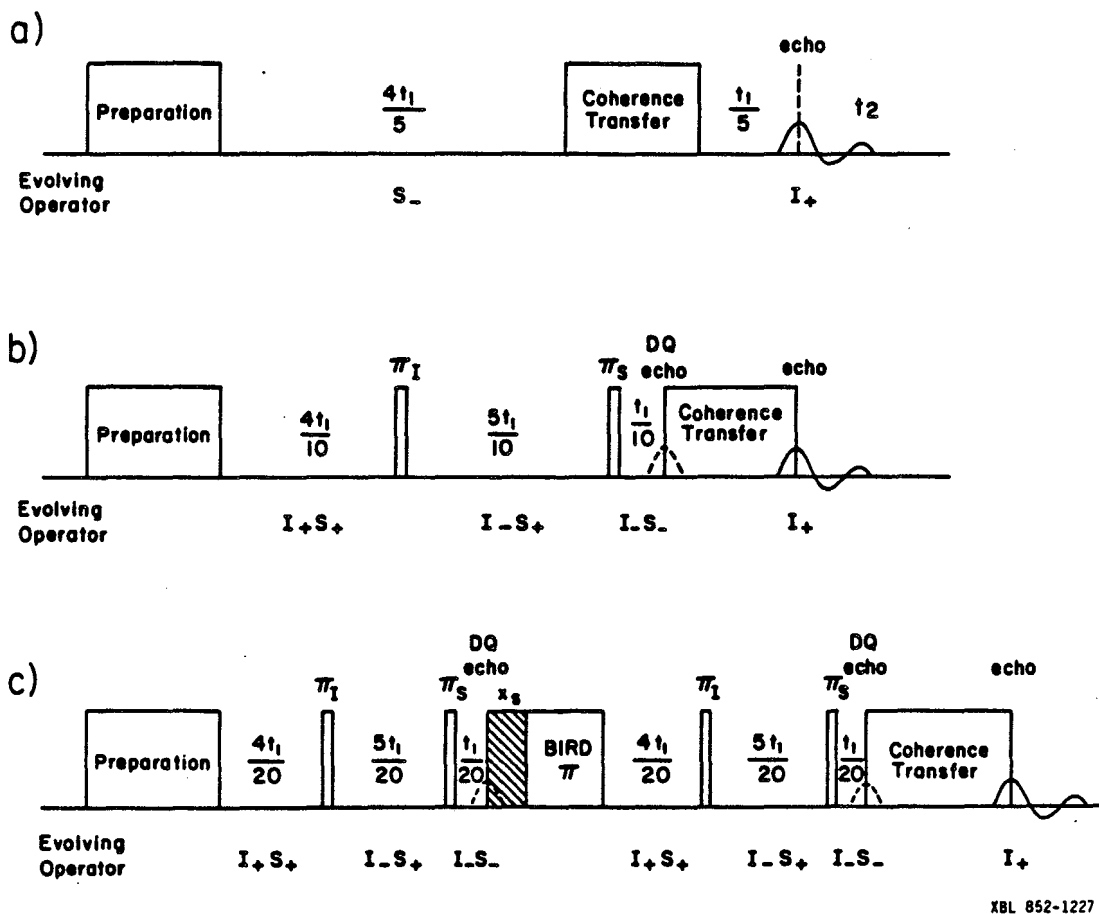
XBL 852-1227

Figure 3.2

Schematic SHARP echo spectra. (a) shows the simple notion of 4:1 heteronuclear and homonuclear evolution; (b), (c) show the use of double quantum SHARP echoes.

essence of the SHARP experiment, in three different versions. All pulse sequences are described for the ^{13}C-^{1}H heteronuclear pair, and timing intervals are adjusted in the ratio of their gyromagnetic constants. Use is made of the relation[31]:

$$\frac{\gamma^{I}(\Delta M)^{I}}{\gamma^{S}(\Delta M)^{S}} = \frac{t_{S}}{t_{I}} \tag{3.6}$$

For ^{13}C - ^{1}H, $\gamma^{I}/\gamma^{S} = 3.977 \cong 4$. The evolution times t_{I} and t_{S} are adjusted so that I spin coherence evolves for 1/4 of the time of S-spin coherence . The result is an average Hamiltonian in t_{1}:

$$\bar{\mathcal{H}}_{1} = \frac{1}{4} \mathcal{H}_{z}^{I} + \mathcal{H}_{z}^{S} \quad (+ f_{1}\mathcal{H}_{J}^{II} + f_{2}\mathcal{H}_{J}^{IS}) \tag{3.7}$$

where the coupling terms are included in brackets with fraction f_{1} and f_{2} to indicate that their contribution may vary with different sequences. For example, in figure 3.2a, $f_{1} = f_{2} = 1/4$, in figure 3.2b, $f_{1} = 1$, $f_{2} = 0$, in figure 3.2c, $f_{1} = f_{2} = 0$ (detailed in Section 3.3). For the Zeeman terms of an $I_{n}S$ spin system:

$$\bar{\mathcal{H}}_{1z} = -\frac{1}{4} \omega_{I}I_{z} - \omega_{S}S_{z} - \frac{1}{4} \Delta H_{0}(\tilde{r})(\frac{1}{4} \gamma^{I}I_{z} + \gamma^{S}S_{z})$$
$$\text{——— (3.8)}$$

The frequency with which a component of S-spin coherence with $\Delta M^{S} = -1$ and a component of I spin coherence with $\Delta M^{I} = +1$ evolves under the influence of $\mathcal{H}_{1}$ is

$$\omega_{1} = (\omega_{S} - \frac{1}{4} \omega_{I}) \qquad (+ \text{ J-terms}) \tag{3.9}$$

since $\gamma_{S} - \gamma_{I}/4 = 0$. This echo signal is purely homogeneous. It is dominated by ^{13}C chemical shifts. Selection of only one component of the evolving magnetization implies the spectrum is in quadrature with

respect to $t_1^{(95)}$.

Figure 3.3 demonstrates the use of SHARP. The ^{1}H, ^{13}C and SHARP spectra of 25% enriched ethanol in an inhomogeneous field are shown. Very narrow lines are obtained for SHARP, close to the frequency of the heteronuclear spins. The need for shimming is eliminated altogether.

Figure 3.4 compares more highly resolved ^{1}H and ^{13}C spectra and the SHARP spectrum to demonstrate the origin of the SHARP chemical shifts. **The SHARP chemical shift is given by ± (^{13}C chemical shift - ^{1}H chemical shift, in ppm)**. In the next section, the spectrum is explicitly calculated and a variety of J-edited sequences presented.

3.3   SHARP SPECTRA OF ETHANOL

The ethanol sample used was a mixture of 25% 1-^{13}C, 25% 2-^{13}C and 50% ^{12}C. The coupling constants are J_{CH}(Me) = 128 Hz; J_{CH}(Et) = 144 Hz; $^3J_{HH}$(Me-Et) = 7 Hz; $^3J_{HH}$(Et-OH) = 5 Hz.

3.3.1   **The 4:1 experiment**

The schematic and full pulse sequences for the 4:1 experiment appear in figure 3.5 and 3.9. At the end of the preparation step, we have, according to equation (2.38) with $\tau = 1/2J_{IS}$,

$$\rho_{SAT}(0) = 2\beta I_x S_x \tag{3.10}$$

$$\rho_{NON}(0) = -\beta I_y \tag{3.11}$$

The next stage is a $4t_1/5$ period of I_x decoupling, which spin-locks I_x, removes $\mathcal{H}_J^{IS}$ from the Hamiltonian and results in S-spin evolution

a) ¹H spectrum
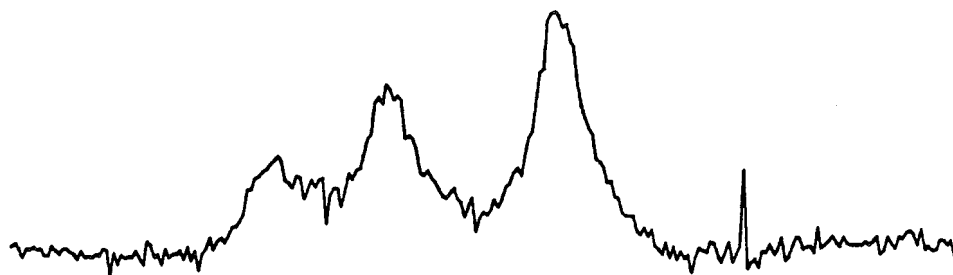
b) ¹³C spectrum

c) SHARP spectrum

-2500   0   2500

Frequency (Hz)
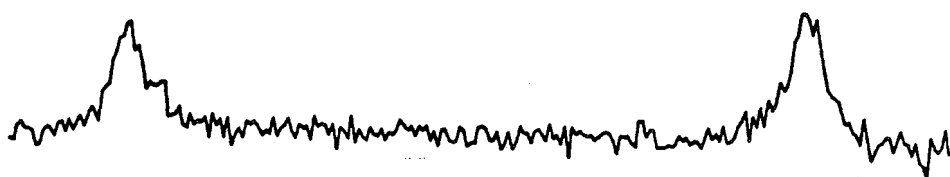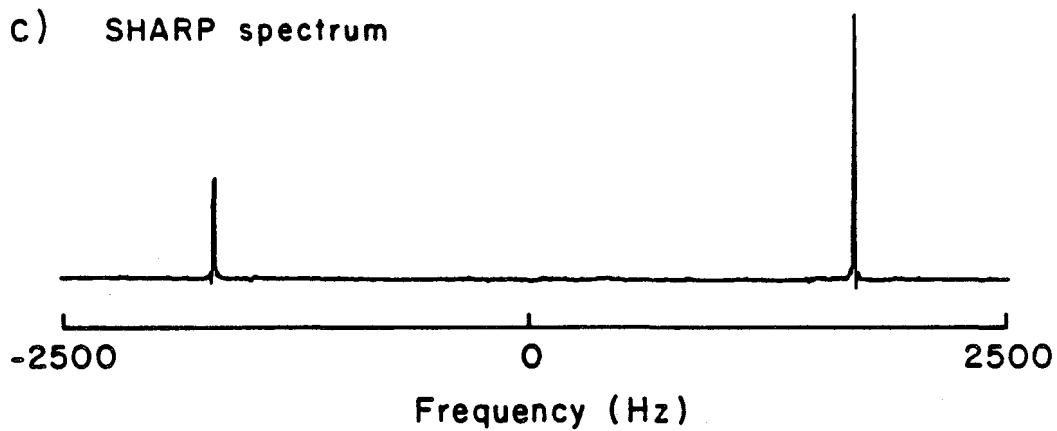
XBL 855-2510

Figure 3.3

^{1}H, ^{13}C and SHARP spectra of 25% ^{13}C enriched ethanol with a
surface coil. The ^{13}C spectrum was recorded for 2h. The SHARP
spectrum took 1 hour, using the sequence of figure 3.9.

SHARP,   J − decoupled   SW = 5000 Hz $\left(\text{wrt } \frac{4}{5} t_1\right)$

−Δ′

−Δ

^{1}H,   SW = 20000 Hz

Δ

Δ′

^{13}C, ^{1}H − decoupled   SW = 5000 Hz

0
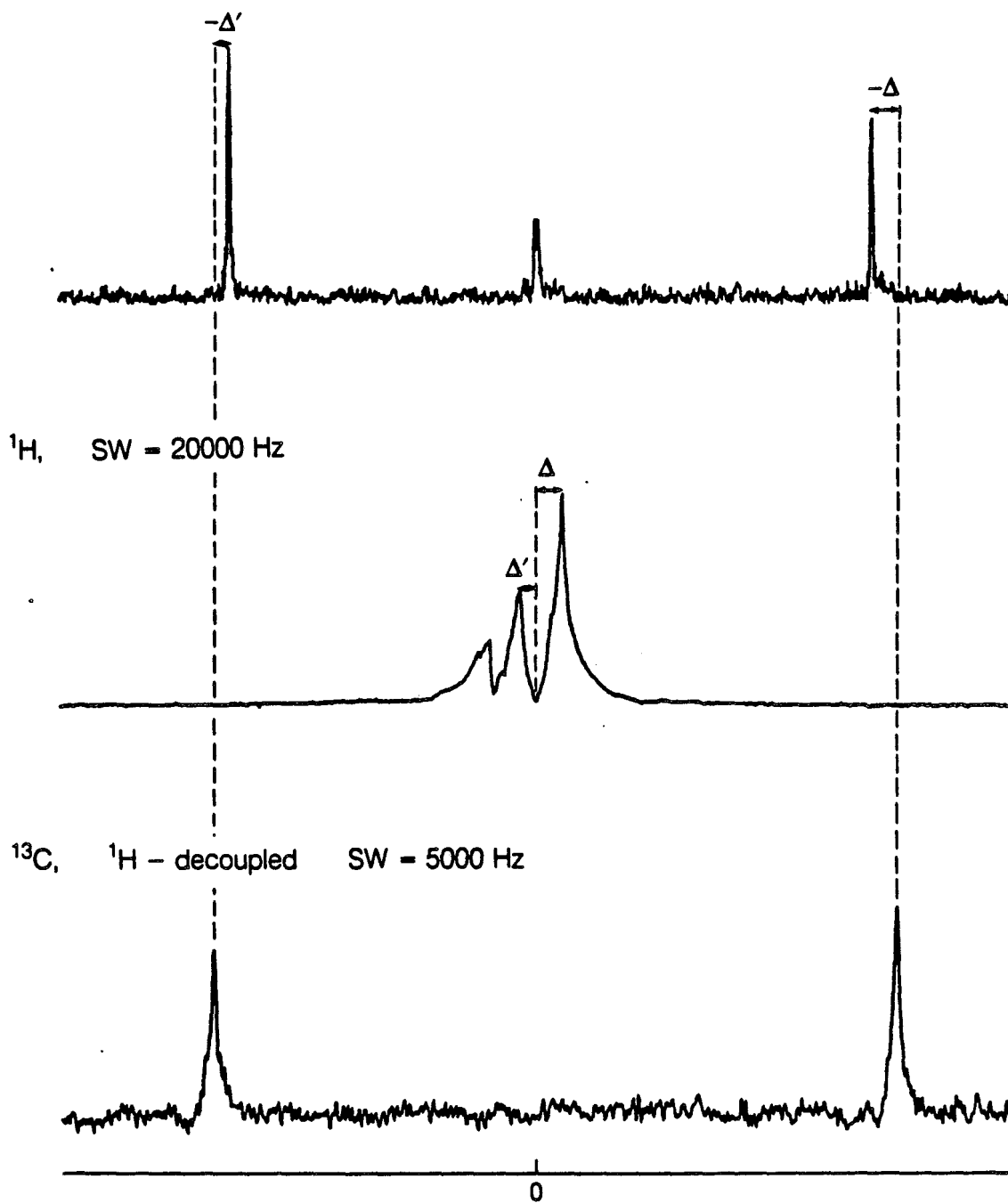
XBL 871-9556

Figure 3.4

The relationship between SHARP and ^{13}C chemical shifts.

to give

$$\rho_{SAT}(\tfrac{4}{5} t_1^-) = 2\beta I_x(S_x \cos(\tfrac{4}{5}\Omega_S t_1) + S_y \sin(\tfrac{4}{5}\Omega_S t_1)) \qquad (3.12)$$

where $\qquad \Omega_S = \omega_S + \gamma_S \Delta H_0(\tilde{r})$

Meanwhile non-satellite magnetization ρ_{NON} dephases rapidly in the yz plane due to the inhomogeneous rf field along I_x.

3.3.1.1 The 4:1 experiment with J_{IS} coupling partly retained

The remainder of pulse sequence 3.5 is a $(\pi/2)^S$ pulse, followed by evolution for $t_1/5$ and detection of the tip of the echo as I_+. A $(\pi/2)_y^S$ pulse results in

$$\rho_{SAT}(\tfrac{4}{5} t_1^+) = -2\beta \, I_x S_z \cos(\tfrac{4}{5}\Omega_S t_1) \qquad (3.13)$$

where only observable terms have been retained. The evolution period $t_1/5$ results in proton precession, according to

$$\rho_{SAT}(t_1) = -2\beta S_z \cos(\tfrac{4}{5}\Omega_S t_1)\Big\{[I_x \cos(\tfrac{1}{5}\Omega_I t_1) + I_y \sin(\tfrac{1}{5}\Omega_I t_1)]\cos(\tfrac{1}{5}\pi J_{IS} t_1)$$
$$+ [I_y S_z \cos(\tfrac{1}{5}\Omega_I t_1) - I_x S_z \sin(\tfrac{1}{5}\Omega_I t_1)]\, 2\sin(\tfrac{1}{5}\pi J_{IS} t_1)\Big\} \cos(\tfrac{1}{5}\pi J_{II} t_1)$$
$$\text{———} \quad (3.14)$$

where $\Omega_I = \omega_I + \gamma_I \Delta H_0(\tilde{r})$,

leaving observable terms

$$\rho_{SAT}(t_1) = -\tfrac{1}{2}\beta \Big\{ I_y[\cos(\tfrac{4}{5}\Omega_S + \tfrac{1}{5}\Omega_I)t_1 + \cos(-\tfrac{4}{5}\Omega_S + \tfrac{1}{5}\Omega_I)t_1]$$
$$- I_x[\sin(\tfrac{4}{5}\Omega_S + \tfrac{1}{5}\Omega_I)t_1 + \sin(-\tfrac{4}{5}\Omega_S + \tfrac{1}{5}\Omega_I)t_1] \Big\}$$
$$\times \sin(\tfrac{1}{5}\pi J_{IS} t_1) \cos(\tfrac{1}{5}\pi J_{II} t_1) \qquad (3.15)$$

Two terms are echo terms and two antiecho. We retain only the former, presuming that antiecho terms are rapidly dephased in the

a)

b)
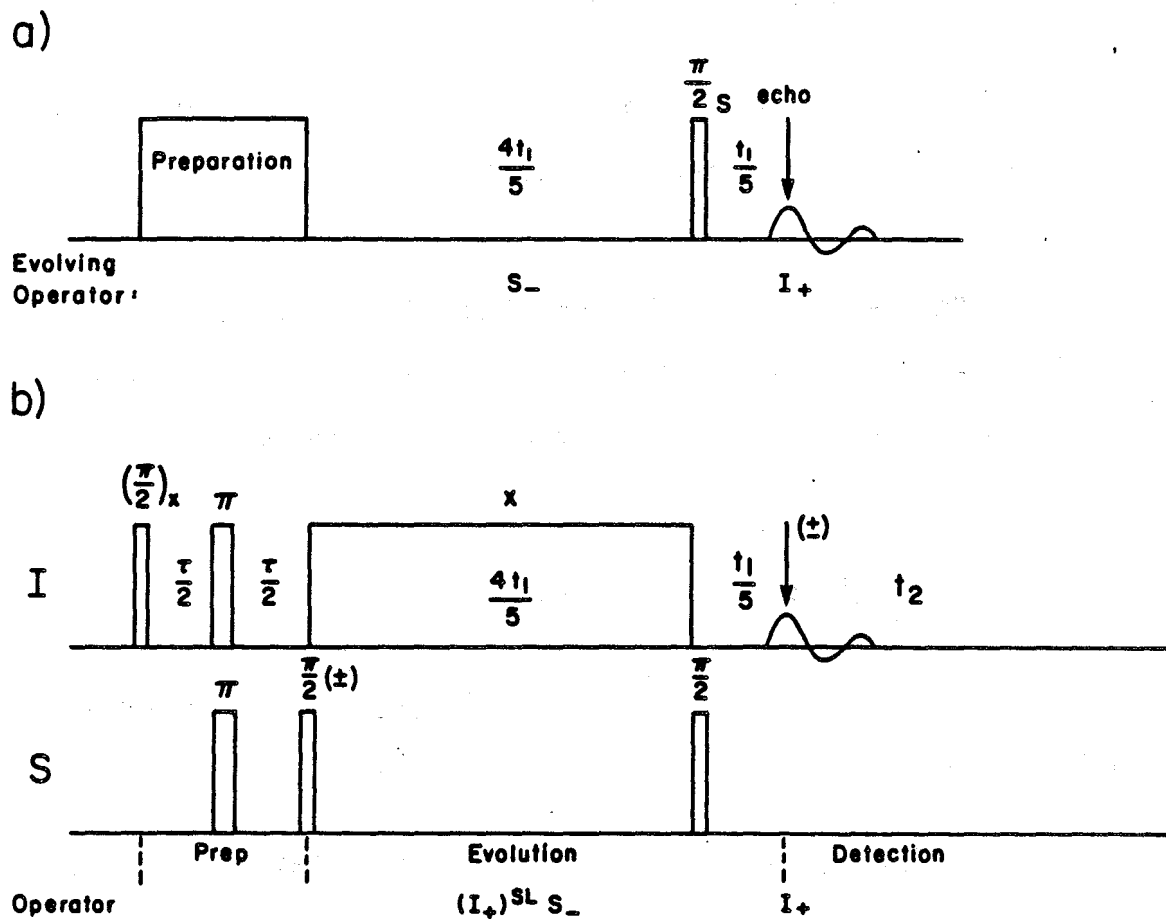
XBL 854-2008

Figure 3.5

A 4:1 SHARP sequence, retaining $J_{CH}/4$ and $J_{HH}/4$.

inhomogeneous field. Thus, for a spectrometer detecting I_+,

$$\rho_{SAT}(t_1) = -\frac{1}{4i}\beta\, I_+\, e^{i(-\omega_S + \omega_I/4)[4t_1/5]}\, \sin(\pi J_{IS}/4\,[4t_1/5])$$

$$\times \cos(\pi J_{II}/4\,[4t_1/5]) \qquad (3.16)$$

The frequencies, on Fourier transformation wrt $4t_1/5$, are given by

$$\boxed{\omega_1 = -\omega_S + \frac{1}{4}\omega_I \quad \pm\ J_{IS}/8 \quad \pm\ J_{II}/8} \qquad (3.17)$$

Equation (3.16) points out several features of the spectrum:

(1) All lines are in phase, independent of the multiplicity n. The spectrum is antiphase with respect to the $J_{IS}/4$ coupling, and in phase with respect to the $J_{II}/4$ coupling.

(2) The spectrum is in quadrature in t_1.

(3) The signal intensity is proportional to the proton $\beta \times \epsilon$ (Section 2.4.3). Also, the choice of recycle delay depends on protons rather than carbon.

(4) The chemical shifts are $-\nu_S + \nu_I/4$, so the spectrum is laterally inverted relative to a regular ^{13}C spectrum, but with peaks in approximately the same relative order.

(5) There is no inhomogeneous broadening, in the absence of diffusion.

Figure 3.6 shows the result of the 4:1 sequence in figure 3.5 on the ethanol sample. In practice, the spectrum is always obtained as the difference between two experiments in which the first $(\pi/2)^S$ pulse and the receiver are alternated in phase to suppress any residual non-satellite magnetization. This is indicated by ($\pm$) in figure 3.5. Note the antiphase J_{IS} doublets. Line intensities depend on τ according to $\tau_{max} = 1/2J_{IS}$. $J_{II}/4 \cong 1.75$ is not resolved, but causes

(a) τ = 3.950

Me   Et

32 Hz

(b) τ = 3.846

(c) τ = 3.571

36 Hz

−500   Frequency (Hz)   500

XBL 871-9555
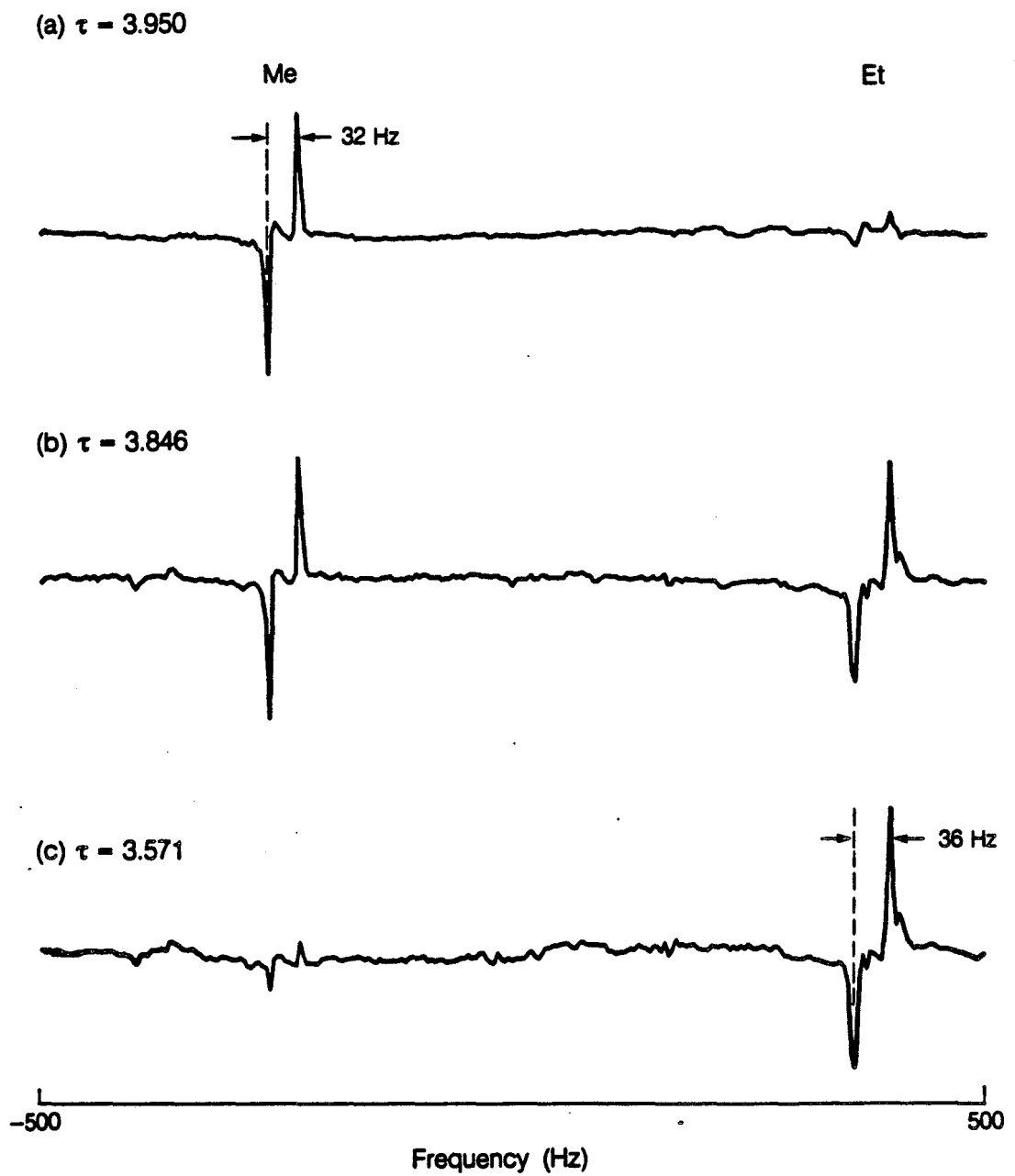
Figure 3.6

Dependence of peak intensities on the choice of τ. Intensity is maximized at τ = 1/2J_{CH}. Spectra were recorded using sequence 3.5. The doublet separations marked are values of $J_{CH}/4$.

line broadening of the order of 8 Hz.

3.3.1.2 Some experimental details

The positions of the peaks depend on the ^{13}C and ^1H transmitter offsets, according to equation (3.17). When different ^1H offsets were tried, strange line structures were found. This was attributed to the inadequacy of the simple decoupling pulse of figure 3.5b which shows poor off-resonance decoupling behaviour. Figure 3.7 demonstrates the peak structure for different types of decoupling. Simple decoupling leads to an incorrect spectrum. WALTZ-4 decoupling[96], or a decoupling pulse consisting of equal lengths of x followed by $\bar{x}$ decoupling lead to an improved result. In all experiments involving decoupling that follow, the x/$\bar{x}$ decoupling sequence was used, since it usually gave better S/N than WALTZ-4.

Figure 3.8 now shows the exact experimental sequence used. The τ' purge pulse along x purges non-satellite signal, which would otherwise re-echo at the end of $4t_1/5$. $\tau' \sim 4\text{-}8$ ms was used. These explicit experimental details are not included in the rest of the sequences illustrated, but they are used.

3.3.1.3 The 4:1 experiment with scalar J_{IS} removed

Figure 3.9 shows a 4:1 experiment in which an extra coherence transfer step is included, in order to bring all lines into positive absorption mode. From equation (3.13) with $\tau = 1/2J_{IS}$, the density matrix after the second coherence transfer step is

$$\rho_{SAT}(\tfrac{4}{5} t_1^+) = \beta\, I_y \cos(\tfrac{4}{5}\, \Omega_S t_1) \qquad (3.18)$$

Simple Decoupling

WALTZ–4 or x/x̄ decoupling

-500

500

Frequency (Hz)
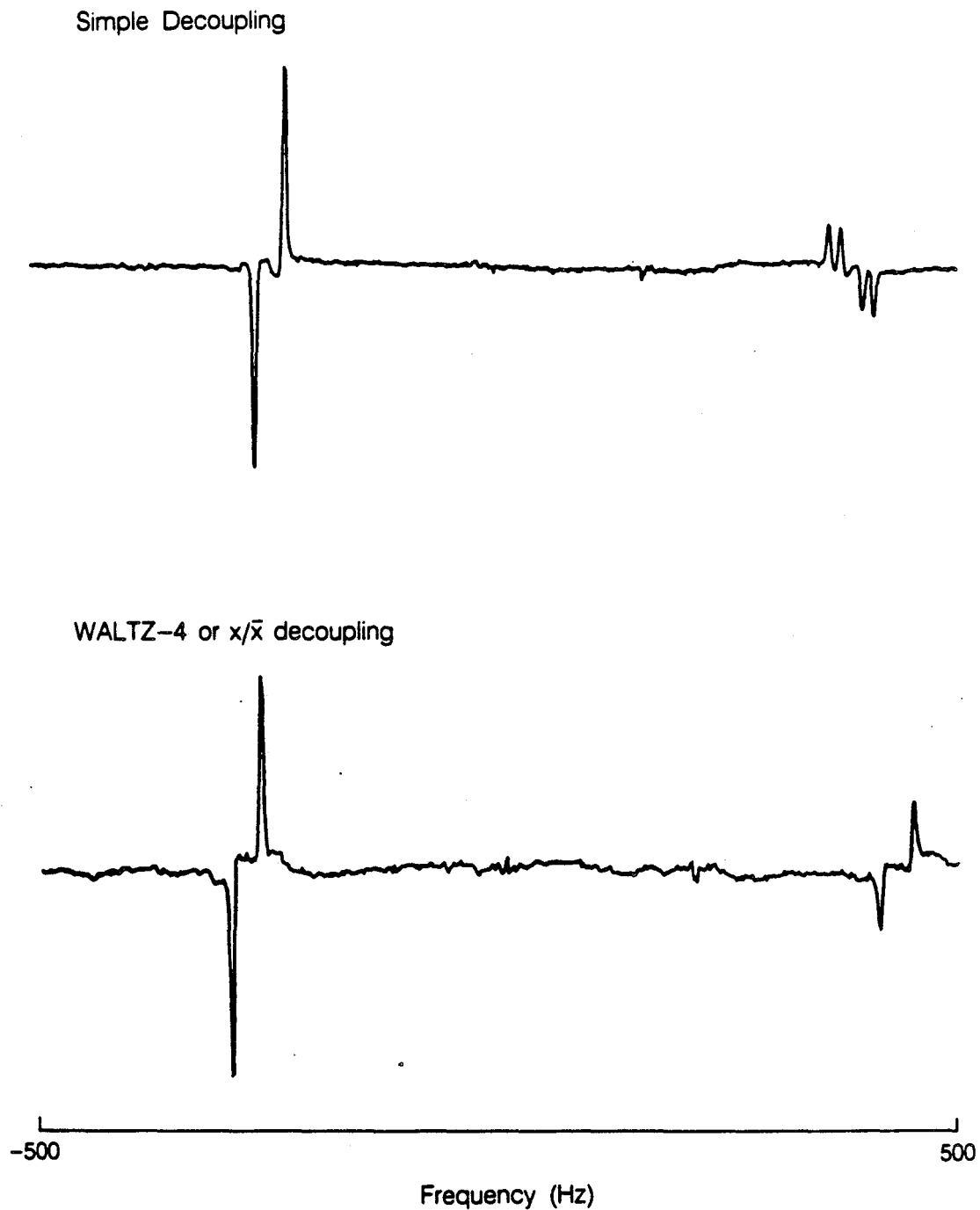
XBL 871-9554

Figure 3.7

(a) The effect of an imperfect spin locking pulse in sequence 3.5.

(b) Replacement of simple decoupling with a WALTZ-4 or x/x̄ sequence.

(a)

(b)
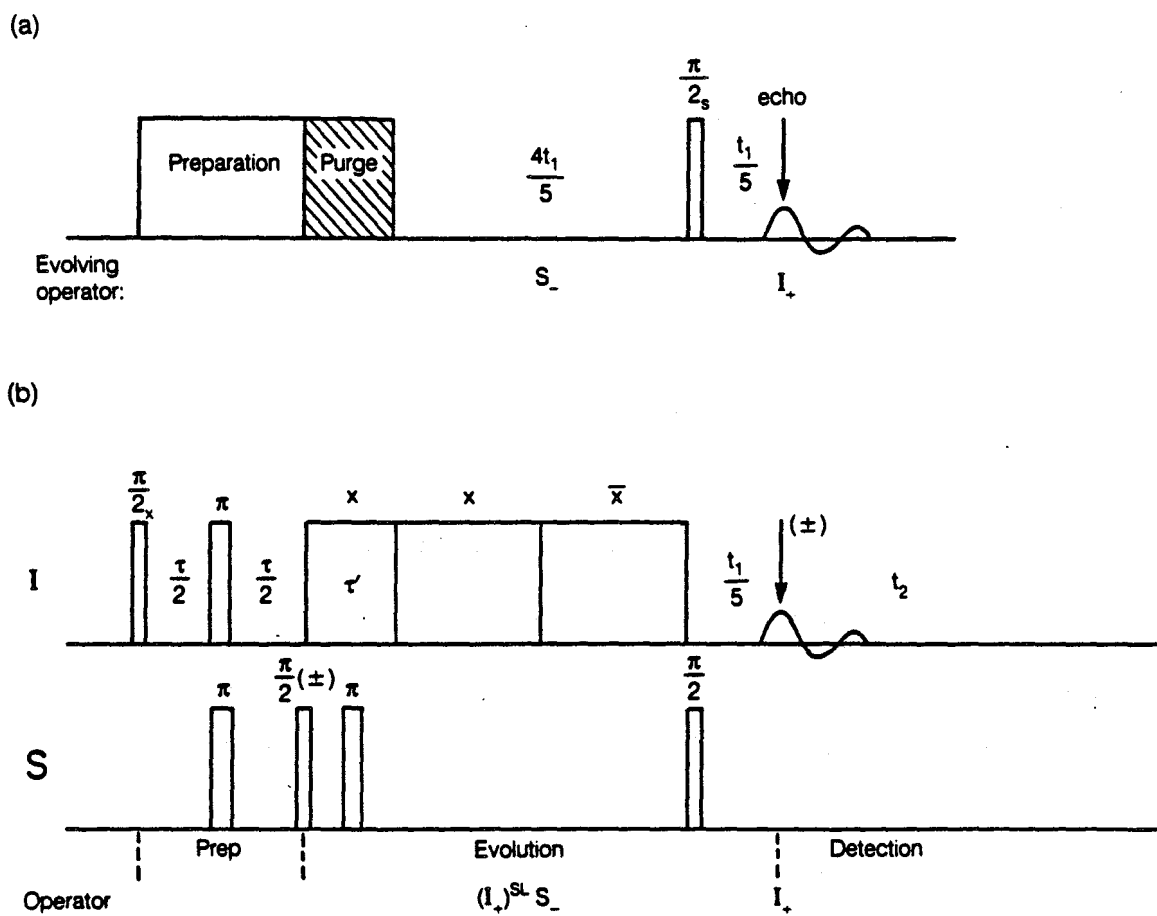
XBL 854-2008A

Figure 3.8

Explicit experimental details of the purge pulse and x/x̄ spin decoupling used in most experiments.

J_{IS} is eliminated during the final $t_1/5$ with a π^S pulse, giving

$$\rho_{SAT}(t_1) = -\frac{1}{4i}\beta\, I_+ \, e^{i(-\omega_S+\omega_I/4)[4t_1/5]} \cos(\pi J_{II}/4)[4t_1/5]$$

—— (3.19)

which has frequencies occuring at

$$\boxed{\omega_1 = -\omega_S + \frac{1}{4}\omega_I \pm J_{II}/8}$$ (3.20)

All lines are in positive absorption mode.

Figure 3.3 shows a SHARP spectrum obtained by this method. The scaled proton-proton couplings are not resolved. Figures 3.10 and 3.11 show 2-D versions of the SHARP experiment. During t_2, an FID is collected in an inhomogeneous static field. In figure 3.10, the J_{IS} coupling is retained during ω_1. In figure 3.11, the J_{IS} coupling is removed. Residual linewidths in ω_1 are ~ 8 Hz, in ω_2 ~ 200 Hz.

TWO-QUANTUM PULSE SEQUENCES

3.3.2 The 4:5:1 experiment

Alternative experiments were devised which improve the linewidth and resolution of the SHARP experiment. The requirement is to avoid the scaling of J_{II}. The experiments involved double quantum coherence interrupted by π pulses at appropriate intervals. Figure 3.12 shows the pulse sequence for the 4:5:1 experiment. The ratio indicates the intervals of free precession. The prepared coherence is again I_xS_x:

$$I_xS_x = 1/4\,(I_+S_+ + I_+S_- + I_-S_+ + I_-S_-),$$

of which we shall follow the component I_+S_+.

For $4t_1/5$ the S-spin component of I_+S_+ evolves freely, while a π

a)

Preparation

$\dfrac{4t_1}{5}$

Coherence
Transfer

echo

$\dfrac{t_1}{5}$

t_2

Evolving
Operator

S_-

I_+

b)

$\left(\dfrac{\pi}{2}\right)_x$ π x π $(\pm)$

I $\dfrac{\tau}{2}$ $\dfrac{\tau}{2}$ $\dfrac{4t_1}{5}$ $\dfrac{\tau'}{2}$ $\dfrac{\tau'}{2}$ $\dfrac{t_1}{5}$ t_2

π $\dfrac{\pi}{2}(\pm)$ $\dfrac{\pi}{2}$ π π

S

Prep   4/5 Evolution   Coherence   1/5 Evol   Detection
                        Transfer

Operator $(I_-)^{SL}S_-$ I_+
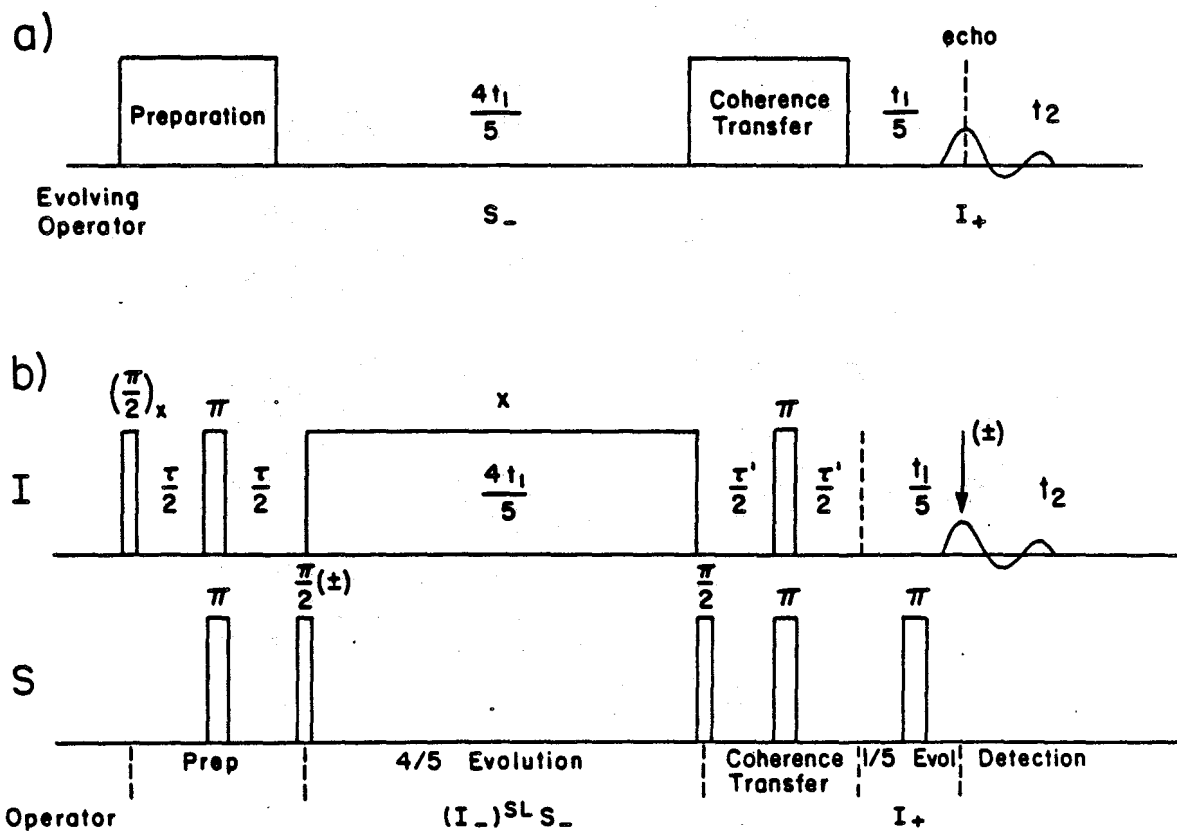
XBL 855-2509

Figure 3.9

4:1 SHARP sequence retaining $J_{HH}/4$ coupling.
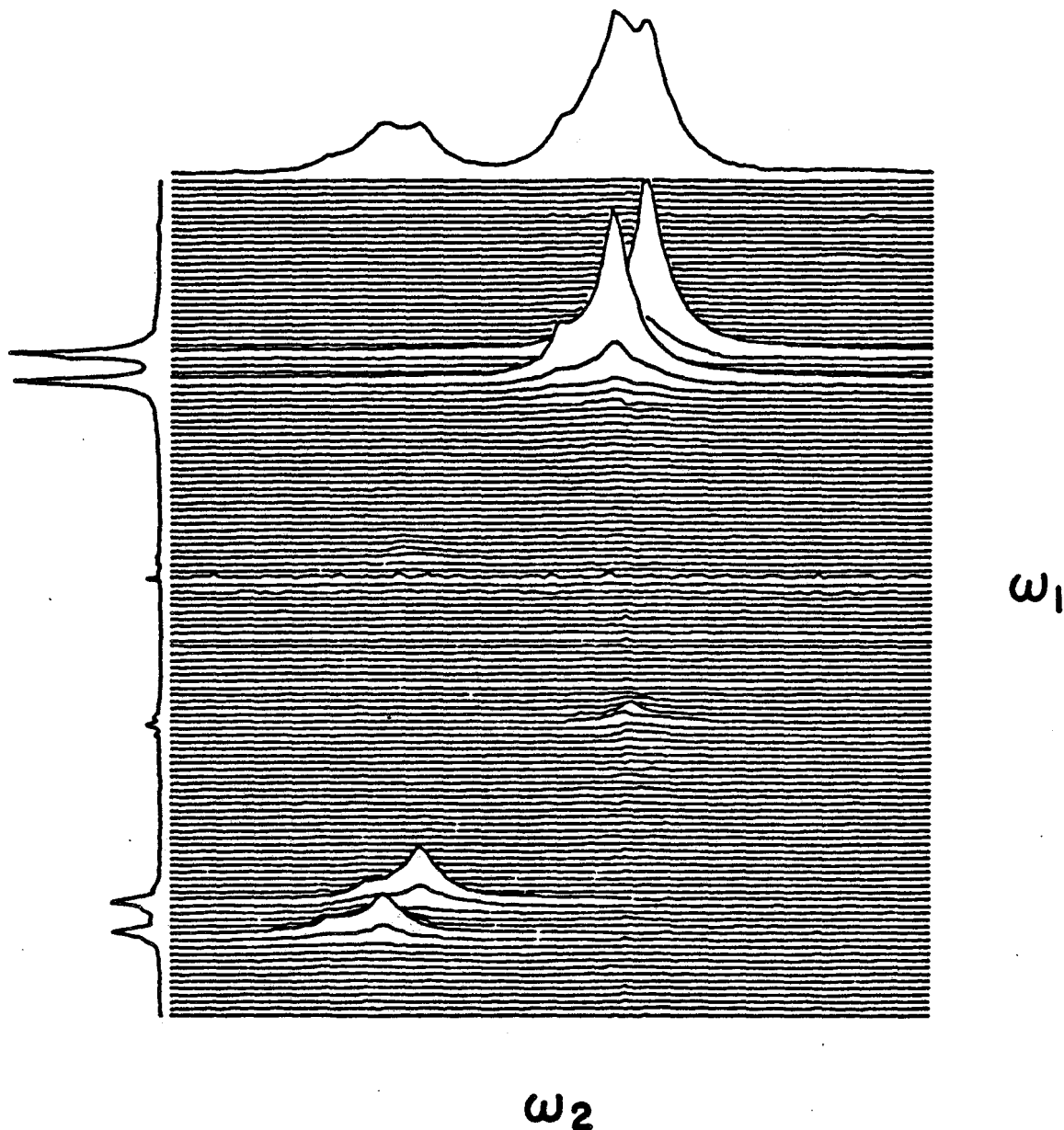
XBL 851-753

Figure 3.10

Two dimensional SHARP spectrum of ^{13}C enriched ethanol taken with pulse sequence 3.5. Narrow lines of the echo spectrum appear in ω_1. The inhomogeneously broadened spectrum appears in ω_2. The spectrum was recorded with 512 × 256 points , at a spectral width of 1 KHz in ω_1 and 5 KHz in ω_2. The peaks are folded in ω_1 and an absolute value spectrum is shown. 2 shots were averaged per t_1 point. $\tau = 3.846$ ms and $\tau' = 8$ ms were used.

ω_1

ω_2
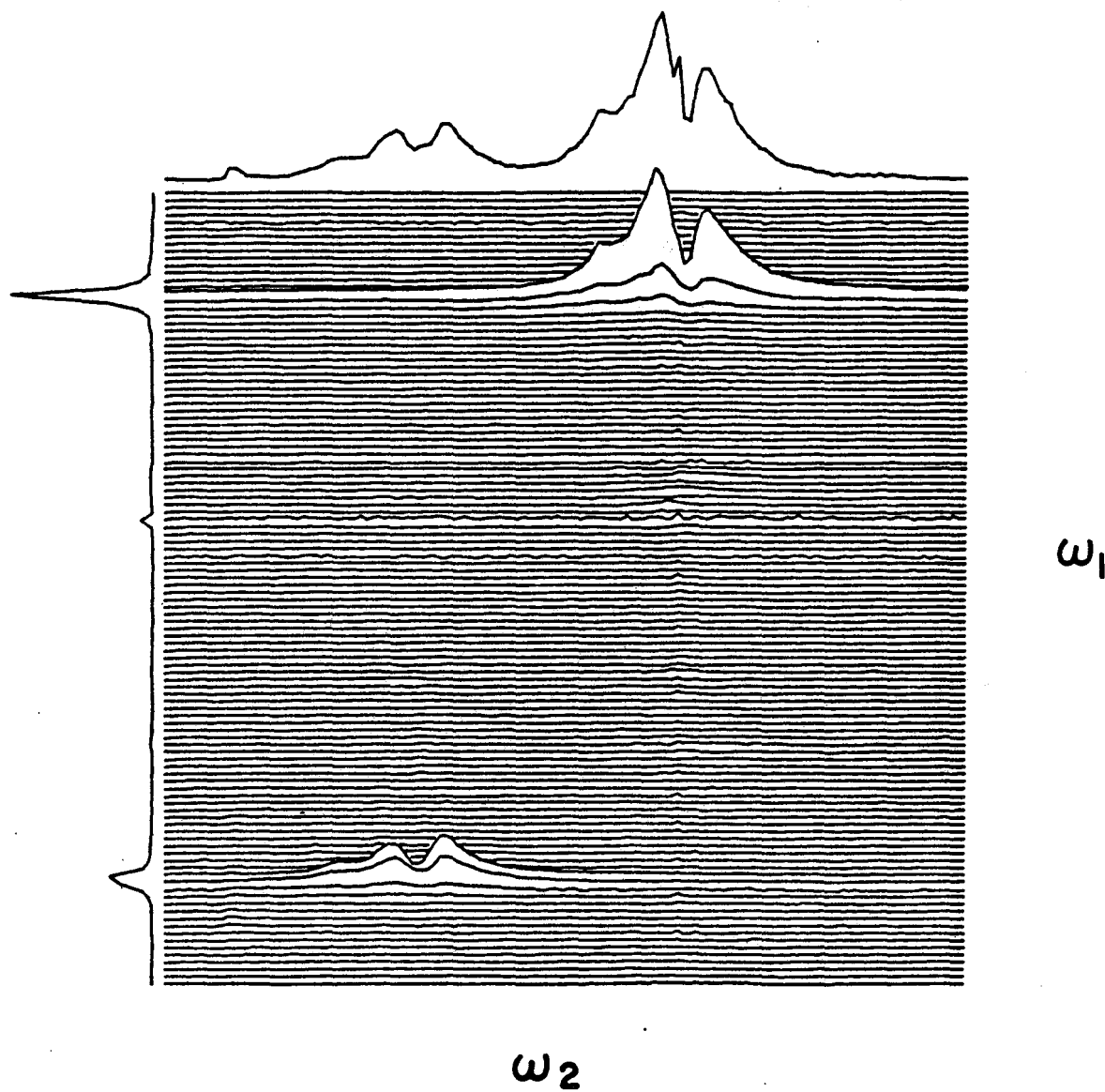
XBL 851-752

Figure 3.11

Two dimensional SHARP spectrum of enriched ethanol, taken with
sequence 3.9, under the same conditions as in figure 3.10.

pulse on I at $2t_1/5$ refocusses the I-spin chemical shift and contribution to the inhomogeneity and creates I_-S_+; the average Hamiltonian during this period is

$$\overline{\mathcal{H}}_1 = \mathcal{H}_z^S + \mathcal{H}_J^{II} \tag{3.21}$$

The evolution can be followed using the example of equation (2.39) for the different double quantum frequencies. During the next $t_1/5$, the I-spin component now evolves freely while the S-spins are refocussed by a π pulse half way through this interval:

$$\overline{\mathcal{H}}_1' = \mathcal{H}_z^I + \mathcal{H}_J^{II} \tag{3.22}$$

At the end of t_1, an invisible double quantum echo is obtained due to the overall cancellation of magnetic field inhomogeneity in the component I_-S_-. The echo, detected as I_+, is given by

$$\rho_{SAT}(t_1) = -\frac{1}{4i}\beta \ I_+ e^{i(\omega_S - \omega_I/4)[4t_1/5]} \cos(\pi J_{II} t_1) \tag{3.23}$$

Frequency labelling as a function of $4t_1/5$ is given by

$$\boxed{\omega_1 = \omega_S - \frac{1}{4}\omega_I \pm J_{II}/2} \tag{3.24}$$

The full proton-proton scalar coupling is retained in this experiment, an example of which is shown in figure 3.13a. $J_{IS} = 0$. Now that the individual fine splittings can be resolved, the linewidth is reduced to the natural linewidth, though there appears to be some broadening due to certain effects of the sequence to be discussed later. The linewidth in figure 3.13 is ~2 Hz. The fine structure of proton spectral lines is superimposed on resonance positions defined mainly by ^{13}C chemical shifts. The methyl resonance is a triplet, and the

XBL 858-3343
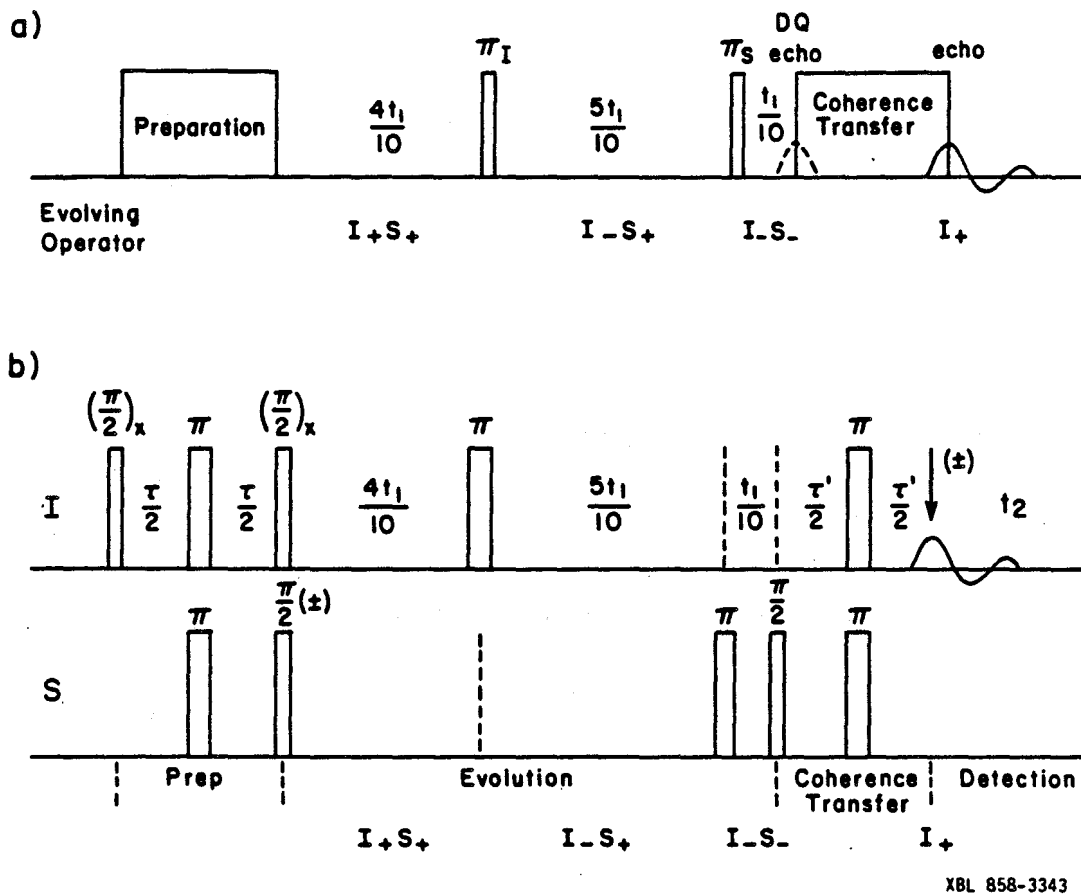
Figure 3.12

The 4:5:1 SHARP double quantum echo sequence, which retains J_{HH}.

a)

CH₃CH₂OH
Coherence Transfer

CH₃

CH₂

b)

Proton Decoupling (with BIRD)

CH₃

CH₂

-500   0   500

Frequency ($\nu_C - 1/4\ \nu_H$) (Hz)
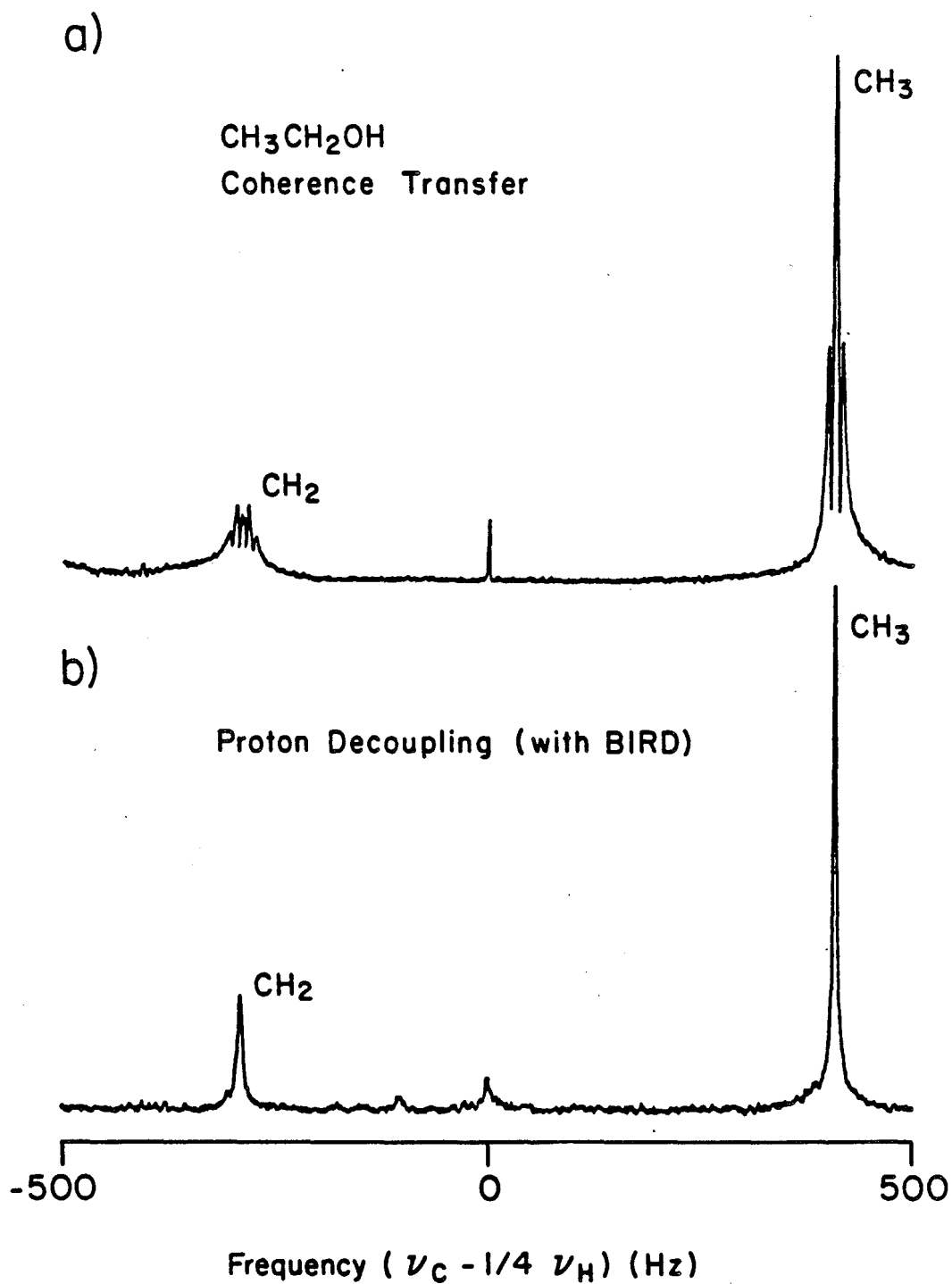
XBL 852-1226

Figure 3.13

SHARP spectra of enriched ethanol, taken (a) with pulse sequence 3.12, (b) with pulse sequence 3.16.

ethyl resonance a doublet of quartets, due to simultaneous coupling to the methyl group and to the partially exchanging -OH group. Note that the spectrum is dominated by positive ^{13}C chemical shifts, so that the lateral inversion of the spectrum of the 4:1 experiment described in Section 3.3.1 does not occur.

The selection of π pulse spacings can most easily be deduced by noting the relative dephasing ratios of the coherences I_+S_+, I_-S_+ and I_-S_-. These are 5 : -3 : -5 respectively, because proton magnetization dephases 4 times as fast as that of carbon. Hence dephasing times of 4 : 5 : 1 result in a total dephasing of 0. In general, if the relative dephasing ratios of the coherences created in each interval between π pulses are given by r_1 : r_2 : r_3, then the relative lengths of these intervals t_1 : t_2 : t_3 must satisfy the equation:

$$r_1 t_1 + r_2 t_2 + r_3 t_3 = 0$$

The additional requirement that $H_J^{IS} = 0$ implies that

$$t_1 + t_3 = t_2.$$

Hence

$$t_1 = \frac{(r_2 + r_3)}{(r_1 + r_2)} \; t_3$$

The remaining components of $I_x S_x$ are not observed; I_-S_+ and I_+S_- cannot be refocussed by any arrangement of π pulses and I_-S_- is precluded because the spectrometer only detects I_+.

3.3.3 The 3:5 experiment

If the requirement $H_J^{IS} = 0$ is not included, then two intervals are sufficient for the creation of a double quantum echo, and

$$r_1 t_1 + r_2 t_2 = 0$$

The equation is fulfilled for interval times in the ratio 3:5 for ^{13}C

a)
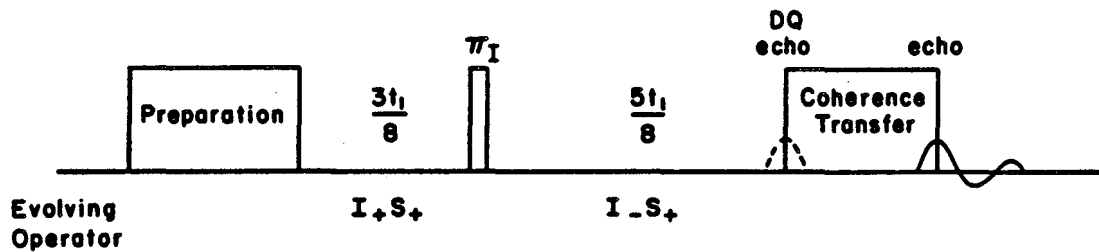
b)
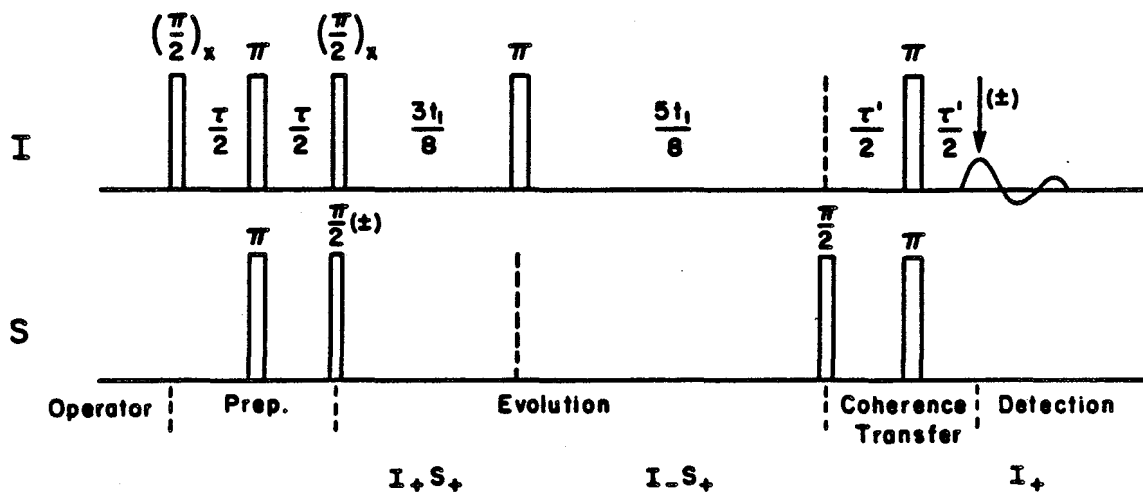
XBL 854-2009

Figure 3.14

The 3:5 SHARP double quantum echo sequence, which retains J_{HH} and $J_{CH}/4$.

- ^{1}H coupled spins (figure 3.14). The result is shown in figure 3.15a, where both heteronuclear and homonuclear coupling are evident and the spectrum is at its most complex form. The frequencies in this spectrum are given by

$$\boxed{\omega_1 - \omega_S - \frac{1}{4}\omega_I \pm J_{IS}/8 \pm J_{II}/2} \tag{3.25}$$

3.3.4 <u>Homonuclear decoupling</u>

In the spectrum of a complex molecule with many overlapping resonances, the most highly resolved spectrum possible would be the proton-proton decoupled spectrum with a single line for each C site. This is possible in the SHARP experiment with each line identifying a particular ^{13}C - ^{1}H pair.

The pulse sequence for decoupling the homonuclear proton-proton interactions is shown in figure 3.16. It consists of two consecutive 4:5:1 t_1 intervals, as described above, separated by a series of pulses involving a BIRD π[62] which inverts only satellite magnetization, leaving non-satellite magnetization unchanged. Since any satellite proton is normally surrounded by a neighbourhood of non-satellite protons, due to the relatively low natural abundance of ^{13}C or due to the careful selection of enriched samples chosen here, this type of selective inversion implies proton-proton decoupling for the observed satellite protons. The BIRD pulse has been described elsewhere and is only briefly reiterated here to demonstrate its usefulness and describe its extension to the case of existing heteronuclear coherence. In essence, a propagator of the form exp(-$iJ_{IS}I_xS_z.4T$) is created by the sequence $(\pi/2)_{\bar{y}} - 2T - \pi - 2T - (\pi/2)_y$

on the protons. Setting $4T = 1/J_{IS}$, this propagator acts as a π-pulse on satellite magnetization, inverting it with respect to non-satellite magnetization, and hence decoupling the two. The propagator shown in figure 3.16 is of a compensated form:

$$\exp(-iJ_{IS}I_yS_z.2T) \cdot \exp(-iJ_{IS}I_xS_z.4T) \cdot \exp(-iJ_{IS}I_yS_z.2T)$$

which looks to satellite protons like $(\pi/2)_y \; (\pi)_x \; (\pi/2)_y$ and compensates for incorrect pulse length that is caused by varying J_{IS} values for different spin pairs. A small complication arises because of the existence of S-spin transverse coherence. For the BIRD π to work, this must be transferred to S_z. This is achieved by first fixing the phase of S-spin coherence with a short spin-locking pulse along x, so that the S_y component dephases, and then applying a 90^0 pulse along y to transfer S_x to S_z. During the proton BIRD π pulse, π pulses on S preserve the J_{IS} coupling. At the end of the BIRD π a $90^0_{\bar{y}}$ pulse reinstates S-spin transverse coherence.

The results of this experiment are shown in figures 3.13b and 3.15b, where 4:5:1 and 3:5 ratios were applied correspondingly in the evolution periods. 3.15b therefore shows no homonuclear coupling, but does show heteronuclear coupling - a triplet for the methyl group and a doublet for the ethyl group, with lines separated by $J_{IS}/4$:

$$\left| \omega_1 - \omega_S - \frac{1}{4}\omega_I \pm J_{IS}/8 \right| \tag{3.26}$$

3.13b is a homo- and heteronuclear decoupled spectrum and consists of a single line at each chemical shift position:

$$\left| \omega_1 - \omega_S - \frac{1}{4}\omega_I \right| \tag{3.27}$$

a) CH_3CH_2OH

Coherence Transfer

CH3

CH2

b) Proton Decoupling (with BIRD)

CH3

CH2

−500   0   500

Frequency $(\nu_C - 1/4\,\nu_H)$ (Hz)
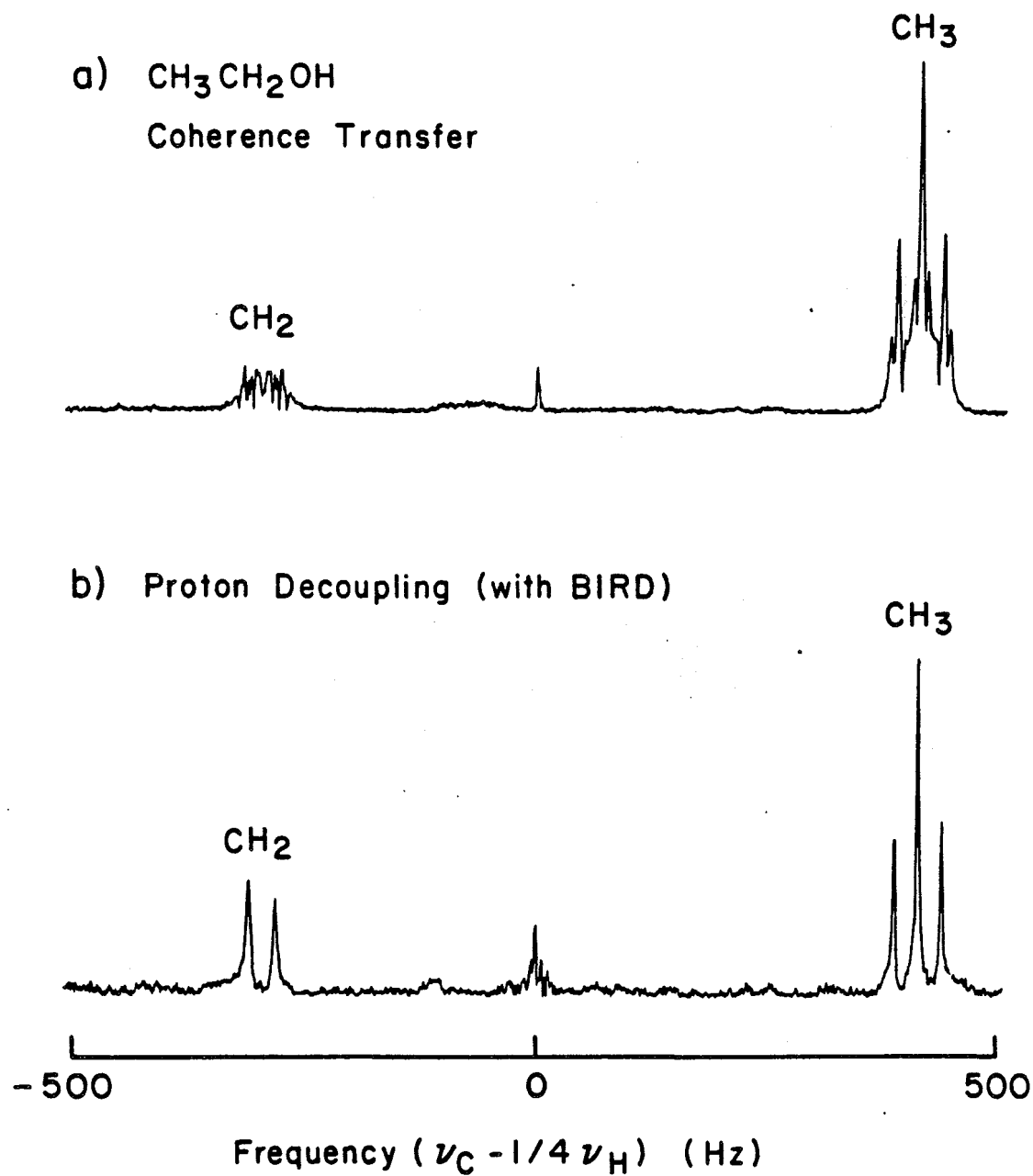
Figure 3.15

SHARP spectra of enriched ethanol, taken (a) with pulse sequence
3.14, and (b) with the equivalent of 3.16 but with 3:5 intervals
before and after the BIRD π.
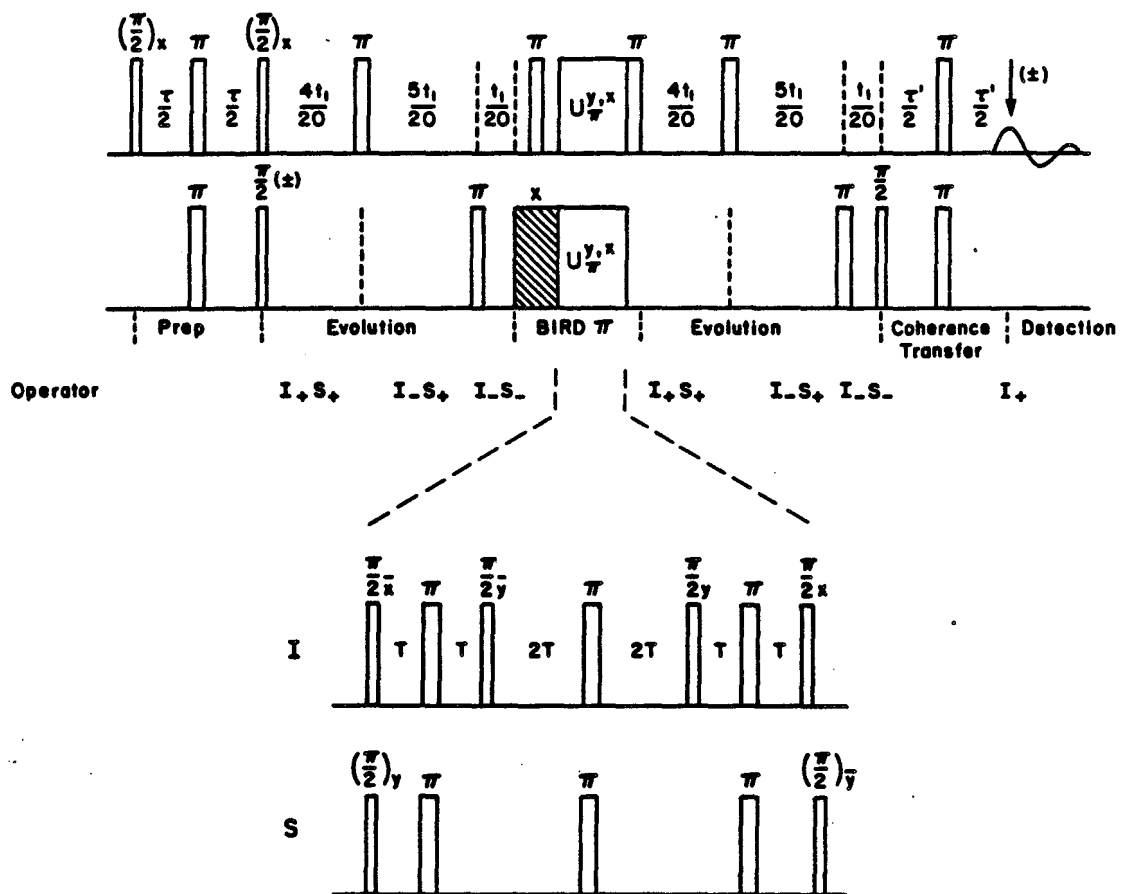
XBL 854-2007

Figure 3.16

The double quantum 4:5:1 : BIRD : 4:5:1 SHARP sequence, which leaves no residual coupling.

As an aside, note in figure 3.17 that an attempt to use the BIRD pulse without ensuring that the heteronuclear coherence be aligned along z results in a broad envelope rather than a narrow decoupled resonance line. This was the result of merely replacing each of the refocussing π pulses in the 4:5:1 sequence or in the 3:5 sequence by the appropriate BIRD π pulse.

3.3.5 **Properties of the SHARP spectra**

The various pulse sequences which give SHARP spectra are summarized in Table 3.I. Scalar interactions, both heteronuclear and homonuclear, may be observed or decoupled as desired. Although theory predicts the same relative intensity for all experiments, it is observed in practice that the 4:1 sequences tend to give higher S/N, probably being less sensitive to pulse errors.

3.3.5.1 **Residual linewidths**

The residual linewidths are ~ 2 Hz in the 2 QT echo experiments. This is due to any or all of the following: (1) recording of absolute value mode spectra, because of foldover in ν_1. (2) inexact measurement of the tip of the echo. Using the ratio 4:1 causes an error of 3 parts in 400, and an increase in linewidth proportional to $\Delta H_0(\tilde{r})$. (3) diffusion, reducing the echo intensity, proportional to $\Delta H_0(\tilde{r})^2$.[97] (4) T_2-limited linewidths, due to e.g. paramagnetic impurities. Processes (2) and (3) can be distinguished by a study of linewidth as a function of ΔH_0.
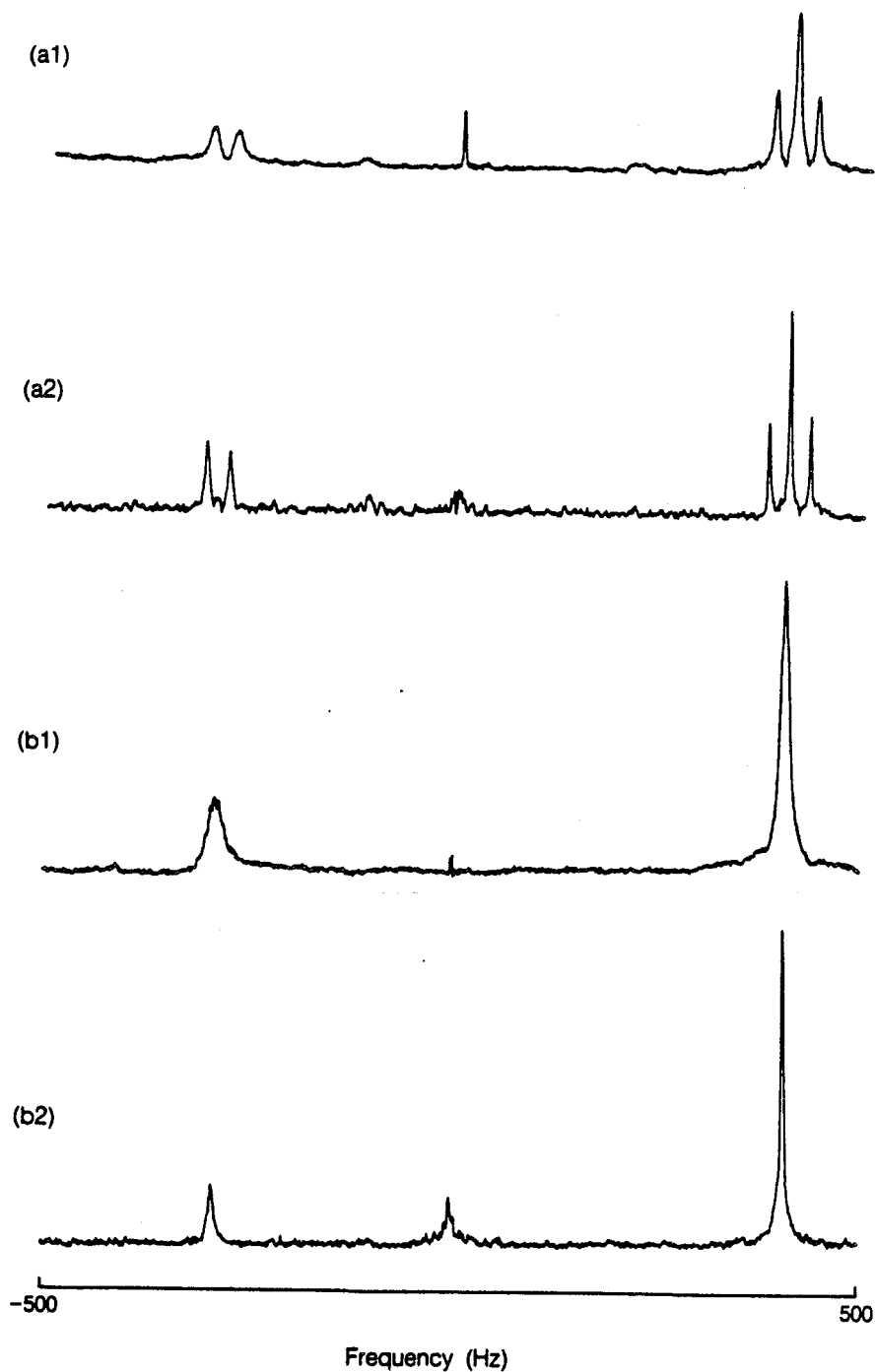
XBL 871-9553

Figure 3.17

(a1), (b1) Replacement of the π pulses in figure 3.12 and 3.14
with BIRD π's does not effect homonuclear decoupling, but leaves broad
envelopes. (a2), b(2) are the properly homonuclear decoupled spectra.

<center>Table 3.I</center>

The various SHARP J-edited spectra

PULSE SEQUENCE	DESCRIPTION	COMPONENTS OF ν_1
Figure 3.5	4:1	$-\nu_C + \frac{1}{4}\nu_H + \frac{1}{4}J_{HH} + \frac{1}{4}J_{CH}$
Figure 3.9	4:1 with π^S during the ^{1}H evolution	$-\nu_C + \frac{1}{4}\nu_H + \frac{1}{4}J_{HH}$
Figure 3.12	4:5:1	$\nu_C - \frac{1}{4}\nu_H + J_{HH}$
Figure 3.14	3:5	$\nu_C - \frac{1}{4}\nu_H + J_{HH} + \frac{1}{4}J_{CH}$
Figure 3.16	4:5:1-BIRD-4:5:1	$\nu_C - \frac{1}{4}\nu_H$
not shown	3:5-BIRD-3:5	$\nu_C - \frac{1}{4}\nu_H + \frac{1}{4}J_{CH}$

3.3.5.2 Line intensities

In some spectra (e.g. figure 3.13a, 3.15a and the natural abundance compounds to be described in Section 3.4), the line intensities are somewhat unquantitative. They depend on τ. Also, proton T_1's are a strong influence, suggesting that full ^{1}H relaxation did not occur during the recycle delay in some cases.

3.3.5.3 SHARP on unknown compounds

The resonance lines of a SHARP experiment occur at

$$\nu_1(i) - \nu_C(i) - \nu_H(i)/4 + X,$$

where $X - \Delta\omega_C - \Delta\omega_H/4.$

If the proton and carbon spectra are independently known, the SHARP spectrum may be calculated up to a constant offset X. If the compound is completely unknown, it may be suspected by comparison of the SHARP and ^{13}C spectra (as in figures 3.4 and 3.19), but its proton spectrum would have to be independently observed to confirm the assignment.

3.3.5.4 Sensitivity and Resolution

Section 3.4.1 calculates that for low S/N, SHARP echo detection may be preferable to direct ^{13}C detection. It is certainly true that if a two-dimensional heteronuclear COSY spectrum is required, there is clearly an advantange to using the SHARP echo in t_1. The gain in resolution is apparent. Figure 3.18 shows some examples of heteronuclear COSY experiments in which the peaks clearly have a narrow dimension at right angles to a line drawn at $\alpha - \tan^{-1}(\gamma_2/\gamma_1)$ to the ω_1 axis[31], where γ_1 and γ_2 are the gyromagnetic ratios of the nuclei precessing during t_1 and t_2 respectively. Use of SHARP will
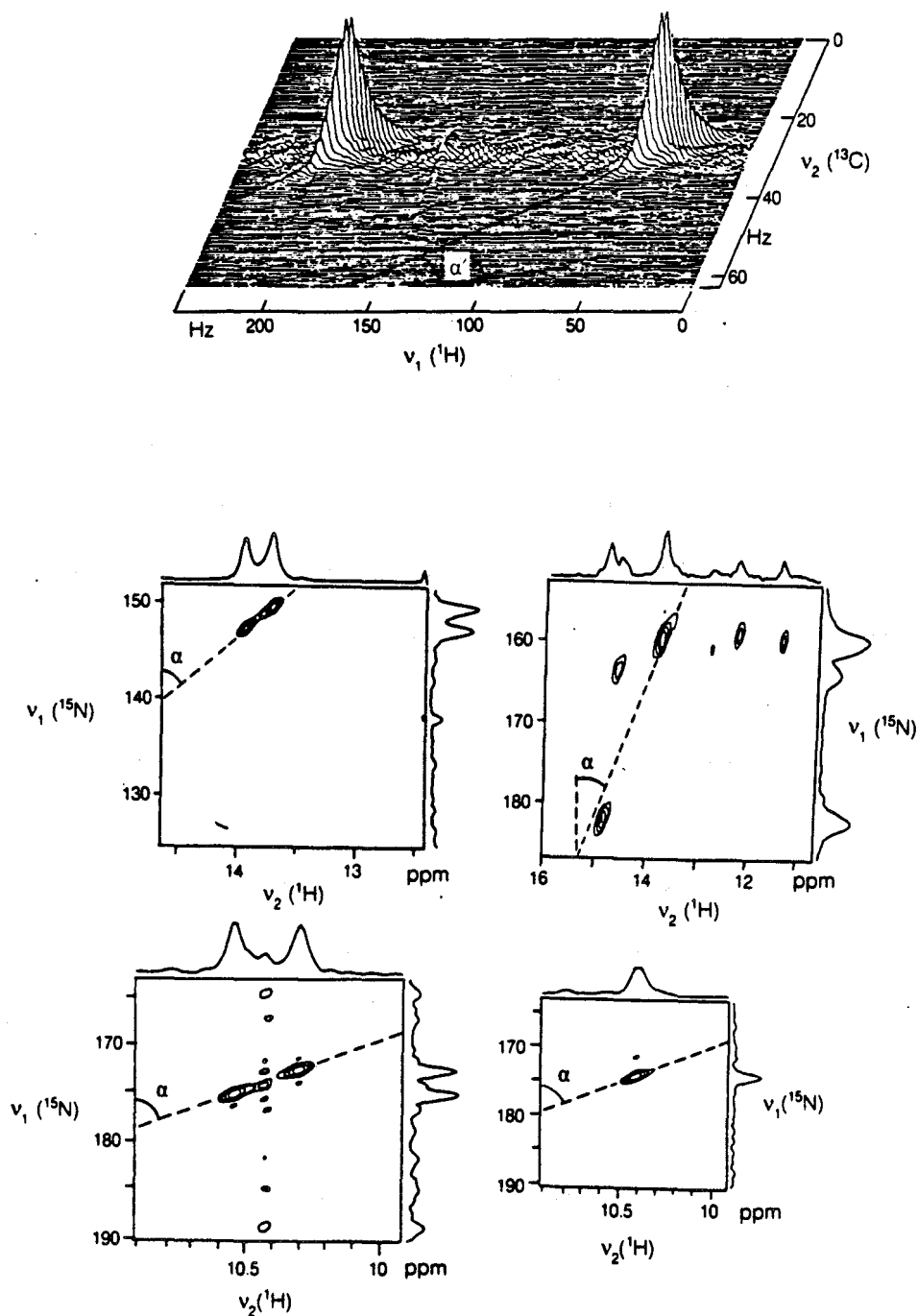
XBL 871-9552

Figure 3.18

Demonstration of a narrow ridge in heteronuclear MQT correlated spectra, taken from the literature[31,68]. Peaks are narrow along a ridge at $\alpha = \tan^{-1}(\gamma_2/\gamma_1)$.

bring α to $90°$. This is precisely the same principle employed in SECSY experiments[20].

3.4 NATURAL ABUNDANCE SAMPLES

The application of SHARP to natural abundance ^{13}C samples has proven straightforward. The overwhelming contribution of non-satellite proton signal is effectively purged at the beginning of the pulse sequence using the constant x-decouple discussed in Section 3.3.1.2. One of the most important additions to the pulse sequences described is the addition of multiple echo sampling during t_2, for improved signal-to-noise (S/N) of weak echoes. Figure 3.19 illustrates the effect by comparing two SHARP spectra on natural abundance ethanol, one with detection of a single echo, and the other with detection of a train of 256 echoes. If the space requirements of collecting a full 2D data set cannot be met, sampling multiple echoes is a practical alternative to compensate for indirect detection.

3.4.1 Multiple echo detection

Figure 3.20 illustrates multiple echoing. Echoes are detected in every second interval of a train of π pulses with alternating phase[98-100]. The π-pulse repetition rate must be faster than the largest interaction in the spectrum so that the echo rephasing is dominated by the pulse phases and not by the internal Hamiltonian. For proton liquid state spectra, where chemical shifts of the order of a few kilohertz prevail, this corresponds to an interval time of some hundreds of μsec. It may be noted in Figure 3.20b that the echo sampling points are displaced from the midpoint between pairs of π-

Ethanol
natural abundance

(a) 1 echo sample in t_2
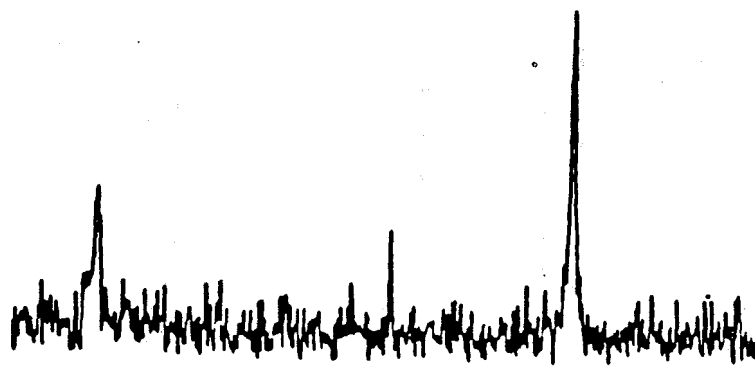
(b) 256 echo sample in t_2

$$-500 \qquad 0 \qquad 500$$

Frequency (Hz)
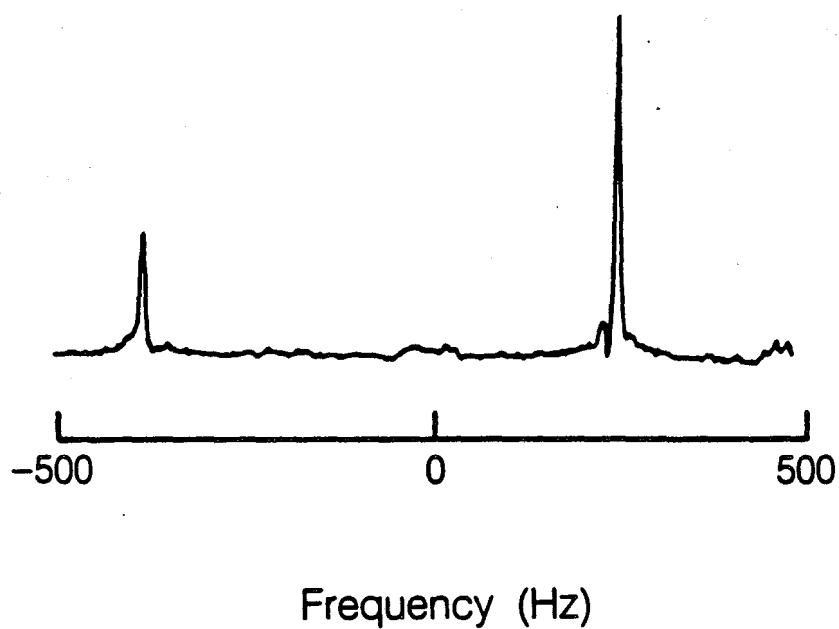
XBL 854-2006A

Figure 3.19

SHARP spectra of natural abundance ethanol illustrating the effect of multiple echoing in t_2.

(a)

(b)

π_x $\pi_{\bar{x}}$ π_x $\pi_{\bar{x}}$ π_x

τ_f

(c)

π_x $\pi_{\bar{x}}$ π_x $\pi_{\bar{x}}$ π_x

TTL
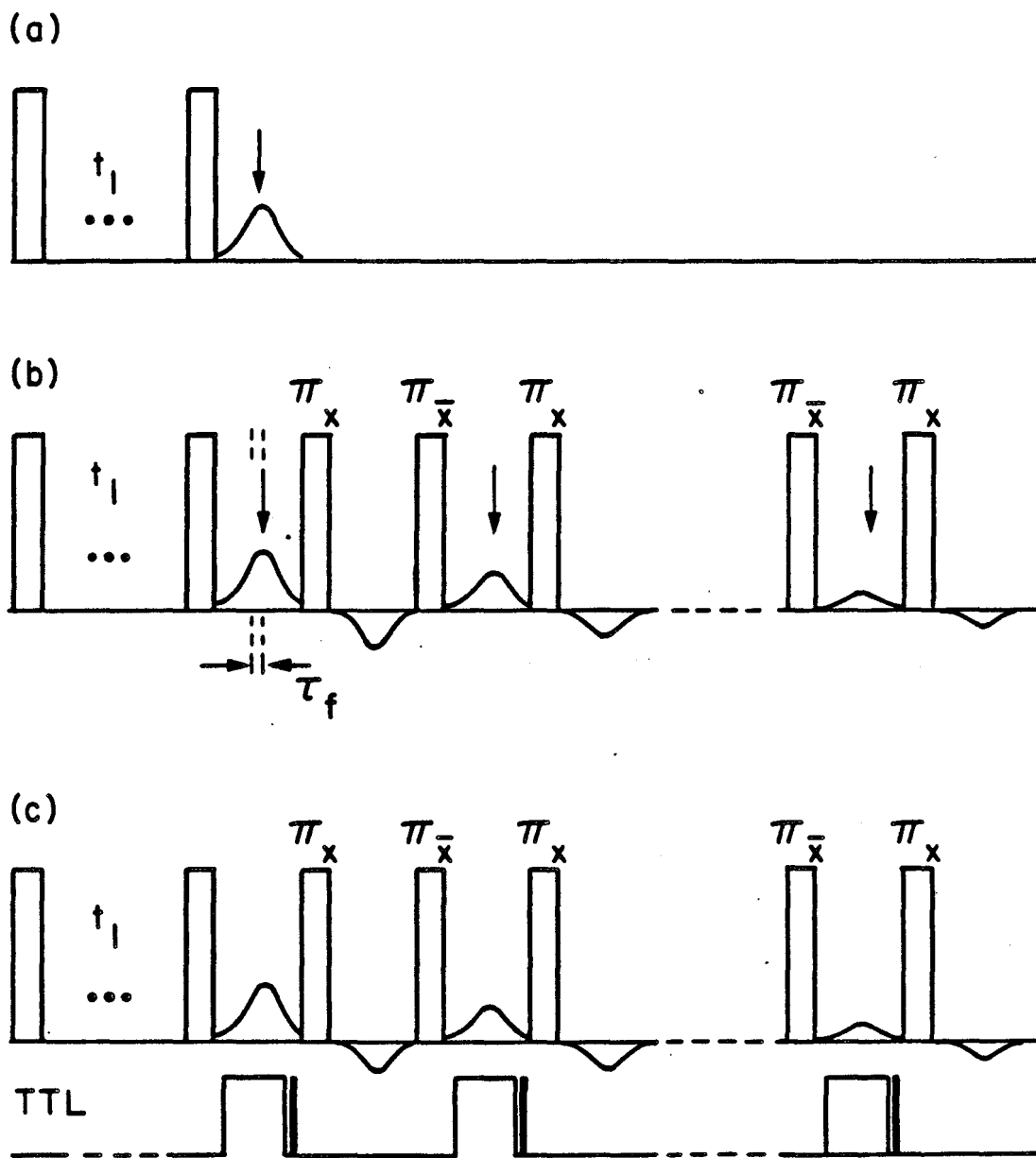
XBL 8610-4075

Figure 3.20

(a) Detection of a single echo after a period of t_1 evolution.

(b) Multiple echo detection, sampling the tip of every second echo in

a $\pi_x/\bar{x}$ train.

(c) Multiple echo sampling using an integrator to sum the signal in

every second interval. The long TTL pulse from an AUX gate triggers

and maintains the integration. The short TP pulse samples the

recorded value and after a delay resets the integrator to 0.

pulses by an amount τ_f = filter delay constant = $1/(2 \times$ filter width(FW)). The filters should be wide enough to minimize this effect and also to prevent pulse breakthrough from adding noise to the sampling.

If sampling just the first echo in Figure 3.20 gives a signal magnitude S, then the signal measured for M+1 sampled and summed echoes is given by:

$$S' = S \sum_{k=0}^{M} e^{-k/K}$$

$$= S \frac{(1-\exp(-M/K)}{(1-\exp(-K)} \; ,$$

where Δt is the time between sampling points, $K = T_2^*/\Delta t$ = number of sampled points up to 1 decay constant of the echo envelope. T_2^* is independent of the magnet inhomogeneity, but may fall short of the natural linewidth T_2 because of pulse misset or diffusion effects. Since $\Delta t \ll T_2^*$,

$$S' = S \; (1-\exp(-M/K)) \; . \; K \qquad\qquad (3.29)$$
$$= 0.63 \; K, \; \text{when} \; M = K$$
$$= 0.95 \; K, \; \text{when} \; M = 3K$$

The S/N enhancement is given by $\sqrt{S'/S}$, and usually lies between 3 and 10. Figure 3.21 shows the S/N by a pair of lines as a function of N. Comparison between the various curves indicates that integration is preferable to single point detection of the signal in the intervals between π pulses. This is the subject of the discussion that follows.

3.4.1.1 Single point detection in the pulse windows

Detecting one point in each appropriate interval of a π train generally requires that FW be larger than in single echo detection.
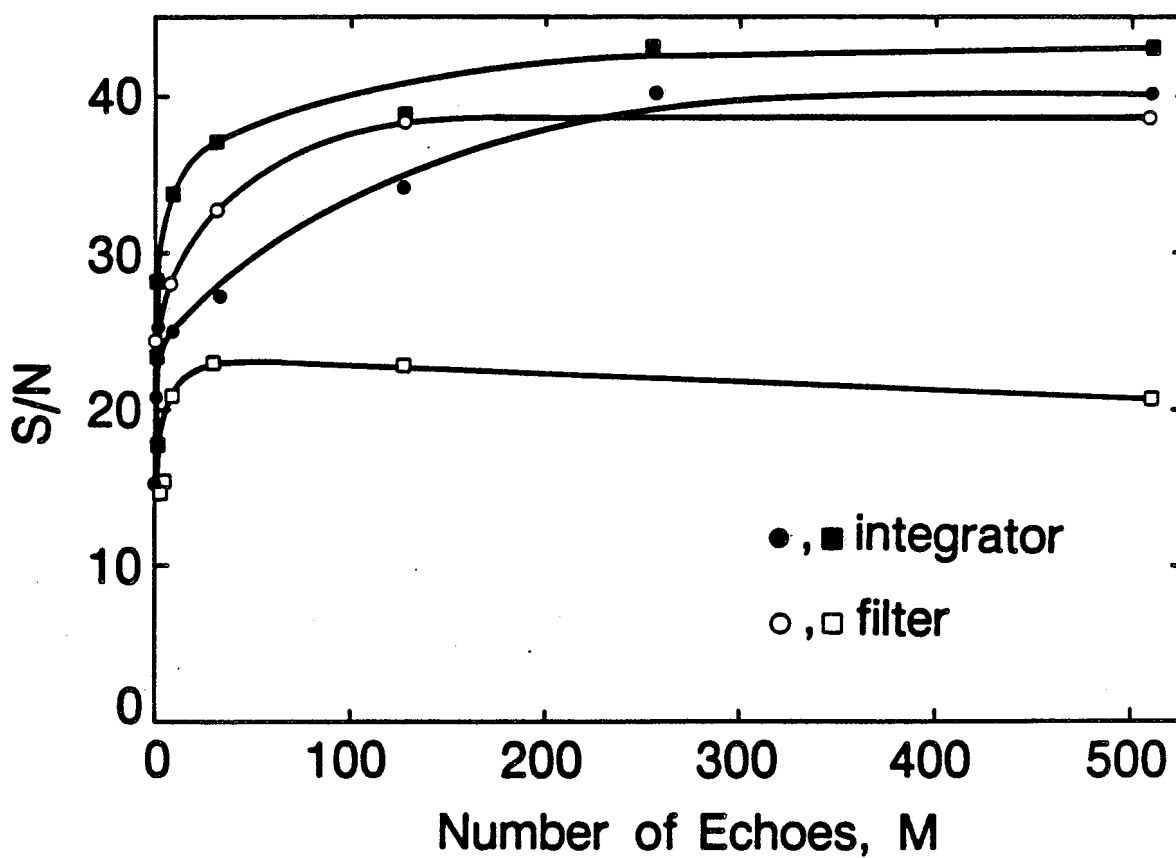
XBL 869-9476

Figure 3.21

Comparison of integration (■,•) and single point sampling (□,○)
of a train of echoes on the methyl(□) and ethyl(○) SHARP resonances of
natural abundance ethanol.

This introduces noise = square root of the fractional increase in FW.

Figure 3.22 shows the effect of varying the filter bandwidth on the quality of the signal produced. Here both + and - echoes are recorded (i.e. sampling in every interval) and the echo envelope is multiplied by an appropriate exponentially decaying function having alternate positive and negative values before summation. The best S/N enhancement is obtained when the filter width is of the order of $1/\Delta t$.

Figure 3.23, parts a and b, illustrate the signal enhancement due to this method. 3.23a is a single echo sample following a SHARP sequence on EtOH, natural abundance. In 3.23b, a train of 1024 echoes were sampled. A factor of 3 in improvement of S/N is observed. There are a number of experimental factors limiting the enhancement:

1) pulse error build-up causing $T_2^* < T_2$;

2) filter bandwidth increase;

3) spectrometer delays causing echo sampling to be misset from the tip of the echo;

4) detection in 1 buffer only since the second buffer contains phase transients which build up from subtle inaccuracies in the pulses, and add only noise to the spectrum. The loss of quadrature information implies a S/N reduction of $\sqrt{2}$. To reinstate quadrature, a second experiment is required with either the preparatory pulses or the π pulse train shifted in phase by 90°.

Some of the experimental difficulties may be overcome by using a sample and hold circuit which integrates the incoming signal over a defined interval, with a time constant T_c. The integration precludes the necessity of determining the tip of the echo, and T_c defines the
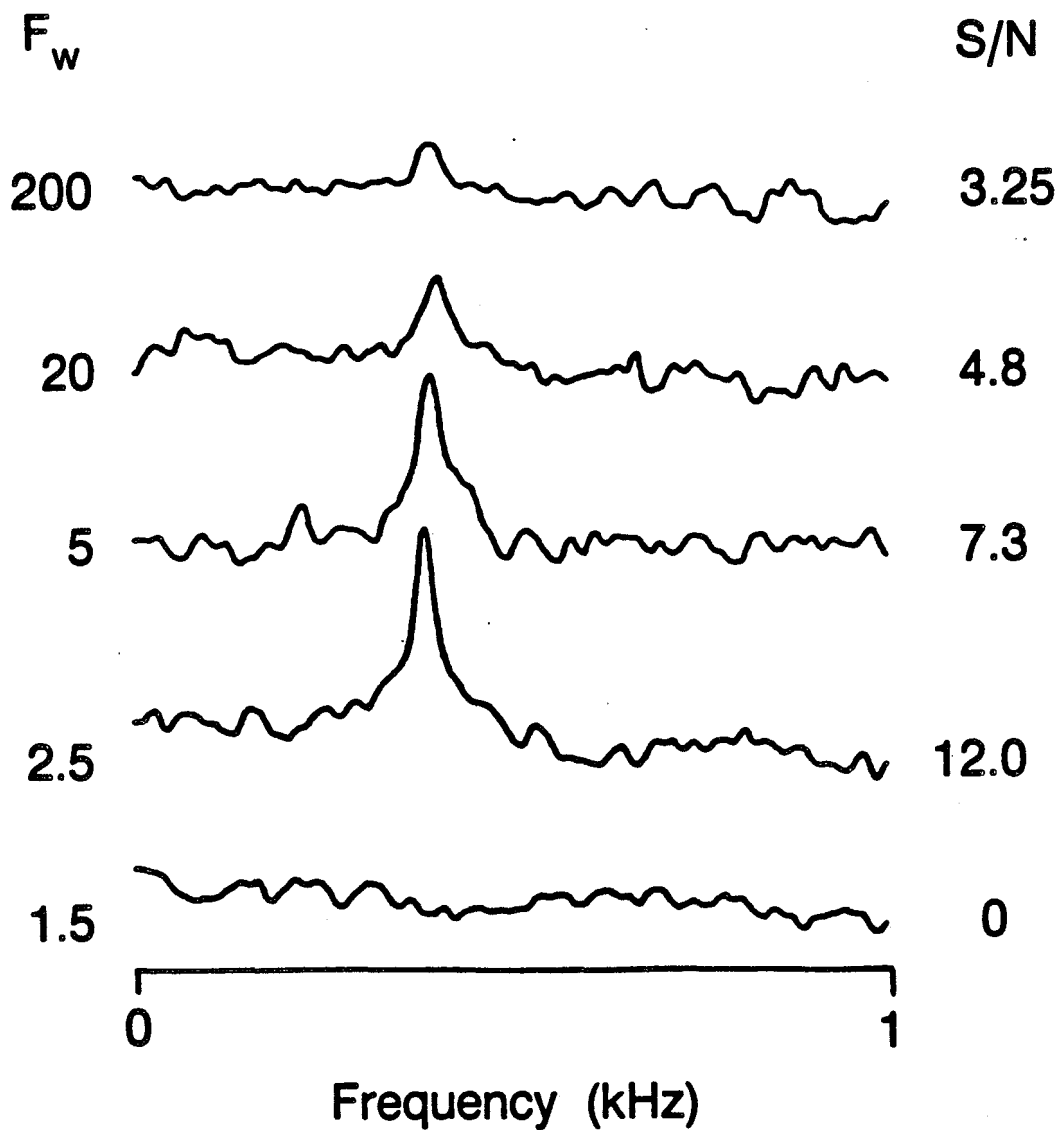
Figure 3.22

The effect of variation of the filter bandwidth F_w on the signal produced by single point sampling of a train of echoes. The π pulses were spaced by 400 μs and the echoes sampled in every interval. The signal in t_2 was multiplied by a +/- decaying exponential function before summing the echoes.

bandwidth, so that the filters become redundant. Such a device was described briefly in an early paper on coherent averaging[101].

3.4.1.2 Integrated sampling in the pulse windows

Two gated integrator modules were purchased from Evans Electronics, Model 4130A, for dual channel capability, and installed prior to the ADC's with the following specifications. Integration is triggered by the rising edge of a TTL pulse and discontinued at the falling edge, with the current value held. A 100 nsec TTL pulse reads this value and after a 500 nsec delay resets the integrator to zero. The integrator was modified for variable time constant $T_c = 1/RC$ by varying resistance R and/or capacitance C so that T_c could be adjusted from 1 μsec to 5 sec.

Figure 3.20c shows the use of the integrator with a π train. T_c is set to be about 1 or 2 times the π pulse spacing so that integration is occurring in the linear regime. The levelled-off region of integration is avoided to prevent level fluctuations from adding to the noise. The filters are opened wide (1 MHz) to minimize the echo delay. The effective filter bandwidth is given by $1/T_c$ which is for liquids in the range of $\sim 10^4$ Hz. The result of an integrated multiple echo sampling in the SHARP experiment in shown in Figure 3.23c. Here the improvement in S/N is about 3 over the multiple echo sampling with the filters.

A final example is shown in Figure 3.24 which compares a single echo sample from a SHARP experiment on a natural abundance ^{13}C compound with an integrated multiple echo sampling. The S/N

(a)

(b)

(c)

Frequency (Hz)

-1000   0   1000
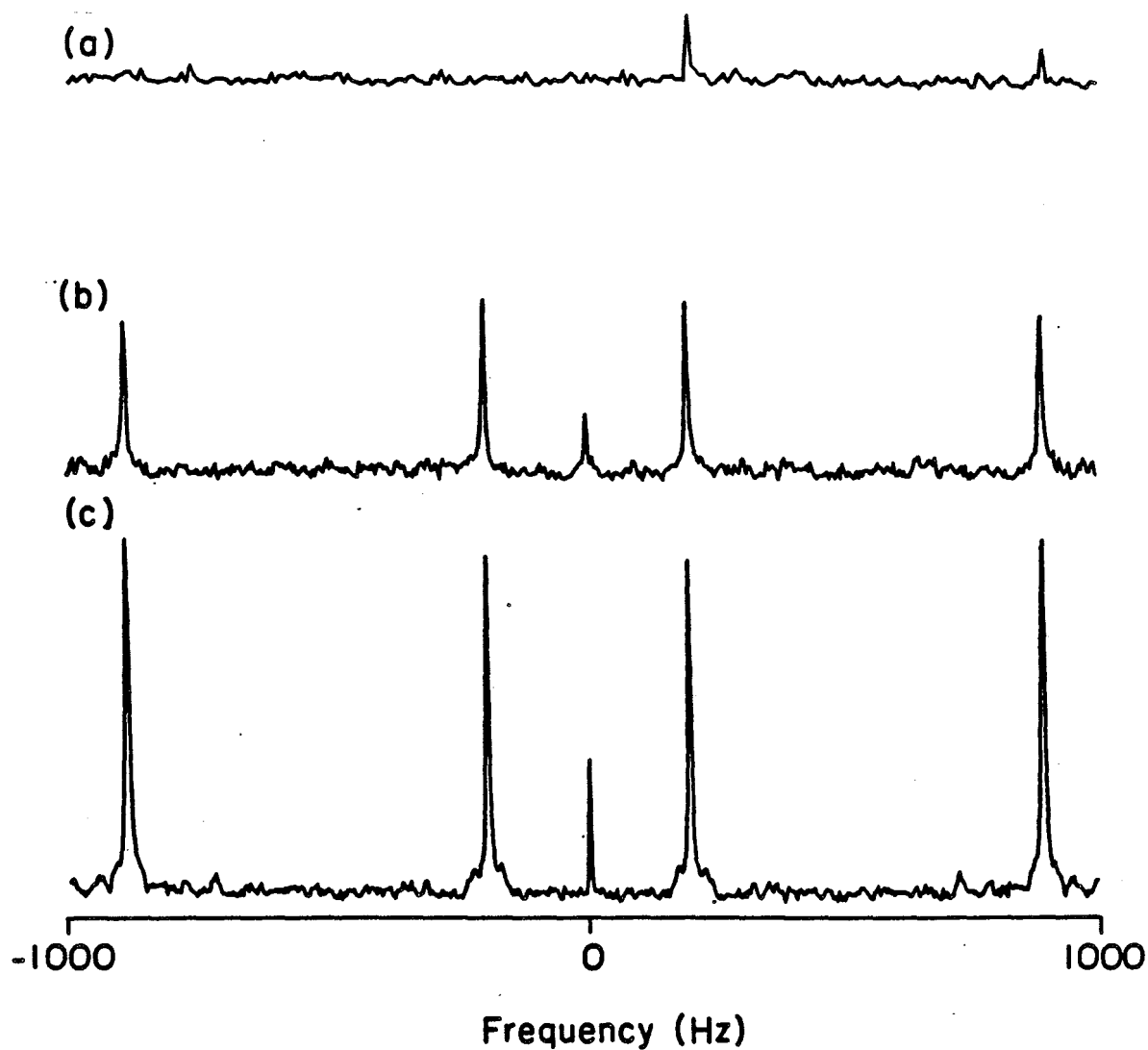
XBL 869-9474

Figure 3.23

Comparison of (a) single echo sampling, (b) multiple echo single point sampling and (c) multiple echo integrated sampling, on ethanol SHARP spectra using sequence 3.9.

enhancement is $10/\sqrt{2} = 7$, accounting for the loss of quadrature information. Since practically no increase in experimental time is involved in integrated multiple echoing, it is strongly recommended for experiments in indirect detection.

3.4.2 Signal-to-noise of SHARP vs. ^{13}C

Part of the S/N improvement of SHARP spectra is due to the natural linewidths vs. the inhomogeneously broadened ^{13}C spectra. This cannot be quantitated and will be ignored in the following treatment.

Gains in S/N

(1) Initiation and detection of the proton magnetization over straight ^{13}C detection adds a S/N improvement of $(\gamma_I/\gamma_S)^2$. (or $\sim(\gamma_I/\gamma_S)$, cf. INEPT[85])

(2) A factor n improvement occurs for the number of protons in the group I_nS representing one ^{13}C site (true only for J_{CH} and J_{HH} decoupled SHARP spectra.)

(3) Multiple echo sampling adds a factor $\sqrt{\sum_{k=0}^{M} e^{-k/K}}$

(4) Finally, we add a factor $\sqrt{T_I/T_S}$ to account for the difference in recycle delay T required when sampling I·spins compared to S spins.

This gives a total improvement in sensitivity of

$$\left(\frac{\gamma_I}{\gamma_S}\right)^2 (n) \sqrt{\sum_{k=0}^{M} e^{-k/K}} \sqrt{T_I/T_S} \approx 300 - 400 \qquad (3.28)$$

(or $\sim$100 cf. INEPT)

(a)

(b)

−500   500

Frequency (Hz)
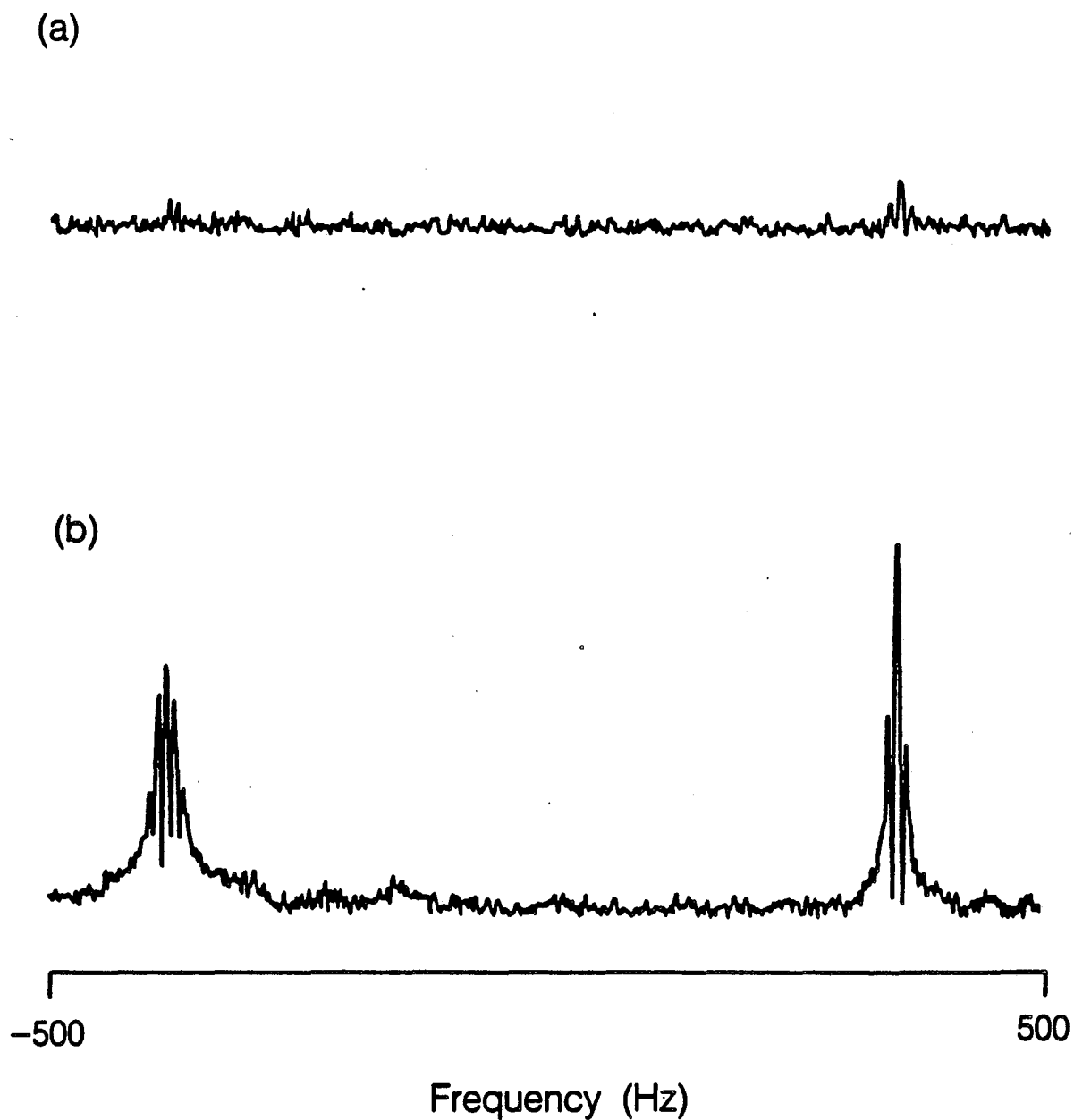
XBL 8610-4074A

<u>Figure 3.24</u>

The effect of multiple echo integrated sampling on the SHARP

spectrum of natural abundance ethanol recorded with sequence 3.12.

(a) is a single echo detection, (b) a multiple echo detection.

Loss in S/N

(1) The total experimental time is increased by N over direct detection, where N is the number of points required in the FID. This results in a reduction of S/N by $\sqrt{N}$.

For a resolution of 1 Hz/point, N = Spectral Width, typically 10000 Hz, implying a S/N reduction of 100.

3.4.3 Examples of natural abundance spectra

3.4.3.1 Sucrose

A fairly high resolution proton spectrum of sucrose is shown in figure 3.25 with assignments[102]. The 4:1 decoupled SHARP spectrum was recorded using the integrated multiple echo method of Section 3.4.2. It is shown compared to the ^{1}H decoupled ^{13}C spectrum in figure 3.26. The assignment of the SHARP spectrum is easily determined using equation (3.20).

Some important features occur in this spectrum. The ordering of the SHARP and ^{13}C signals is identical. This occurs because of similar ordering of the proton resonances, and because the small ppm shift range of protons has hardly any effect on the SHARP spectrum. The relative line intensities correspond very closely to the proton spectrum, not the ^{13}C spectrum. This implies that the SHARP spectrum is proton T_2 (or T_1) limited.

3.4.3.2 Camphor

The proton spectrum of camphor is shown in figure 3.27, with assignments[103]. The inhomogeneously broadened ^{1}H-decoupled ^{13}C

Sucrose
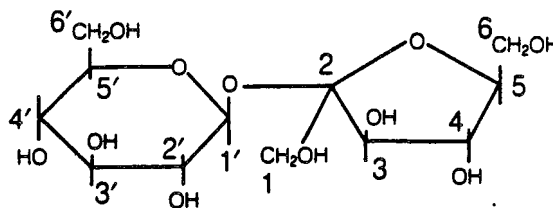
^{1}H spectrum

ppm
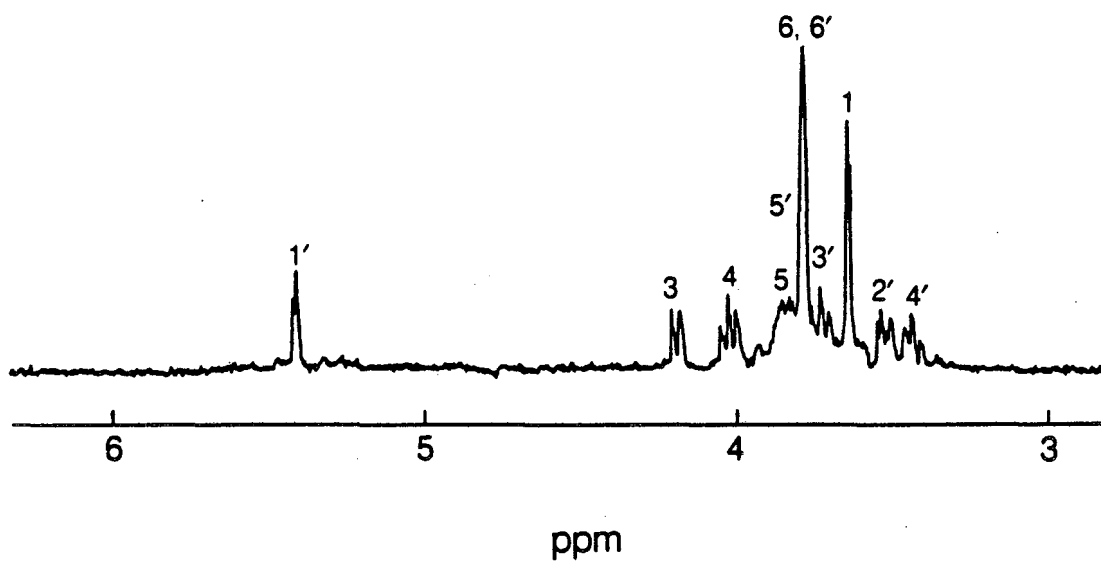
XBL 871-9547

Figure 3.25

^{1}H spectrum of sucrose.

Sucrose

(a) ^{13}C

(b) SHARP echo

ppm
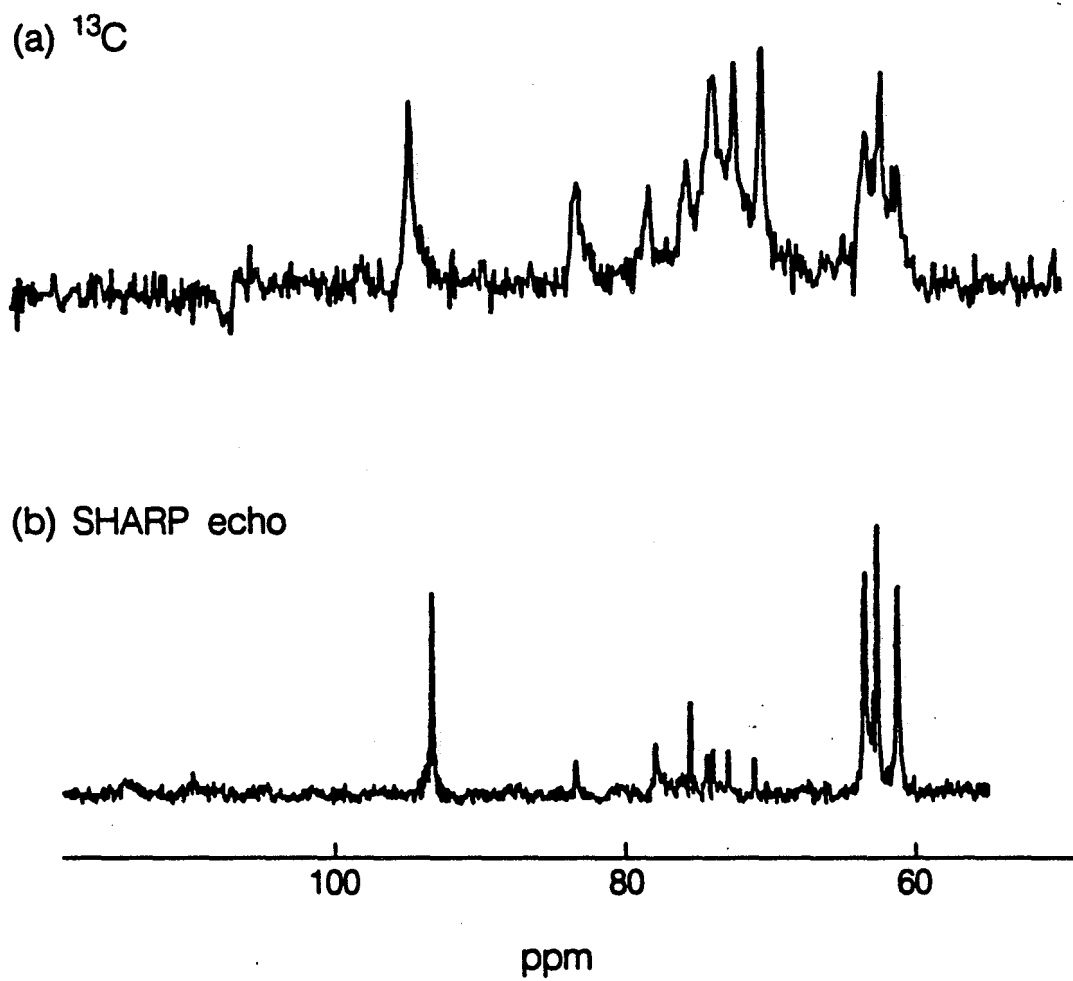
XBL 871-9548

Figure 3.26

^{13}C and SHARP spectra of sucrose.

spectrum and the SHARP spectrum appear in figure 3.28. The same characteristics of peak positions and intensities occur as in the sucrose experiment.

The inequivalent protons at each C site can be easily identified in the SHARP spectrum. The pair splitting in ppm of peaks d, e and g is exactly identical to the ppm splitting in the ^{1}H spectrum. These two spectra can be cross referenced for assignments.

3.5 SHARP WITH A SURFACE COIL

One of the difficulties in surface coil or volume selective NMR is shimming the field in the region of interest[104]. The difficulty may be intrinsic, i.e. due to the sample itself[105], or may be experimental: usually spatial selection is the result of a series of phase cycled FID's[106-7], so that shimming on individual FID's is inappropriate. Linewidths of the order 1/2 - 1 ppm are typical.

Measuring SHARP echoes is a means of circumventing the problem. It may also provide an answer to the question of whether the inhomogeneously broadened spectra typically observed in vivo are inherent or the result of local susceptibility gradients.

As a preliminary investigation, we have shown that SHARP sequences can be applied using surface coils[108], despite the notoriously poor rf homogeneity[109-11]. In fact, the inhomogeneity of the rf enables SHARP to also be used as a spatially selective sequence. Figure 3.3 was taken with a single turn 1 cm diameter surface coil and a bulb of 25% ^{13}C-enriched ethanol 2mm on axis from the coil. Note the narrow lines and greatly enhanced sensitivity of this method over direct detection of ^{13}C in an inhomogeneous magnet.

Camphor

^{1}H spectrum
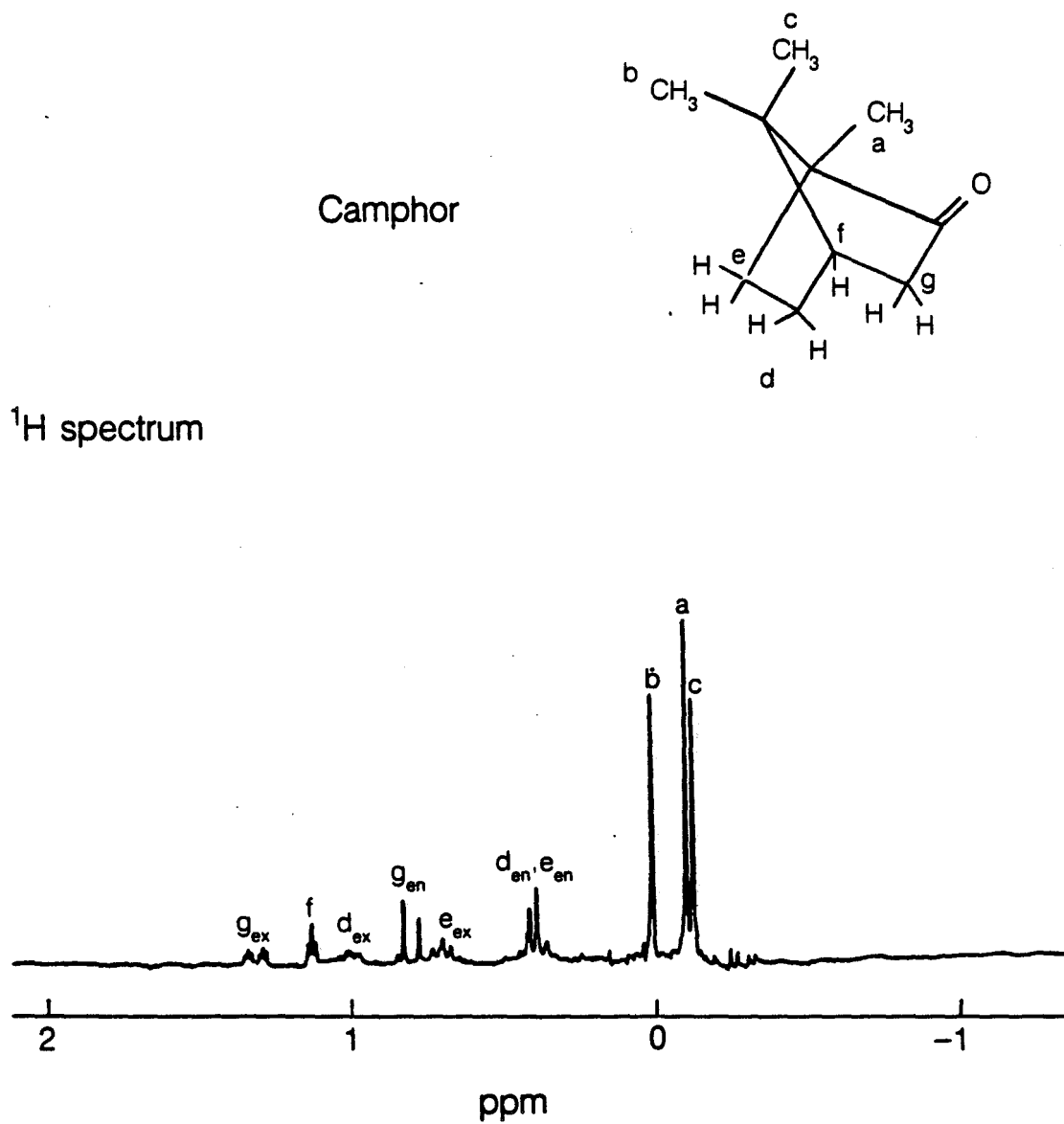
XBL 871-9550

Figure 3.27

^{1}H spectrum of camphor.

Camphor

(a) ^{13}C

(b) SHARP echo

40   30   20   10

ppm
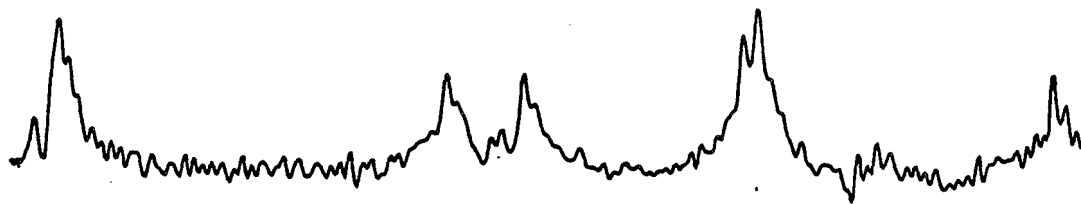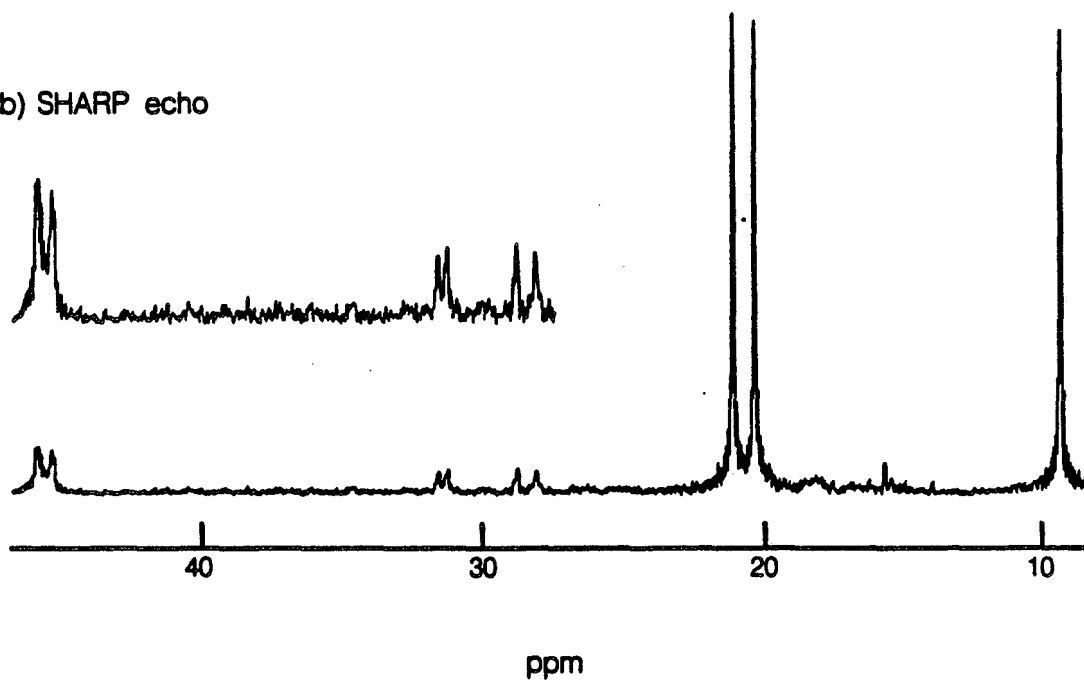
XBL 871-9551

Figure 3.28

^{13}C and SHARP spectra of camphor.

Figure 3.29 shows that SHARP inherently exhibits some spatial selectivity. Two capillary tubes, containing alanine and ethanol, were placed at 2 and 4 mm from the surface coil. Figure 3.29a shows the ^{13}C spectrum after a single pulse. It is non-selective and poorly resolved; resonances from both tubes appear, but the methyl groups on alanine and ethanol are not separated. Figures 3.29b, c, and d are SHARP spectra. The spectrum in 3.29b is non-selective, and was obtained by setting the pulses in figure 3.9 for a point half way between the two tubes. Spectra 3.29c and d were obtained by setting the pulses for the first and second tubes respectively; distinction of the contents of the two tubes illustrates a spatial separation of high resolution.

Thus SHARP yields high resolution spectra which are easy to interpret, and which can be combined with methods of accurate spatial selection designed for heteronuclear systems[110,112]. It should therefore prove a useful addition to topical NMR. The two-quantum pulse sequences of Section 3.3.2 - 3.3.4 can retain or remove heteronuclear or homonuclear couplings or both, providing additional information and resolution. Background water does not interfere, since it has no heteronuclear coupling. The technique could be used for natural abundance studies of isotopes such as ^{13}C, ^{15}N, or for following the metabolic pathway of specifically labelled compounds such as lactic acid, glucose or drugs.
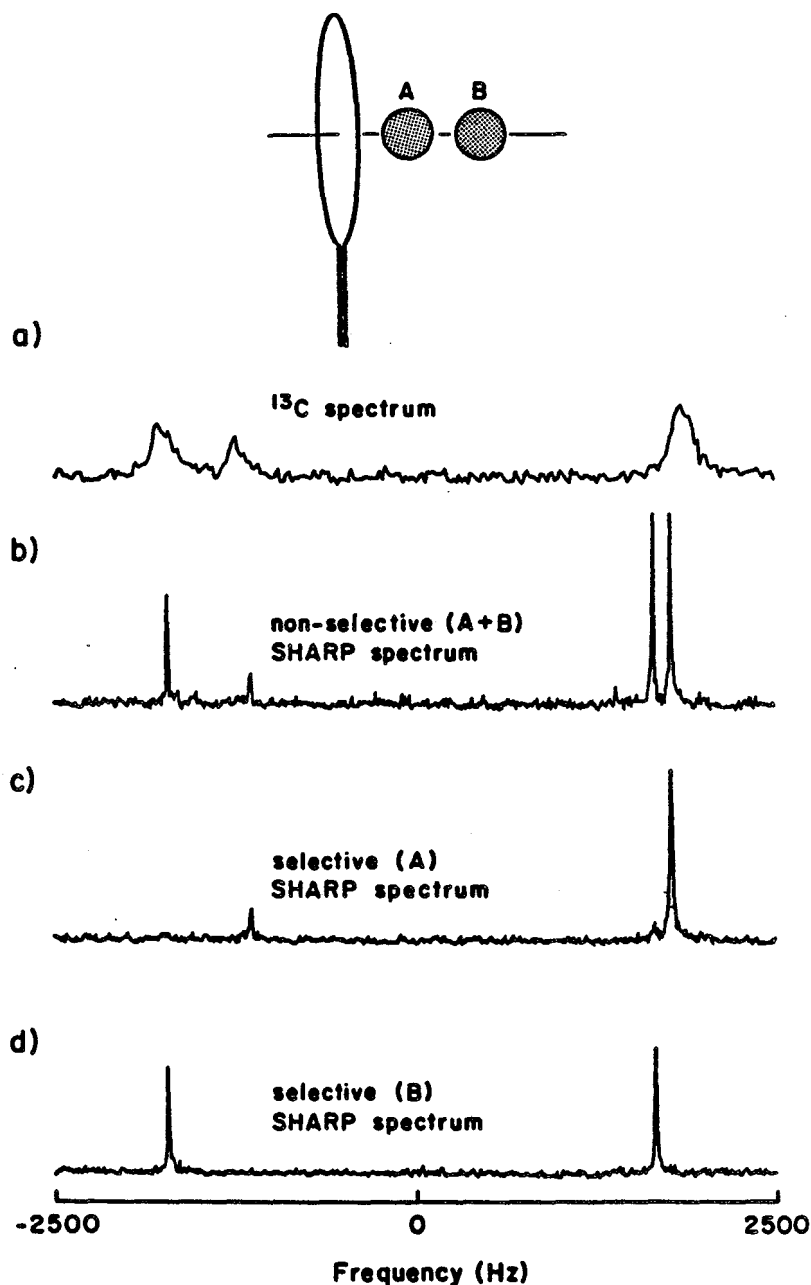
Figure 3.29

Surface coil selectivity experiment on two capillary tubes. The first coil contained $3\mu l$ of 50% $2 \text{-}^{13}C$ and 50% $3 \text{-}^{13}C$ enriched alanine, the second constained $2\mu l$ enriched ethanol (25% $1 \text{-}^{13}C$ and $2 \text{-}^{13}C$ on different molecules). (a) ^{13}C spectrum with 10ms proton presaturation and proton decoupling, (b) SHARP spectrum, pulse times intermediate between A and B. (c) SHARP spectrum, pulse times set for A, (d) SHARP spectrum, pulse times set for B.

<center>**CHAPTER 4**</center>

<center>

Two-Dimensional and Multiple Quantum NMR in Liquid Crystals -

Determination of Dipole Coupling Constants

Calculation of Molecular Structure

</center>

In this chapter, 2-D NMR and multiple quantum NMR are used for the determination of the dipole coupling constants of molecules dissolved in liquid crystals. Section 4.1 briefly introduces a technique we call CRASY, by which molecules are randomly deuterated and examined spectroscopically for the identification of all coupling constants. Section 4.2 gives a background into the usefulness and limitations of using liquid crystals in NMR. Sections 4.3 - 4.5 describe the tools necessary for approaching real examples by CRASY. The cases of benzene and hexane are often referenced as examples. Section 4.3 describes the theory of random isotopic labelling and isomer enumeration. Sections 4.4 and 4.5 detail the spectroscopic method and information content of 2, 3 and N spin single quantum and multiple quantum spectra. Section 4.6 gives an example of CRASY on benzene. Section 4.7 shows the method on n-hexane and goes on to describe an interpretation of the dipole coupling constants in terms of the conformation of the hexane chain in solution. Section 4.8 discusses the merits of the technique and its future application.

4.1 Introduction

The importance of ascertaining the values of the dipole coupling constants lies in their relation to molecular structure and

conformation[6,7]. The liquid crystalline phase provides an anisotropic environment in which (partially averaged) intramolecular dipolar and quadrupolar interactions can be measured, whilst intermolecular dipole couplings are eliminated. To date, many of the conformational studies on alkyl chains and flexible molecules have been restricted to analysis of the deuterium quadrupole spectra[7,113-121] or ^{13}C chemical shielding tensors[112-13], which describe local segmental order. On the other hand, the use of dipole coupling constants has been very limited. Inherently, dipole coupling constants describe both segmental and intersegmental order, providing a much more complete description of molecular conformation. The main reason for their limited use is the extreme complexity of dipolar spectra of molecules beyond a certain size and lack of symmetry - typically 8-10 protons in an acyclic system. The number of lines in the spectrum grows in an exponential way with the number of protons N. The number of dipole couplings grows quadratically with N. Spectra become not only rapidly intractable, but have many redundant transitions.

The key to solving a complex dipolar spectrum for its dipole coupling constants is to remove this redundancy. We do so with a technique we call CRASY, which stands for Correlated RAndom label SpectroscopY. It is a simple and direct process whereby all of the dipole coupling constants of a given molecule can be read off essentially from a single experiment. It is based on random labelling of a complex molecule to a level which reduces each individual molecule in the sample to a small spin system having just 2 or 3 protons. Such a spin system is analytically tractable, once it is

isolated. A spectroscopic method is developed to separate the constituents of the isotopic mixture.

4.1.2 CRASY: Correlated Random Label Spectroscopy

CRASY is described by figure 4.1. CRASY consists of two experimental steps:

1) Random Labelling

The first step is isotopic substitution, a common prodecure for simplifying a spectrum[124-5]. CRASY requires random labelling (deuteration), yielding a statistical mixture of partially protonated molecules. The level of deuteration is chosen high enough so that mainly 2 and 3 spin molecules abound. Such a mixture will give a complicated spectrum - so that the problem seems to have been compounded (see, for example, figures 2.3 and 2.4). But actually, a large network of multiply strongly coupled spins has been broken up into small sub-networks, and a representation of the whole molecule exists in components in the mixture. If the spectra of the individual components can be separated, they may be simply analysed. The method is synthetically less demanding than specific labelling. It also need only be done once.

Random deuteration has been used before in the analysis of the spectra of various cyclic compounds[125-8].

2) Spectroscopic Filtration

Step 2 is clearly to separate the spectrum of the mixture of different isotopomers into individual sub-spectra. Two-dimensional (2-D) MQT - filtered correlation spectroscopy[17,18,80,82] is used, whereby peaks arising from selected molecules in the mixture can be
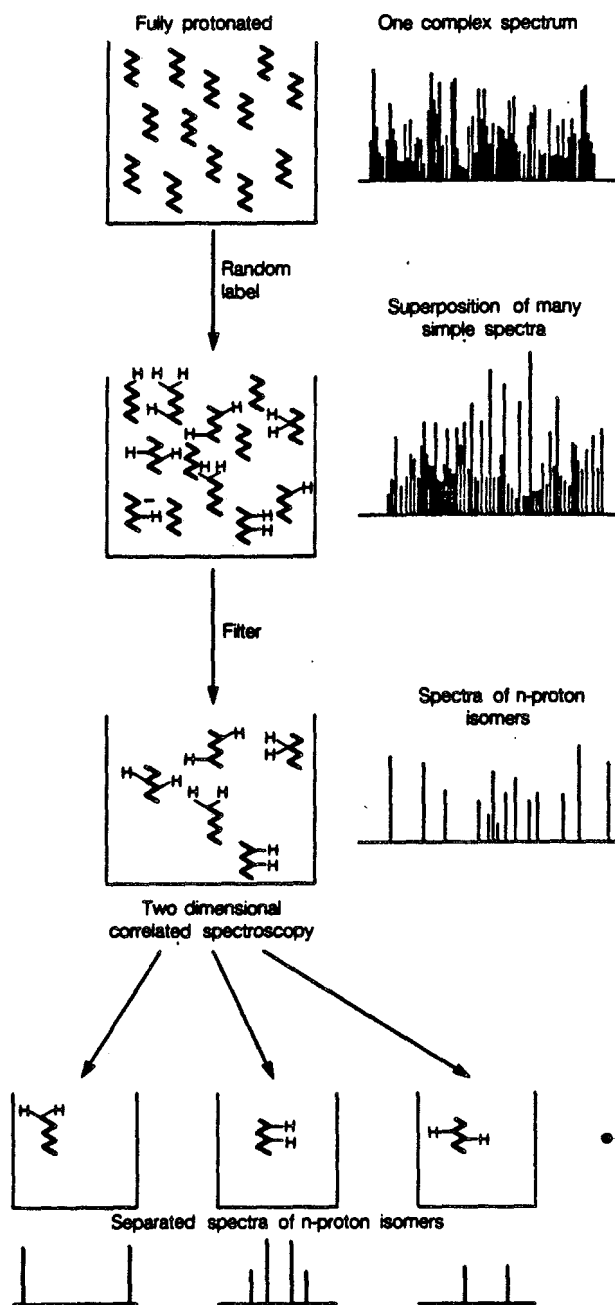
Figure 4.1

A schematic description of the CRASY experiment. A large

molecule gives a complex single quantum spectrum. Random labelling

produces a mixture of simpler molecules, still with a complicated

spectrum. MQT filtered COSY leads to spectroscopic separation of the

individual components of the mixture, each with a simple spectrum.

easily identified. In what follows, we chemically and spectroscopically select for pairs. Each subspectrum can thus be very easily interpreted.

The complexity of the problem has changed from one defined by the number of coupled spins to the number of sub-networks. The latter will be seen to be an easier problem to handle. By choosing pairs, we create the simplest possible situation. However information on the connectivity between pairs is lost. We will also show how 3-spin spectra or MQT NMR can provide the exact connectivity, unique down to the exchange of two identical vertices. Thus, the assignment of the dipole coupling constants is complete.

4.2 BACKGROUND

NMR of molecules dissolved in nematic liquid crystals was first demonstrated in 1953 using benzene dissolved in 4,4'-di-n-hexyloxyazoxybenzene[129]. A complex narrow line spectrum was obtained. This was the first demonstration of the free translational motion and restricted rotational motion of a solute molecule in a liquid crystal host. Many solutes have been studied[6,7,125-32], but only in a few cases of small rigid molecules or highly symmetric ones could dipolar information leading to structure determination be obtained. The problems are two-fold:

4.2.1 Spectral Complexity

Figure 4.2 shows the increase in complexity of dipolar spectra with molecular size. For an asymmetric molecule with N protons, the

(a) N = 4   1 kHz   CH₃CHO

(b) N = 6   C₆H₆

(c) N = 8

(d) N = 14   n—C₆H₁₄

(e) N = 16
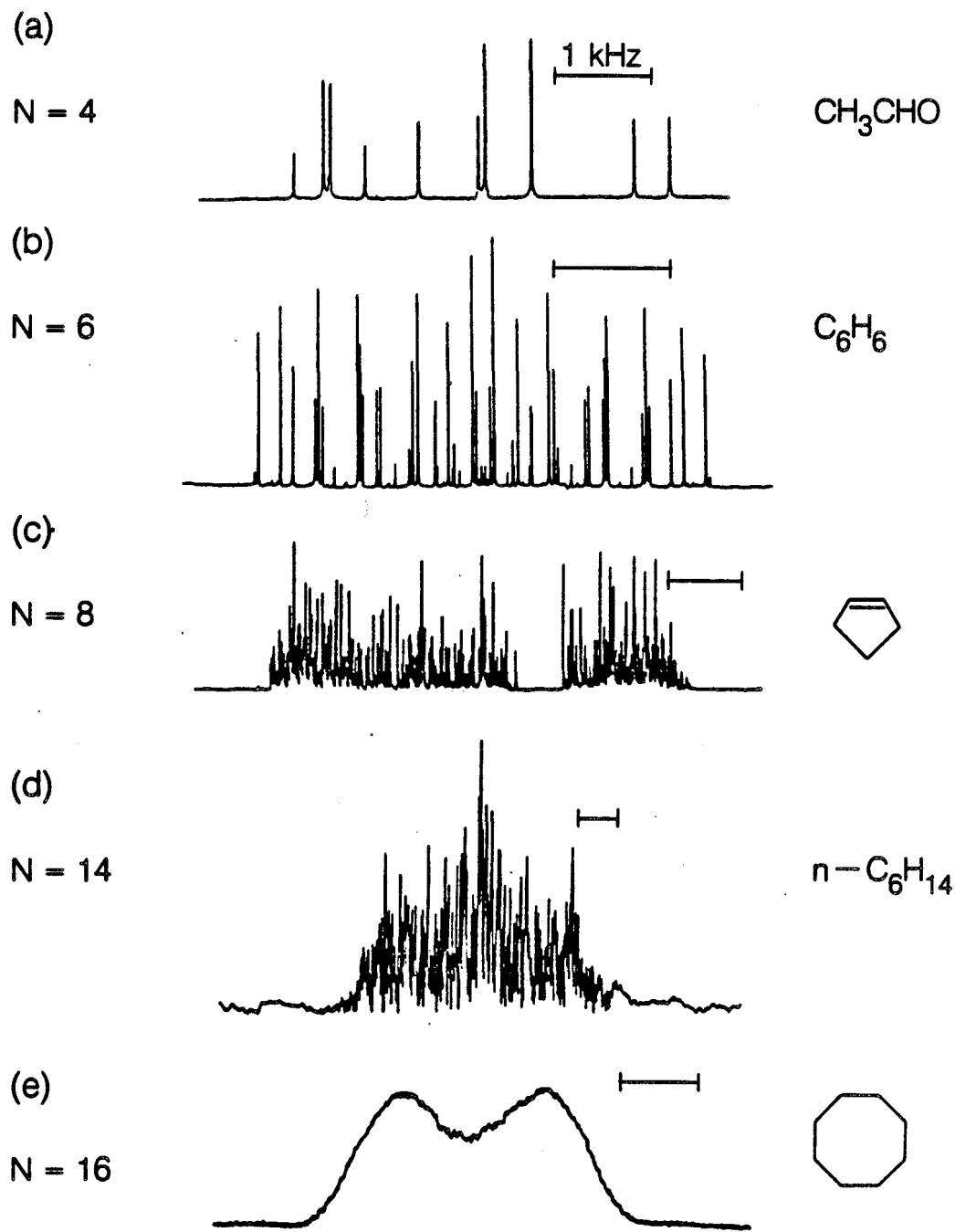
XBL 8612-12878

Figure 4.2

Proton NMR spectra of (a) acetaldehyde, (b) benzene, (c) cyclopentene, (d) n-hexane, (e) cyclo-octane, showing the increasing complexity with increasing proton number.

number of one quantum transitions is $^{2N}C_{N-1}$ [35]. This number increases exponentially with N as $\sim 4^N e^{-1/N} / \sqrt{N\pi}$ [58]. For example, for N = 8, there will be 11440 transitions, usually lying within a 15 KHz bandwidth. The result is an intractably complex spectrum, with many overlapping lines from which frequency information cannot be readily obtained. Symmetry will cause multiple degeneracies and a considerable reduction in the number of transitions. An 8-spin system with C_{2h} symmetry has 2860 expected transitions[133]. This is still a very large number; in general, for $N \geq 8$, symmetry is not enough to completely resolve the spectrum. In a flexible molecule, additional problems may arise when symmetry that may be defined for one rigid conformer no longer exists after conformational change, or when molecular motion broadens the resonances.

4.2.2 Interpretation Problem

Each NMR - measured dipole coupling constant is the projection of the desired internuclear dipole coupling constant onto the z axis of the laboratory frame. The relative orientation of the laboratory frame and the internuclear axis is unknown. In the case of a rigid molecule, each internuclear vector can be specifically related to an overall molecular frame. The unknown orientation parameters then form the order tensor matrix, which defines the average orientation of the solute with respect to the liquid crystal director (and the static field). Equation 1.32 can be written:

$$D_{ijzz} = \frac{2}{3} \sum_{\alpha,\beta} S_{\alpha\beta} D_{ij\alpha\beta} \qquad (4.1)$$

α,β are summed over the molecular axes 1,2,3. $D_{ij\alpha\beta}$ is the $\alpha\beta$ component in the molecular frame of the dipole coupling constant between nuclei i and j, and D_{ijzz} is the z-component in the direction of the field. $D_{ij\alpha\beta}$ is given by equation (1.30).

$S_{\alpha\beta}$ is the $\alpha\beta$ component of the order tensor in the molecular frame, and is given by equation (1.17). It is a time-average over molecular reorientation. The order parameter is a symmetric traceless tensor, with up to 5 independent elements. Molecular symmetry plays a role in determining the number of non-zero elements (Section 1.9), and therefore the number of dipole coupling constants needed for equation (4.1) to be soluble. Because of the form of the equation, it is only possible to solve for ratios of internuclear distances, and not for exact distances[7].

In a non-rigid molecule, the problem is compounded because the orientation of the internuclear vector with respect to the molecular frame is not rigidly defined. Equation (4.1) now becomes:

$$D_{ijzz} = \frac{2}{3} \sum_{\alpha,\beta} \langle S_{\alpha\beta} D_{ij\alpha\beta} \rangle \qquad (4.2)$$

where D_{ijzz} is now the result of both internal and orientational averaging. For a fixed number of conformational states, this equation may be written:

$$D_{ijzz} = \frac{2}{3} \sum_{n} P_n \sum_{\alpha,\beta} S_{\alpha\beta}^{n} D_{ij\alpha\beta}^{n} \qquad (4.3)$$

P_n is the probability of conformer n occurring, and a sum over all

conformers produces the required average.

From equation (4.3) it is no longer possible to find the molecular structure. The set $\{p_n\}$ and S must be defined and yet they cannot be separately determined, since they appear as a product $p_n \times S_{\alpha\beta}^n$ in equation (4.3). To solve for the average structure of a flexible molecule, approximations must be made or a molecular field theory invoked.

With these problems in mind, we turn our attention to a full description of CRASY as, at least, a partial solution for intermediate sized molecules.

4.3 RANDOM DEUTERATION, SYMMETRY AND ISOMER COUNTING

We define for convenience a few terms with respect to an arbitrary molecule containing carbon, hydrogen and deuterium.

Isomer: One or more molecules with the same formula ($C_nH_mD_x$), but differing in respect to the arrangement or configuration of the atoms.

Isotopomer: An isotopically substituted molecule, $C_nH_mD_x$, defined by m. A distribution of isotopomers results from statistical deuteration.

Stereo-position isomers: The set of all isomers including isomers related by a mirror plane (enantiomers).

NMR isomers: The set of all isomers excluding the distinction between enantiomers.

Position isomers: The set of all isomers in $C_nH_mD_x$ formed by distributing m protons over n sites with only one unique proton occupancy per site.

4.3.1 Random Deuteration

The effect of random deuteration on a molecule is to produce a statistical distribution of isotopomers as shown in figure 4.3. The probability of finding m protons and N-m deuterons is given by a binomial distribution:

$$p(m) - d^{N-m}(1-d)^m \begin{pmatrix} N \\ m \end{pmatrix} \qquad (4.4)$$

where d is the fraction of deuteration and N is the total number of protons and deuterons in the molecule. This distribution depends on N. Shown in figure 4.3 are curves for N=6 and N=14 for a 66% and 83% deuterated sample respectively. Examples will be given later with benzene and hexane. In CRASY, two proton systems are maximized by adjusting the deuteration level. It needs to be higher for higher N. The deuteration levels of 66% and 83% were chosen to illustrate high 2 proton intensities.

For each isotopomer, the number of isomers is defined by the symmetry of the molecule. Counting schemes[134] are necessary for evaluating the number of isomers, and hence the feasibility of using random deuteration as a simplifying step. It is also important to count the number of transitions in the one quantum spectrum of the parent molecule to estimate the advantage of using statistical deuteration over direct spectral analysis.

4.3.2 Isomer count

Balasubramanian has derived a method[134] for the determination
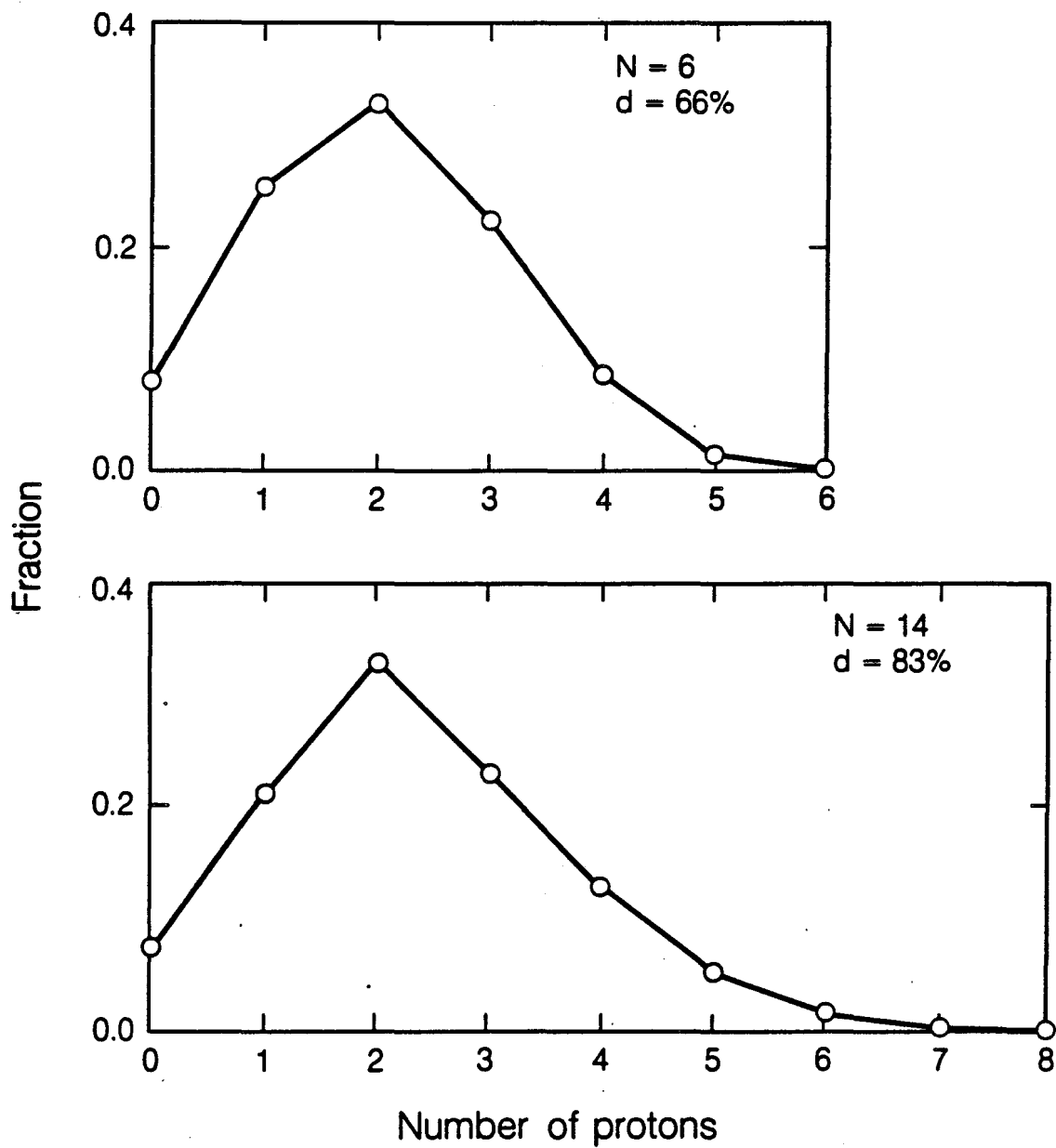
XBL 8612-12886

Figure 4.3

The fraction p(m) of m protons remaining in (a) a 6 proton

molecule, 66% deuterated, and (b) a 14 proton molecule, 83%

deuterated. The curves are calculated from equation (4.4) in the

text.

of the number of isomers of a compound $C_nH_mX_{N-m}$ for any m. He
describes the symmetry of the compound by its permutation group or
wreath product, and shows methods by which the cycle index of the
wreath product can be calculated. The cycle index taked the form of
an equation which has terms in $\alpha^m\beta^{N-m}$. The collected coefficients of
such a term give the number of isomers of $C_nH_mX_{N-m}$. Balasubramanian
identifies the different types of isomers listed above by different
wreath product symmetries assigned to the molecule for each case. For
example, in hexane:

$C_2[C_3,E_2,E_2]$ is the permutation group for all stereo-position isomers

$C_{2h}[C_3,E_2,E_2]$ is the permutation group for all NMR isomers.

$S_2[S_3,S_2,S_2]$ is the permutation group for all position isomers.

In benzene, the count of the number of isomers in $C_6H_mD_{6-m}$ is
straighforward. It is shown in Table 4.I. The table can be derived
using the cycle index method stated above. The combinatorial isomer
count shown has no bearing on the number of subspectra to be expected
for a given value of m, but is important in determining the intensity
of the subspectra (equation 4.4).

Table 4.I also gives the fraction of each isotopomer in 66%
deuterated benzene, the fraction of each unique m-proton isomer, and
the intensity expected for a single line in each case.

For the alkane chains, Balasubramanian has derived equations for
the cycle index of each of the three isomer types[135]. Computer
programs based on these equations have been written which can
calculate the number of stereo-position isomers, number of enantiomer
pairs and number of position isomers of an alkane $C_nH_mX_{2n+2-m}$, given n

TABLE 4.I

Statistical data for benzene $C_6H_mD_{6-m}$

m	0	1	2	3	4	5	6
Combinatorial Isomer Count	1	6	15	20	15	6	1
NMR Isomers	1	1	3	3	3	1	1
						66% deuteration	
p(m)	.083	.256	.329	.226	.087	.018	.002
p (unique isomer)	.083	.256	.110	.075	.029	.018	.002
I^1	—	.256	.055	.0083	9.10^{-4}	2.10^{-4}	3.10^{-5}

[1] Calculation of intensity per line uses:

2 lines / 2 ^{1}H isomer

9 lines / 3-^{1}H isomer

32 lines / 4-^{1}H isomer

108 lines / 5-^{1}H isomer

76 lines / 6-^{1}H isomer

(see Appendix C). The count for hexane is given in Table 4.II and illustrated in detail for $C_6H_2D_{12}$ in Table 4.III. There are 16 NMR-distinguishable ways that a pair of protons can be substituted on n-hexane, 38 ways that three protons can be placed and 86 ways that four protons can be placed. Table 4.II details the fraction of m-proton isotopomers and unique isomers for an 80% deuterated n-hexane sample, and gives the approximate intensity for a single transition in each case. The NMR spectrum of the isotopic mixture will consist of three subspectra of one proton substituted molecules in the highest intensity, 16 subspectra of two proton molecules at 10^{-1} of the intensity, 38 subspectra of three proton molecules at 10^{-2} of the intensity and 86 four proton subspectra at 10^{-3} of the intensity.

4.3.3 Line Count

Next, we evaluate the number of transitions in the NMR spectrum of the parent molecule. Traditionally, this is calculated from the point group of the molecule. The number of states in each representation can be counted, and hence the number of expected transitions of any order ΔM. The states of each representation are given for benzene in Table 4.IV[58]. There are 76 one quantum lines in the spectrum of benzene. Figure 4.2(b) shows this spectrum. Note from Table 4.I that the set of all 2 proton isomers will give a spectrum containing 6 lines, with the intensity of each line occurring at 4.2 of the intensity of a single line in 100% C_6H_6. This factor is not large, owing to the high symmetry of benzene. In the example of hexane shown below, it is much more significant.

n-hexane, as a flexible molecule, cannot be easily assigned to a

TABLE 4.II

Statistical data for hexane $C_6H_mD_{14-m}$

m	0	1	2	3	4	5	6	7
Combinatorial Isomer Count	1	14	91	364	1001	2002	3003	3432
Stereo-Position Isomer Count	1	5	26	70	156	251	345	372
NMR Isomer Count	1	3	16	38	86	133	185	196
Position Isomer Count	1	3	12	26	53	78	105	110

(80% deuteration)

	0	1	2	3	4	5	6	7
p(m)	.044	.154	.250	.250	.172	.086	.032	.009
p (unique isomer)	.044	.051	.016	.0066	.002	6.10^{-4}	2.10^{-4}	5.10^{-5}
I^1	—	.051	.004	5.10^{-4}	6.10^{-5}	$<10^{-6}$	$<10^{-6}$	$<10^{-6}$

[1] calculation of intensity approximate, using

4 lines / 2-^{1}H isomer

12 lines / 3-^{1}H isomer

32 lines / 4-^{1}H isomer

>100 lines / 5-^{1}H isomer

TABLE 4.III

Isomer enumeration in 2-^{1}H hexane

hexane-d_{12} (only ^{1}H indicated)	total count $^{14}C_2$	stereo-isomers optical pairs in brackets	NMR isomers	position isomers 1 for each structure
	6	1	1	1
	2	1	1	1
	2	1	1	1
	9	1	1	1
	12	2(1pr)	1	1
	12	2(1pr)	1	1
	12	2(1pr)	1	1
	12	2(1pr)	1	1
	8	4(2pr)	2	1
	8	4(2pr)	2	1
	4	3(1pr)	2	1
	4	3(1pr)	2	1
	91	26(10 pr)	16	12

TABLE 4.IV

Benzene energy levels

M	A 1	A 2	B 1	B 2	E *2 1	E *2 2
-3	1					
-2	1		1		1	1
-1	3		1	1	2	3
0	3	0	3	1	3	3
1	3		1	1	2	3
2	1		1		1	1
3	1					

↑

position isomers

point group. The conformational distortions can however be considered to occur symmetrically about the all trans conformer, resulting in average C_{2h} symmetry. With this interpretation, about 60000 transitions are expected in the 1 quantum spectrum. This calculation does not include degeneracies caused by free rotation of the methyl groups, but even so, the spectrum is intractably complex, as shown in figure 4.4.

A lower limit on the number of lines may be calculated by determining the number of A_1 transitions. In fact, the number of A_1 states in a manifold with m spins up and l spins down is equal to the number of inequivalent spins in the isomer $C_nH_mX_1$ [136]. This is exactly the number of position isomers, which have already been calculated. Table 4.V gives the A_1 states of n-hexane. From it, we calculate 28106 one quantum transitions. This is a minimum number, because transitions of other symmetries also occur.

We compare the number of transitions in the one quantum spectrum of hexane to the number of lines in the spectra of all two-proton isomers. There are at least 28000 one quantum transitions, and $\leq 4 \times 16 = 64$ lines! from two proton isomers, a vast reduction in complexity. The intensity of a single line from a two proton molecule in 80% deuterated hexane will be at least 115 times greater than a single line in 100% C_6H_{14}.

4.3.4 Note on random deuteration as a filter

Isotopomers having four or more protons will give spectra of such low relative intensity that they may be disregarded. For example, in 66% deuterated benzene and 80% deuterated hexane, a line from a 4

Frequency (kHz)
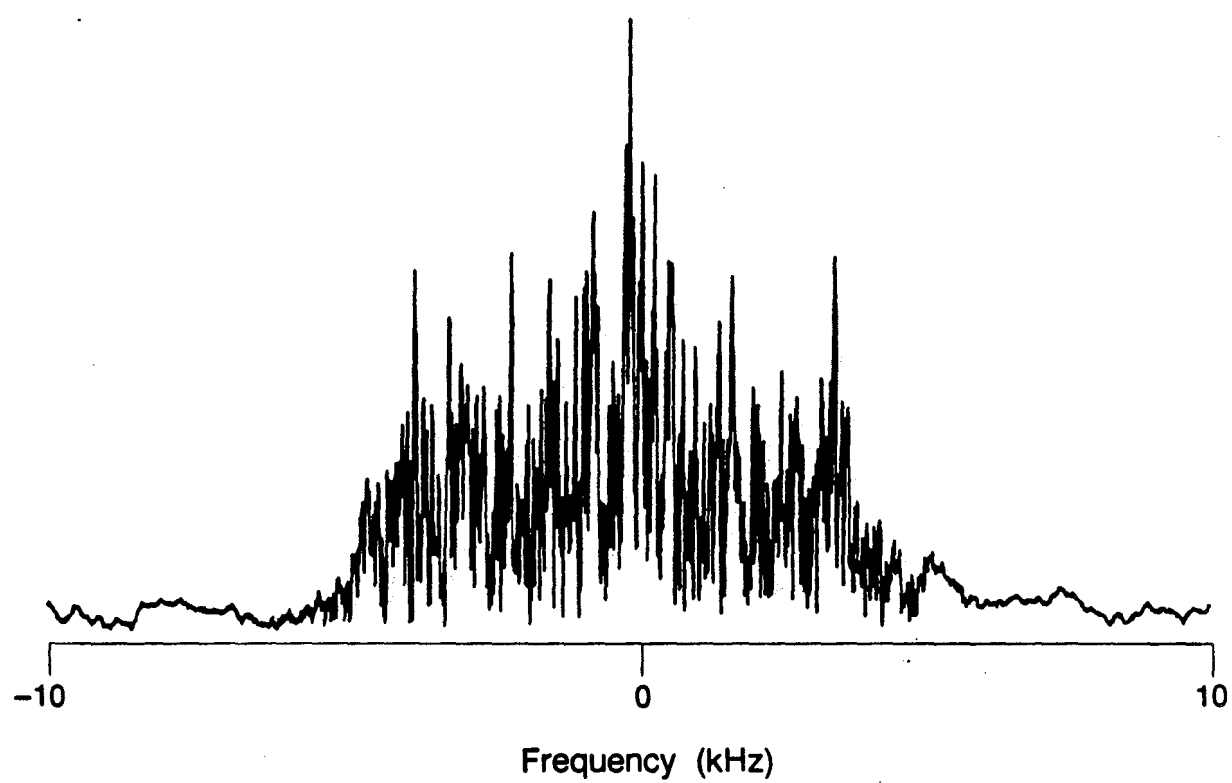
XBL 8610-11728

Figure 4.4

The one quantum spectrum of n-hexane in the liquid crystalline phase EK 11650; taken with the Hahn echo sequence $\pi/2$-$\tau/2$-π-$\tau/2$, τ = 2ms. 500 shots were recorded at a recycle time of 7.5s.

TABLE 4.V

Energy levels of hexane

M	A_1 States	Total States
-7	1	1
-6	3	3
-5	12	16
-4	26	38
-3	53	86
-2	78	133
-1	105	185
0	110	196
1	105	185
2	78	133
3	53	86
4	26	38
5	12	16
6	3	3
7	1	1

proton isotopomer will be less than 2% as intense as a line from a 2
proton isotopomer. This is an extremely important result of random
deuteration. A low pass filter for m has been generated
(spectroscopically very difficult to do) and the more complex spectra
of higher spin systems have been eliminated. At the same time, the
information available from higher spin systems is still present, since
the random nature of the deuteration implies that all dipole coupled
pairs are represented in the combined subspectra of 2 and 3 proton
isotopomers.

4.4 SEPARATION OF THE COMPONENTS OF THE MIXTURE

2-D correlated spectroscopy (COSY) is the obvious choice in
separating the components of an isomeric mixture[18,137]. Signals
arising from the same molecule are correlated in the two domains
because of the intramolecular coupling. Fine selection of only
certain components may be obtained by using a multiple quantum filter.
For example, figure 4.5 shows the distribution curve for a 75%
deuterated 10 spin molecule. Statistical probability effectively
removes all molecules having 4 or more protons. A two quantum filter
removes all molecules having less than 2 protons from contributing to
the final signal. It can be designed to eliminate signal from 3
proton molecules as well. Thus a 2-D double quantum filtered COSY is
a well-tuned narrow band filter which selects for and identifies all
AB coupled pairs in the statistical mixture[138].
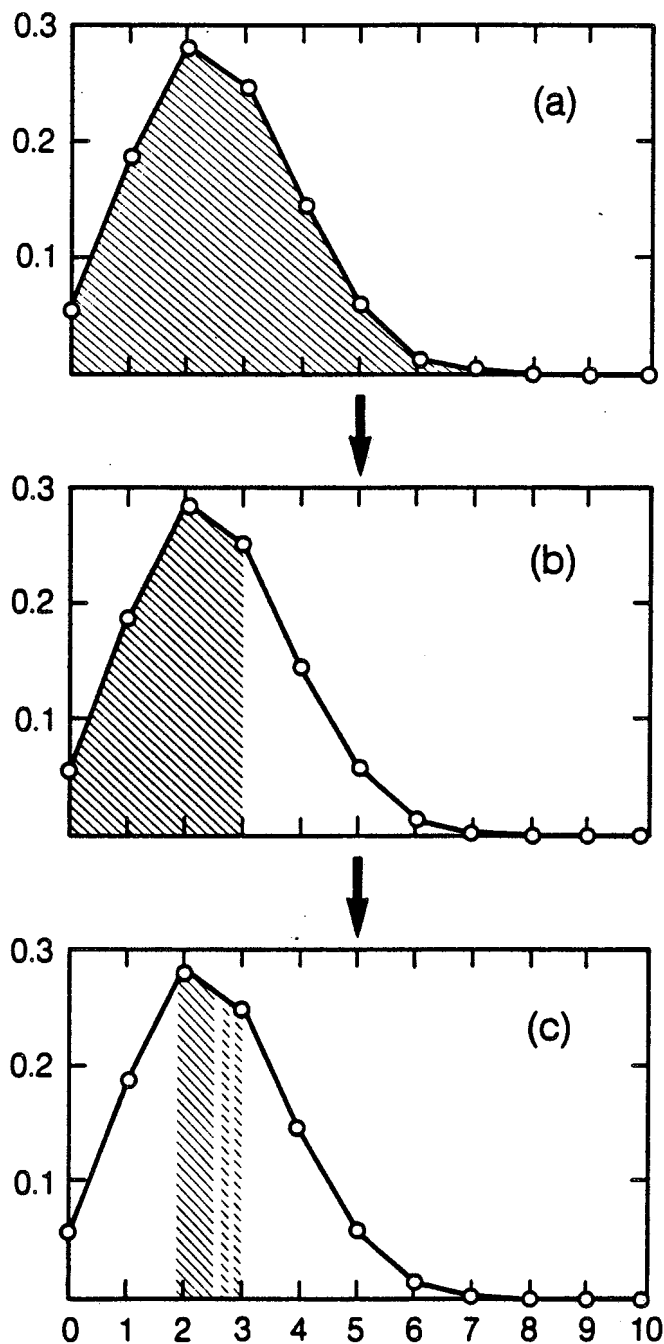
XBL 8612-12885

Figure 4.5

The statistics of isotopomer and isomer probabilities in a 75% deuterated 10 spin molecule. (a) shows the isotomer fractions p(m) as a function of m. (b) shows the statistical selection of isomers, based on intensity, which tends to zero at about m - 4. (c) shows the selection of a band around m - 2 (and/or 3) by two-quantum filtered spectroscopy.

4.4.1 AB Spectra

One dimensional AB spectra have been described in sections 1.4.1 and 1.5.1. In 2-D, the line splittings remain the same, with diagonal and cross peaks forming square patterns. The dipole coupling constants can be easily read off from the size of the square.

Figure 4.6 illustrates schematically the expected two dimensional COSY patterns for (a) A_2, (b) AB, (c) AB with an echo in t_1, and gives the frequencies and intensities. Figure 4.6 is drawn for strong coupling, i.e. $|D| \gg C$. These spectra are calculated from a two-quantum filtered COSY experiment[80,82] taken with the pulse sequence

$$\left(\frac{\pi}{2}\right)_y - t_1 - \left(\frac{\pi}{2}\right)_y - \frac{\tau_1}{2} - \pi - \frac{\tau_1}{2} - \left(\frac{\pi}{2}\right)_x - t_2 \qquad (4.A)$$

(or the equivalent with a π in the centre of t_1). The effect of the two quantum filter is produced by zeroing all but the two quantum coherence in the density matrix at $\tau_1 = 0$. Note that there is no resultant evolution of an AB system during the τ_1 period with a refocussing π pulse, so it may be ignored altogether in the calculation. During the experiment, however, the τ_1 period is very important for the selection of two-proton isomers only[82].

In the calculated spectra, lines appear antiphase with respect to J and D and in absorption mode. In the actual experiment, there is an additional delay τ_2 after the third pulse (see next section) to allow for decay of the solvent magnetization. The result is an additional phase modulation which leaves lines with phases depending on J and D. The spectra recorded were therefore in absolute value mode.

(a) $\bar{v} - 3D/4$, $\bar{v} + 3D/4$

(b) $\bar{v} - v_1$, $\bar{v} - v_2$, $\bar{v} + v_2$, $\bar{v} + v_1$

(c) $-\dfrac{J+D}{2}$, $\dfrac{J+D}{2}$, $\bar{v} - v_1$, $\bar{v} - v_2$, $\bar{v} + v_2$, $\bar{v} + v_1$, $-v_1$, $-v_2$, v_2, v_1

XBL 8612-12875
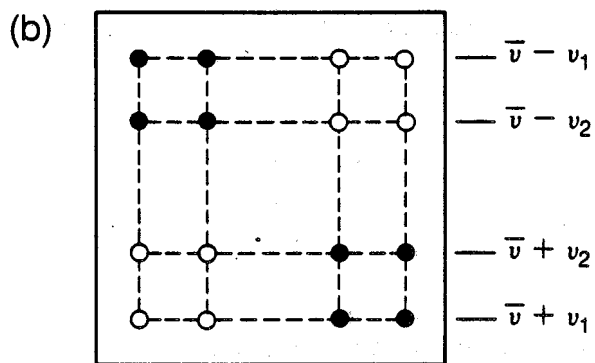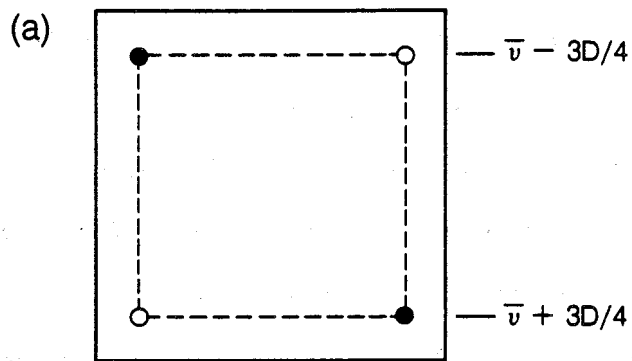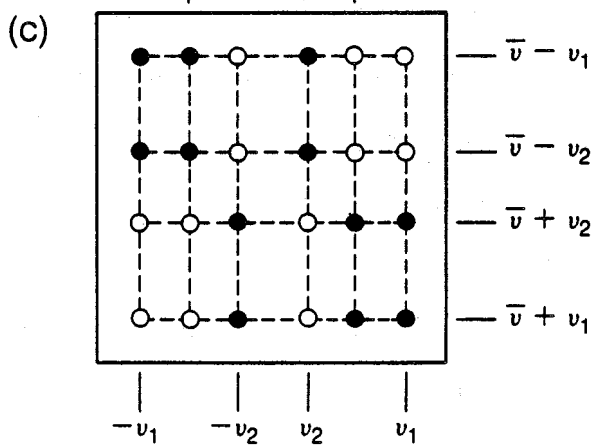
Figure 4.6

Schematic A$_2$ and AB two dimensional spectra calculated for various pulse sequences (see text). (a) and (b) are two-quantum filtered COSY-type spectra of an A$_2$ and an AB spectrum, calculated from pulse sequence (4.A). Open circles are negative and closed circles positive intensity. In (a) all lines have equal intensity. In (b), the intensities of the 4 peaks in one quadrant are (working clockwise from the corner): $(1-\sin 2\theta)^2$, $(1-\sin^2 2\theta)$, $(1+\sin 2\theta)^2$, $(1-\sin^2 2\theta)$ (c) is a two-quantum filtered refocussed COSY AB spectrum (sequence (4.A) with a π in t$_1$). Intensities in one quadrant are given by (working clockwise from the corner): $(1-\sin 2\theta)^2 \sin 2\theta$, $2\cos^2 2\theta (1-\sin 2\theta)$, $(1-\sin^2 2\theta)\sin 2\theta$, $(1+\sin 2\theta)^2 \sin 2\theta$, $2\cos^2 2\theta (1+\sin 2\theta)$, $(1-\sin^2 2\theta)\sin 2\theta$.

For figures 4.6 and 4.7, $\bar{\nu} = (\nu_A + \nu_B)/2$; $\nu_1 = (J+D)/2 + C/2$, $\nu_2 = (J+D)/2 - C/2$, $C = (\Delta\nu^2 + (J-D/2)^2)^{1/2}$, $\tan 2\theta = (J-D/2)/\Delta\nu$.
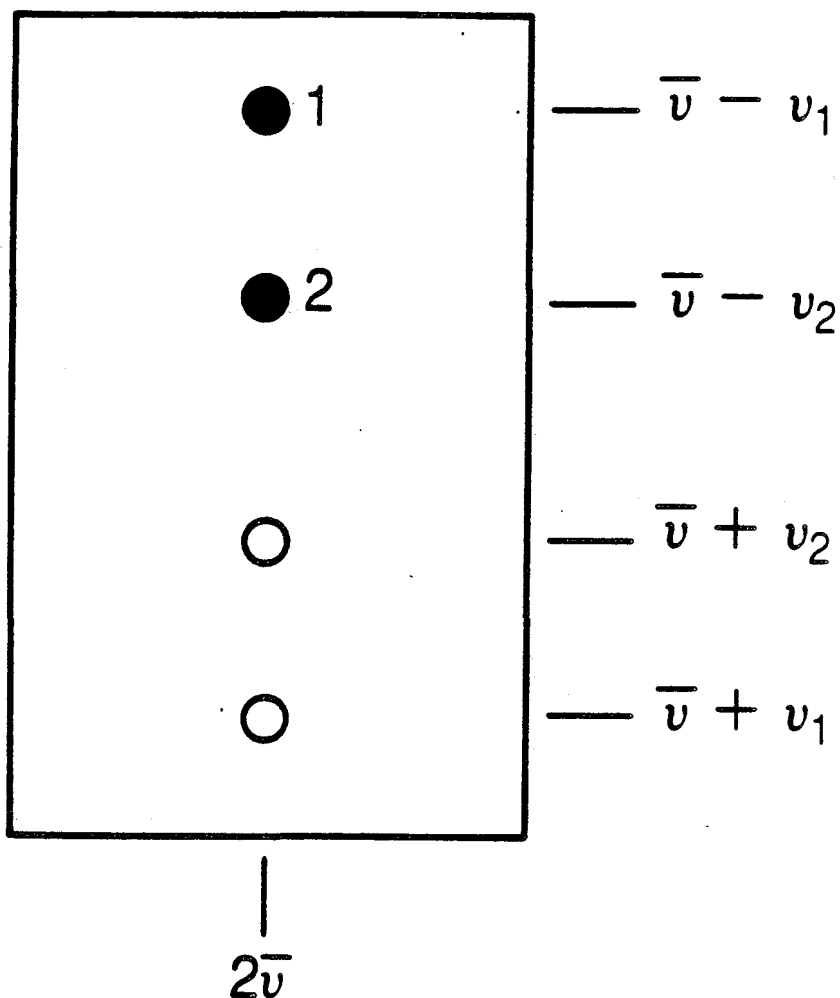
XBL 8612-12884

Figure 4.7

A two-quantum vs. 1 quantum correlation spectrum calculated from pulse sequence (4.B). The line intensities are given by (1) $(1-\sin2\theta)K$, (2) $(1+\sin2\theta)K$, where K is a phase factor depending on J and D.

Another two dimensional method used for the evaluation of the dipole coupling constants was the INADEQUATE experiment[39,139-40]. Along the two quantum axis, signals appear at the sum of chemical shifts, $\nu_A+\nu_B$. Along the one quantum axis, the normal AB spectrum is obtained. The schematic form of such a spectrum is shown in figure 4.7, together with the frequencies and intensities. It is calculated for the pulse sequence

$$\left(\frac{\pi}{2}\right)_y - \tau - \left(\frac{\pi}{2}\right)_y - t_1 - \left(\frac{\pi}{2}\right)_x - t_2 \qquad (4.B)$$

with the two quantum preparation presumed to operate with no chemical shift (in the experiment a refocussing π is used during τ), and with only double quantum signals followed through t_1. Note that this spectrum is not generally phaseable, with the phase of individual AB patterns depending on a complex combination of D and J. To obtain absorption mode spectra, a time - reversal sequence could be used for two quantum excitation[37].

4.5 ASSIGNMENT OF THE COUPLING CONSTANTS

The line-splitting of each AB pattern gives the dipole coupling constant between protons A and B. The chemical shift of each AB pattern, $\bar{\nu}_{AB}$, can be used to identify the position of protons A and B in the molecule, in the case where the protons have distinct chemical shifts. All possible AB pairs exist with equal likelihood in the mixture. Thus, all dipole coupling constants (and possibly site assignments) can be obtained by reading the 2D correlated spectrum.

The result of such an analysis is a set of magnitudes of all the dipole coupling constants and perhaps assignments to carbon atoms, if the chemical shifts permit distinction. Specific assignments to exact protons and sign assignment is not possible from AB spectra. The tensor nature of the dipole coupling does not permit a plausible assignment based on relative magnitudes, as is the case with scalar coupling. The information is a prerequisite for structural analysis.

4.5.1   2,3 and N-spin spectra

4.5.1.1   The missing information in 2-spin systems

Figure 4.8 illustrates the missing information in an hypothetical two-dimensional molecule with four protons. Figure 4.8(a) depicts the six measured D_{ijzz}. Figure 4.8(b) shows their indirect relationship to D_{ij} and internuclear distance:

$$D_{ijzz} = D_{ij} \cdot R \qquad\qquad (4.5)$$

A curve of R vs. θ is shown and an internuclear vector D_{ij} drawn from origin C to the curve R in two possible orientations and lengths. In both cases, the same absolute value of $|D_{ijzz}|$ is obtained, but their sign is different. This shows how sign is important in restricting the possible orientation of D_{ij}. Note, however, that the same projection $|D_{ijzz}|$ could be obtained by changing the length of D_{ij} almost arbitrarily and adjusting the angle(s) θ accordingly to get the right projection along z. Measurement of D_{ijzz} sets constraints on the minimum size of D_{ij} and the upper limit is defined by the minimum internuclear distance (here chosen as 1 Å):

(a) 6 Dijzz

(b) Unknown orientation

H_o

Dijzz

R

Dij

−

C

0

Dij

+

1/2

0　　　　　　　90°

θ

(c) Coupling networks

A　2　B
5
4
1　　　　C
6
3
D

A　4　B
2　1
C
6　5　3
D

A　4　B
5
2
1
6　C
3
D

Dij

i　　?

j
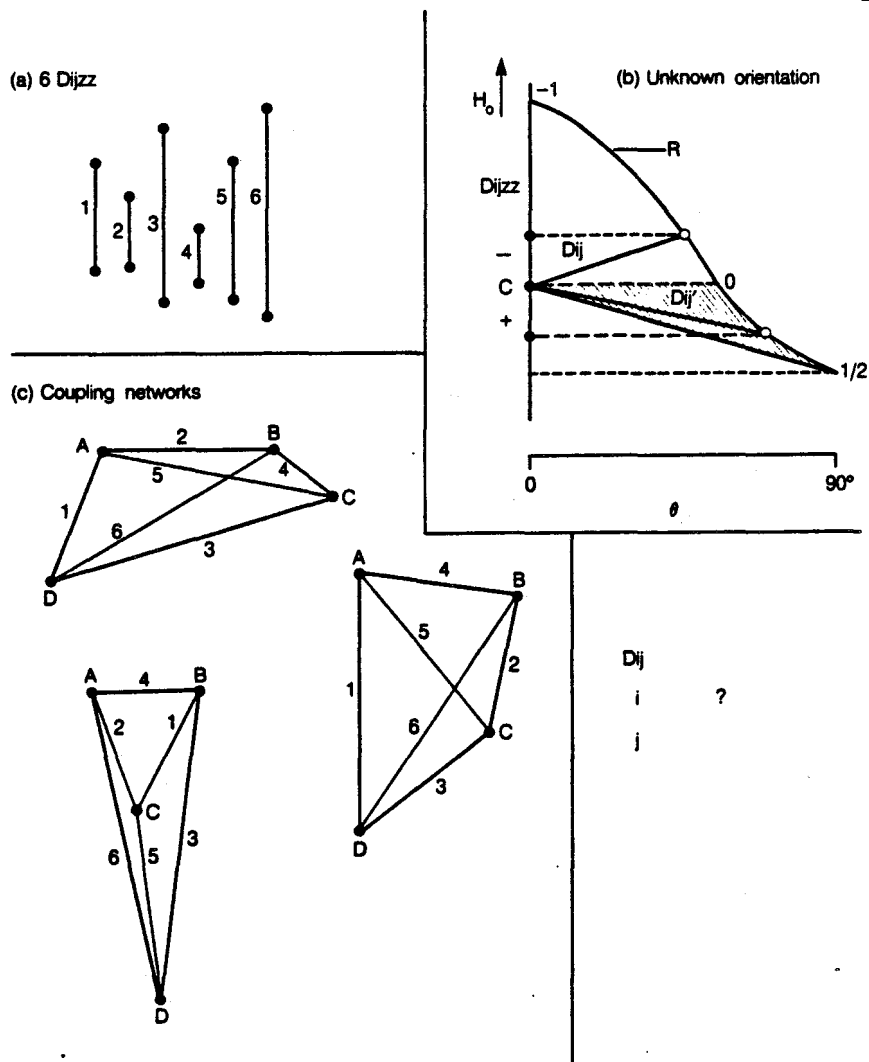
Figure 4.8

XBL 8612-12877

Measurement of the dipole coupling constants in an hypothetical 4-spin two dimensional molecule. (a) The 6 experimental D_{ijzz}. (b) Graph of R = $(1-3\cos^2\theta)/2$ as a function of θ, the angle between the internuclear vector and the z-axis. Internuclear vectors drawn from C to different locations on R illustrate two orientations and lengths which give positive and negative D_{ijzz} of the same magnitude. The shaded area corresponds to all orientations for which D_{ijzz} is negative. (c) 3 out of many possible coupling networks which could describe the molecule. The only restriction on the networks is that the sides of the triangles must be at least as long as the corresponding measured D_{ijzz}. The upper limit on the length is defined by the minimum internuclear distance (see text).

$$D_{ijzz} \text{ +ve :} \quad 2D_{ijzz} \leq D_{ij} \leq 120 \text{ KHz}$$

$$D_{ijzz} \text{ -ve :} \quad D_{ijzz} \leq D_{ij} \leq 120 \text{ KHz,} \qquad (4.6)$$

Figure 4.8(c) shows some examples of possible combinations of the 6 D_{ij} connecting the four vertices with each other. Three networks are shown, but there are an almost limitless number of possibilities, because the sides of the triangles can be "stretched" almost indefinitely to fit different patterns. The study of AB systems gives no indication of how the coupling constants must be joined together.

4.5.1.2 <u>3 Spin Systems</u>

Some of the missing information can be obtained from studying the one quantum spectra of three spin systems[128]. Each 3 spin system defines one of the triangles in our coupling network. The frequencies are determined by linear combinations of dipole coupling constants; for example in the weakly coupled limit AMX by

$$- \nu_A \pm (D_{AM} \pm D_{AX})/2; \; - \nu_M \pm (D_{AM} \pm D_{MX})/2; \; - \nu_X \pm (D_{MX} \pm D_{AX})/2$$

$$\text{------ (4.7)}$$

This is a spectrum of 3 doublets of doublets. Suppose diagram I in figure 4.8(c) was correct. A three spin system would then exist with frequencies corresponding to triangle ABC at

$$- \nu_A \pm (D_2 \pm D_5)/2: \; - \nu_B \pm (D_2 \pm D_4)/2; \; - \nu_C \pm (D_4 \pm D_5)/2$$

However, a spectrum with frequencies at

$$- \nu_A \pm (D_1 \pm D_2)/2; \; - \nu_B \pm (D_2 \pm D_4)/2; \; - \nu_C \pm (D_4 \pm D_1)/2$$

will never occur because the coupling constants D_1, D_2 and D_4 span four vertices and do not form a closed triangle. The absence of such a spectrum among the three spin systems would immediately discount

solution 4.8(c)-III, for example. In a strongly coupled system, the same principle holds, independent of the existence of chemical shifts, although the frequencies are not a simple linear combination of coupling constants. The solution is unique up to exchange of two identical vertices, under which the Hamiltonian is invariant. By identical vertices is meant the same chemical shift and the same set of couplings emanating from each vertex. The solution is also sign specific; one incorrect sign will affect many of the calculated frequencies of the three spin spectrum. However, it is insensitive to an inversion of all signs.

The final step is not complete until the network is moved onto the molecule and the vertices assigned to atoms. This is not a trivial problem, but in a real molecule is usually possible by making one or two reasonable assignments. For example, if we know the assignment of couplings 2 and 4 in figure 4.8(c)-I, then vertices A,B,C and hence D are automatically specified. Knowing only coupling 2, however, will not allow us to unambiguously define which atom is C and which is D. An example of the use of 3-spin systems in assignment will be given for benzene in Section 4.6.

4.5.1.3 N Spin Systems

We extend the concept in Section 4.5.1.2 to the general case of the (N-2) quantum spectrum of an N-spin molecule. The N-quantum spectrum contains only chemical shift, $\Sigma \nu_i$. The (N-1)-quantum spectrum has N pairs of lines, since there are N ways of selecting (N-1) protons out of N, and the local field of the Nth atom causes a doublet[136]. Similarly, with the (N-2)-quantum spectrum, the

resonance frequencies of (N-2) coherent protons are defined by the local field of the remaining two. In the weak coupling limit (if it existed), the spectrum would consist of N(N-1)/2 quartets, each given by

$$- \sum_{\substack{i \\ \neq k,l}}^{N} \nu_i \pm \frac{1}{2} \sum_{\substack{i \\ \neq k,l}}^{N} D_{ki} \pm \frac{1}{2} \sum_{\substack{i \\ \neq k,l}}^{N} D_{li} \qquad (4.8)$$

k,l, the protons not in the coherent set, can be chosen in N(N-1)/2 ways, hence generating the whole spectrum. It is exemplified by the one quantum spectrum of the weakly coupled 3 spin system AMX in equation (4.7), which consists of 3 quartets. In the strongly coupled spectrum, the same principle applies, with a more complex combination of the dipole coupling constants. N(N-1)/2 quartets can be expected in general. In hexane, the C_{2h} symmetry reduces many quartets to triplets, because many pairs of protons are related by a symmetry operation[136]. In addition, there will be a highly degenerate transition at the centre of the (N-2) quantum spectrum, resulting from a flip of all spins between the manifolds M = N/2-1 and M = -N/2+1. This transition is forbidden in the directly detected one quantum spectrum of a 3 spin system.

The same sign and connectivity information is available from the (N-2) quantum spectrum as from the study of 3 spin systems. The two are in fact equivalent. When N > 3, the frequency of each line depends on a combination of more than two coupling constants, in fact of 2(N-2) of the N(N-1)/2 coupling constants. The multiple quantum

spectrum is extremely sensitive as a whole to a change in just one coupling constant. Only selected 3-spin spectra will be sensitive to a change in one dipole coupling constant. For hexane, it easier to study one well-resolved multiple quantum spectrum than to study the 38 three-spin subspectra of randomly deuterated n-hexane.

4.6 BENZENE

The techniques of sections 4.3 - 4.5 were initially applied to benzene as a test molecule[138].

4.6.1 Experimental

Randomly deuterated benzene was prepared by room temperature exchange of benzene with 85% sulphuric acid in D_2O. A 33% deuterated sample was selected from the reaction of C_6H_6 with D_2SO_4. An 80% deuterated sample was made from C_6D_6 with H_2SO_4. The reaction time was approximately 40 hours. Figure 4.9 shows the mass spectral analysis of each sample, together with the calculated curves for random deuteration.

All samples for NMR were prepared by dissolving approximately 15 mole percent of the appropriate deuterated benzene in the nematic liquid crystal EK 11650 (p-pentylphenyl-2-chloro-4-(p-pentylbenzoyloxy)-benzoate). They were sealed in 5 mm NMR tubes. The experiments were performed on a home-built spectrometer operating at 360 MHz for protons and interfaced to a VAX 11/730 by a parallel MDB-DCHIB/DR11W data channel interface. The interface is described in detail in Chapter 5. Two-dimensional data sets up to 4096 × 1024 in size were recorded directly on the VAX for processing.
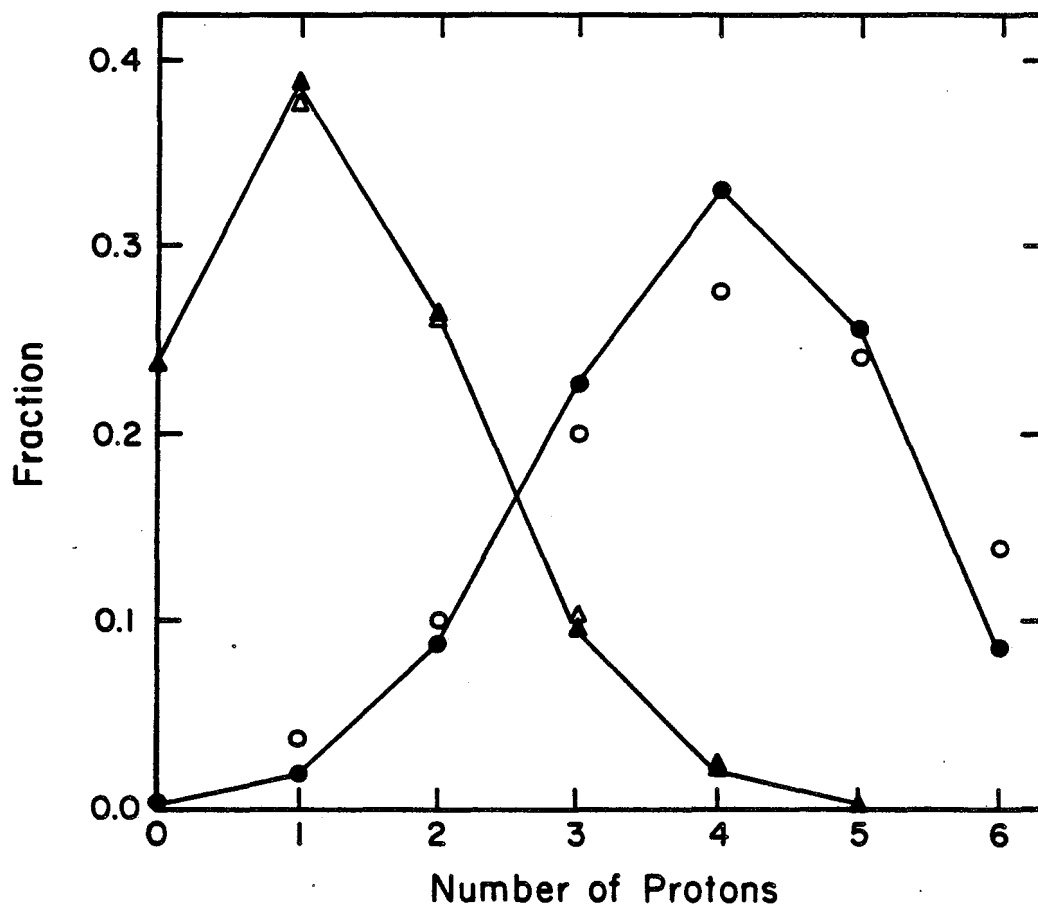
XBL 866-2357

Figure 4.9

Mass spectral data from 34% (o) and 79% (Δ) randomly deuterated benzene. Open symbols are the measured relative intensities at masses 84 (0 protons) through 78 (6 protons). Solid symbols show the calculated statistical distribution.

4.6.2 The Dipole Coupling Constants

Figure 4.10 shows the spectrum of 78.7% randomly deuterated benzene. The spectrum was taken with a two quantum filter using the pulse sequence:

$$\left(\frac{\pi}{2}\right)_\phi - \frac{t_1}{2} - \pi_\phi - \frac{t_1}{2} - \left(\frac{\pi}{2}\right)_\phi - \frac{\tau_1}{2} - \pi_x - \frac{\tau_1}{2} - \left(\frac{\pi}{2}\right)_x - \frac{\tau_2}{2} - \pi_x - \frac{\tau_2}{2} - t_2 \quad (4.C)$$

Phae ϕ was incremented by 90^0 and the receiver phase varied between 0 and 180 ^{0}. The Hahn echo during τ_2 was included to eliminate any contribution of the liquid crystal solvent to the spectrum. Figure 4.10 is a superposition of isotopomers having 2 - 3 protons. The spectra of the diprotonated species provide the dipole coupling constants directly. They are easily recognized by their intensity and because they each consist of only a pair of lines.

Peaks arising from the same molecule were correlated on a 2-D COSY-type map, using sequence 4.C. The result is shown in figure 4.11 together with projections of the 2 and 3 spin spectra that can be singled out. The three $|D_{ij}|$ values were read off from the line splitting in the spectra of diprotonated species as 1529, 307 and 193 Hz.

4.6.3 Assignment of the Coupling Constants

The dipole coupling constants obtained from the diprotonated species were assigned by simulation of the spectra of the triprotonated species. Only three coupling constants which close on

Frequency (kHz)
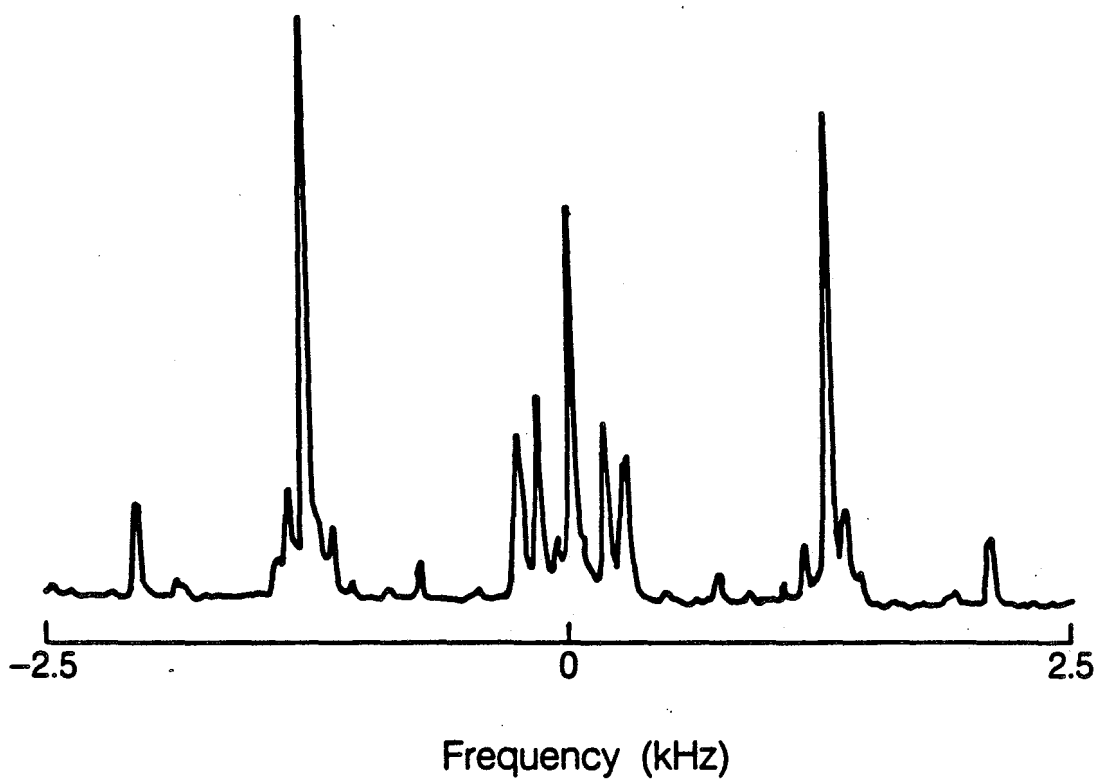
XBL 872-9567

Figure 4.10

The 1 quantum spectrum of 79% randomly deuterated benzene in the liquid crystal phase EK 11650, taken with a Hahn echo sequence.

500Hz
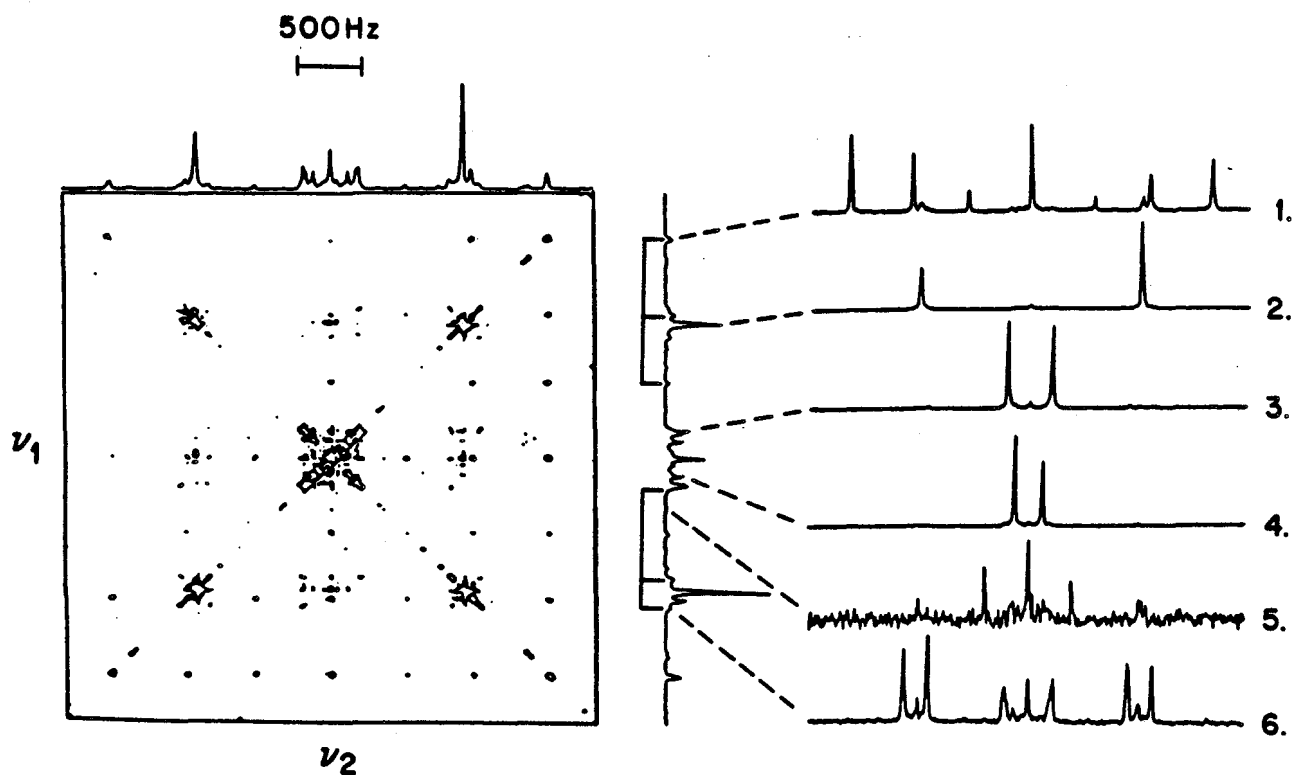
XBL 866-2355

Figure 4.11

Two-quantum filtered correlation spectrum of 79% randomly deuterated benzene dissolved at 20 mole% in EK 11650. 1024 t_1 × 1024 t_2 points were recorded with deuterium decoupling and spectral widths of 10 KHz in ω_1 and ω_2, using sequence (4.C). 12 FID's were collected for each t_1 point, with a recycle delay of 5 seconds. The quadrant shown has been symmetrized along the diagonals. The slices indicate the 6 species present: 3 diprotonated and 3 triprotonated species.

the molecule to form a triangle will give an observed 3 spin spectrum, as discussed in section 4.5.1.2. Since cross-checks are possible, only the correct assignment will accurately simulate all possible 3 spin spectra. The relative signs of the dipole coupling constants were obtained by this method.

Figure 4.12 illustrates the assignment process for benzene. In Table 4.VI the dipole coupling constants used for the various simulations in figure 4.12 are given. 4.12(a) shows the assignment of the meta coupling constant. With this assignment, all possible alternatives of the remaining 2 coupling constants were tried in 4.12(b), with only one successful fit (not counting the absolute sign). This assignment was verified in spectrum 4.12(c).

Thus, we obtain $D_{ortho} = +/- 1529$; $D_{meta} = +/- 307$; $D_{para} = +/- 193$; with all 3 coupling constants having the same sign. Given the geometry of benzene, θ_{ij} in equation (1.30) is 90°. Thus, $D_{ij33} = K / r_{ij}^{3} > 0$, where K is defined in equation 4.5. The single non-zero order parameter in six-fold symmetric benzene reduces equation (4.1) to:

$$D_{ijzz} = \frac{2}{3} S_{33} D_{ij33} \tag{4.9}$$

The axial alignment of benzene in a nematic implies that the C_6 axis (axis 3) will be approximately perpendicular to the director $\hat{d}$ and the field. Hence, $S_{33} < 0$ and $D_{ijzz} < 0$. The appropriate angles are marked in figure 4.13. We finally have $D_{ortho} = -1529$, $D_{meta} = -307$, $D_{para} = -193$ Hz. This result can also be obtained by noting that the J_{ij} are determined to be positive from studies in isotropic solution[141], and they are known to be opposite in sign to the D_{ij}.
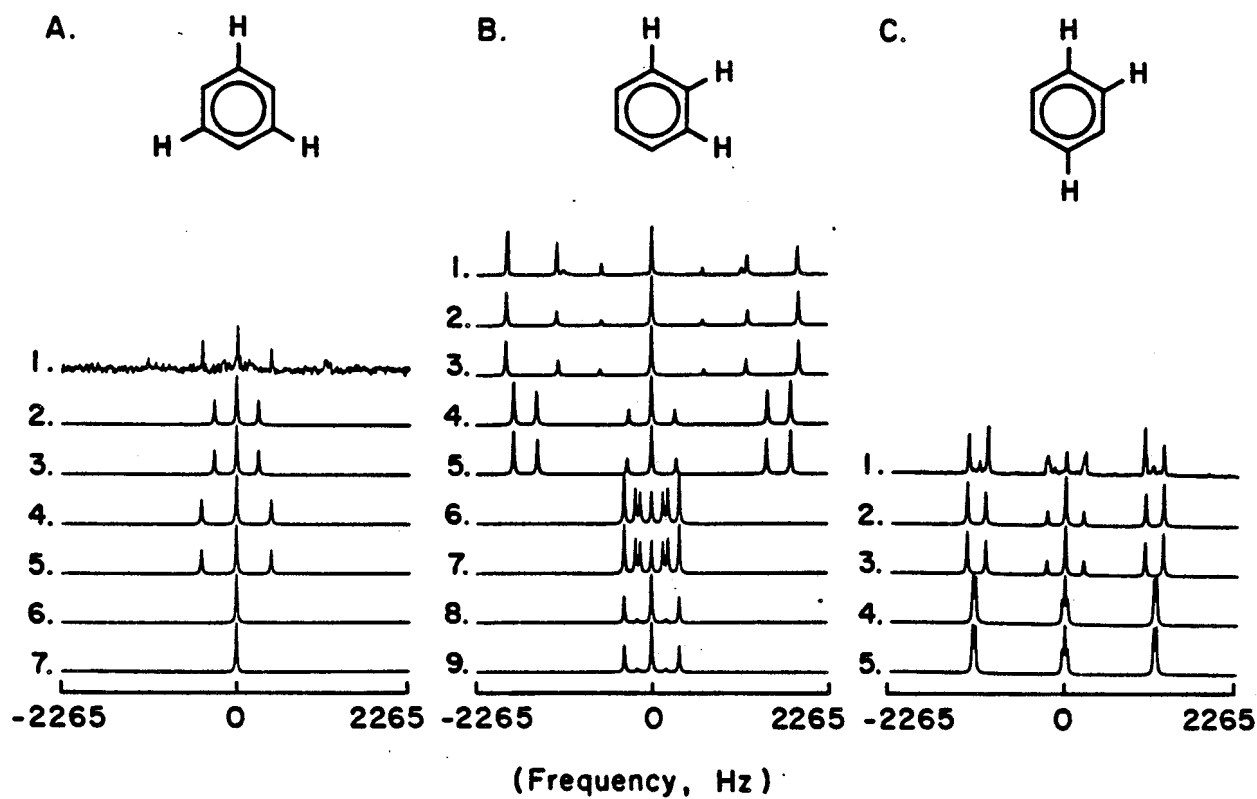
Figure 4.12

Simulations of spectra of triprotonated species. The dipole coupling constants used for the various simulations are listed in Table 4.VI.

XBL 866-2354

TABLE 4.VI

Dipole coupling constants used for the simulations of Figure 4.12

$\underline{A}$			$\underline{B}$			$\underline{C}$		
1,3,5-d_3 -benzene			1,2,3-d_3 -benzene			1,2,4-d_3 -benzene		

1. experimental			1. experimental			1. experimental		
	D_m			D_o	D_m		D_o	D_m	D_p
2.	-193		2.	-1529	-307	2.	-1529	-307	-193
3.	+193		3.	+1529	+307	3.	+1529	+307	+193
4.	-307		4.	-1529	+307	4.	-1529	-307	+193
5.	+307		5.	+1529	-307	5.	+1529	+307	-193
6.	-1529		6.	+193	-307			
7.	+1529		7.	-193	+307			
			8.	-193	-307			
			9.	+193	+307			
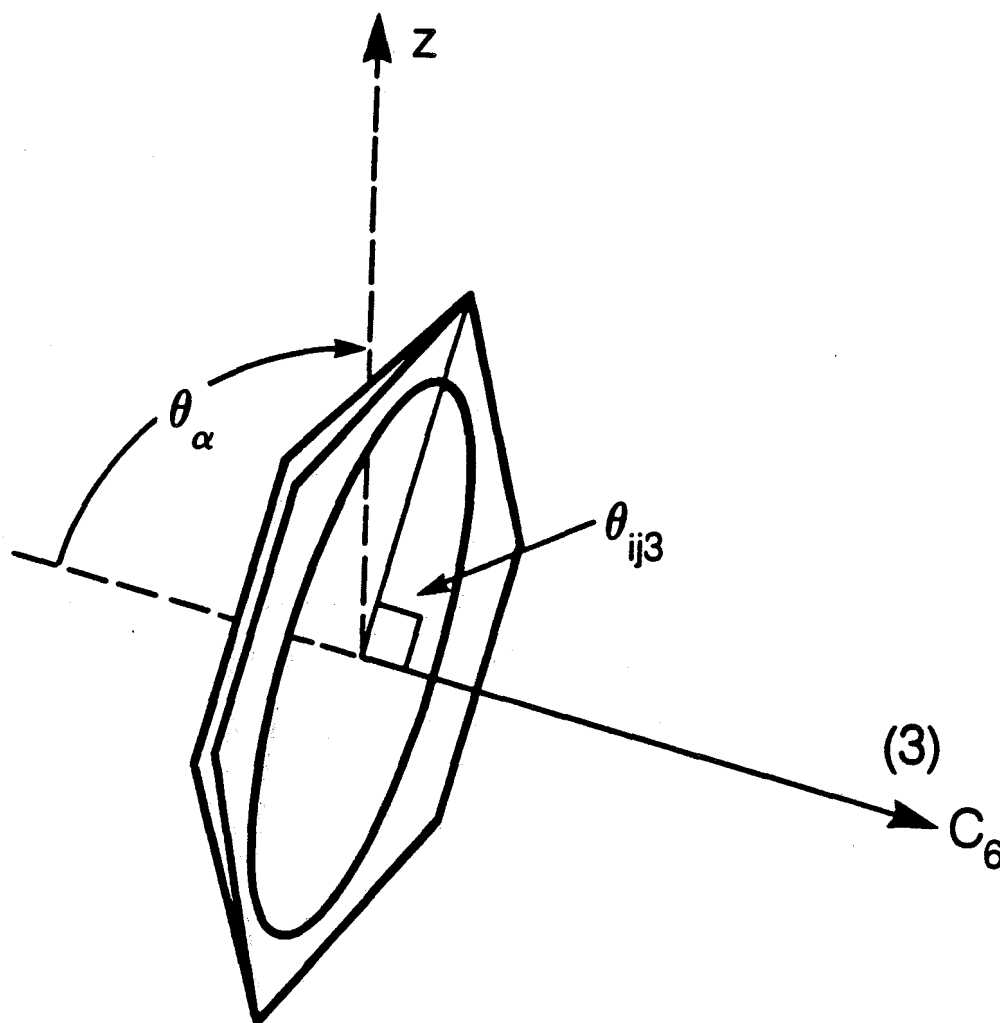
XBL 871-8909

Figure 4.13

The axis system of oriented benzene showing the angles used in the text.

4.6.3.2 Multiple Quantum NMR

In section 4.5.1.3, it was shown how correct simulation of the (N-1) and (N-2) quantum spectra is an alternative method of obtaining an unambiguous assignment.

Figure 4.14(a) shows an experimental 5 quantum vs. 1 quantum correlation spectrum of 33% randomly deuterated benzene in the nematic phase. Only benzene and d_1-benzene have sufficient protons to generate 5 quantum coherence, a singlet at $\omega_1 = 0$ for d_1-benzene and a doublet centred around $\omega_1 = 0$ for benzene. The simulated spectrum, resulting from the correct assignment of the dipole coupling constants, is shown in figure 4.14(b). The dipole coupling constants obtained were within experimental error of the values obtained from the COSY experiment.

4.6.4 Structural Interpretation

Equation 4.9 is a set of 3 equations in 1 unknown, provided the hexagonal geometry of benzene is assumed, or of 3 equations in 4 unknowns, if nothing is assumed. This latter interpretation means that only a ratio of distances can be obtained.

$$ -1529 = \frac{K}{r_{ortho}^3} \cdot S_{33} \quad ; \quad -307 = \frac{K}{r_{meta}^3} \cdot S_{33} ; \quad -193 = \frac{K}{r_{para}^3} S_{33} . $$

Therefore: $r_{meta} = 1.7077 \, r_{ortho}$ $r_{para} = 1.994 \, r_{ortho}$

These values correspond to the geometry of a hexagon, in which $r_{meta} = \sqrt{3} \, r_{ortho}$; $r_{para} = 2 \, r_{ortho}$. If r_{ortho} is taken to be 2.482 Å, then $S_{33} = 0.195$.
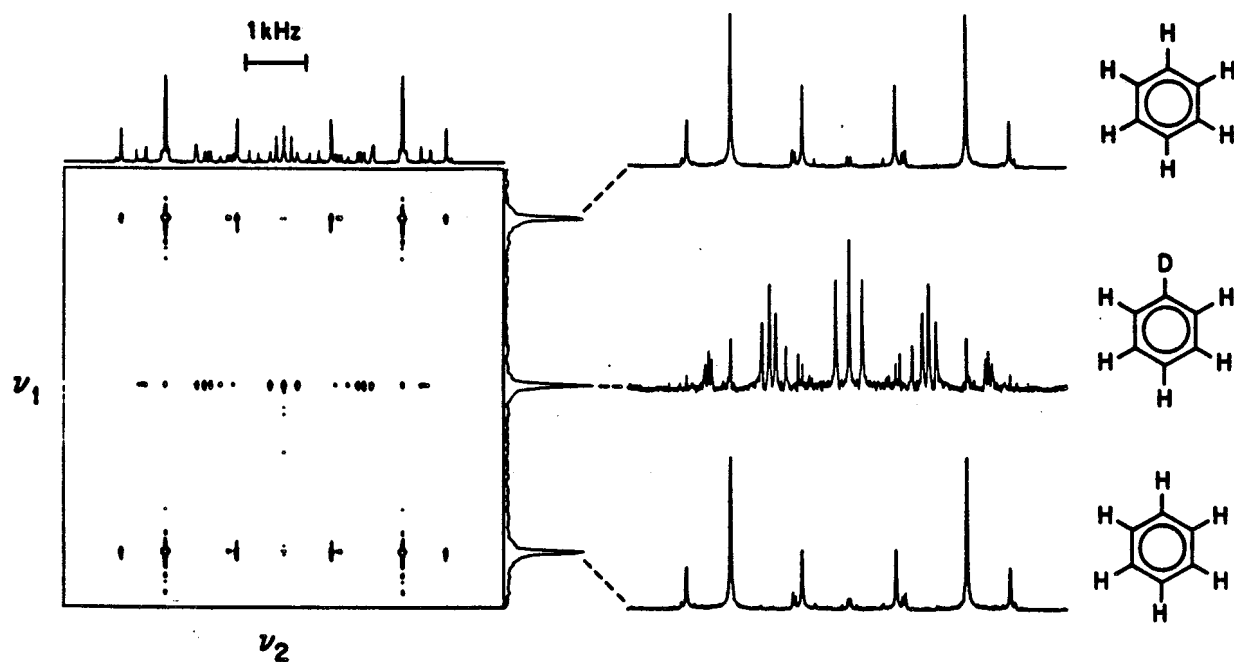
XBL 866-2353

Figure 4.14

(a) 5 quantum vs. 1 quantum spectrum of 34% randomly deuterated benzene in EK 11650, obtained using the TPPI sequence. The phase ϕ of the preparation pulses was incremented in 26.7° steps. 3000 t_1 × 1024 t_2 points were recorded with deuterium decoupling and spectral widths of 125 KHz in ω_1 and 8 KHz in ω_2. 4 FID's were averaged per t_1 point. The data were zero filled to 4096 points prior to Fourier transformation. The plot shown has been symmetrized about $\nu_1(5QT)$ = 0. The 3 projections along ν_2 show benzene and d_1-benzene.

XBL 866-2352
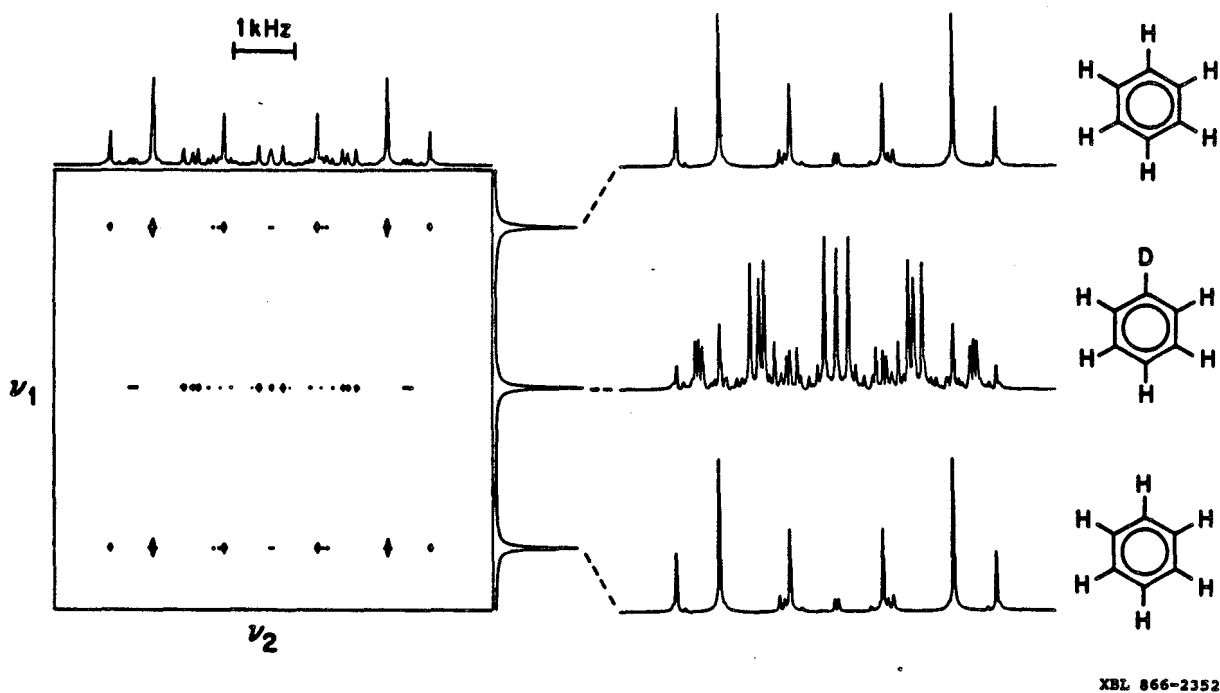
Figure 4.14 (b)

Simulation of the spectrum shown in (a), using D_{ij} values determined from the two-quantum filtered correlated spectrum.

4.7 HEXANE

The second example of CRASY was applied to n-hexane, a molecule with 14 protons and seven conformers, some of which have no symmetry. This provides a challenging problem: to precisely determine all 16 of the dipole coupling constants, including sign and pair assignments[137], and to relate them to molecular structure.

Figure 4.15 shows the all trans conformation of hexane with carbon and proton labels. These will be referred to throughout this section.

4.7.1 Experimental

Randomly deuterated n-hexane was synthesized by exchange of n-hexane in the gaseous phase with D_2 over Pd on charcoal at 190°C. An 81% deuteration level resulted after about 5 days. The results of mass spectroscopy on the sample are shown in figure 4.16, together with the calculated statistical distribution of different isotopomers for an 81% level of deuteration. The excellent agreement implies that the sample is randomly deuterated to 81% and can be confidently expected to contain a selection of all possible isomers. We refer to it as n-hexane-d_{81}.

The NMR experiments were carried out at 360 MHz. Two-dimensional data sets, up to 8192×1024 points, were recorded directly on the VAX for ease of storage and data processing.

The liquid crystal used for all measurements was Eastman Kodak 11650. About 20 mole % solutions were made up for the NMR work. Proton spectra were observed, with continuous two quantum deuterium decoupling[126,142] over a 15KHz bandwidth. The effect of the
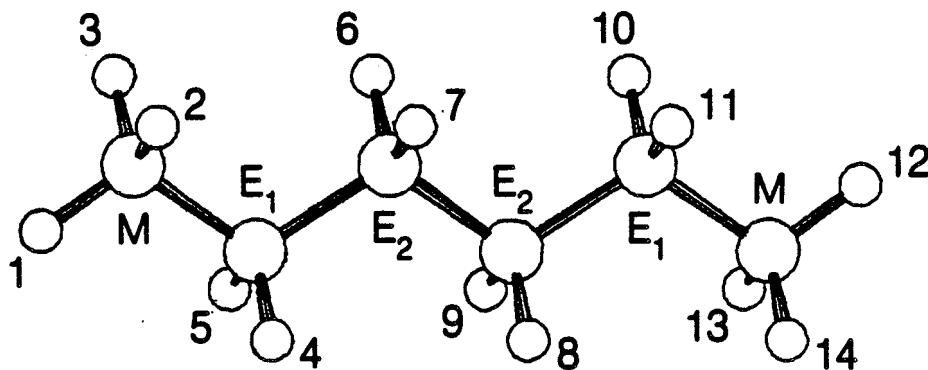
XBL 8610-9662

Figure 4.15

The all trans conformer of hexane. The carbon sites are labelled as M, E_1 or E_2, and the protons as 1-14.
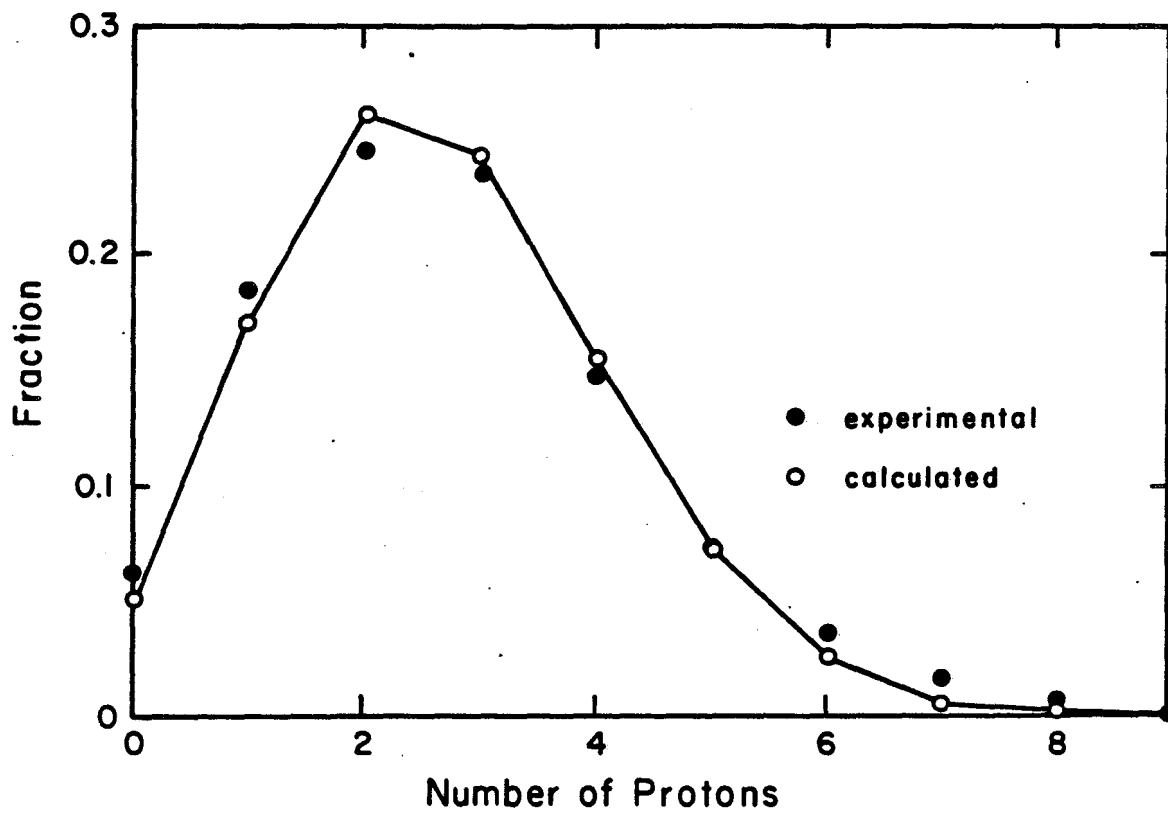
XBL 864-1593A

Figure 4.16

Mass spectral data for n-hexane after 80 hours exchange with D_2; shown are the measured relative intensities (•) at masses 100 (0 protons) through 91 (9 protons) and calculated statistical fraction (o) assuming 81% deuteration.

irradiation was to cause considerable heating, despite air flow temperature regulation, raising the temperature of the sample by about $20^{\circ}C$. The sample temperature was calibrated using a capillary of ethylene glycol centred in a tube of EK 11650/CCl_4. Decoupling was applied for extended periods at the same duty cycle as in the hexane experiments, and the temperature calibrated from the line separation in the ethylene glycol spectrum.

4.7.2 The Dipole Coupling Constants

The spectrum of n-hexane-d_{81} is shown in figure 4.17. The 1 proton isomers are prominent and provide the chemical shift identification of the three groups M, E_1 and E_2 (shown in figure 4.15). They are otherwise uninstructive, since they contain no dipolar information. The isomers of interest are those which contain 2 spins. Two quantum filtered correlation is used to isolate and identify the diprotonated species.

The result of a two-quantum filtered Hahn echo sequence on n-hexane - d_{81} is shown in figure 4.18. In figure 4.18(a), τ_1 was kept constant and four shots completed the cycle. Signals from molecules having two or three protons are present. As described earlier, higher proton numbers do not contribute. In figure 4.18(b) a "two-proton" filter was used, by incrementing τ_1 successively by $20\mu s$ after every 4th shot. The cycle was completed after 2000 shots. Two quantum coherence which oscillates due to dipole coupling during τ_1 and does not echo at the end of τ_1 is averaged to zero. Thus three proton molecules no longer contribute. Figure 4.18(b) is a superposition of the 8 A_2 and 8 AB spectra of the isotopomers of $C_6H_2D_{12}$.
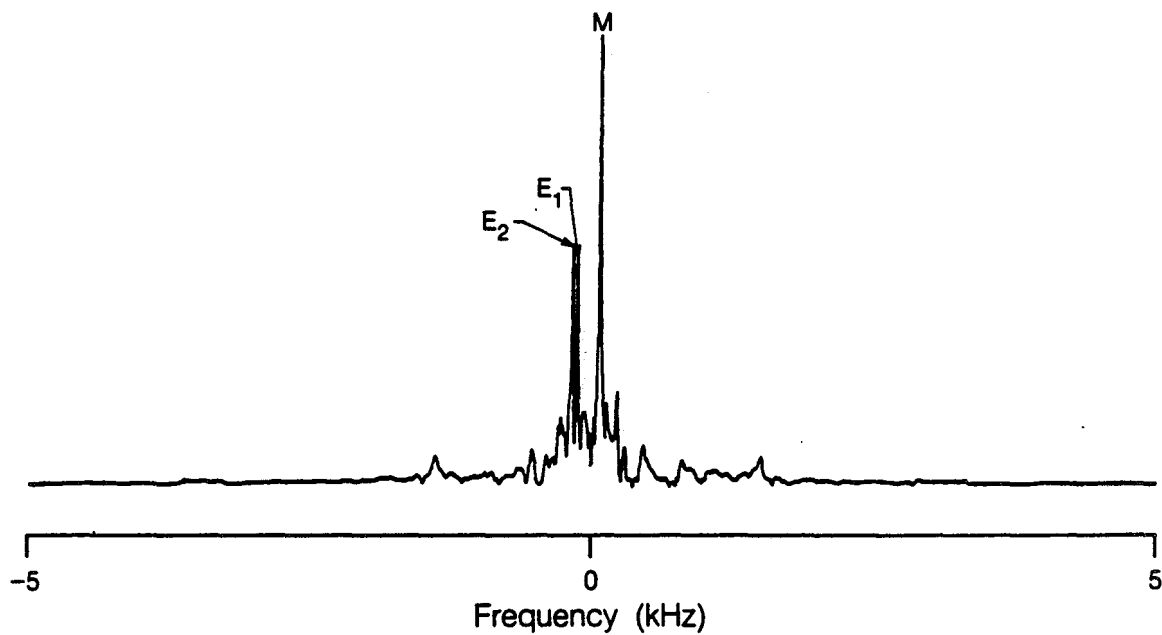
XBL 8612-12883

Figure 4.17

The one quantum spectrum of n-hexane-d$_{81}$ in the liquid
crystalline phase EK 11650; taken with a Hahn echo sequence, $\tau = 1ms$,
and with ^{2}D decoupling. 1000 shots were recorded at a recycle time of
7.5s.

(a)

(b)

Frequency (kHz)

-5   0   5
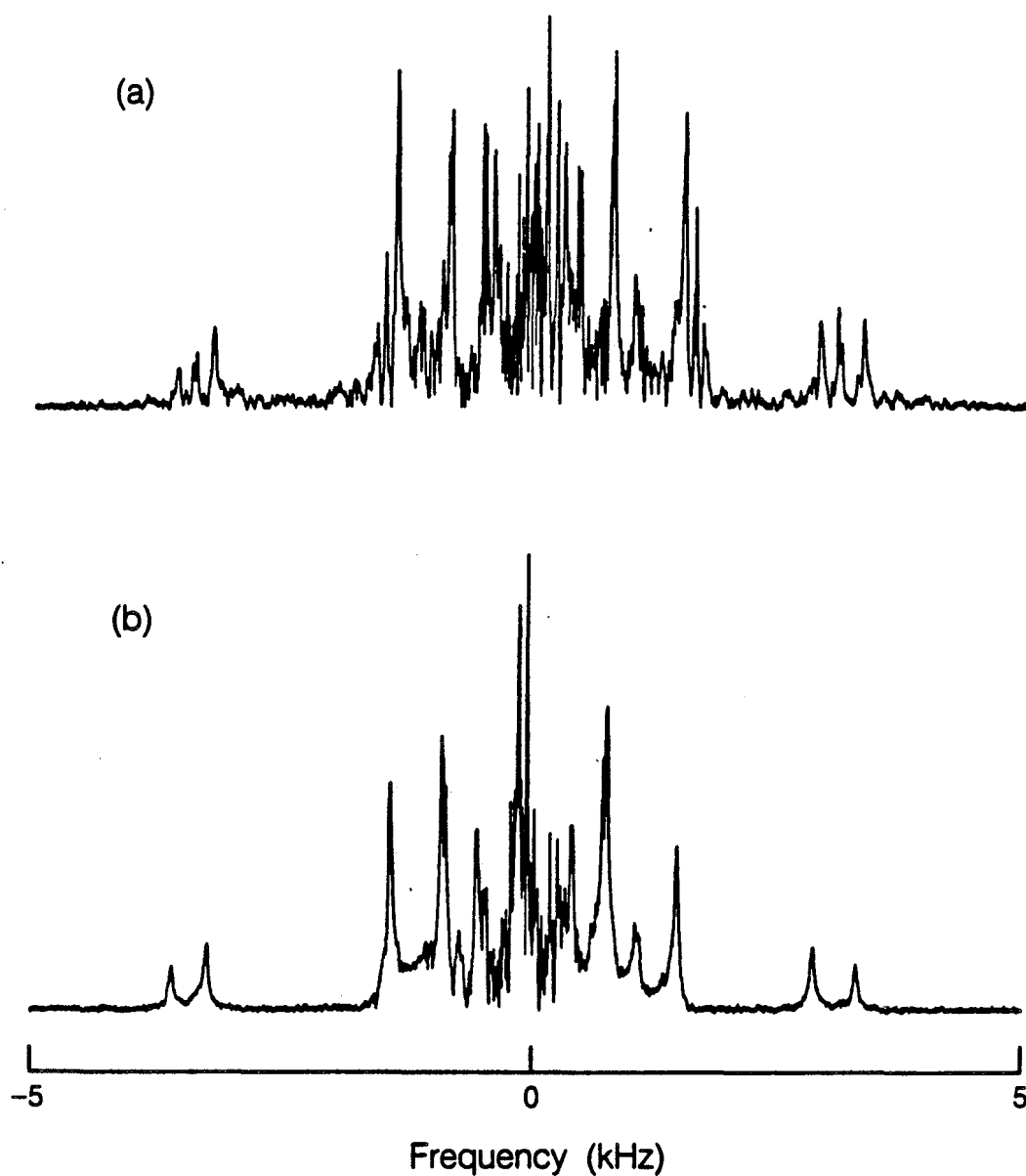
XBL 8612-12880

Figure 4.18

(a) Two quantum filtered Hahn echo spectrum on n-hexane-d_{81} taken with pulse sequence (4.C), $r_1 = 2\mu s$, $t_1 = 500\mu s$, $r_2 = 4ms$. ^2D decoupling was used. 6600 shots were acquired, with a recycle time of 7.5s. (b) Two-proton filtered Hahn echo spectrum on n-hexane-d_{81} taken with pulse sequence (4.C), $t_1 = 500\mu s$, $r_2 = 4ms$. r_1 was varied from 0 to 9.8ms in 20 μs increments. ^2D decoupling was applied. 4000 shots were acquired, with a recycle time of 7.5s.

A_2 pairs can easily be identified in the outer regions of the spectrum. The three largest splittings must correspond to the three possible vicinal hydrogen couplings, i.e. E_2E_2, E_1E_1 and MM, working inwards. To decipher the inner, somewhat overlapped region of figure 4.18(b) and to check peak connectivities, two-dimensional COSY-type and INADEQUATE-type spectra were recorded.

4.7.2.1   COSY-type Spectra

The COSY-type spectra were taken with the pulse sequence described above, both with and without a π - pulse in t_1, and with a varying two quantum time τ_1. Examples of the results of these sequences are shown in figures 4.19 to 4.23. Figure 4.19 shows a stacked plot of a COSY type spectrum. In figure 4.20(a) and 4.20(b), some of the squares have been superimposed on a contour plot, to illustrate the pattern finding procedure. In the absence of a π pulse in t_1, the Hamiltonians in ω_1 and ω_2 are identical, leading to AB patterns that are centred about the chemical shift position $\bar{\nu}_{AB}$ along the main diagonal. Lines connecting the cross peaks of all valid squares must cross the diagonal at one of the six possible frequencies. Figure 4.21 shows how squares may be identified in this manner.

In the refocussed COSY experiment, the square patterns become concentric about the centre $\omega_1 = 0$. The fact that the peaks are shifted in one dimension, relative to those in the experiment above, allows for any accidental overlap of peaks to be resolved. Assignments may be checked because of the necessity for concentricity. Strongly coupled AB patterns can easily be recognized because of their

-4.17

ν_1 (kHz)

4.17

-4.17

4.17

ν_2 (kHz)
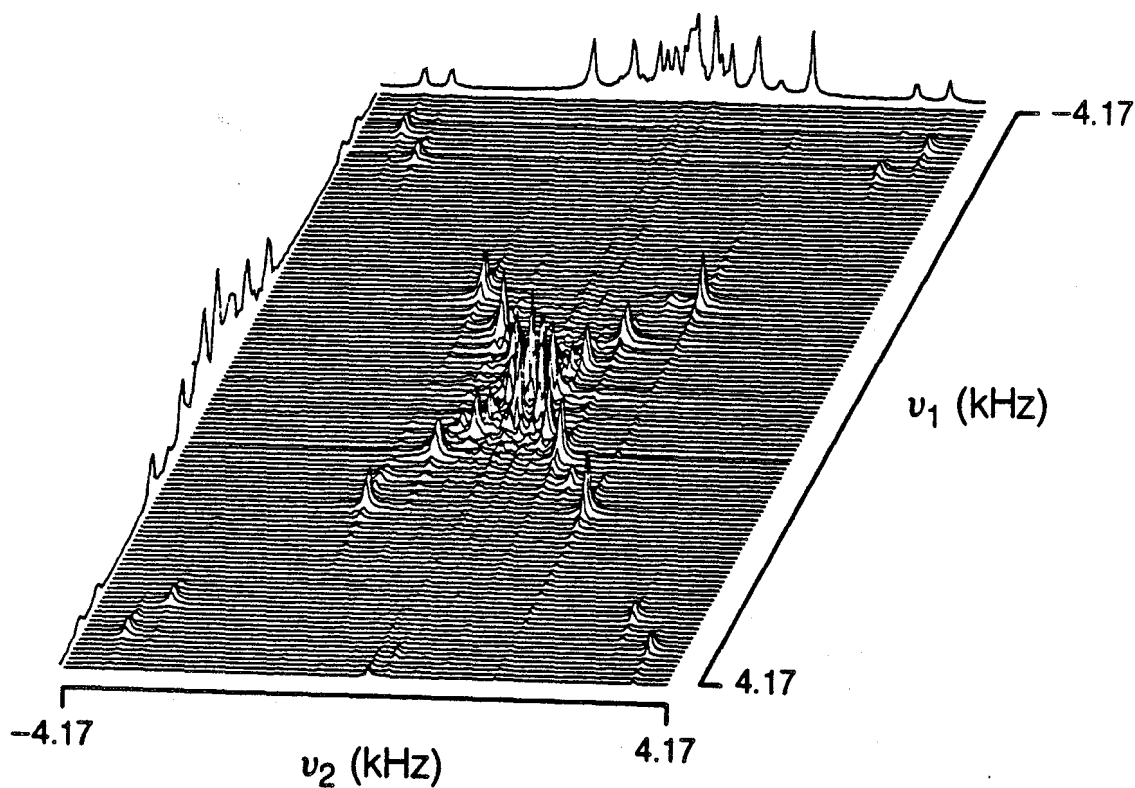
XBL 865-1352A

Figure 4.19

Two quantum filtered COSY-type spectra of n-hexane-d_{81} taken with pulse sequence (4.C) in the text, excluding the π pulse in t_1. 128 t_1 points and 1024 t_2 points were recorded with 2 QT deuterium decoupling in both dimensions, non-quadrature in t_1 and a spectral width of 16.667 KHz in both dimensions. 200 FID's were accumulated for each t_1 point with a recycle delay of 5s, while the double quantum mixing time τ_1 was incremented from 0 to 9.8ms in 0.2ms steps. The data set was zero-filled to 512 × 2048 points prior to Fourier transformation.
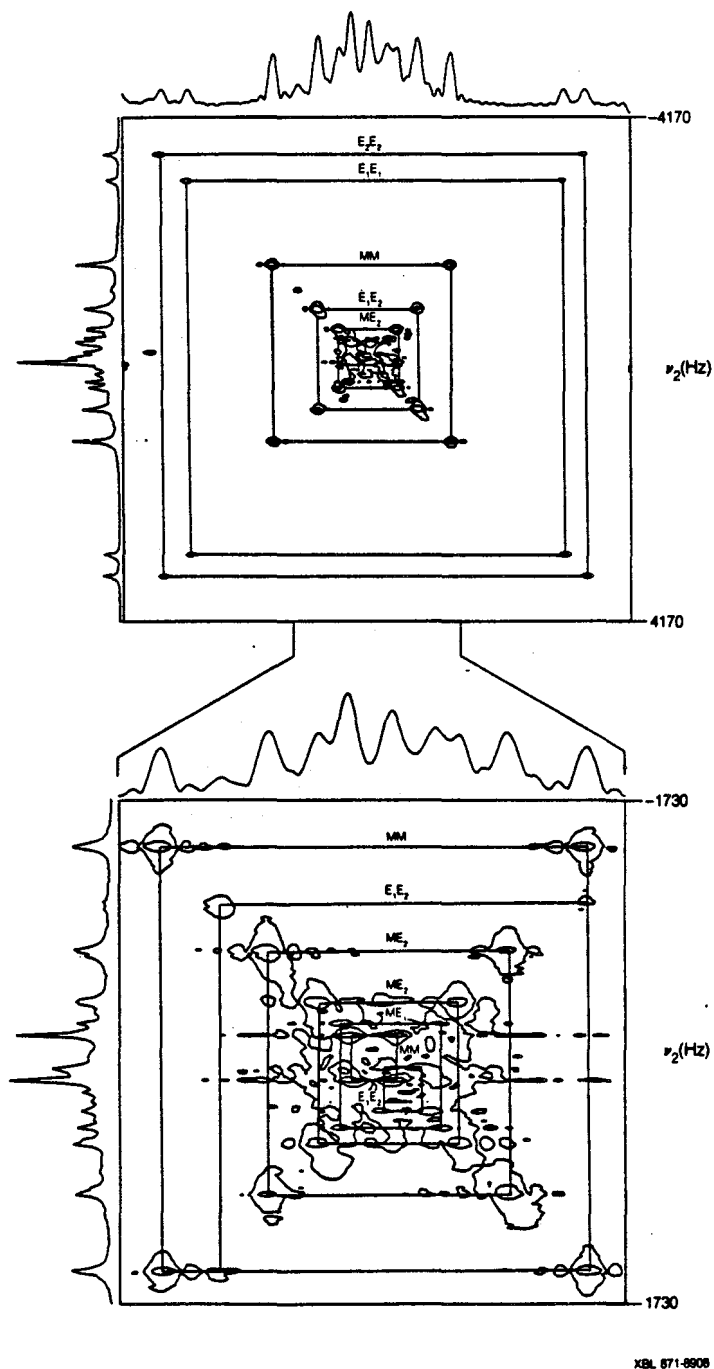
Figure 4.20

(a) Contour plot of the spectrum of 4.19. Several square patterns which give the dipole coupling constants are illustrated. (b) The central region of (a), illustrating some of the smaller squares.

XBL 871-8902
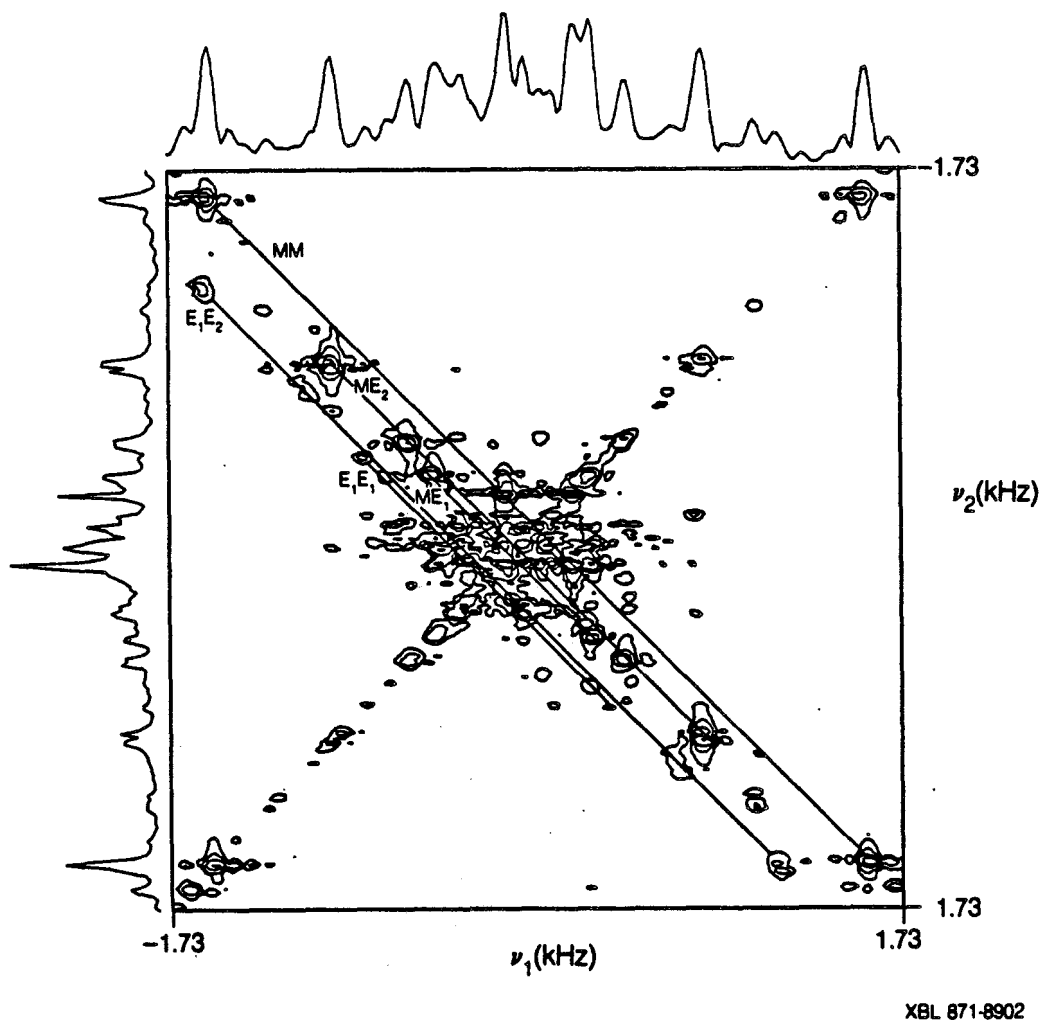
Figure 4.21

A spectrum taken under similar conditions as in figure (4.19) except that 256 t_1 points were recorded with 144 FID's accumulated per point. The data was zero-filled to 1024×2048 points prior to Fourier transformation. 5 of the 6 possible chemical shift positions are drawn perpendicular to the main diagonal, illustrating how the squares patterns may be identified.

complex pattern in the refocussed experiment (figure 4.6(c)). The additional complexity has not proved to be a barrier to analysis in this case. The slightly narrower lines and absence of quadrature information in t_1 makes this latter experiment easier to perform and analyse for the interpretation of the central region. Figure 4.22 shows all 16 of the dipole squares in a set of 3 consecutive drawings.

The inner region of the hexane spectrum is shown in figure 4.22(c). The two ME_1 patterns are typical strongly coupled AB spectra, since $|D/(\nu_A - \nu_B)| \approx 1.4$. The inner lines of the AB pattern become clearly prominent. Another obvious AB pattern is that of the smallest E_1E_2 coupling, for which $|D/(\nu_A - \nu_B)| \approx 1.0$. In many cases of AB patterns, the ratio of coupling constant to chemical shift difference is large, greater than 2, so the inner peaks are very small. These spectra resemble A_2 patterns, but are still interpreted in terms of their splitting as AB. Figure 4.23 shows a stacked plot of the inner region of the spectrum. Note the excellent S/N and resolution of the inner peaks.

Dipole coupling constants were read off from the size of the square patterns. Each of the sites M, E_1 and E_2 have different chemical shifts, so that the six chemical shift positions $\bar{\nu}_{MM}$, $\bar{\nu}_{ME1}$, $\bar{\nu}_{ME2}$, $\bar{\nu}_{E1E1}$, $\bar{\nu}_{E1E2}$ and $\bar{\nu}_{E2E2}$ can be used to group the proton pairs into six categories, which narrows down the search for the exact assignment. In the initial assessment, J couplings were ignored, because of their unknown size (especially J_{E1E2}) and sign and because they are small relative to D.

Figure 4.24 is a series of all 16 of the dipole coupled AB / A_2 spectra, produced by projection from the refocussed COSY experiment.
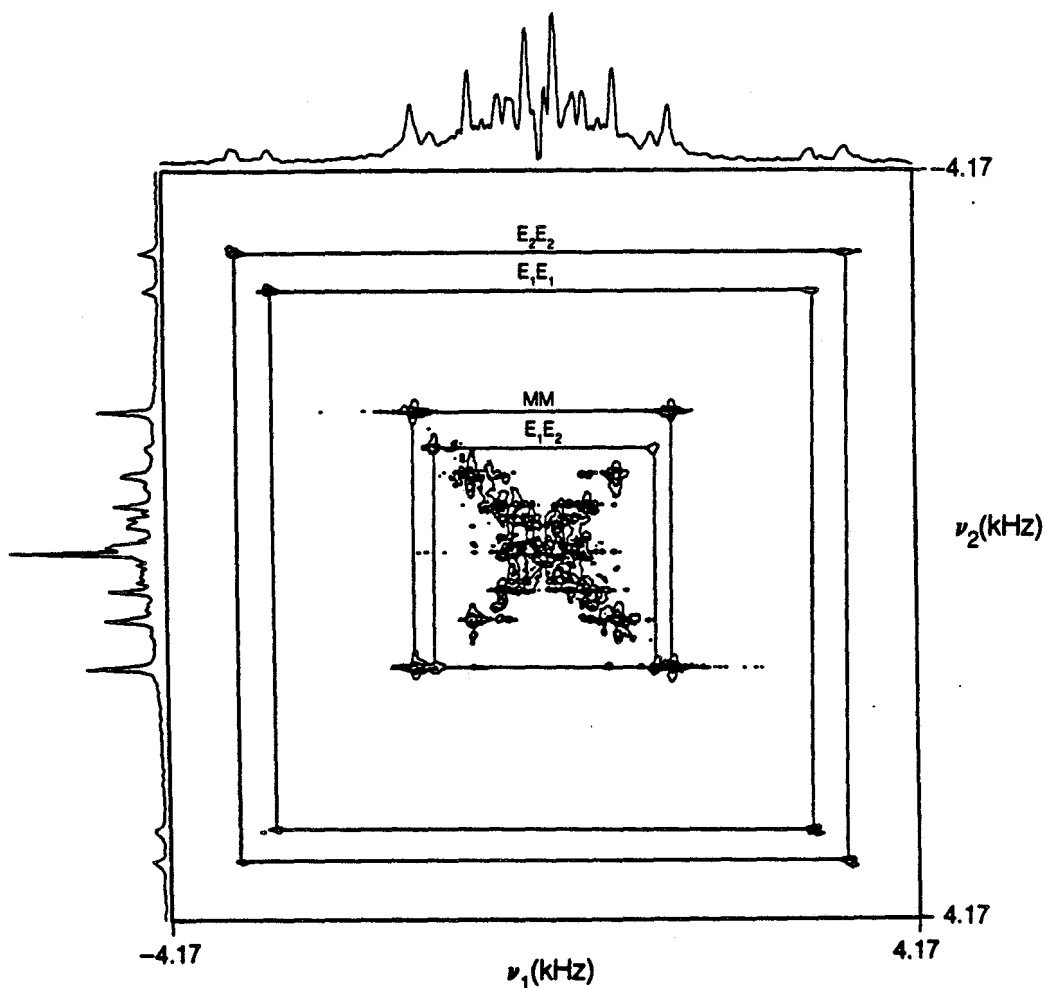
Figure 4.22

The refocussed COSY experiment, taken with pulse sequence (4.C) in the text. (a), (b) and (c) show successively more expanded regions of the spectrum. Superimposed on the diagrams are the 16 dipole squares of n-hexane. 512 t_1 points and 1024 t_2 points were recorded with decoupling in both dimensions and a spectral width of 8.333KHz in both dimensions. 80 FID's were accumulated per t_1 point at a recycle delay of 6s, while the τ_1 time was incremented from 0 to 9.8ms in 500μs steps. The data was zero-filled to 2048 × 2048 points prior to Fourier transformation. In (c) a Lorenzian-to-Gaussian filter was used.
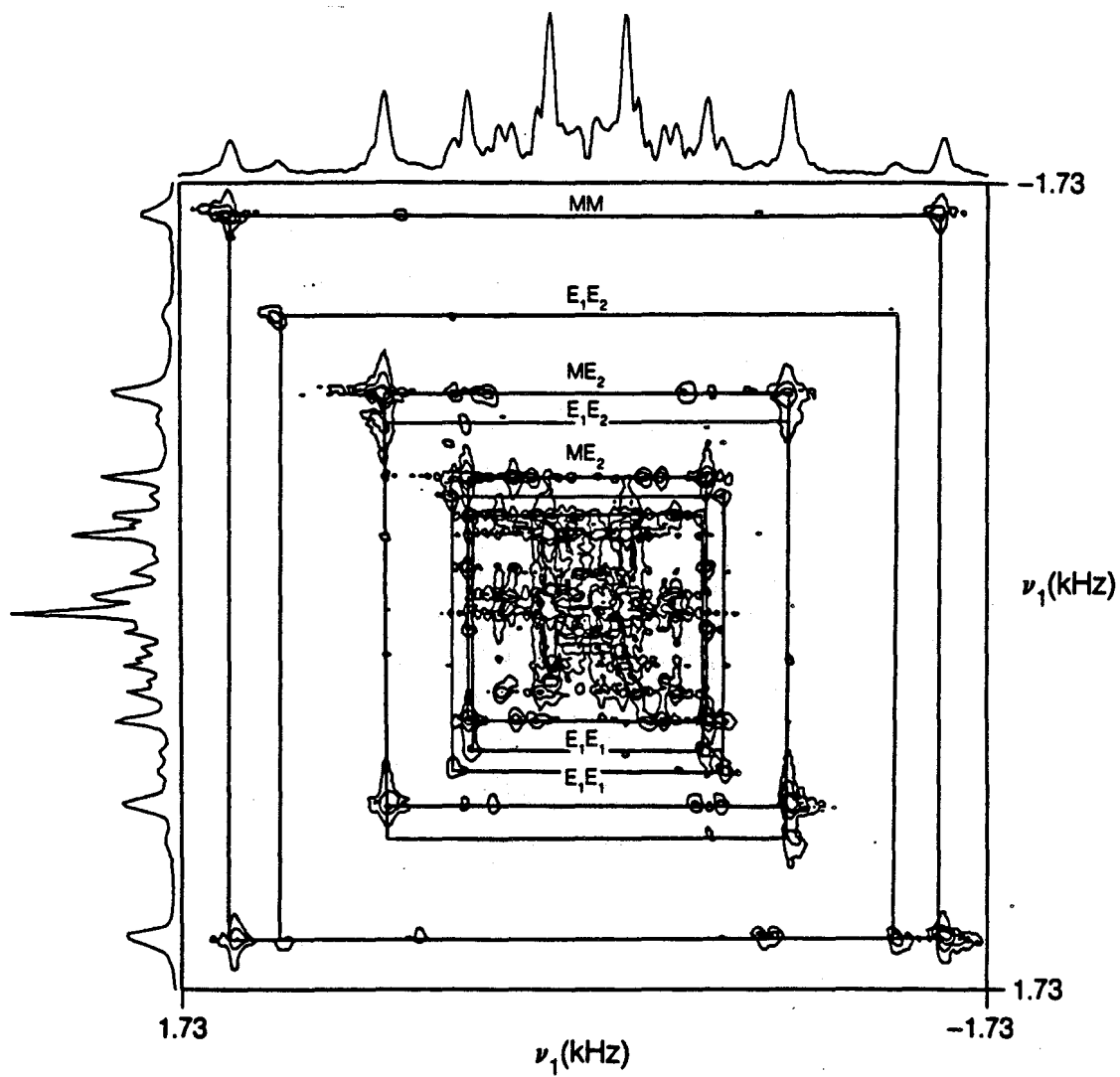
Figure 4.22(b)

XBL 871-8906

Figure 4.22(c)

v_1 (kHz)

v_2 (kHz)

2.08

−2.08

2.08

−2.08
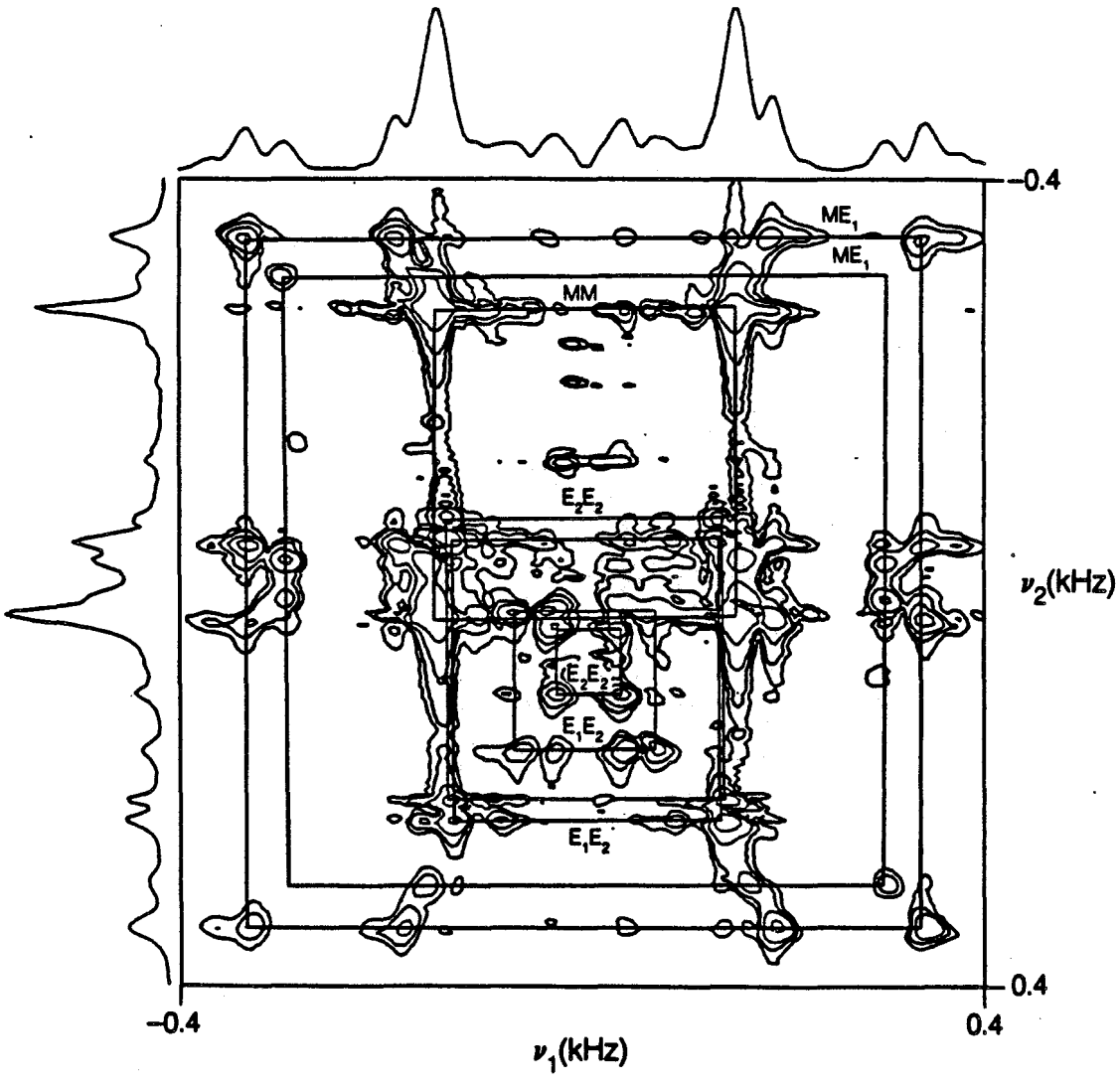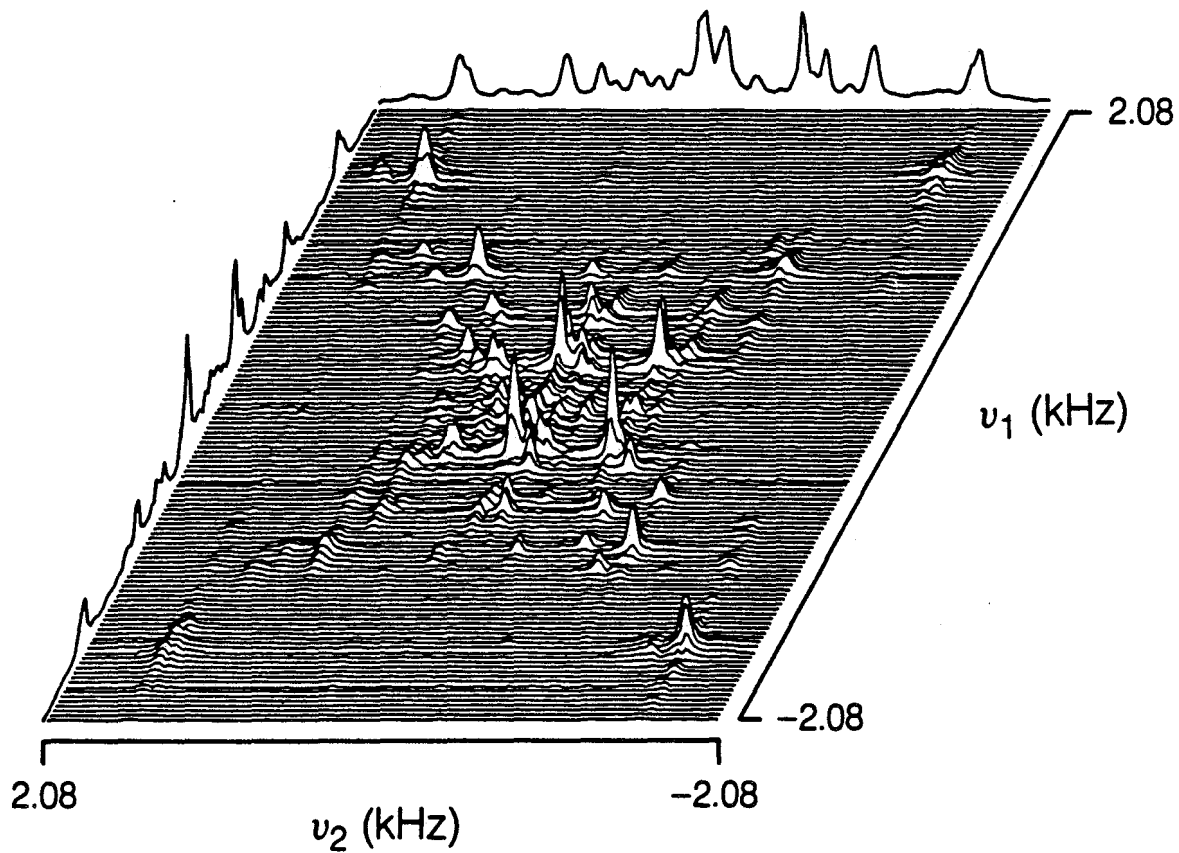
XBL 8612-12881

Figure 4.23

Part of the inner region of the spectrum of figure 4.22, drawn as a stacked plot to show the S/N and resolution.
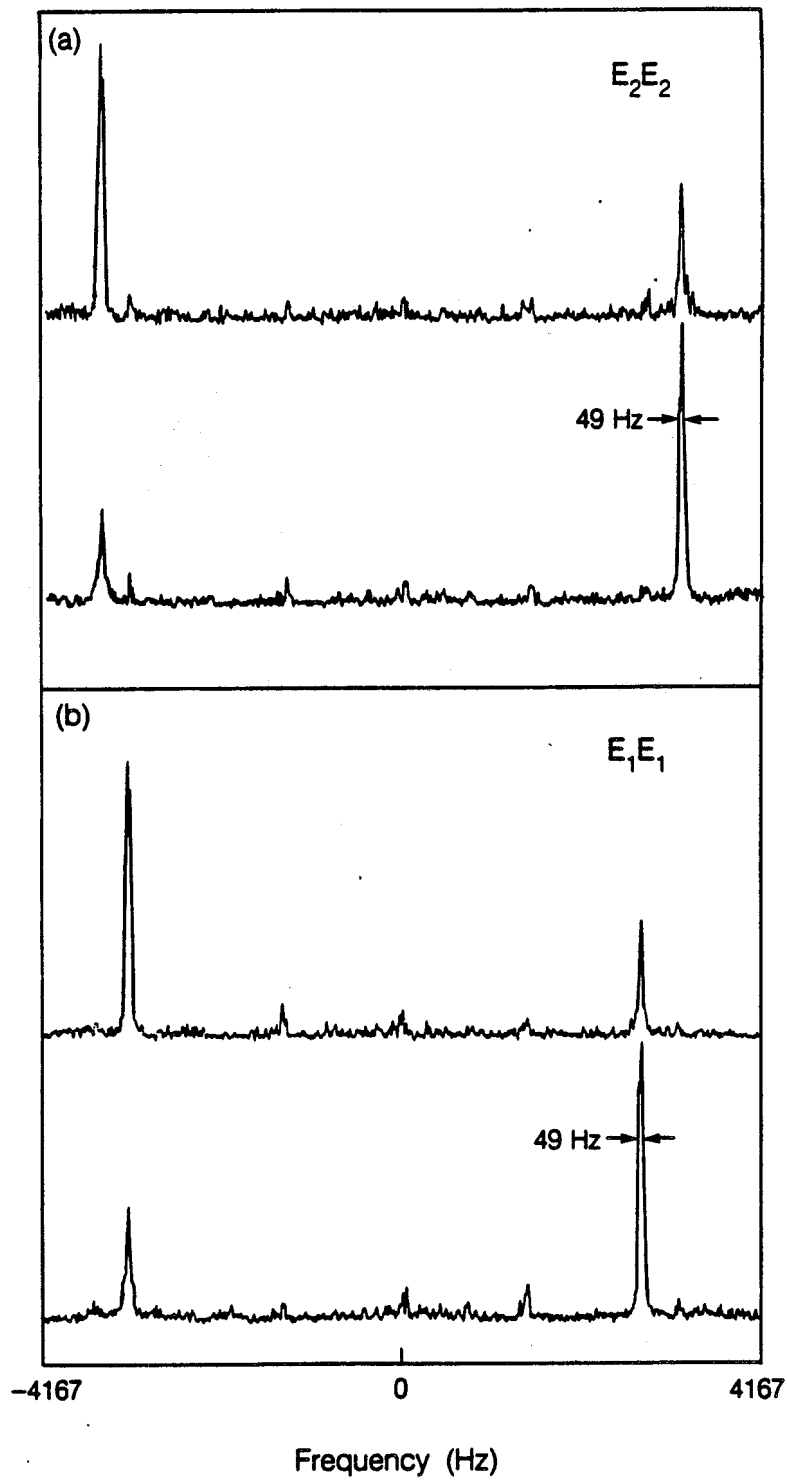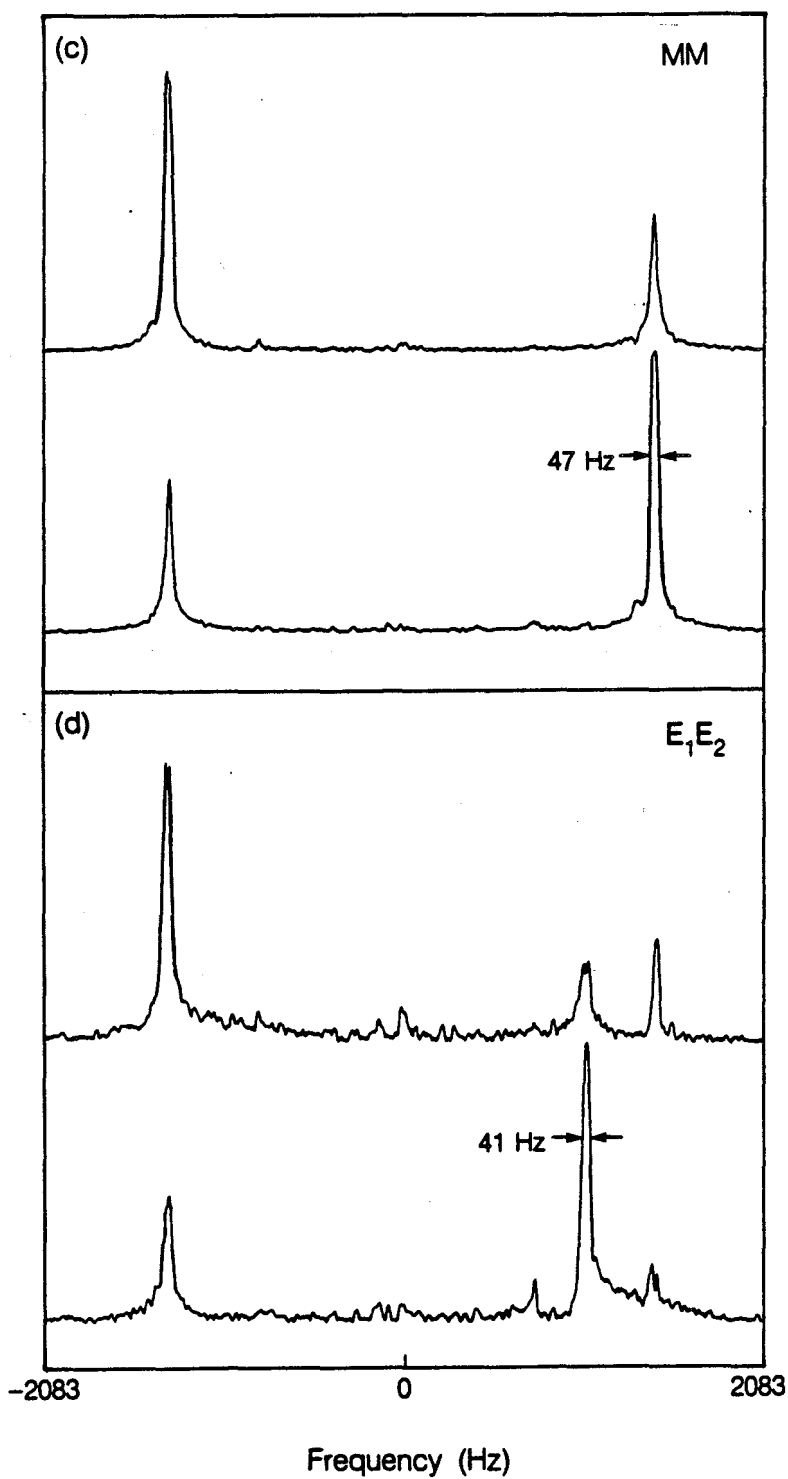
Figure 4.24

XBL 871-9560
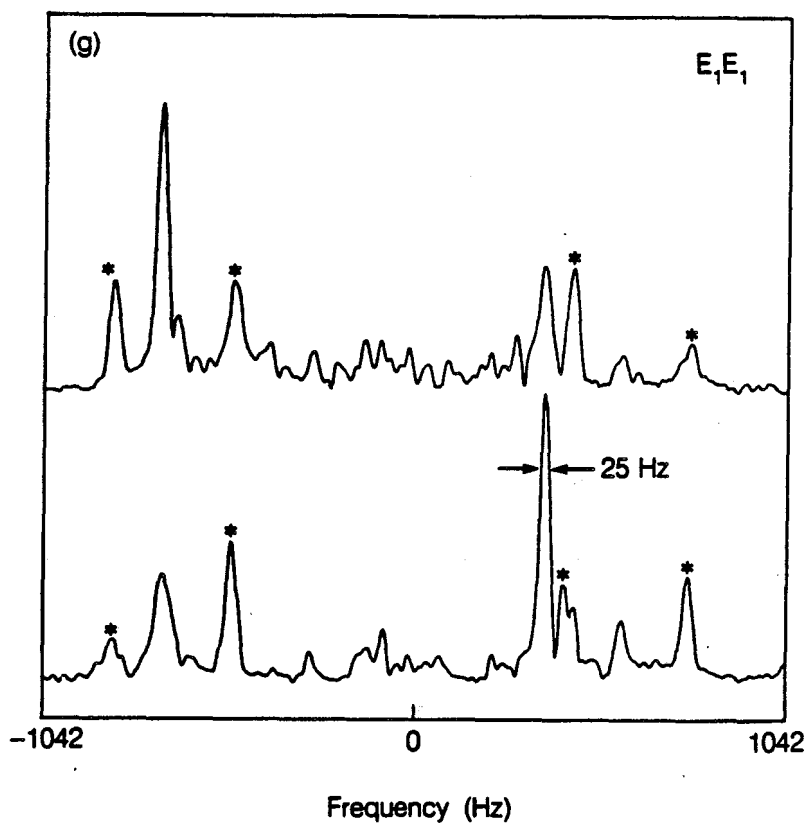
Figure 4.24

Figure 4.24

Figure 4.24(a-m)

The set of all 16 A_2/AB sub-spectra which correspond to the 16
unique dipole coupling constants in n-hexane. These spectra are
projections in ω_2 from figure 4.22. The widths at two-thirds height
are indicated to give an estimate of the experimental error.
* indicates overlap of signals from other AB patterns in the
projection indicated

Frequency (Hz)
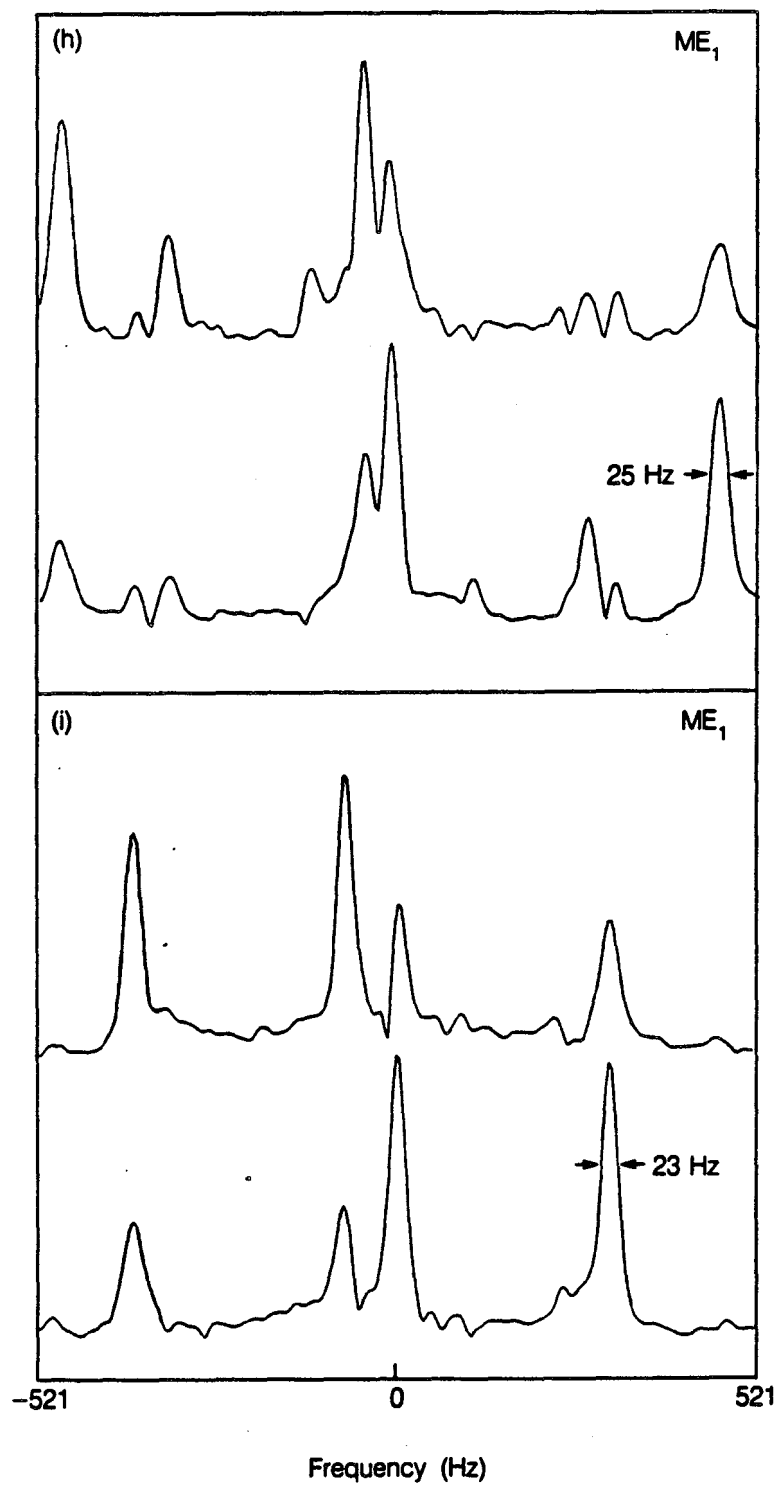
XBL 871-9563

Figure 4.24

Frequency (Hz)
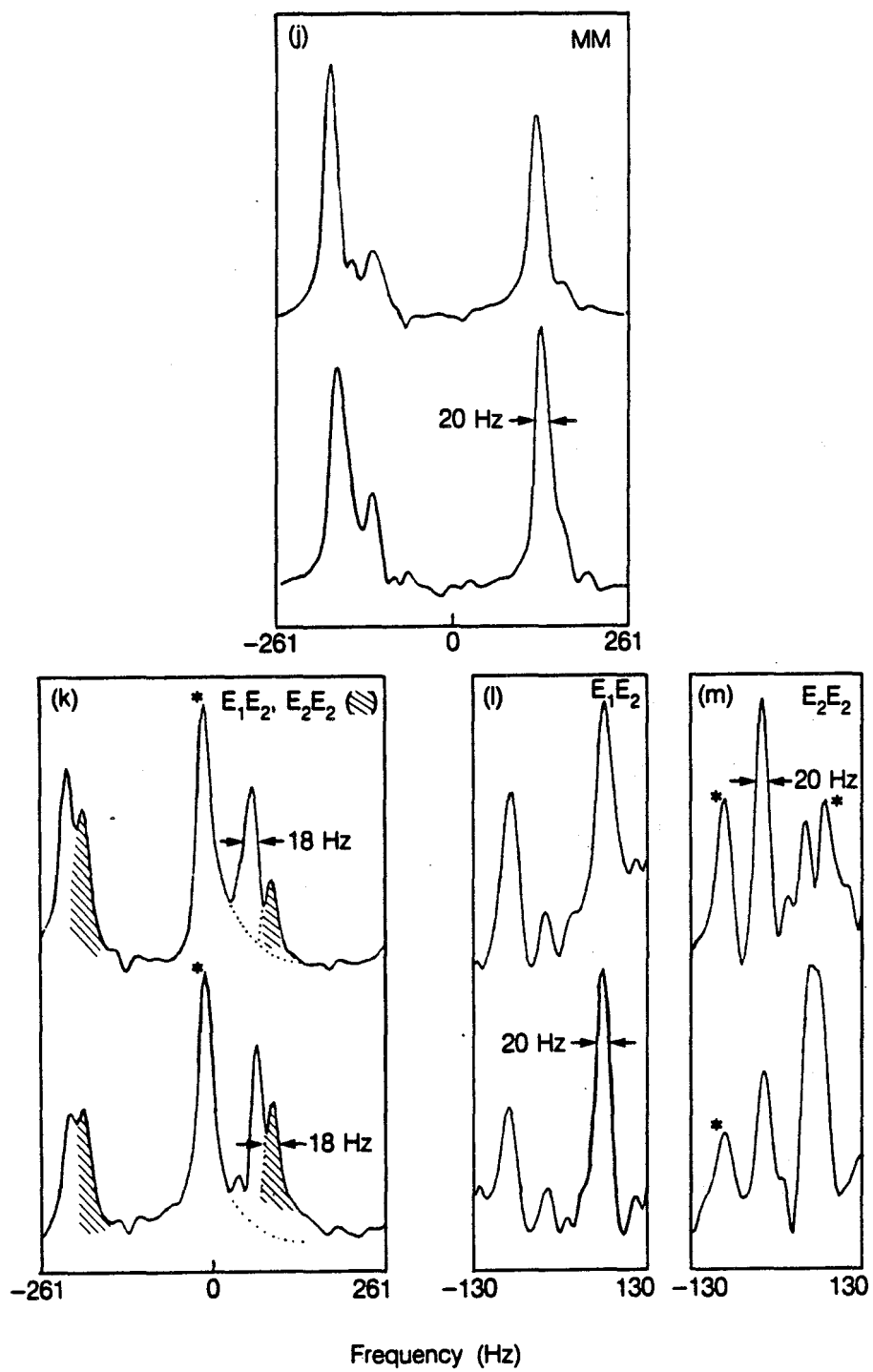
XBL 871-9564

Figure 4.24

These spectra show the resolution of each AB pattern from the next, and the residual linewidths from which the experimental error was estimated.

4.7.2.2 INADEQUATE-type Spectra

In the two-dimensional INADEQUATE-type experiment, the pulse sequence used was:

$$\left(\frac{\pi}{2}\right)_\phi - \frac{\tau_1}{2} - \pi_\phi - \frac{\tau_1}{2} - \left(\frac{\pi}{2}\right)_\phi - t_1 - \left(\frac{\pi}{2}\right)_x - \frac{\tau_2}{2} - \pi_x - \frac{\tau_2}{2} - t_2 \qquad (4.D)$$

where ϕ was incremented by 90° and the receiver alternated between 0 and 180°. Here, two quantum and one quantum signals were correlated in a two dimensional map, as shown in figure 4.25. For two proton molecules, signals along the two quantum axis lie in one of 6 possible chemical shift positions $2\nu_M$, $\nu_M + \nu_{E1}$, $\nu_M + \nu_{E2}$, $\nu_{E1} + \nu_{E1}$, $\nu_{E1} + \nu_{E2}$ and $\nu_{E2} + \nu_{E2}$. The six slices parallel to the one quantum axis are drawn in figure 4.25. Within each slice, one quantum AB patterns can be easily identified due to their symmetric disposition around the appropriate chemical shift position in ω_2. There are 2 MM, 2 ME_1, 2 ME_2, 3 E_1E_1(2 shown), 4 E_1E_2 (3 shown) and 3 E_2E_2(1 shown) subspectra. Figure 4.25 is an expansion of the central region of the spectrum, so the two geminal E_1E_1 and E_2E_2 resonances lie outside the range of the ω_2 shown. The INADEQUATE-type experiment was repeated for different values of the two quantum preparation time τ_1, in order to vary the relative intensities of the different subspectra. For higher values of τ_1, the more weakly coupled pairs appear at greater intensity, since $\tau_1 \propto 1/D$. Higher τ_1 values revealed especially the weaker E_1E_2,
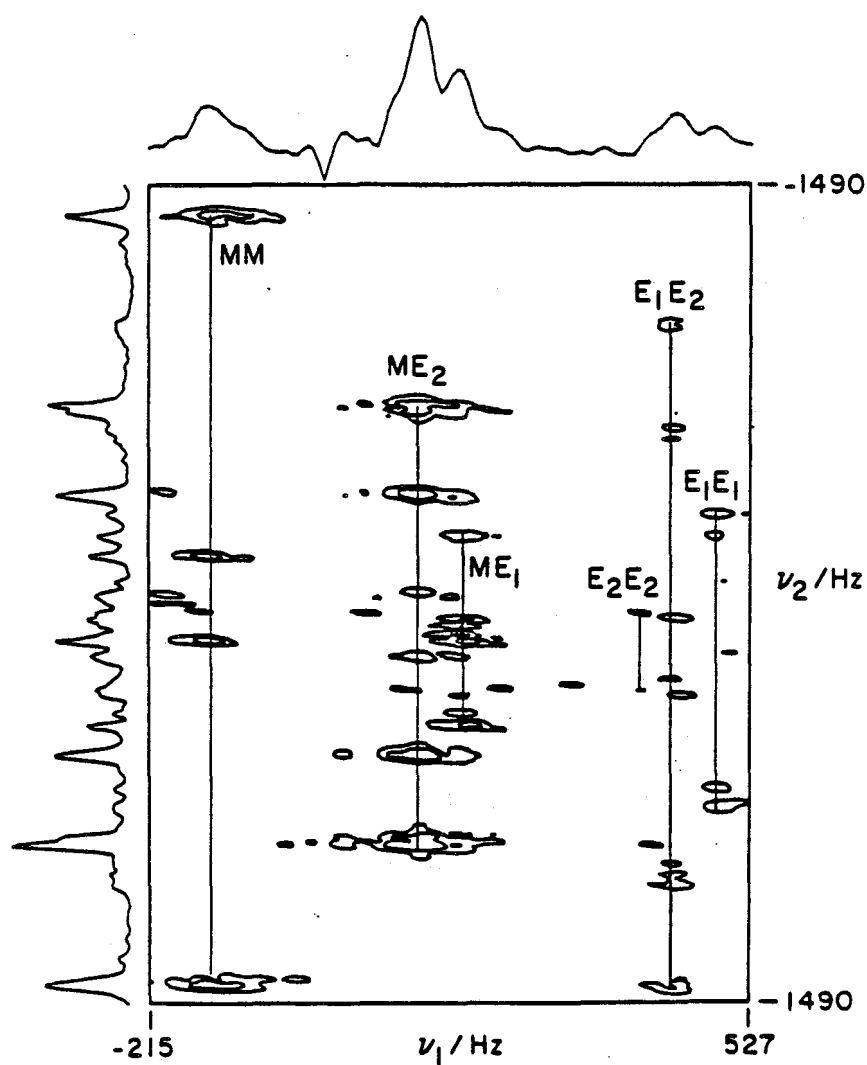
XBL 864-1591

Figure 4.25

Part of a double quantum vs. single quantum spectrum of n-hexane-d_{81} in the liquid crystalline phase EK 11650, obtained using pulse sequence (4.D) in the text, $r_1 = 250\mu s$, $r_2 = 4ms$. 128 t_1 points and 1024 t_2 points were recorded with quadrature phase detection and ^2D decoupling in both dimensions. The spectral width was 3.3 KHz in ω_1 and 7.35 KHz in ω_2. Vertical lines parallel to the one quantum axis illustrate the six double quantum frequencies of molecules with two protons along which the A_2 and AB spectra can be identified.

E_1E_1 and E_2E_2 couplings.

Three proton spin systems tend not to interfere in the INADEQUATE experiment. Their signals in ω_1 are modulated by the large dipole coupling term and tend to lie outside the small chemical shift range of two proton signals. Signals lying within this region are unlikely except by accident to be aligned symmetrically about the correct chemical shift position. It can be seen from figure 4.25 that they do not present a problem.

Table 4.VII is a compiled list of couplings obtained by the COSY method, and by the INADEQUATE method with two preparation times 250 μs and 2.5 ms. The values of D_{ij} agree rather well, given the experimental error in the measurement. The error originates mainly from imperfect decoupling of deuterium from protons, leaving residual linewidths up to 45 Hz in some cases. Methyl groups are more easily decoupled from ethylene groups, than ethylene groups from each other, resulting in varying peak widths throughout the spectrum. The effect of temperature gradients, caused by continuous deuterium decoupling is also observed, with lines becoming increasingly broad with increased dipolar frequency shift. The error margins for each coupling constant are also given in Table 4.VII. Additional experimental data provided are the chemical shifts, quadrupole couplings and the deuterium isotopic shift.

4.7.2.3 Comparison of COSY and INADEQUATE Methods

The COSY and INADEQUATE type experiments are briefly compared, either of which may be the experiment of choice depending on the

TABLE 4.VII

Experimental data on hexane

A. <u>Dipole Couplings</u>   B. <u>Quadrupole Couplings</u>

Sites	$\|\underline{D}_{ij}\|^{(a)}$	$\|\underline{D}_{ij}\|^{(b)}$	exptl error	Sites	Q_i
E_2E_2	4487	4482	±34	E_2	33550
E_2E_2	190	189	±12	E_1	29700
E_2E_2	43	48	±12	M	9750
E_1E_1	3974	3968	±34		
E_1E_1	713	706	±18		
E_1E_1	609	612	±14		
E_1E_2	1616	1626	±25	C. <u>Chemical Shifts</u>	
E_1E_2	1086	1106	±27		
E_1E_2	186	183	±14	Sites	ν_i
E_1E_2	81	81	±12		
MM	1876	1862	±28	E_2	241
MM	206	203	±13	E_1	200
ME_2	1034	1041	±25	M	0
ME_2	598	591	±15		
ME_1	386	382	±15		
ME_1	322	314	±14		

D. <u>^2D Isotopic Shift</u>: ~ 7 Hz

molecule studied. The COSY experiment has evolution frequencies determined by

$$\nu_1 = \nu_2 = \bar{\nu}_{AB} \pm (J+D)/2 \pm C + \Delta\nu_z(\hat{r}), \qquad (4.10)$$

or for a refocussed COSY,

$$\nu_1 = \pm (J+D)/2 \pm (C \text{ or } 0)$$

$$\nu_2 = \bar{\nu}_{AB} \pm (J+D)/2 \pm C + \Delta\nu_z(\hat{r}). \qquad (4.11)$$

The INADEQUATE experiment has

$$\nu_1 = 2 \bar{\nu}_{AB} + 2 \Delta\nu_z(\hat{r})$$

$$\nu_2 = \bar{\nu}_{AB} \pm (J+D)/2 \pm C + \Delta\nu_z(\hat{r}). \qquad (4.12)$$

$\Delta\nu_z(\hat{r})$ is the spatial inhomogeneity of the static field.

The immediate implication is that for a molecule where no or very small chemical shift differences occur, the COSY experiment, which spreads signals in ν_1 according to D, is preferable. Additionally, the $2\Delta\nu_z(\hat{r})$ term in the INADEQUATE experiment implies twice the inhomogeneous broadening in t_1, and induces overlap between close resonances if field inhomogeneity is significant.

On the other hand, in a less symmetric molecule where there is a large range of chemical shifts, the INADEQUATE experiment may prove more versatile. The chemical shift range is doubled (term $2\nu_{AB}$), enhancing chemical shift dispersion. Resolution is improved in the case where the field inhomogeneity does not dominate the linewidth. Since the ν_1 bandwidth is much reduced ($|\Delta(2\nu_{AB})| \ll |\Delta(D)|$) compared to the COSY experiment, the experimental time can be shorter.

The INADEQUATE experiment must be repeated with different preparation times, to cover the range of dipole coupling constants. The COSY experiment need only be done once. The COSY experiment includes a varying two quantum filter, which selects only for two

proton molecules and excludes three proton molecules. This prevents

complication due to extra resonances, although it is impossible to

implement a perfect two-quantum filter. This is apparent from the one

dimensional spectrum shown in figure 4.18(b). The central region

contains many extraneous peaks belonging to three spin systems. These

are retained because the minimum requirement of $1/\tau_1 \leq \nu_{2QT}$ cannot be

met as ν_{2QT}, the two quantum frequency of three spin systems, tends to

0. In the INADEQUATE experiment, the chances are that three proton

lines will not fall on the same ν_1 frequency as sums of chemical

shifts, because they involve dipole couplings. It will normally be

easy to distinguish these resonances and a two proton filter is not

necessary.

Finally, we note that less than half the number of peaks occur in

the INADEQUATE experiment compared to the COSY experiment. Each AB

spectrum is 4 peaks instead of 16; each A_2 spectrum is 2 peaks instead

of 4. This apparent advantage is of course belied by the fact that

the ν_1 spectral width is much less than half of the COSY ν_1.

4.7.3 Multiple Quantum NMR on the Ethylene Chain

4.7.3.1 The (N-2) Quantum Spectrum

We studied the (N-2) quantum spectrum of $1,1,1,6,6,6-d_6$-n-hexane.

This was done partly because of the expected low sensitivity of the 12

quantum spectrum of n-hexane, but mainly because there is no ambiguity

in the assignment of the coupling constants to methyl protons. The

methyl protons have a distinct and large chemical shift from ethylene

protons. The free rotation of methyl groups removes the biggest

ambiguity - the assignment of cis and trans couplings between protons on the same or opposite sides of the C - C bonds.

The 6 and 7 quantum spectra of d_6-hexane have been recorded previously in an attempt to determine the dipole coupling constants from the high order frequencies[133]. The number of 6 quantum frequencies is of the same order as the number of dipole coupling constants. The fit of complex combinations of 10 unknowns to a set of as many resolved frequencies proved to be an unsympathetic task.

High order multiple quantum transitions were measured using the TPPI phase cycling scheme[38,75]. The sequence used was:

$$\left(\frac{\pi}{2}\right)_\phi - \frac{\tau}{2} - \pi_\phi - \frac{\tau}{2} - \left(\frac{\pi}{2}\right)_\phi - \frac{t_1}{2} - \pi_\chi - \frac{t_1}{2} - \left(\frac{\pi}{2}\right)_x - \frac{\tau}{2} - \pi - \frac{\tau}{2} - t_2 \qquad (4.E)$$

ϕ is incremented proportionately with t_1 in 22.5° increments, allowing 16 phase separated intervals for the 0 - ±8 quantum spectra (±8 quantum at the edge). The phase χ was cycled through four values for each t_1 point as in Section 2.5.3.6.

Figure 4.26 shows the experimental 6 and 7 quantum spectra of d_6-hexane. The 7 quantum spectrum has two pairs of lines, which corresponds to the number of distinct ways of selecting 7 out of 8 protons. The 6 quantum spectrum consists of 10 triplets, 10 being the number of distinct ways of selecting 6 out of 8 protons. Degeneracies in the sums of dipole coupling constants has reduced the quartets to triplets. Figure 4.27 shows simulations using different assignments of certain coupling constants. Many couplings were kept fixed. They were deduced from the known primary structure of hexane, the chemical shift information, and the known average orientation of the long axis

XBL 8610-9663A
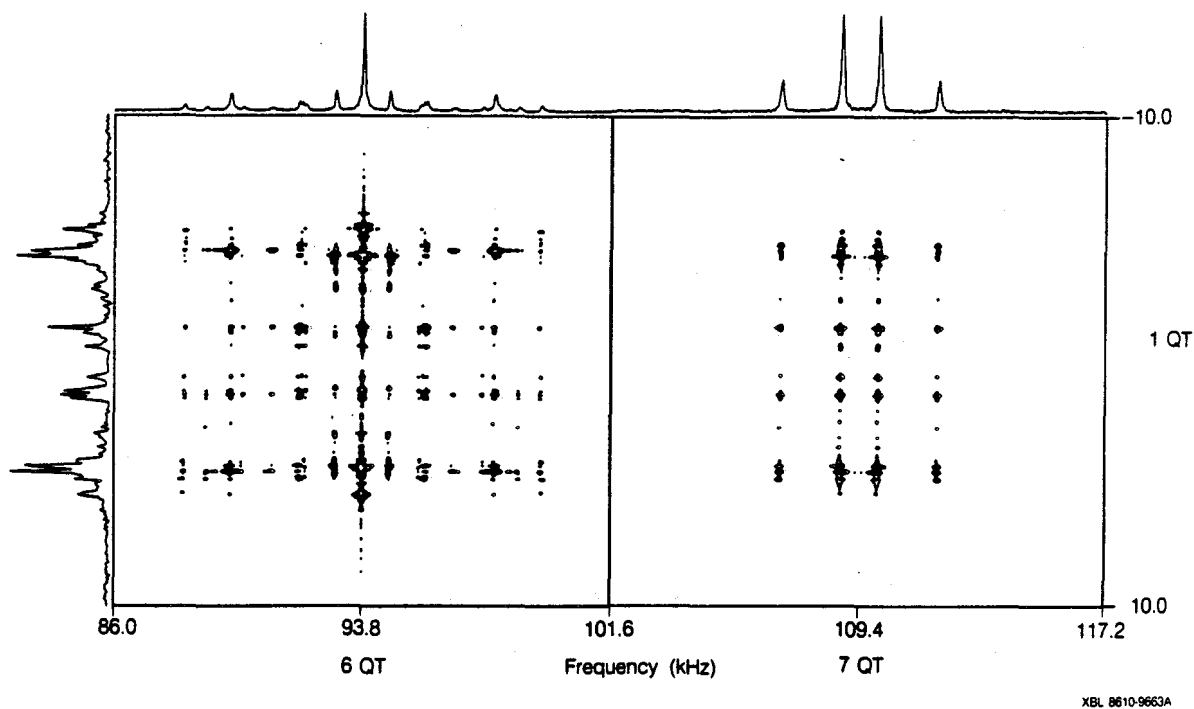
Figure 4.26

Experimental 6 and 7 quantum spectra of d_6-n-hexane deuterated at the methyl positions, taken with pulse sequence (4.E); τ = 11.706 ms for even quanta and 12.000 ms for odd quanta. The two absolute value spectra were added. 8192 points were recorded in t_1 and 1024 points in t_2. Total spectral width for 16 orders was 250 KHz in ω_1 and 20 KHz in ω_2. Different multiple quantum orders were separated by a phase increment $\Delta\phi$ = 22.5°. 6 shots were averaged per t_1 point with a recycle time of 4.5s. ^{2}D decoupling was used in t_1 and t_2.

along the magnetic field direction. Different sign and pair assignments were tried only for uncertain cases. A π pulse was used in the middle of the multiple quantum evolution period, and the simulations were done without chemical shift.

According to equation (1.30), the sign of a coupling constant will be positive along the C_2 rotational axis of hexane, which is perpendicular to the long axis of the molecule. Thus, vicinal coupling constants will be positive in sign, and will be large because the protons are close together, and the direction of the internuclear vector is far from the magic angle. Their assignment is obvious in figure 4.18(b). Any internuclear coupling that extends along the long axis of the molecule, such as the intermethyl coupling, will be negative. For protons ~ 7 Å apart, we see a significant coupling constant of -206 Hz, partly because θ in equation 2 is close to zero. The largest longitudinal couplings are the E_1E_2 coupling constants between the proton pairs (4,8) and (4,9). Model calculations show that the largest of these two must be (4,8) which is shorter in a predominantly all trans configuration and has θ close to 0 as well.

Many assignments can be made by deduction. This simplifies the task of using the 6 quantum spectrum to narrow down the correct assignment, and enables identification of the coupling network vertices with atoms.

Figure 4.27(b) and (c) compare the two possible assignments of the E_1E_2 (4,6) and (5,6) vicinal couplings. The spectrum changes in only two of the frequencies. In 4.27(b), these two frequencies are not resolved within the experimental digital resolution of 30 Hz. In 4.27(c), they are 97 Hz apart. They correspond to the 6-proton

(a)
Experimental

(b)

$D_{4,6} = 186$
$D_{5,6} = 81$
$D_{6,7} = 4487$
$D_{7,8} = -190$

(c)

$D_{4,6} = 81$
$D_{6,5} = 186$
$D_{6,7} = 4487$
$D_{7,8} = -190$

(d)

$D_{4,6} = -186$
$D_{5,6} = 81$
$D_{6,7} = 4487$
$D_{7,8} = -190$

(e)

$D_{4,6} = 186$
$D_{5,6} = 81$
$D_{6,7} = -190$
$D_{7,8} = 4487$

86.0   6 QT   7 QT   117.2

Frequency (kHz)

XBL 8610-9579
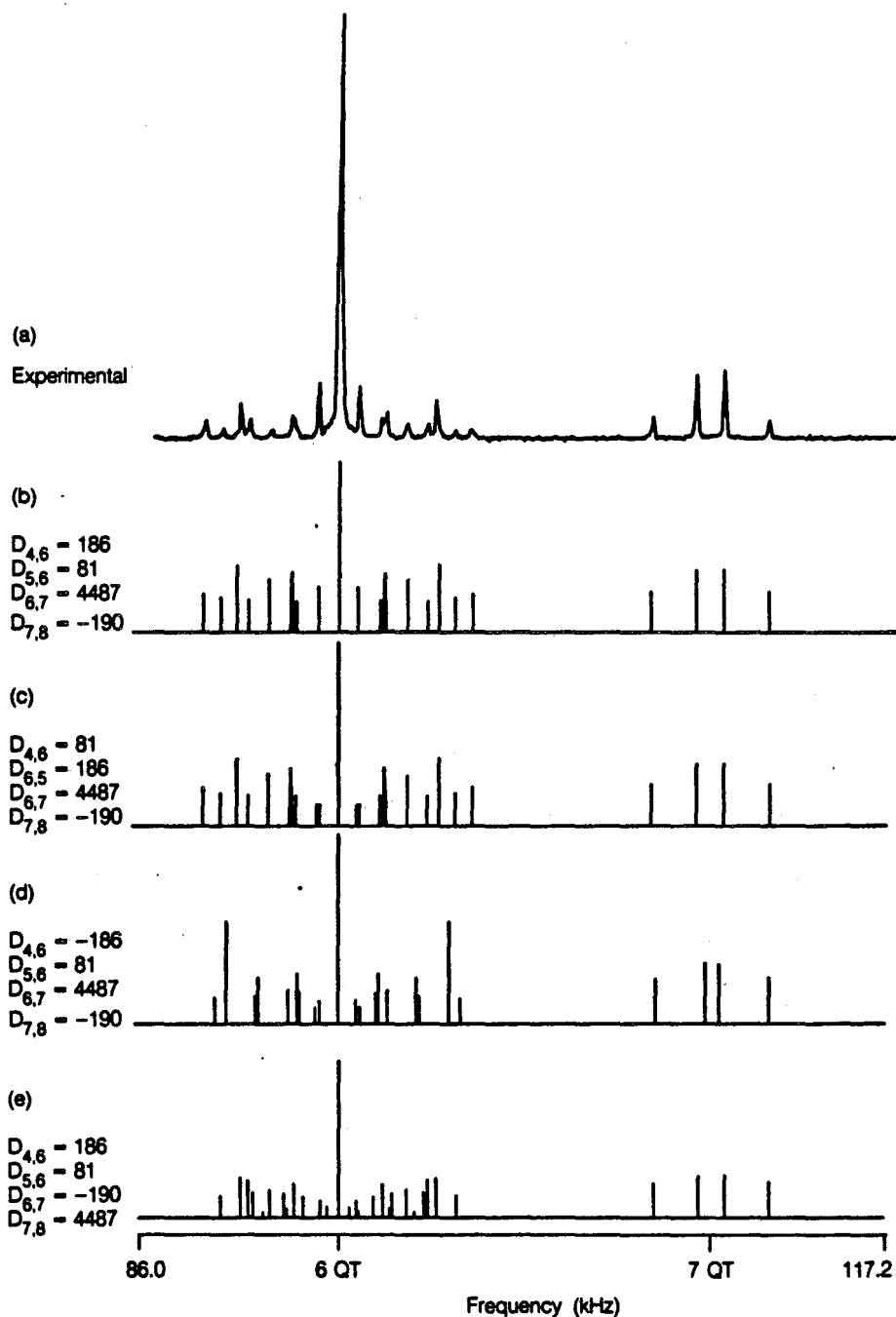
Figure 4.27

A comparison of the experimental 6 and 7 quantum spectra and
spectra calculated for various possible assignments and signs of the
dipole coupling constants. All spectra have a digital resolution of
30.5 Hz/point. (a) is the projection along ω_1 of the spectra in
figure 4.26. (b)-(e) are calculated according to the assignments in
Table IV with the exceptions specified on the left hand side of the
figure.

coherent sets which exclude protons 4 and 6 (or the equivalent) and protons 5 and 6 (or the equivalent), since all other combinations are insensitive to the ordering of these two dipole coupling constants. Solution 4.27(b) appears to be more likely than 4.27(c). Figure 4.27(d) shows the effect of changing the sign of one of the coupling constants. Almost all lines are affected. Figure 4.27(e) shows the effect of switching a geminal and a vicinal coupling constant in the group E_2E_2, resulting in more lines.

The assignments corresponding to figure 4.27(b) are given in Table 4.VIII. Table 4.IX compares the calculated and experimental 6 and 7 quantum frequencies. Assignments were aided by calculation of the dipole couplings from a model. A least squares fit procedure, described in the next section, could be used to assess the probable signs and values of unidentified couplings from the calculation of a model based on known couplings. The fit of the 6 quantum spectrum assured correctness. Topologically the solution is unique, except for an exchange of two protons on the same ethylene group, including all associated couplings. To preserve symmetry, this would imply for n-hexane, a interchange of two ethylene groups simultaneously. By knowing just one assignment of a cis/trans set, such as (4,8) and (4,9) above, all the remaining cis/trans assignments become unambiguous. This is an improvement over the study of the 3-proton systems, for which at least two cis/trans sets must be predetermined.

There is an alternative solution to that in Table 4.VIII which gives exactly the same 6 quantum spectrum as figure 4.27(b). Swop the E_1E_2 vicinal couplings (i.e. (4,6) with (4,7); (5,6) with (5,7); (8,11) with (9,11); (8,10) with (9,10)) and the E_1E_2 couplings across

TABLE 4.VIII

Assignment of the dipole coupling constants

Site	$\underline{D}_{ij}$	Assignment[1]
E_2E_2	+ 4487	6,7
E_2E_2	- 190	7,8
E_2E_2	+ 43	6,8
E_1E_1	+ 3974	4,5
E_1E_1	- 713	5,10
E_1E_1	- 609	4,10
E_1E_2	- 1616	4,8
E_1E_2	- 1086	5,8
E_1E_2	- 186	6,4
E_1E_2	- 81	6,5
MM	+ 1876	1,2
MM	- 206	1,12
ME_2	- 1034	1,6
ME_2	- 598	1,8
ME_1	- 386	1,4
ME_1	- 322	1,10

[1] determined by 6 quantum spectrum and by computer calculations

TABLE 4.IX

Six and Seven Quantum Frequencies

Experimental[1]	Calculated[2]
7 QUANTUM:	
±2472	±2488
±580	±574
6 QUANTUM:	
±5646	±5581
±4898	±4869
±4166	±4199
±3738	±3737
±2853	±2893
±2014	±1972
±1892	±1914
±1785	±1779
±854	±848
	±822

[1] Digital resolution 30 Hz
[2] From coupling constants in Table IV, scaled by a factor 1.09

3 carbon atoms (i.e. (4,8) with (4,9); (5,8) with (5,9); (6,10) with (7,10); (6,11) with (7,11)). This corresponds to the permutation of vertices (atoms) 6 and 7 and vertices 8 and 9 (or of vertices 4 and 5 and vertices 10 and 11). This permutation is taken to be incorrect, because of the logical choice of couplings (4,8) and (4,9).

4.7.4   The Conformational Structure of Hexane

Tables 4.VII and 4.VIII are a complete NMR description of hexane. Interpretation of the structure from this data is not straightforward because they are the end result of unknown molecular and reorientational averaging (eqn. 4.2). Most of the structure determination on flexible molecules in nematics has involved interaction potential calculations[121,143], or assumptions about the non-zero values of S[115,119], and the separability of internal motion and orientational motion[131-2]. In many cases, these models were tested against the measured quadrupole couplings in alkane chains.

Equation (4.3) can be expanded in the molecular principal axis system (PAS) as:

$$D_{ijzz} = \sum_{n=1}^{7} P_n \left\{ S_{33}^n D_{ij33}^n + \frac{1}{3}(S_{11}^n - S_{22}^n)(D_{ij11}^n - D_{ij22}^n) \right.$$
$$\left. + \frac{4}{3} S_{12}^n D_{ij12}^n + \frac{4}{3} S_{13}^n D_{ij13}^n + \frac{4}{3} S_{23}^n D_{ij23}^n \right\} \quad (4.13)$$

S^n is the order parameter of conformer n and p_n its probability. $D_{ij\alpha\beta}$ are the components of the ijth dipole tensor along the molecular axes of conformer n. We use equation (4.13) for hexane by enumerating the conformers from the Rotational Isomeric State (RIS) model of

Flory [144]. Local minima in the potential energy occur for dihedral bond angles of $0°(t)$, $+112.5°(g^+)$ and $-112.5°(g^-)$ [117]. It is assumed that only these discrete dihedral angles occur. The sequence g^+g^- in two consecutive bonds is energetically unfavourable. Thus, n-hexane has seven allowed conformers: ttt, ttg, tgt, tgg, g^+tg^+ g^+tg^-, ggg, occuring with weights 1,4,2,4,2,2,2.

Equation (4.13) can be written in matrix form:

$$
\begin{bmatrix} D_{zz}^1 \\ \cdot \\ \vdots \\ D_{zz}^{16} \end{bmatrix}
-
\begin{bmatrix} D_{33}^{ttt} & D_{33}^{ttg} & \cdots & D_{33}^{ggg} \\ \cdot & & & \cdot \\ \vdots & & & \vdots \\ D_{33}^{ttt} & D_{33}^{ttg} & \cdots & D_{33}^{ggg} \end{bmatrix}
\begin{bmatrix} p^{ttt}S_{33}^{ttt} \\ \cdot \\ \vdots \\ p^{ggg}S_{33}^{ggg} \end{bmatrix}
\quad \begin{array}{l} \text{other} \\ + \text{ terms} \end{array}
\qquad (4.13b)
$$

$$
\underset{\sim}{D}_z - \sum_{\alpha,\beta} \underset{\approx}{D}_{\alpha\beta} \cdot \underset{\sim}{pS}_{\alpha\beta}
$$

It is a set of 16 equations in 35 unknowns. The unknowns are of the form $p_n S_{\alpha\beta}{}^n$, which excludes any possibility of separately determining conformer probabilities and order parameter elements. The only direct solution for molecular structure is to consider the limiting case in which the orientational and conformational motions are independent. Equation (4.2) becomes

$$
D_{ijzz} - \frac{2}{3} \sum_{\alpha,\beta} <S_{\alpha,\beta}> <D_{ij\alpha\beta}> \qquad (4.14)
$$

and equation (4.13) can be written

$$
D_{ijzz} - S_{33} \sum_n p_n D_{ij33}{}^n + \frac{1}{3} (S_{11}-S_{22}) \sum_n p_n (D_{ij11}{}^n - D_{ij22}{}^n)
$$
$$
+ \frac{4}{3} S_{12} \sum_n p_n D_{ij12}{}^n + \frac{4}{3} S_{13} \sum_n p_n D_{ij13}{}^n + \frac{4}{3} S_{23} \sum_n p_n D_{ij23}{}^n \qquad (4.15)
$$

or

$$
\begin{bmatrix} D_{zz}^1 \\ \vdots \\ \vdots \\ D_{zz}^{16} \end{bmatrix} = \begin{bmatrix} D_{33}^{ttt} & D_{33}^{ttg} & \cdots & D_{33}^{ggg} \\ \vdots & & & \vdots \\ \vdots & & & \vdots \\ D_{33}^{ttt} & D_{33}^{ttg} & \cdots & D_{33}^{ggg} \end{bmatrix} \begin{bmatrix} p^{ttt} \\ \vdots \\ \vdots \\ p^{ggg} \end{bmatrix} S_{33} \quad + \text{ other} \atop \text{terms}
$$

(4.15b)

i.e.

$$
\underset{\sim}{D}_z = \sum_{\alpha,\beta} \underset{\approx}{D}_{\alpha\beta} \cdot \underset{\sim}{p} \cdot S_{\alpha\beta}
$$

This is a set of 16 equations in 12 unknowns. The assumption implies one average order parameter for all conformers. It allows the separate determination of S and $\{p_n\}$. This step of separating internal motions from orientational averaging has been suggested on the basis of relatively rapid conformational fluctuations[131], appropriate choice of the molecular axis system[131], independence of the external potential from the internal coordinates [132], and, not least, successful application of equation (4.15) to various examples[132,145-6].

We applied a least squares fit of the vector $\underset{\sim}{D}_{zz}$ to the set of measured couplings, using equation (4.15). The matrix $\underset{\sim}{D}$ of dipole coupling terms was calculated in the PAS of the inertia tensor from the known conformer geometries. Bond lengths and angles used were : $r_{CH} = 1.09$ Å, $r_{CC} = 1.533$ Å, $\angle HCH(Et) = 109.0°$, $\angle HCH(Me) = 109.47°$, $\angle CCC = 112.0°$, $\phi_{dih} = 112.5°$. The five S parameters and seven populations $\underset{\sim}{p}$ were varied to obtain the best fit. A bounded solution space (Table 4.X) was searched.

A fairly good fit was obtained, considering the approximations of the model. Table 4.XI lists the calculated vs. experimental dipole coupling constants. The rms deviation of a calculated coupling

TABLE 4.X

Limits on parameter space

Parameter	lower limit	upper limit	result
P_{ttt}	0.12	0.43	0.367
P_{ttg}	0.03	0.09	0.072
p_{tgt}	0.05	0.18	0.084
P_{tgg}	0.00	0.03	0.021
$P_{g^+tg^+}$	0.00	0.07	0.006
$P_{g^+tg^-}$	0.00	0.12	0.041
P_{ggg}	0.00	0.03	0.000
S_{33}	0.05	0.8	0.2066
S_{11-22}	0.0	0.1	0.0839
S_{12}	-0.03	0.03	-0.0048
S_{13}	-0.03	0.03	-0.0232
S_{23}	-0.03	0.03	0.0138

TABLE 4.XI

Comparison of calculated and experimental D_{ij}

Experimental D	Calculated D	Difference
1876	1895	19
-386	-414	-28
3974	3959	-15
-1034	-1003	31
186	157	-32
81	54	-27
4487	4489	2
-598	-602	-4
-1616	-1642	-26
-1086	-1043	43
43	98	56
-190	-187	3
-322	-291	31
-609	-612	-3
-713	-772	59
-206	-181	25

$$\sqrt{\frac{1}{N-1} \sum_{}^{N} | D_{zz} - D_{calc}|^2} = 31.47$$

constant from an experimental one is ~31 Hz, which is of the order of the experimental error. Table 4.XII lists the calculated conformational probabilities and the order tensor elements. Also shown are the transformation matrix from the PAS of the inertia tensor to the PAS of the order tensor, and the Euler angles which correspond to that transformation. The order tensor 3-axis deviates by 3.6^0 from the z-axis of the inertia tensor. The accuracy of the solution does not allow too literal an interpretation of this result. The accuracy is defined by the fitting program in terms of a tolerance factor X_{tol}, such that

$$||\underline{X}_{sol} - \underline{X}_{true}|| < X_{tol}(1+||\underline{X}_{true}||).$$

$\underline{X}_{sol}$ is the estimated solution and $\underline{X}_{true}$ the true value of the solution at the constrained minimum. A value of <0.05 was found for X_{tol}, implying approximately a 15% error in the results.

The quadrupole splittings were calculated from the list of $\{p_n\}$ and S, and are given in Table 4.XIII with the experimental quadrupole couplings . The agreement is quite good.

4.7.4.1 <u>A Brief Analysis of the Result</u>

The calculated populations of the different conformers are quite plausible. The all-trans conformer occurs in a relatively high percentage compared to the ttg conformer. It complies with a trans to gauche energy of conversion of ~0.960 kcal/mole (calculated at 50^0 C), employing the Rotational Isomeric Model of Flory[144]. This is considerably higher than the generally accepted value of 0.5 kcal/mole for liquid n-hexane[147]. However, there has been considerable discrepancy in the literature on the interpretation of Raman data,

TABLE 4.XII

Calculated populations and order parameters

Populations		Order Parameters	
ttt	36.7	S_{33}	0.2066
ttg	28.7	S_{11-22}	0.0560
tgt	16.8	S_{12}	-0.0032
tgg	8.4	S_{13}	-0.0155
g^+tg^+	1.2	S_{23}	0.0092
$g^{\pm}tg^-$	8.2		
ggg	0.0		

Transformation matrix to Diagonal **S**:

$$\begin{bmatrix} 0.997 & 0.050 & -0.055 \\ -0.048 & 0.998 & 0.028 \\ 0.056 & -0.025 & 0.998 \end{bmatrix}$$

→ Euler angle rotation:

$R(\alpha,\beta,\gamma) = R(-24^\circ, 3.6^\circ, 27^\circ)$

TABLE 4.XIII

Quadrupole Couplings

Experimental	Calculated
0.2930	0.2782
0.8870	0.8791
1.0000	1.0000

Experimental ^{1}H-decoupled deuterium spectrum of n-hexane - d_{81}

Frequency (kHz)

−25   25
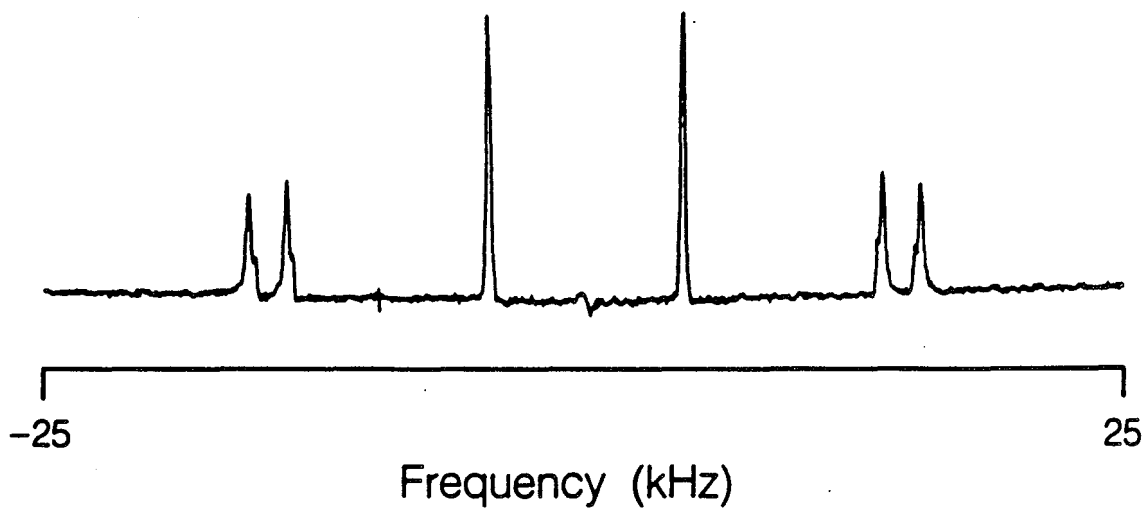
XBL 8612-12882

with some authors calculating a 0.9 kcal/mole energy difference[148].
Our populations agree well with their interpretation of the liquid
hexane Raman data. In addition, computer model calculations of
alkanes dissolved in liquid crystals show much greater success at
fitting quadrupole coupling constants using higher than the accepted
0.5 kcal/mole value[121].

Also noteworthy is the much higher percentage of the g^+tg^-
conformer than g^+tg^+. Study of a model shows that the g^+tg^+ conformer
has greater steric hindrance between the end groups. There is no
precedent for observation of this effect in hexane, but in higher
homologues such as octane, the much lower occurrence of the g^+tg^+
sequence over g^+tg^- has been noted.

The ratio S_{xx-yy}/S_{zz} is 0.271, high compared to most observed
values. Figure 4.28 depicts all possible positions the 6 carbon atoms
can take in the 15 allowed conformations ($g^+g^+g^+$, $g^-g^-g^-$ excluded).
The projection along the x axis is compared to the projection along
the y axis. It shows the high degree of asymmetry in the xy plane,
justifying the high value obtained for S_{xx-yy}/S_{zz}.

Figure 4.29 gives a diagram of each conformer and specifies its
relative population.

4.8 DISCUSSION

We have illustrated the usefulness of applying random deuteration
to a molecule as a means of simplifying its NMR spectrum, while
retaining information content. Two-dimensional multiple quantum
filtered correlation spectroscopy was shown to be an ideal method for
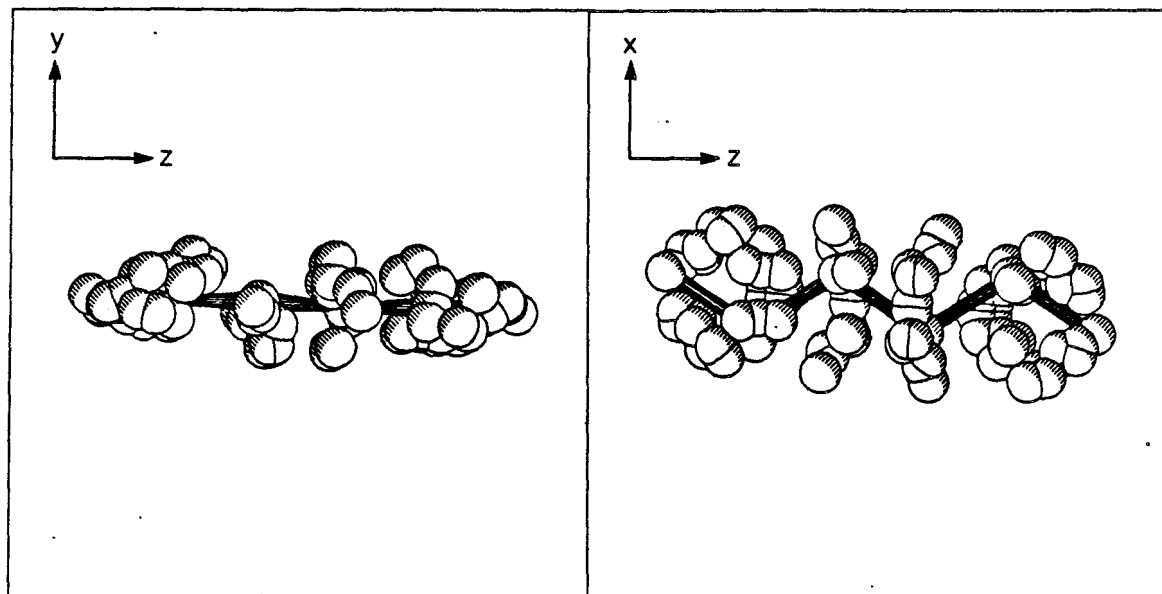
XBL 8612-12879

Figure 4.28

A superposition of the 15 allowed conformations of n-hexane: ttt, ttg$^\pm$, g$^\pm$tt, tg$^\pm$t, tg$^\pm$g$^\pm$, g$^\pm$g$^\pm$t, g$^\pm$tg$^\pm$, g$^\pm$tg$^\mp$. Two projections, in the xz and yz planes show the high asymmetry of the molecular shape in the xy plane.

ttt P = 0.37

ttg 0.29

tgt 0.17

tgg 0.08

g$^+$tg$^+$ 0.01

g$^+$tg$^-$ 0.08

ggg 0.00
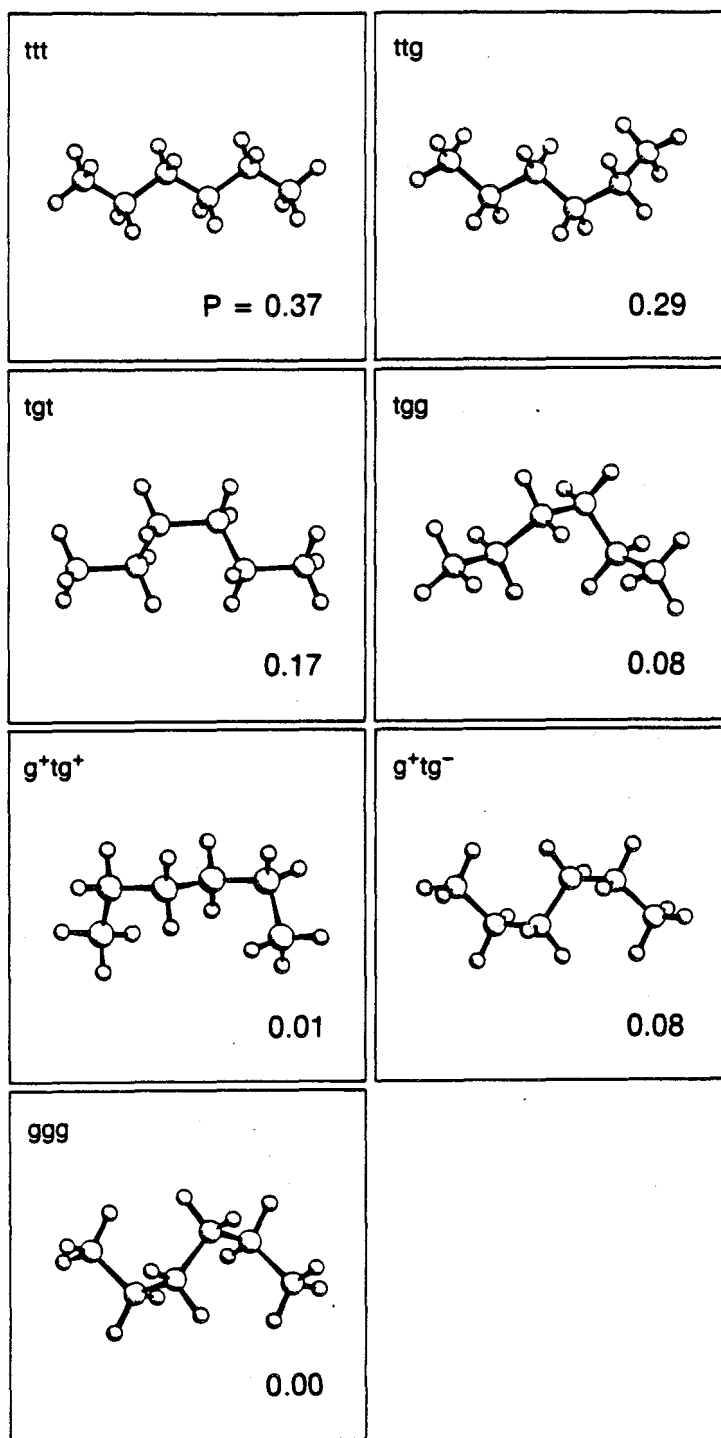
XBL 871-9525

Figure 4.29

The seven conformers of n-hexane and their calculated probabilities.

reading off the dipole coupling constants in a very straightforward way. The set of potentially unidentified couplings could then be specifically assigned using the $3-^1H$ spectra or multiple quantum spectroscopy on the parent compound or an appropriate derivative. Finally we showed how even a very simple model enabled us to arrive at a reasonable conformational structure for a flexible molecule. This structure agreed well with the experimentally determined dipole and quadrupole coupling constants and with previous literature interpretation of the liquid state structure.

4.8.1 A Structural Tool

This kind of result is extremely important for providing information about dynamic structure. NMR is already established as a useful technique in this area. Longitudinal magnetization transfer via the Nuclear Overhauser Effect (NOE) has been used extensively in large molecules to derive distance information. The intensity of cross peaks in a two dimensional NOE experiment (NOESY) is related to the inverse sixth power of the distance between the corresponding pair of coupled nuclei[149]. NOESY exploits the dipolar relaxation mechanism between nuclei. 5Å is the limit for NOE in most experiments. Because of the inaccuracies in measuring absolute intensities and interference caused by surrounding protons, NOE values can typically define only a range of distances by which a pair of protons may be separated.

Dipolar spectra provide distance information in a different way. The dipolar coupling is directly measured as a frequency shift, and is therefore extremely sensitive and accurate. The inverse cube

dependence of the dipole coupling on r implies that much larger distances can be probed. The dipole coupling is 120KHz per Å^3 along the internuclear axis.

Dipolar coupling constants suffer from the unfortunate drawback that they are orientation dependent. NOE is a scalar quantity, and can be readily related to distance. Distance geometry algorithms can be used to assess the probable separation of sets of protons using triangle rules. For a triangle of sides r_i, r_j and r_k,

$$r_i + r_j > r_k \qquad \text{(or any index permutation)}.$$

The corresponding constraint derived from dipole couplings in a liquid crystal would be

$$\sqrt[3]{S_i}\ \bar{r}_i + \sqrt[3]{S_j}\ \bar{r}_j > \sqrt[3]{S_k}\ \bar{r}_k \qquad \text{(and permutations)}$$

where S_i defines the orientation of the internuclear vector:

$$S_i = \langle(1-3\cos^2\theta)/2\rangle,$$

and $\bar{r}_i$ is the distance estimated from $|D_{izz}|$:

$$|D_{izz}| = K\ /\ \bar{r}_i.$$

Nothing can be said about r_i, r_j and r_k unless S_i, S_j and S_k are known. Because of the inseparability of products $\sqrt[3]{S_i}\ \bar{r}_i$, a model is necessary to interpret the $|D_{izz}|$. One might imagine molecular dynamics calculations which use experimental dipole coupling constants as a test of correctness. It is harder to use dipole couplings to restrict phase space at the beginning of the calculation in the way that NOE's are used.

4.8.2 The case of a general N-spin molecule

What is the effect of random deuteration on a molecule of arbitrary size and symmetry? How high in N can we go before the

number of lines in the isotopomer sub-spectra competes with the number of lines in the single quantum spectrum of the unlabelled molecule? This questions both sensitivity and resolution.

Figure 4.30(a) shows the fraction of two-proton isotopomers expected for various N-spin molecules as a function of the percentage deuteration. For n-hexane-d_{81}, we were not working at the peak of the two proton sensitivity, but the signal to noise (S/N) was excellent for a reasonable experimental time. We see that for $N > 30$, we can continue to obtain this level of two-proton substitution.

This plot is relevant for larger N only in cases of high symmetry where there are just a few (~ 20 or less) two-proton isomers among which the total two-proton intensity will be distributed. Correspondingly an uncrowded two-quantum filtered COSY spectrum can be obtained.

By comparison, figures 4.30(b),(c) show plots of the fraction of unique two-proton isomers as a function of percentage deuteration for a molecule of (b) no symmetry, and (c) alkane symmetry. A similar Gaussian-like falloff of unique two-proton intensity occurs in both cases, though it is much more severe for the case of no symmetry. Increasing perecentage of deuteration is required to maximize the two-proton intensity with increasing N. The maximum two-proton intensity of n-dodecane-d_{92} is 0.24 of the two proton intensity of n-hexane-d_{81}. A reduction in S/N of 4 compared to the hexane experiment is not too severe. In terms of sensitivity, the CRASY experiment on a 26 proton alkane chain is practical.

Figure 4.30(d) illustrates the rate of increase of the number of 1,2 and 3 proton substituted isomers of the alkane series with N. A
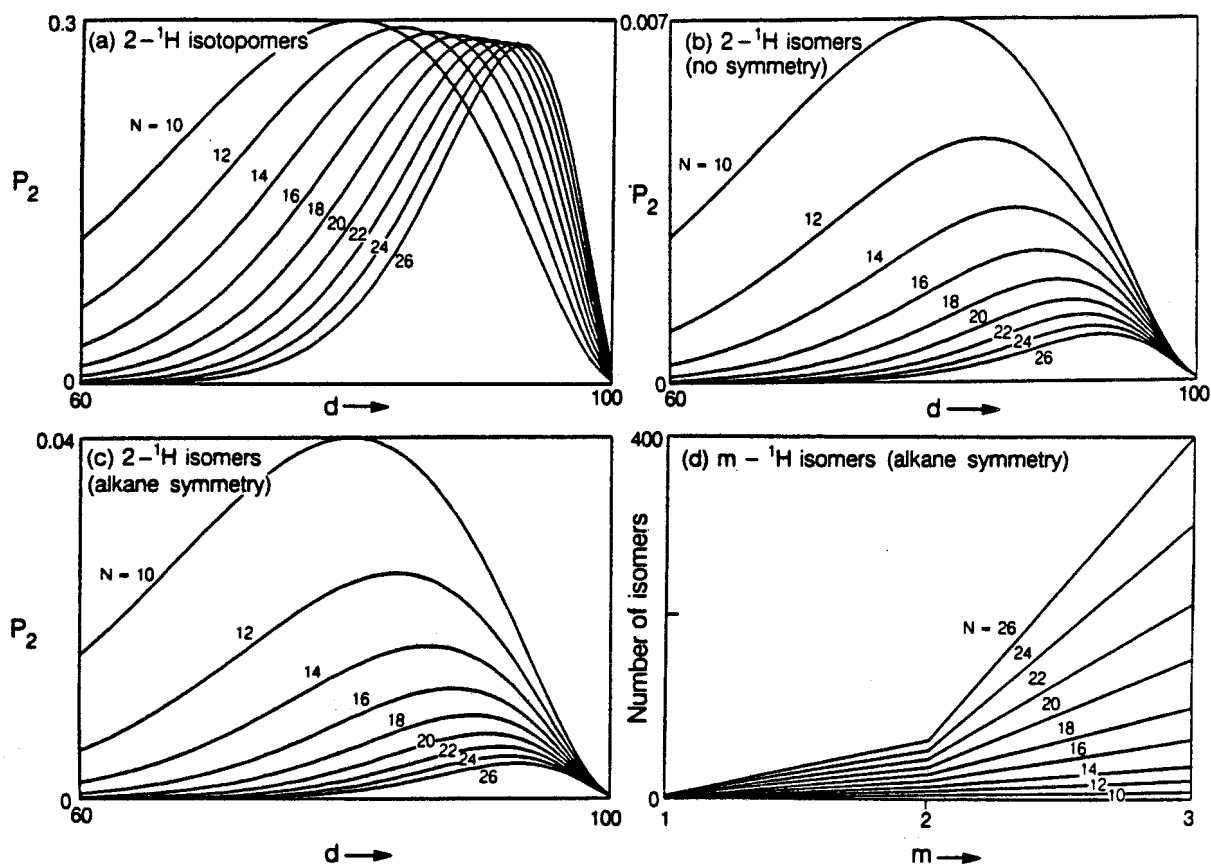
XBL 872-9568

Figure 4.30

Isomer counting statistics for different numbers of protons, N.
(a) gives the fraction of two proton isotopomers as a function of N.
Marked on the curve is the fraction 0.26 of two-proton isotopomers in
n-hexane-d_{81}. (b),(c) are corresponding fractions of isomers of two-
protons in the case of (b) no symmetry and (c) alkane symmetry for N =
10,12,...,26. Marked in (c) is the fraction 0.016 of a unique two-
proton isomer in n-hexane-d_{81}. (d) illustrates the number of isomers
of isotopomers k - 1,2 and 3 as a function of N.

steady increase of 2 proton molecules and a much more rapid increase of 3 proton molecules occurs. For an asymmetrical molecule, the number of isomers is given by the coefficients of the binomial expansion. There are over 4 times as many two-proton isomers in dodecane as in hexane. Difficulties with resolution are likely to occur in the central region of the two-proton filtered COSY experiment. The (N-2) quantum spectrum is also the method of choice for assignment at higher N because of the multitude of 3 proton molecules. The low intensity of higher order spectra would probably mean that one or more derivatives of the parent compound would be necessary.

The two proton spectra will always be much better resolved than the single quantum spectrum. Unlike the latter, they contain no redundant transitions. In fact, some information has been lost - namely the connectivity mapping. However, the amount of information that these spectra yield is much greater than has previously been obtainable. Often, the connectivity can be estimated from model calculations. The two-proton spectra are really the only practical alternative at intermediate values of N.

4.8.3 Future developments

The main difficulty observed with the experimental procedure was decoupling of deuterium from protons. Two quantum decoupling is extremely sensitive to offset, and the high powers used resulted in significant sample heating. The decoupling was not equally effective for all resonances. The problem is caused by large quadrupole couplings and by a spread of chemical shifts. Homonuclear dipole

couplings between deuteriums are also a factor. A new multiple pulse decoupling scheme called COMARO has been developed[150-1], which demonstrates effective decoupling that is orders of magnitude less sensitive than continuous irradiation to resonance offset $\Delta\omega/\omega_1$ and pulse power ω_1/ω_Q. The scheme is easy to implement and will clearly give better resolution and more accurate dipole frequencies. With higher resolution data, inclusion of J couplings will also be necessary.

Higher homologues of the alkane series are being studied. For example, figure 4.31 shows a contour plot of a refocussed COSY experiment on octane. Figure 4.31(a) shows the 4 vicinal couplings of octane. They are assigned presuming no even-odd effect in the free alkane[121]. Figure 4.31(b) shows an inner region of the octane spectrum. A fair number of assignments can be made. Table 4.XIV lists the present state of the study.

Application of CRASY to biological systems is being considered.
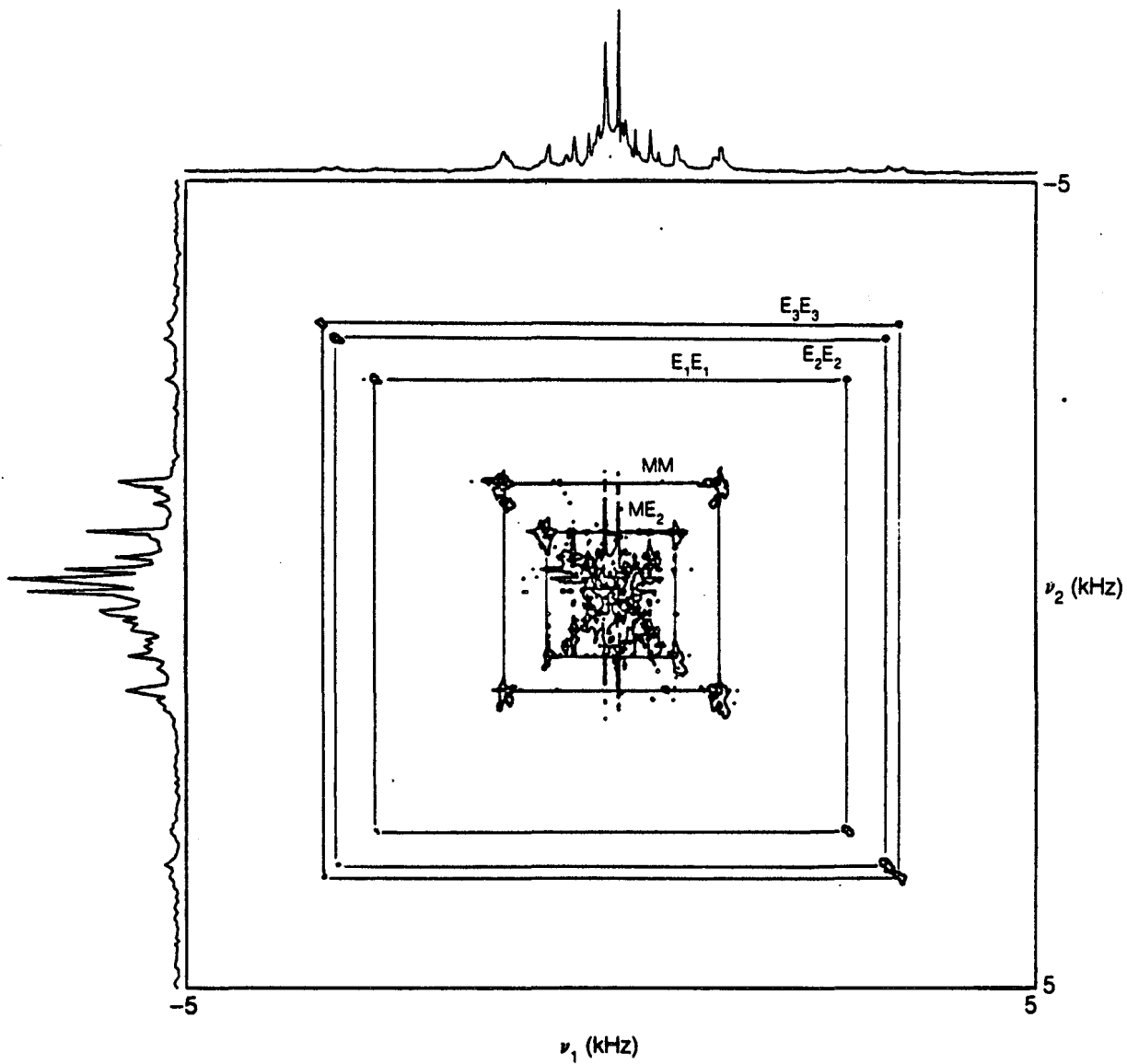
XBL 871-9549

Figure 4.31

Contour plot of the spectrum of n-octane-d_{82}, taken under identical conditions to figure 4.22 for hexane. (a) and (b) show progressively expanded regions of the spectrum. Some of the squares have been marked. In (b) a sine filter was used.
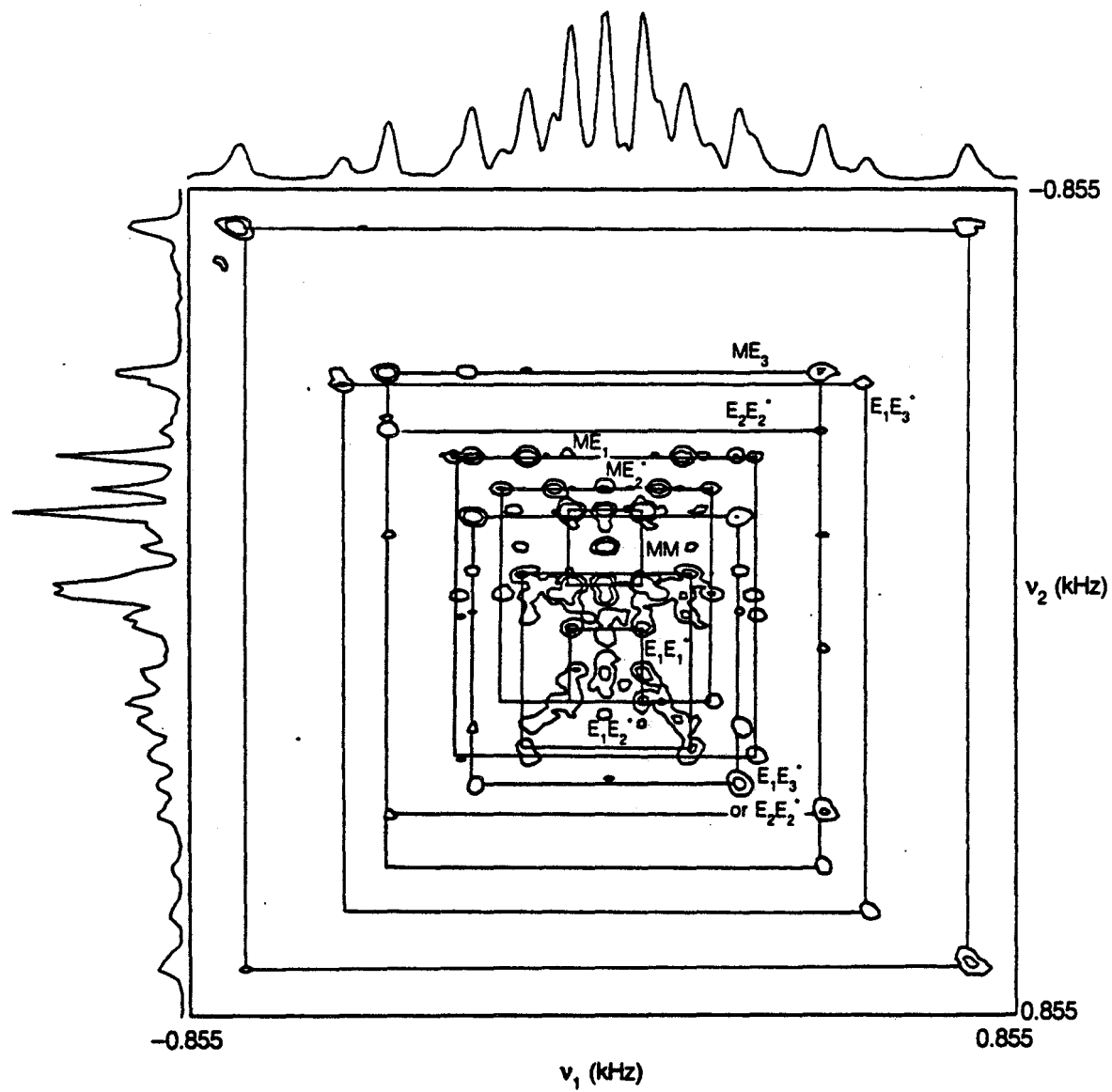
XBL 871-9543

Figure 4.31 (b)

TABLE 4.XIV

Dipole coupling constant data on n-octane (in Hz)

Site	$\lvert D_{ij} \rvert^1$
MM	1705
	101
ME_1	325
	134
ME_2	978
	210
ME_3	566
	314
E_1E_1	3705
	99
	?
E_2E_2	4317
	594
	363 or 238 ?
E_3E_3	4531
	238 or 106 ?
	92
E_1E_2	722
	362
	231
	?
E_1E_3	1604
	1063
	357 ?
	?
E_2E_3	1789
	1114
	?
	?

Chemical shifts

Site	ν_i
M	0
E_1	240
E_2	200
E_3	180

[1] Suggested assignments

CHAPTER 5:

Parallel Data Channel Interface between the δ Spectrometer and

and the VAX 11/730

5.1 PHYSICAL SPECIFICATIONS AND INSTALLATION

The components of the parallel data link between the DG Nova 820 and the VAX 11/730 are two data channel interface boards, one at each computer, and two 40-pin 50 foot shielded cables for sending data in both directions. The specification on these items are:

1) The MDB-DR11W fits into a unibus slot in the main or extension chassis of the VAX. It is configured with W-ENABLE up and W-LINK-M up and all other switches down. The present vector address is non-standard:

        vector address − 500

        device address − 777000.

When the board is idle, no LED's are lighted. Side connectors J3 and J4 are attached to the two 50 foot cables, which are looped back into the main body and appear out the back of the computer. The red strip on each cable goes into pin 1 on each connector on the DR11W (on the right hand side).

2) The MDB-DCHIB can replace the DG Scope board on the δ, but there is no slot available for its permanent insertion. (The computer must be completely powered down before exchanging devices on the bus.) The
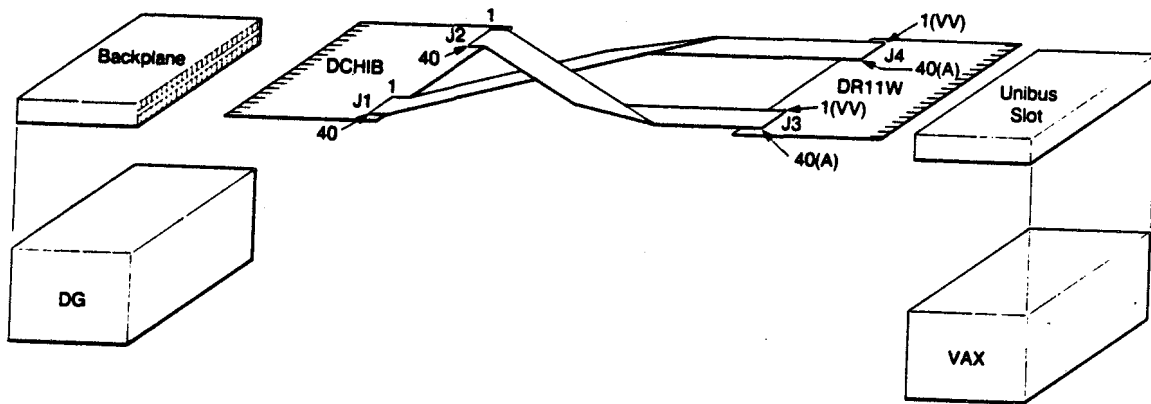
XBL 869-9477

Figure 5.1

Connection of two devices with a parallel data channel interface.

device code (device address) is set at 42_8. The link mode switch is open, and all other switches are closed. Jumper 8 has been etched to provide the correct bit translation between the DG and the VAX (see manual: 'The MDB - DG Data Channel Interface Board')

On first powering up the computer, the READY,ATTN and CRQ LED's are lit. After booting, the ATTN LED goes off. When the board is idle, the READY and CRQ LED's remain lit. The CRQ light must be lit for the board to be functioning; READY goes off while the board is transmitting data.

The cable from J3 on the VAX - DR11W goes into J2 on the DG - DCHIB, and that from J4 on the DR11W goes into J1 on the DCHIB. The cables are twisted so that the red strip on each cable goes into pin 40 on each connector on the DCHIB (on the left hand side) (see figure 1).

3) The two 50 foot cables are supplied by DIGITAL under the catalogue name BC06R-50. They are shielded, grounded 40-pin cables. 50 feet is the maximum length over which parallel data may be transmitted without error.

The speed of data transmission is expected to be about 250 000 words per second.

5.2 SOFTWARE

5.2.1. Installation

a) VAX   When the VAX is booted, an autoconfiguration routine is run which places all known devices on line. The DR11W, called 'XAA0:' by VMS routines, is not included, being in a non-standard position on the bus. It may be placed on line by executing the following instructions in SYS$MANAGER:XACONNECT.COM:

```
$ RUN SYS$SYSTEM:SYSGEN

$ LOAD XADRIVER

$ CONNECT

XAA0/ADAPTER=3/CSR=%0777000/VEC=%0500/NUMVEC=2/DRIVER=XADRIVER

$ EXIT
```

XAA0: should then appear on line in a show devices request.

b) DG   There appears to be no need for any software to identify the DCHIB to the system. It merely responds to device code 42_8.

A routine called IDCH has been included in the subroutine package which uses the RDOS function .IDEF to identify the DCHIB to the system at run time. The routine tells the system what to do if an interrupt is received from that device, which is to clear DONE, the source of the interrupt, i.e. to silence the device (set it idle) until it is required again.

IDCH does not appear to be needed at least in the data channel mode.

5.2.2 Testing the boards individually

For this testing, a loopback cable is placed between the input (J2 or J4) and output (J1 or J3) ports on the same board.

a) VAX

VMS supplies a driver for the DR11W, which is described in the I/O manual. It means that queue I/O requests in a high level language may be used to run the interface. VMS also provides a test program SYS$EXAMPLES:XATEST. In the loopback mode, XATEST, initiated by a run command and then SYSGEN GO, works only for transmit and hangs up on receive.

Other testing programs are in directory [GOCHIN.DR11W].

In the loopback mode, SELFTEST writes 1 word to the Output Data Register (ODR), and then reads it back in 2000 times, checking the transcription each time. If no errors are reported during the WRITE and READ stages, the interface is functioning correctly. The program reports a status, the contents of the Control and Status Register (CSR), the Error and Information Register (EIR) and the number of bytes transferred. For the meaning of these values, see the manual: 'MDB - DR11W'.

b) DG

An assembly language driver for the DCHIB interface, MIRIAM:

DCH.SR, has been written which has the following Fortran callable subroutines and functions:

CALL SDCH(IBUF,NWORD)	send out NWORD words from starting location IBUF (or BUF(1)) to the VAX via the DCHIB
CALL RDCH(IBUF,NWORD)	read in NWORD words from starting location IBUF (or IBUF(1)) from the VAX via the DCHIB
CALL CDCH*	clear the BUSY and DONE flags on the DCHIB
CALL IDCH	RDOS only - mask out interrupts (non-essential in DCH mode)
I = DCHST(STATUS,NW)	tests for completion of a transfer; returns -1 if transfer not complete
(DCHST, STATUS must be declared integer)	0 if transfer complete, BUSY=0, DONE=0
	1 if transfer complete, BUSY=0, DONE=1

STATUS will contain the contents of the status register on completion of the transfer.

NW will contain the word count which should be 0 to indicate that all words have been transmitted. If it is not 0, the status register should be examined for an error. (See manual: MDB-DG Data Channel Interface Board)

*A version of DCH.SR called DCHSPEC.SR was incorporated into SPEC and

has this routine name replaced by CLDCH, because CDCH was needed in the labelled COMMON statement.

In directory MIRIAM, the program SELF2.FR tests the interface in the loopback mode by writing out a word to the ODR and reading it back in 1024 times. It reports any errors in transmission, and a status and word count.

5.2.3 Testing the boards connected

The boards are set up in the final configuration with the cables twisted once.

a) VAX

[GOCHIN.DR11W]DGREAD requests from the user the size of a block of words (integer*2) to be read in from the DG, and then goes into read mode in which it waits 5000s for the requested transfer.

[GOCHIN.DR11W]DGWRITE again requests a block size and transmits this number of words out the DR11W to the DG.

These programs are run in conjunction with MIRIAM:SPH on the DG. They return a status on completion, the contents of the CSR and the number of bytes transferred. There are two bytes per word.

b) DG

MIRIAM:SPH probes the user for the direction of data transfer and

the block size and then proceeds accordingly. The program returns
status and word count.

Note:

(i) The computer that is to receive should always be set in receive
mode before the transmitting computer sends its data.

(ii) The same number of words for transfer should always be indicated
at both ends.

(iii) N.B. The following problems have been noted:

(1) When transfers of the type described above are checked, the first
block of data sent after a power-up is always completely
meaningless, and must be discarded.

(2) Subsequent transfers are correct, except that the first word
transferred is almost always the last word left in the ODR from
the previous transfer; an extra word is therefore always sent,
and the first word discarded. This is not described in the
manuals; further there is an inconsistency in the case of
multiple transfers using TRANS (see below), where many times the
first word is correct and not from a previous transfer, but
occasionally it is. Due to the sporadic nature of this error, a
means of circumventing it has not been found. However, single
transfers in the form used when sending data interactively during
running of the spectrometer are consistent and the first word is
always discarded.

5.2.4 Programs for transmitting data

a)   Under RDOS, MIRIAM:TRANS will read any number of SPEC archives into main memory and transmit these out to the VAX. The VAX is first prepared by running [GOCHIN.DR11W]TRANS2 which asks for the number of spec archives to be received and the size in complex words of each, and then goes into READ mode. The time taken for transfer is limited by the disk I/O access on the DG. To avoid error in the first word (Section 5.2.3), an extra word is stored in each record, and program CHECK should be run to check for error.

b)   Under SPEC, a new command DCHOUT n transfers n complex words to the VAX from starting location BUF1. This command relaces COMPLOT in a version of SPEC called MGMUNOSPEC (which also incorporates the changes made by M. Munowitz in 1984). In addition, a TEMP program, loaded using MIRIAM:<TEMP2D,RAVE> in the TEMP load statement, runs an entire 2D experiment. It has four parameters:

1) Number of t_1 points

2) 1st t_1 point (ms, in register 04)

3) Increment in t_1 (μs, in register 02)

4) Number of run averages per t_1 point

On the VAX, any of the programs DCHREAD, DCHOLD, DCHKEEP may be used. They are all almost identical in that they read a specified number of FID's of specified length, but differ in the file storage handling: DCHREAD closes the file of data only at the end of the run; DCHOLD similarly, but also saves a HOLD file at any intermediate point during the run; DCHKEEP closes the file at the end of each FID input, and reopens it for the next input - it also has a HOLD file option. The

last is the best alternative for a long run, since the data recorded

so far is retained in the event of a computer crash. However, it can

be very slow if other time consuming jobs are running on the VAX.

<u>Note</u>:

The first FID sent should always be discarded.

5.3   <u>INTERNAL STRUCTURE AND OPERATION</u>

This section describes the way in which the parallel data

transfer operates. The description is schematic in that it does not

specify all possible pin connections in terms of their number or exact

physical location, and omits register bits and pin connections that

are not necessary for the basic understanding. It is merely to give a

general idea of the function of a Data Channel (DCH) interface, in

order to clarify the way in which the interface programs work. In

particular, DCH.SR, written in assembler language on the DG, is the

easiest to follow, since it exhibits direct communication with

registers on the board. Figure 5.1 illustrates the general layout of

the two boards and the connection between computers.

5.3.1   <u>Logical Structure of the Interface Board</u>

The data channel interface board is a device which transmits data

in words, or blocks of words (or bytes) and for this purpose there are

a number of registers on the board which can contain information.

They are:

(i) Word Count Register (WCR)

Stores a count of the number of words, n, to be sent out or received, and is varied from -n up to 0 as these words are transmitted.

(ii) Bus Address Register (BAR)

Stores the address in memory of the next word to be transmitted. In the data channel link mode of operation, the WCR and BAR are automatically incremented by 1 after each data transfer.

(iii) Output Data Register (ODR)

Receives a word from main memory to be sent out to the other computer.

(iv) Input Data Register (IDR)

Receives a word from the other computer which will be strobed into main memory.

(v) Error and Information Register (EIR)

Stores a possible lead to the error in the event of a failure in data transmission.

(vi) Control and Status Register (CSR)

Controls initiation and direction of data transfer, and records present status of the board.

This description applies to the registers as they are defined for the DR11W. In the MDB-DCHIB, the Status and Command Registers replace (v) and (vi), with similar functions.

Other important features associated with the boards are a BUSY

and READY/DONE flag.

BUSY	READY/DONE	
1	1	end of cycle
0	1	device waiting for processor
1	0	device in use
0	0	

5.3.2 Operation

(a) Conditioning the Interface

The interface is conditioned by a data channel program as illustrated in figure 5.2. The program loads the WCR and BAR and clears the DONE flag. It sets the FUNCT bits to condition the interface to receive or transmit data. In particular, FUNCT1 = 0 implies that the device is to transmit, FUNCT1 = 1 implies that it is to receive.

The program then sets the GO flag which negates READY. While both READY and BUSY are low in device A, the bus control lines C0 and C1 are asserted in device B. This causes the status bits to be set in device A, informing the CPU of the direction of data transfer. This loop occurs at both ends of the link. It is the beginning of a data cycle.

(b) Sending Data

The program in CPU B now sets the CYCLE bit to initiate a data cycle. This is shown in figure 5.3. CYCLE causes BUSY to go high which has two effects: (1) a data fetch from the CPU B into the ODR; once the data word is latched into the ODR, the BUSY line of device B goes low. (2) While BUSY is still high in B, CYCLE RQ will be asserted

XBL 869-9478
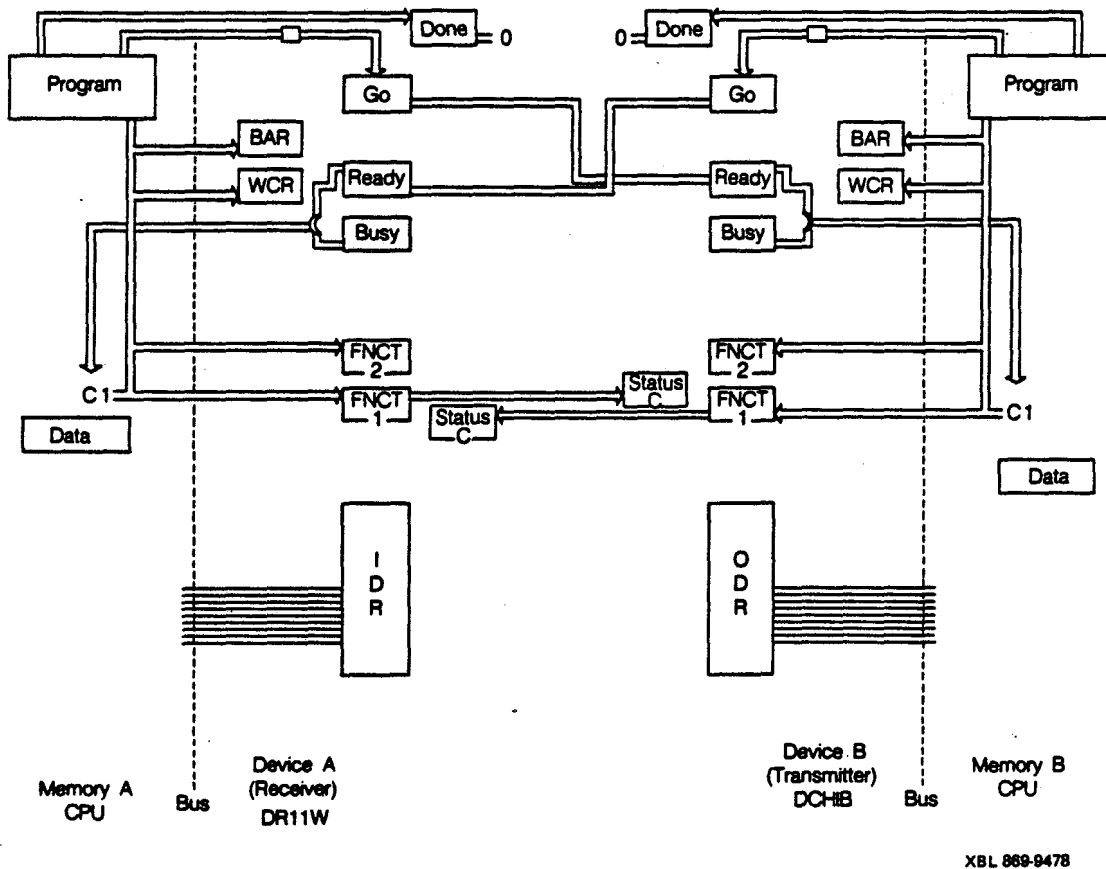
Figure 5.2

Readying of the data channel for a transmit/receive cycle.
Porgrams at both computers load the Word Count and Bus Address
registers and set the FUNCT bits to specify the direction of data
transfer. GO is then set, which causes the status bits in the other
computer to be set, confirming the direction of the data transfer.

in CPU A. Cycle request sets BUSY A high. Once BUSY is high in device A, a data transfer is initiated from the IDR to CPU A memory. BUSY high in device A meanwhile causes CYCLE RQ in CPU B and, if the BUSY in device B has by now been negated, the CYCLE RQ will cause BUSY B to go high again, a new word to be loaded into the ODR and another cycle to ensue. The BUSY/CYCLE RQ interlock continues until WCR = 0, so that a whole buffer of words may be transmitted without program interference. At the point where WCR = 0, during the last word transfer, READY is asserted and while BUSY is also asserted, this signifies the last cycle. DONE is set, which sends an interrupt to the program.
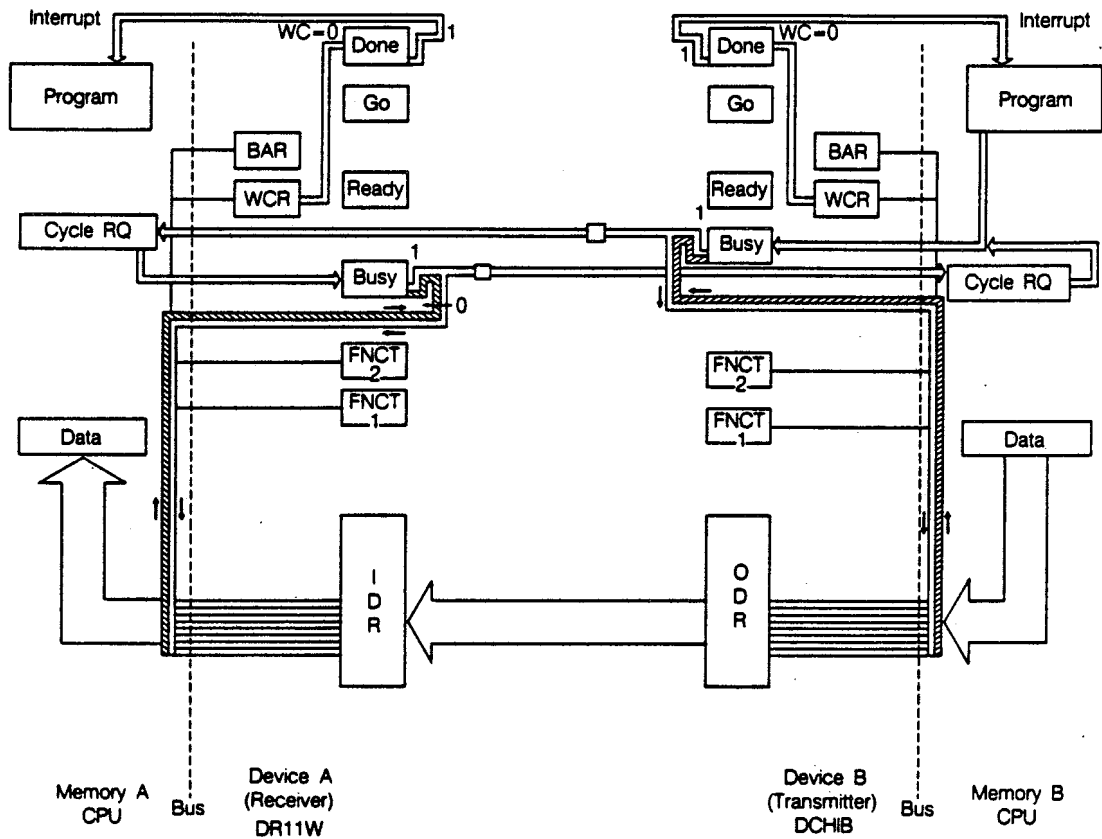
XBL 869-9479

Figure 5.3 Sending data from device B to device A (in our case, this is from the DG DCHIB to the VAX DR11W). The program in device B sets BUSY to initiate a data cycle. Setting BUSY causes the data word to be latched into the Output Data Register, and asserts cycle request in CPU A. Cycle request sets BUSY in A, and latches a word from the Input Data Register into CPU A memory.

REFERENCES

(1) G. Bodenhausen, Multiple Quantum NMR", Progr. in NMR Spectr. 14 (Pergamon Press, Oxford, 1981)

(2) D.P. Weitekamp, "Time-Domain Multiple Quantum NMR", Adv. in Magn. Reson. 11, 111 (1983)

(3) M. Munowitz and A. Pines, Adv. Chem. Phys., 66, 1 (1985)

(4) M. Munowitz and A. Pines, Science, 233, 501 (1986)

(5) C.P. Slichter, "Principles of Magnetic Resonance" (Springer Verlag, Berlin, 1980)

(6) J.W. Emsley and J.C. Lindon, "NMR Spectroscopy using Liquid Crystal Solvents" (Pergamon Press, Oxford, 1975)

(7) "Nuclear Magnetic Resonance of Liquid Crystals", ed. J.W. Emsley, (Reidel, Dordrecht, 1985)

(8) A. Bax, "Two-Dimensional Nuclear Magnetic Resonance in Liquids", PhD Thesis, Delft, November 1981

(9) A. Carrington and A.D. McLachlan, "Introduction to Magnetic Resonance" (Harper and Row, New York, 1967)

(10) R. Poupko, Z. Luz and H. Zimmerman, J. Am. Chem. Soc. 104, 5307 (1982)

(11) U. Haeberlin, "High Resolution NMR in Solids" (Acad. Press, New York, 1976)

(12) C. Cohen-Tannoudji, B. Diu and F. Laloë, "Quantum Mechanics", Vol. I (Wiley, 1977)

(13) M.E. Rose, "Elementary Theory of Angular Momentum" (Wiley, 1957)

(14) M. Mehring, "High Resolution NMR Spectroscopy in Solids", NMR Basic Principles and Progress, ed. P. Diehl, E. Fluck, R. Kosfeld, 11

(Springer-Verlag, Berlin, 1976)

(15) Reference (7): Ch. 1, C. Zannoni, "Quantitative Description of Orientational Order: Rigid Molecules"

(16) Note that my definition of the Euler angles in Appendix A is reversed relative to the definition in reference (15). Therefore, the symmetry operations cause a change in the first index m of $D_{m,n}(\alpha,\beta,\gamma)$ rather than n.

2-D SPECTROSCOPY - GENERAL

(17) J. Jeener, Ampere Int. Summer School II, Basko, Polje, Yugoslavia, 1971

(18) W.P. Aue, E. Bartholdi and R.R. Ernst, J. Chem. Phys. <u>64</u>, 2229 (1976)

(19) D.L. Turner, Progr. In NMR Spectr. <u>17</u>, 281 (1985)

(20) K. Nagayama, A. Kumar, K. Wüthrich and R.R. Ernst, J. Magn. Reson. <u>40</u>, 321 (1980)

(21) G. Wider, S. Macura, A. Kumar, R.R. Ernst and K. Wüthrich, J. Magn. Reson. <u>56</u>, 207 (1984)

COSY

(22) K. Nagayama, P. Bachman, K, Wüthrich and R.R. Ernst, J. Magn. Reson. <u>31</u>, 133 (1978)

(23) K. Nagayama, K. Wüthrich and R.R. Ernst, Biochem. Biophys. Res. Commun. <u>90</u>, 305 (1979)

(24) L. Müller, J. Magn. Reson. <u>38</u>, 79 (1981)

(25) T. Mareci and R. Freeman, J. Magn. Reson. <u>48</u>, 158 (1982)

(26) R.K. Harris and M.J. O'Connor, J. Magn. Reson. <u>57</u>, 115 (1984)

HETERONUCLEAR COSY

(27) G. Bodenhausen, R. Freeman, R. Niedermeyer and D. L. Turner, J.

Magn. Reson. 26, 133 (1977)

(28) A.A. Maudsley and R.R. Ernst, Chem. Phys. Lett. 50, 368 (1977)

(29) G. Bodenhausen and R. Freeman, J. Magn. Reson. 28, 471 (1977)

(30) A.A. Maudsley, L. Müller and R.R. Ernst, J. Magn. Reson. 28, 463
(1977)

(31) A.A. Maudsley, A. Wokaun and R.R. Ernst, Chem. Phys. Lett. 55, 9
(1978)

(32) M.G. Munowitz, W.P. Aue and R.G. Griffin, J. Chem. Phys. 7, 1686
(1982)

MQT CORRELATED

(33) S. Vega and A. Pines, J. Chem. Phys. 66, 5624 (1977)

(34) S. Vega, T.W. Shattuck and A. Pines, Phys. Rev. Lett. 37, 43
(1976)

(35) A. Wokaun and R.R. Ernst, Mol. Phys. 36, 317 (1978)

(36) G. Drobny, A. Pines, S. Sinton, D.P. Weitekamp and D. Wemmer,
Farad. Div. Chem. Soc. Symp. 13, 49 (1979)

(37) W. Warren. D.P. Weitekamp and A. Pines, J. Chem. Phys. 73, 2084
(1980)

(38) G. Bodenhausen, R.L. Vold and R.R. Vold, J. Magn. Reson. 37, 93
(1980)

(39) A. Bax, R. Freeman and T.A. Frenkiel, J. Am. Chem. Soc. 103, 2102
(1981)

(40) D.P. Weitekamp. J.R. Garbow, J.B. Murdoch and A. Pines, J. Am.
Chem. Soc. 103, 3578 (1981)

(41) W.S. Warren and A. Pines, J. Chem. Phys. 74, 2808 (1981)

(42) D.P. Weitekamp, J.R. Garbow and A. Pines, J. Chem. Phys. 77, 2870
(1982)

(43) P.J. Hore, R.M. Scheek, A. Volbeda and R. Kaptein, J. Magn. Reson. <u>50</u>, 328 (1982)

(44) L. Braunschwiller, G. Bodenhausen and R.R. Ernst, Mol. Phys. <u>48</u>, 535 (1983)

(45) V.W. Miner and J.H. Prestegard, J. Am. Chem. Soc. <u>103</u>, 5919 (1981)

(46) J.B. Murdoch, W.S. Warren, D.P. Weitekamp and A. Pines, J. Magn. Reson. <u>60</u>, 205 (1984)

(47) W.S. Warren, J.B. Murdoch and A. Pines, J. Magn. Reson. <u>60</u>, 236 (1984)

(48) M.A. Thomas and A. Kumar, J. Magn. Reson. <u>54</u>, 319 (1983)

2-D NOE, CHEMICAL EXCHANGE

(49) J. Jeener, B.H. Meier, P. Bachmann and R.R. Ernst, J. Chem. Phys. <u>71</u>, 4546 (1979)

(50) A. Kumar, R.R. Ernst and K. Wüthrich, Biochem. Biophys. Res. Commun. <u>95</u>, 1 (1980)

(51) S. Macura, Y. Huang, D. Suter and R.R. Ernst, J. Magn. Reson. <u>43</u>, 259 (1981)

(52) S. Macura, K. Wuthrich and R.R. Ernst, J. MAgn. Reson. <u>46</u>, 269 (1982)

J-SPECTROSCOPY

(53) G. Bodenhausen, R. Freeman and D.L. Turner, J. Magn. Reson. <u>27</u>, 511 (1977)

(54) A. Kumar, J. Magn. Reson. <u>30</u>, 227 (1978)

(55) G. Bodenhausen, J. Magn. Reson. <u>39</u>, 175 (1980)

(56) A.J. Shaka, J. Keeler and R. Freeman, J. Magn. Reson. <u>56</u>, 294 (1984)

MISCELLANEOUS

(57) J. Keeler and D. Neuhaus, J. Magn. Reson. <u>63</u>, 454 (1985)

(58) J.B. Murdoch, PhD. Thesis, University of California, Berkeley, November, 1982

(59) J. R. Garbow, D.P. Weitekamp and A. Pines, J. Chem. Phys. <u>79</u>, 5301 (1983)

(60) L. Müller, J. Am. Chem. Soc. <u>101</u>, 4481 (1979)

(61) L. Müller and R.R. Ernst, Mol. Phys. <u>38</u>, 963 (1979)

(62) J.R. Garbow, D.P Weitekamp and A. Pines, Chem. Phys. Lett. <u>93</u>, 504 (1982)

(63) J.R. Garbow, PhD. Thesis, University of California, Berkeley, July, 1983

(64) G.A. Morris and R. Freeman, J. Am. Chem. Soc. <u>101</u>, 760 (1979)

(65) D.T. Pegg, D.M. Doddrell and M.R. Bendall, J. Chem. Phys. <u>77</u>, 2745 (1982)

(66) O.W. Sørenson, G.W. Eich, M.H. Levitt, G. Bodenhausen and R.R. Ernst, Progr. NMR Spectr. <u>16</u>, 163 (1983)

(67) G. Bodenhausen and R. Freeman, J. Am. Chem. Soc. <u>100</u>, 320 (1978)

(68) A. Bax, R.H. Griffey and B.L. Hawkins, J. Magn. Reson. <u>55</u>, 301 (1983)

(69) A. Bax, R. Freeman, T.A. Frenkiel and M.H. Levitt, J. Magn. Reson. <u>43</u>, 478 (1981)

(70) D.H. Live, D.G. Davis, W.C. Agosta and D. Cowburn, J. Am. Chem. Soc. <u>106</u>, 6104 (1984)

(71) A.D. Bain, J. Magn. Reson. <u>56</u>, 418 (1984)

(72) G. Bodenhausen, H. Kogler and R.R. Ernst, J. Magn. Reson. <u>58</u>, 370 (1984)

(73) D.J. States, R.A. Haberkorn and D.J. Ruben, J. Magn. Reson. <u>48</u>, 286 (1982)

(74) D. Marion and K. Wuthrich, Biochem. Biophys. Res. Commun. <u>113</u>, 967 (1983)

(75) G. Drobny, A. Pines, S. Sinton, W.S. Warren and D.P. Weitekamp, Phil. Trans. Royal Soc. London, <u>A299</u>, 585 (1981)

(76) A. Wokaun and R.R. Ernst, Chem. Phys. Lett. <u>52</u>, 407 (1977)

(77) A. Pines, D. Wemmer, J. Tang, and S. Sinton, Bull. of Amer. Phys. Soc. <u>23</u>, 21 (1978)

MQT FILTERS

(78) P.J. Hore, E.R.P. Zuiderweg, K. Nicolay, K. Dijkstran and R. Kaptein, J. Am. Chem. Soc. <u>104</u>, 4286 (1982)

(79) U. Piantini, O.W. Sørenson and R.R. Ernst, J. Am. Chem. Soc. <u>104</u>, 6800 (1982)

(80) A.J. Shaka and R. Freeman, J. Magn. Reson. <u>51</u>, 169 (1983)

(81) P.J. Hore, R.M. Scheek and R. Kaptein, J. Magn. Reson. <u>52</u>, 339 (1983)

(82) O.W. Sørenson, M.H. Levitt and R.R. Ernst, J. Magn. Reson. <u>55</u>, 104 (1983)

(83) H. Kessler, H. Oschkinat, O.W. Sørenson, H. Kogler and R.R. Ernst, J. Magn. Reson. <u>55</u>, 329 (1983)

HETERONUCLEAR MQT

(84) A. Minoretti, W.P. Aue, M. Rheinhold and R.R. Ernst, J. Magn. Reson. <u>40</u>, 175 (1980)

(85) D.P. Burum and R.R. Ernst, J. Magn. Reson. <u>39</u>, 163 (1980)

(86) G. Bodenhausen and D.J. Ruben, Chem. Phys. Lett. <u>69</u>, 185 (1980)

(87) A. Bax, R.H. Griffey and B.L. Hawkins, J. Am. Chem. Soc. <u>105</u>,

7188 (1983)

(88) A. Bax, J. Magn. Reson. $\underline{53}$, 517 (1983)

(89) V. Rutar, J. Am. Chem. Soc. $\underline{101}$, 4481 (1983)

(90) V. Rutar, J. Am. Chem. Soc. $\underline{105}$, 4095 (1983)

(91) A. Bax, J. Magn. Reson. $\underline{52}$, 330 (1983)

(92) V. Rutar, J. Magn. Reson. $\underline{58}$, 132 (1983)

(93) V. Rutar and T.C. Wong, J. Magn. Reson. $\underline{60}$, 333 (1984)

(94) M. Gochin, D.P. Weitekamp and A. Pines, J. Magn. Reson. $\underline{63}$, 431 (1985)

(95) R. Freeman, T.H. Mareci and G.A. Morris, J. Magn. Reson. $\underline{42}$, 341 (1981)

(96) A.J. Shaka, J. Keeler and R. Freeman, J. Magn. Reson. $\underline{53}$, 313 (1983)

(97) E.L Hahn, Phys. Rev. $\underline{80}$, 450 (1950)

(98) H.Y. Carr amd E.M. Purcell, Phys. Rev. $\underline{94}$, 630 (1954)

(99) S. Meiboom and D. Gill, Rev. Sci. Instr. $\underline{29}$, 688 (1958)

(100) I. Solomon, Phys. Rev. Lett. $\underline{2}$, 301 (1959)

(101) U. Haeberlin, Phys. Rev. $\underline{175}$, 453 (1968)

(102) G.A. Morris and L.D. Hall, J. Am. Chem. Soc. $\underline{103}$, 4703 (1981)

(103) C. Yu and G.C. Levy, J. Am. Chem. Soc. $\underline{106}$, 6533 (1984)

(104) W.P. Aue, S. Müller, T.A. Cross and J. Seelig, J. Magn. Reson. $\underline{56}$, 350 (1984)

(105) S.J. Cox and P. Styles, J. Magn. Reson. $\underline{40}$, 209 (1980)

(106) M. R. Bendall, D.T. Pegg, J. Magn. Reson. $\underline{57}$, 337 (1984)

(107) A.J. Shaka, J. Keeler, M.B. Smith and R. Freeman, J. Magn. Reson. $\underline{61}$, 175 (1985)

(108) M. Gochin and A. Pines, J. Am. Chem. Soc. $\underline{107}$, 7193 (1985)

(109) J.J.H. Ackerman, T.H. Grove, G.C. Wong, D.G. Gadian and G.K. Radda, Nature, 283, 167 (1980)

(110) M.R. Bendall, Chem. Phys. Lett. 99, 310 (1983)

(111) A. Haase, C. Malloy and G.K. Radda, J. Magn. Reson. 55, 164 (1983)

(112) W.P. Aue, S. Müller and J. Seelig, J. Magn. Reson. 61, 392 (1985)

LIQUID CRYSTALS

(113) S. Marcelja, J. Chem. Phys. 60, 3599 (1974)

(114) R.Y. Dong, Can. J. Phys. 56, 678 (1978)

(115) S. Hsi, H. Zimmermann and Z. Luz, J. Chem. Phys. 69, 4126 (1978)

(116) R.Y. Dong, J. Lewis, E. Tomchuk, C.G. Wade and E. Bock, J. Chem Phys. 74, 633 (1981)

(117) E.T. Samulski and R.Y. Dong, J. Chem. Phys. 77, 5090 (1982)

(118) M.E. Moseley, R. Poupko and Z. Luz, J. Magn. Reson. 48, 354 (1982)

(119) E.T. Samulski, Isr. J. Chem. 23, 329 (1983)

(120) K. Müller, P. Meier and G. Kothe, Progr. in NMR Spectr., 17, 211 (1985)

(121) B. Janik, E.T. Samulski and H. Toriumi, J. Phys. Chem. (submitted, 1986)

(122) A. Pines and J.J. Chang, J. Am. Chem. Soc. 96, 5590 (1974)

(123) A. Pines, D.J. Ruben and S. Allison, Phys. Rev. Lett. 33, 1002 (1974)

(124) J. Charvolin and B. Deloche, Mol. Phys. of Liq. Cryst., ed. G.R. Luckhurst and G.W. Gray, Ch. 15 (Acad. Press, London, 1979)

(125) R. Poupko, Z. Luz and H. Zimmermann, J. Am. Chem. Soc. 104,

5307-14(1982)

(126) R.C. Hewitt, S. Meiboom and L.C. Snyder, J. Chem. Phys. 58, 5089 (1973)

(127) Z. Luz and S. Meiboom, J. Chem. Phys. 59, 1077-91 (1973)

(128) S. Meiboom, R.C. Hewitt and Z. Luz, J. Chem. Phys. 66, 4041-51 (1977)

(129) A. Saupe and G. Englert, Phys. Rev. Lett., 11, 462 (1963)

(130) S. Meiboom and L.C. Snyder, Acc. Chem. Res. 4, 81-7 (1971)

(131) E.E. Burnell and C.A. de Lange, Chem. Phys. Lett. 76, 268 (1980)

(132) J.W. Emsley and G.R. Luckhurst, Mol. Phys. 41, 19 (1980)

(133) G. Drobny, D.P. Weitekamp and A. Pines, Chem. Phys. 108, 179-185 (1986)

(134) K. Balasubramanian, J. Chem. Phys. 73, 3321-37 (1980)

(135) K. Balasubramanian, Theor. Chim. Acta (Berl), 51, 37-54 (1979)

(136) W. S. Warren and A. Pines, J. Am. Chem. Soc. 103, 1613-1617 (1981)

(137) M. Gochin, K.V. Schenker, H. Zimmerman and A. Pines, J. Am. Chem. Soc., 108, 6813-4 (1986)

(138) M. Gochin, D. Hugi-Cleary, H. Zimmerman and A. Pines, Mol. Phys. in press (1986)

(139) A. Bax, R. Freeman and S.P. Kempsell, J. Am. Chem. Soc. 102, 4849 (1980)

(140) M. A. Thomas and A. Kumar, J. Magn. Reson. 47, 535-8 (1982)

(141) J.M. Read, R.E. Mayo and J.H. Goldstein, J. Mol. Spectr. 21, 235 (1966)

(142) A. Pines, S. Vega and M. Mehring, Phys. Rev. B 18, 112-125 (1978)

(143) G.R. Luckhurst, Recent Adv. in Liquid Cryst. Polym., ed. L.L. Chapoy (1985), p105

(144) P.J. Flory, "Statistical Mechanics of Chain Molecules", Wiley, New York (1969)

(145) E.E. Burnell and C. A. de Lange, J. Magn. Reson. 39, 461-480 (1980)

(146) "Nuclear Magnetic Resonance of Liquid Crystals", ed. J.W. Emsley, D. Reidel, Dordrecht (1985): C.A. Veracini and M. Longeri, Ch. 6, p139, and ref. therin; L. Lunazzi, "Determination of Organic Structures by Physical Methods", 6, Acad. Press, New York (1976)

(147) I. Kanesaka, R.G. Snyder and H.L. Strauss, J. Chem. Phys. 84, 395 (1986)

(148) P.T.T. Wong, H.H. Mantsch and R.G. Snyder, J. Chem. Phys. 79, 2369 (1983). (R.G.S. expresses some doubt as to the validity of this paper)

(149) I. Solomon, Phys. Rev. 99, 559 (1955); A. Kumar, G. Wagner, R.R. Ernst and K. Wuthrich, 103, 3654-58 (1981)

(150) K.V. Schenker, D. Suter and A. Pines, J. Magn. Reson., submitted (1986)

(151) D. Suter, K.V. Schenker and A. Pines, J. Magn. Reson., submitted (1986)

APPENDIX A

ROTATIONS

The set of three Euler angles α,β,γ specify the orientation of an axis system in space. They are defined as follows for the orientation of a molecular axis system $\underline{1},\underline{2},\underline{3}$ with respect to the laboratory frame x,y,z (refer to figure 1.1):

1) Rotate by α around $\underline{3}$ to bring axis $\underline{2}$ perpendicular to the plane containing $\underline{3}$ and z. New axis positions are $\underline{1}',\underline{2}',\underline{3}'=\underline{3}$.

2) Rotate by β around the new position $\underline{2}'$ to bring $\underline{3}'$ parallel to z. New axis positions are $\underline{1}'',\underline{2}''=\underline{2}',\underline{3}''$.

3) Rotate by γ about $\underline{3}''(z)$ to bring $\underline{1}''$ parallel to x and $\underline{2}''$ parallel to y. New axis positions are $\underline{1}''',\underline{2}''',\underline{3}'''=\underline{3}''$.

In the axial symmetry of high field NMR, this last rotation by γ is not necessary when defining the projection of a tensor along z. The polar angle θ may be equated with β, and the azimuthal angle ϕ with α (figure 1.1).

$$R(\alpha,\beta,\gamma) = R_{\underline{3}''}(\gamma)\ R_{\underline{2}'}(\beta)\ R_{\underline{3}}(\alpha)$$
$$= R_{\underline{3}}(\alpha)\ R_{\underline{2}}(\beta)\ R_{\underline{3}}(\gamma) \tag{A.1}$$

Transformation of a tensor from the PAS to the laboratory frame is given by

$$T_{L,m}^{LAB} = R(\alpha,\beta,\gamma)\ T_{L,m}^{PAS}\ R^{-1}(\alpha,\beta,\gamma)$$
$$= \sum_{n=-L}^{L} D_{n,m}^{L}(\alpha,\beta,\gamma)\ T_{Ln}^{PAS} \tag{A.2}$$

with the Wigner matrix elements:

$$D_{n,m}^{L}(\alpha,\beta,\gamma) = e^{-in\alpha} \, d_{n,m}^{L}(\beta) \, e^{-im\gamma}$$

Tables of reduced rotation matrix elements $d_{n,m}^{L}$ appear in several texts[13,14]. $L = 2$, and for a nematic, $m = 0$, giving

$$T_{2,0}^{LAB} = \sum_{n=-2}^{2} D_{n,0}^{2}(\alpha,\beta,\gamma) \, T_{2,n}^{PAS} \tag{A.3}$$

$$= \sum_{n=-2}^{2} e^{-in\alpha} \, d_{n,0}^{2}(\beta) \, T_{2,n}^{PAS} \tag{A.4}$$

The Wigner rotation elements in Table 1.II are defined from equation (A.4), using tabulated values of the reduced rotation matrices. The equation can be expanded and represented in the Cartesian frame, using Table 1.III for the definition of $T_{2,n}^{PAS}$. The transformation of equation (A.4) into equation (1.19) leads to the definitions of the order parameters given in Table 1.I.

APPENDIX B

Expansion of the terms $\cos(2\pi J_{IS}I_p t)$ and $\sin(2\pi J_{IS}I_p t)$ for the spin systems $I_n S$, $n = 1, 2\ 3$

For 1 proton

$$I_p^{\ 2} = -\frac{1}{4} \ ; \qquad I_p^{\ 3} = -\frac{1}{4}I_p \ ; \qquad I_p^{2n} = \left(\frac{1}{4}\right)^n \ ; \qquad I_p^{2n+1} = \left(\frac{1}{4}\right)^n I_p$$

The cosine and sine functions are expanded in a Taylor series:

$$\cos(2\pi J_{IS}I_p t) = 1 - \frac{(2\pi J_{IS}I_p t)^2}{2} + \frac{(2\pi J_{IS}I_p t)^4}{4} - \ldots$$

$$= 1 - \frac{(\pi J_{IS}t)^2}{2} + \frac{(\pi J_{IS}t)^4}{4} - \ldots$$

$$= \boxed{\cos(\pi J_{IS}t)}$$

Similarly,

$$\sin(2\pi J_{IS}I_p t) = 2\pi J_{IS}I_p t - \frac{(2\pi J_{IS}I_p t)^3}{3} + \ldots$$

$$= 2I_p\left\{ \pi J_{IS}t - \frac{(\pi J_{IS}t)^3}{3} + \ldots \right\}$$

$$= \boxed{2\,I_p \sin(\pi J_{IS}t)}$$

Typically, J_{IS} (sp) $\cong$ 240 Hz.

For 2 protons

$$I_p = I_p + I_{p'} \ ; \quad I_p^2 = \frac{1}{2} + 2I_p I_{p'} \ ; \quad I_p^{2n} = \frac{1}{2} + 2\,I_p I_{p'} \ ; \quad I_p^{2n+1} = I_p$$

Expanding, as before:

$$\cos(2\pi J_{IS} I_p t) = 1 - \frac{(2\pi J_{IS} t)^2}{2}\left(\frac{1}{2} + 2I_p I_{p'}\right) + \frac{(2\pi J_{IS} t)^4}{4}\left(\frac{1}{2} + 2I_p I_{p'}\right) \dots$$

$$= \boxed{1 + \left(\frac{1}{2} + 2I_p I_{p'}\right)(\cos(2\pi J_{IS} t) - 1)}$$

$$\sin(2\pi J_{IS} I_p t) = I_p\left\{2\pi J_{IS} t - \frac{(2\pi J_{IS} t)^3}{3} + \dots\right\}$$

$$= \boxed{I_p \sin(2\pi J_{IS} t)}$$

$J_{IS}(sp^2) \cong 140 - 160$ Hz.

For 3 protons

$$I_p : = I_p + I_{p'} + I_{p''}$$

$$\cos(2\pi J_{IS} I_p t) = \cos(2\pi J_{IS}(I_p + I_{p'})t)\cos(2\pi J_{IS} I_{p''} t) -$$
$$\sin(2\pi J_{IS}(I_p + I_{p'})t)\sin(2\pi J_{IS} I_{p''} t)$$

$$\sin(2\pi J_{IS} I_p t) = \sin(2\pi J_{IS}(I_p + I_{p'})t)\cos(2\pi J_{IS} I_{p''} t) +$$
$$\cos(2\pi J_{IS}(I_p + I_{p'})t)\sin(2\pi J_{IS} I_p'' t)$$

Expanding these equations as in the above leads to the final result:

$$\cos(2\pi J_{IS} I_p t) = \boxed{\cos^3 \pi J_{IS} t - 4(I_p I_p + I_p I_p + I_{p'} I_{p''})\sin^2(\pi J_{IS} t)\cos(\pi J_{IS} t)}$$

$$\sin(2\pi J_{IS} I_p t) = \boxed{2I_p \cos^2 \pi J_{IS} t \sin \pi J_{IS} t - 8I_p I_{p'} I_{p''} \sin^3 \pi J_{IS} t}$$

$J_{IS}(sp^3) \sim 120$ Hz.

APPENDIX C

Summary of computer programs on VAX

DATA CHANNEL TRANSFER AND TEST PROGRAMS

(1) XATESTMG:

(2) SELFTEST: test DR11W internally

(3) DGREAD: read in n blocks of words from the DG; test accuracy

(4) DGWRITE: write out n blocks of words to the DG; test accuracy

(5) DCHREAD: read from DG (concurrently running TEMP) into a single open file

(6) DCHOLD: read from DG (concurrently running TEMP) into 2 files, one of which holds a portion of the data for viewing prior to the end of the experiment

(7) DCHKEEP   read from DG (concurrently running TEMP) into 2 files, one a hold file; the main file is closed after each record written; this is slow - it protects the contents against total loss in the event of a system crash.

(8) TRANS2:   accept data from SPEC archives using TRANS on the DG

(9) CHECK: run to check first word of TRANS2 data

(10) XA.LIB; XATERM : link with above files